2-1-2008

Multimodal breast imaging: Registration, visualization, and image synthesis

Karl Baum

MULTIMODAL BREAST IMAGING: REGISTRATION, VISUALIZATION, AND IMAGE SYNTHESIS

by

Karl G. Baum

B.S. Syracuse University (2003)
M.S. Syracuse University (2004)

A dissertation submitted in partial fulfillment
of the requirements for the degree of Ph.D. in the
Chester F. Carlson Center for Imaging Science
of the College of Science
Rochester Institute of Technology

February 2008

Signature of the Author _____

Accepted by _____
Coordinator, Ph.D. Degree Program Date

CHESTER F. CARLSON
CENTER FOR IMAGING SCIENCE
COLLEGE OF SCIENCE
ROCHESTER INSTITUTE OF TECHNOLOGY
ROCHESTER, NY

CERTIFICATE OF APPROVAL

Ph.D. DEGREE DISSERTATION

The Ph.D. Degree Dissertation of Karl G. Baum
has been examined and approved by the
dissertation committee as satisfactory for
the dissertation requirement for the
Ph.D. degree in Imaging Science

_____
Dr. María Helguera, Dissertation Advisor

_____
Dr. Andrzej Krol

_____
Dr. Joseph Hornak

_____
Dr. John Kerekes

_____
Dr. Roxanne Canosa

_____
Dr. Daniel Phillips

_____
Date

DISSERTATION RELEASE PERMISSION
ROCHESTER INSTITUTE OF TECHNOLOGY
ROCHESTER, NY

MULTIMODAL BREAST IMAGING: REGISTRATION, VISUALIZATION, AND IMAGE SYNTHESIS

I, Karl G. Baum, hereby grant permission to the Rochester Institute of Technology to reproduce my dissertation in whole or in part. Any reproduction will not be for commercial use or profit.

_____
Karl G. Baum

_____
Date

MULTIMODAL BREAST IMAGING: REGISTRATION, VISUALIZATION, AND IMAGE SYNTHESIS

by

Karl G. Baum

Submitted to the Center for Imaging Science
in partial fulfillment of the requirements
for the Ph.D. Degree
at the Rochester Institute of Technology

February 2008

Abstract

The benefit of registration and fusion of functional images with anatomical images is well appreciated in the advent of combined positron emission tomography and x-ray computed tomography scanners (PET/CT). This is especially true in breast cancer imaging, where modalities such as high-resolution and dynamic contrast-enhanced magnetic resonance imaging (MRI) and F-18-FDG positron emission tomography (PET) have steadily gained acceptance in addition to x-ray mammography, the primary detection tool. The increased interest in combined PET/MRI images has facilitated the demand for appropriate registration and fusion algorithms.

A new approach to MRI-to-PET non-rigid breast image registration was developed and evaluated based on the location of a small number of fiducial skin markers (FSMs) visible in both modalities. The observed FSM displacement vectors between MRI and PET, distributed piecewise linearly over the breast volume, produce a deformed Finite-Element mesh that reasonably approximates non-rigid deformation of the breast tissue between the MRI and PET scans. The method does not require a biomechanical breast tissue model, and is robust and fast. The method was evaluated both qualitatively and quantitatively on patients and a deformable breast phantom. The procedure yields quality images with average target registration error (TRE) below 4 mm.

The importance of appropriately jointly displaying (i.e. fusing) the registered images has often been neglected and underestimated. A combined MRI/PET image has the benefits of directly showing the spatial relationships between the two modalities, increasing the sensitivity, specificity, and accuracy of diagnosis.

Additional information on morphology and on dynamic behavior of the suspicious lesion can be provided, allowing more accurate lesion localization including mapping of hyper- and hypo-metabolic regions as well as better lesion-boundary definition, improving accuracy when grading the breast cancer and assessing the need for biopsy. Eight promising fusion-for-visualization techniques were evaluated by radiologists from University Hospital, in Syracuse, NY. Preliminary results indicate that the radiologists were better able to perform a series of tasks when reading the fused PET/MRI data sets using color tables generated by a newly developed genetic algorithm, as compared to other commonly used schemes.

The lack of a known ground truth hinders the development and evaluation of new algorithms for tasks such as registration and classification. A preliminary mesh-based breast phantom containing 12 distinct tissue classes along with tissue properties necessary for the simulation of dynamic positron emission tomography scans was created. The phantom contains multiple components which can be separately manipulated, utilizing geometric transformations, to represent populations or a single individual being imaged in multiple positions. This phantom will support future multimodal breast imaging work.

Acknowledgements

I would like to express my gratitude to those who have supported me and contributed to this research:

My academic advisor Dr. María Helguera. My dissertation committee members for their guidance and constructive criticism: Dr. María Helguera, Dr. Andrzej Krol, Dr. Joseph Hornak, Dr. John Kerekes, Dr. Roxanne Canosa, and Dr. Daniel Phillips.

The breast registration team: Dr. Andrzej Krol, Dr. James Mandel, Dr. Edward Lipson, and Dr. Ioana Coman. Along with fellow students who have continued to refine the registration procedure: Mehmet Unlu and Alphonso Magri.

The individuals who aided in design, implementation, and evaluation of the fusion techniques study: Kimberly Rafferty, Evan Schmidt, Dr. María Helguera, and Dr. Andrzej Krol. Including those that conducted and participated in the study: Alphonso Magri, Michele Lisi, Daniel Tam, Mary McGrath, and Mehr Khan.

Contributors to the breast phantom and synthetic image generation: Kevin McNamara and Dr. María Helguera. Research Computing at the Rochester Institute of Technology and its director Dr. Gurcharan Khanna for providing computational resources. The developers of the software packages SIMRI and SimSET.

The organizations that provided financial support for this research: Center for Imaging Science at the Rochester Institute of Technology, Kodak, Center for Advanced Technology for Electronic Imaging Systems, Virtual Scopics, SUNY

Upstate Medical University, the Research Foundation of SUNY, and the National Science Foundation.

A special thanks goes out to my family, including my wife Lauren, parents David and Pamella, and siblings Rose and Luke, for all of their support.

To Lauren

Table of Contents

Detailed Table of Contents

Chapter 1 Introduction

1.1 Statement of Problem

The aim of the work presented in this thesis is to advance research in multimodal breast imaging. Specific aims include:

1. Develop, implement, and test a registration and warping approach for estimating and correcting deformation of the breast tissue that occurs during imaging.

2. Design algorithms and develop a software toolbox for advanced PET/CT and MR image visualization and exploration, with a focus on development, implementation, and evaluation of image fusion operators.

3. Develop supporting tools for validating multimodal breast imaging procedures such as registration. Specifically, develop tools for the simulation of multimodal medical images with known ground truth.

1.2 Motivation

Breast cancer is the most common malignant disease in women, and the second leading cause of cancer death among American women today.[1] Major goals include increasing early detection rates and improving diagnosis and management techniques. The primary tool for detection and diagnosis of breast cancer is x-ray mammography. However, the use of other modalities such as F-18-FDG positron emission tomography (PET),[2,3,4,5,6,7] and high-resolution and

dynamic contrast-enhanced magnetic resonance imaging (MRI)[8,9,10,11,12] have steadily gained acceptance.

Application of a multimodality approach is advantageous for detection, diagnosis, and management of breast cancer. Initial experiences with utilizing PET, for physiological information, and CT, for anatomical localization, have demonstrated sizable improvements in diagnostic accuracy, allowing better differentiation between normal and pathological uptake and by providing positive finding in CT images for lesions with low metabolic activity.[5] Similar recent research has shown that MRI and PET can complement each other primarily utilizing MRI for localization and extent, and PET for detection and identification.[13,14]

Regular screening utilizing mammography increases the chance of early detection and decreases mortality rates.[15,16,17] The normal follow-up diagnostic treatment after equivocal or difficult to interpret screening mammography is breast biopsy.

Breast biopsy is performed on over 600,000 women annually.[18] It is a relatively expensive (average billed charges in US are $3,400),[18,19] highly invasive, and sometimes painful procedure that can result in complications such as hematomas (7%), infection, echymosis, and pain (in 33-69% of patients).[20] In addition, it produces scar tissue that can complicate future mammographic examinations. Repeat biopsies need to be performed in 14-17% of the cases, usually due to imaging-histologic discordance.[20]

A number of biopsy techniques exist with several of them being less invasive than normal surgical biopsy, such as fine needle aspiration, core needle biopsy, vacuum-assisted biopsy, and ABBI (advanced breast biopsy instrumentation). These attempts to decrease the invasiveness of biopsies have been successful, however they should still be considered highly invasive. They also have limitations placed on their usage by tumor location, size, and composition, as well as the specific imaging modality used during the procedure,[21] and have complications similar to surgical biopsy.[22]

Since a large number of women who undergo breast biopsy do not have cancer (~80%),[23] it would be highly desirable to have an alternative, noninvasive approach to use prior to biopsy in appropriate situations. It is hoped that the additional information provided by combined PET and MRI breast images could be used for this purpose. If it is determined that a biopsy is necessary, the combined information could be used to precisely guide it to the most metabolically active (i.e. most malignant) region.

In addition to early detection and identification of breast cancer, personalized treatment, monitoring, and management can have a significant effect on mortality rates. The complimentary information provided by using different modalities can aid in identifying patient response to treatment.[14] It is hoped that continued research will improve the ability to identify patients who will be non-responsive to a chosen treatment early on, so that treatment can be modified as appropriate. The time saved by identifying patient response early instead of at the end of a long course of treatment, can have a significant effect on survival rates.

1.3 Overview of Thesis

This dissertation is divided into three sections. Each section addresses one of the aims stated in Section 1.1. The first portion, presented in Chapter 2, focuses on the registration of images formed using positron emission tomography and magnetic resonance imaging. After reviewing registration, a novel procedure is presented. This procedure is then evaluated using images of a phantom as well as patient images.

The second aim is addressed in Chapter 3. A review of joint display techniques is presented along with a genetic algorithm for generating two-dimensional color tables satisfying specific requirements. A new software package for easy implementation and evaluation of fusion techniques is discussed. The section concludes with a study designed to evaluate use of the techniques in the context of reading breast images.

Chapter 4 addresses the final aim. Simulated images are proposed as a way of obtaining data sets with a known ground truth. The section begins by presenting the state of the art positron emission tomography and magnetic resonance image simulators. A robust geometric phantom format is then presented along with a digital breast phantom with the appropriate tissue properties for use with the positron emission tomography simulator. The section concludes with the presentation of simulated images of the phantom.

1.4 Anatomical Terms of Location

Prior to proceeding it is necessary to first discuss the terminology used to identify subject positioning and image location. The anatomical coordinate

system defines a location on the human body using the terms: superior, inferior, posterior, anterior, right, and left. Superior means towards the subject's head, while inferior is towards the feet. Anterior refers to the subject's front (chest) while posterior is used to reference the subject's back. Right and left are used to refer to the right and left side of the patient's body, respectively. The use of these terms is demonstrated pictorially in Figure 1.1.

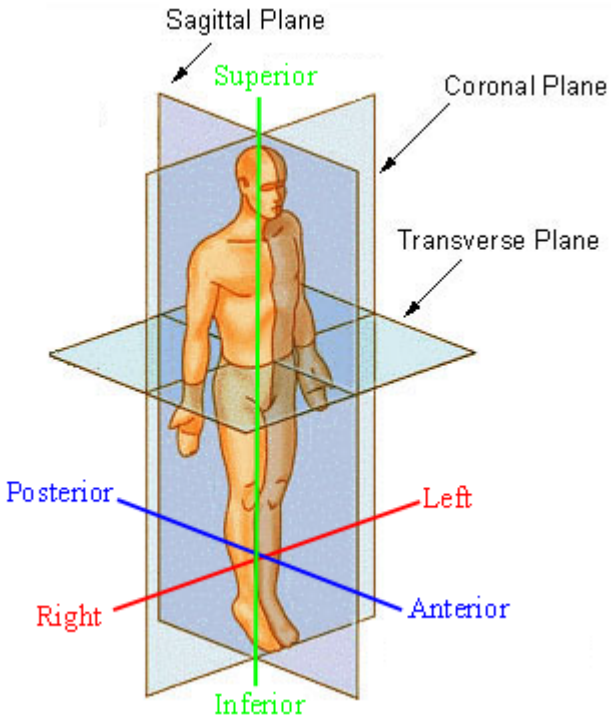

Figure 1.1[A] Anatomical coordinate system and imaging planes.

In addition to describing locations on the subject, we need to be able to describe the location of an image acquired using a medical device. Often these images are acquired as a series of tomograms or slices through the subject. A set or stack of tomograms provide a three dimensional image. The orientations of the tomograms are described using the terms: coronal, sagittal, and axial (or

[A] Figure modified from [24], used with permission.

transaxial). A coronal image runs from right to left and from inferior to superior, a sagittal image from posterior to anterior and from superior to inferior, and an axial image from right to left and posterior to anterior. These planes are indicated in Figure 1.1. It should be noted that these planes are orthogonal and the location within these three planes identifies a specific location within the subject's body.

The final terms defined here describe the location of a subject within the imaging system. The term supine refers to a subject who is lying on their back, while the term prone refers to a subject who is lying on their stomach.

1.5 Imaging Modalities

This section will provide a brief introduction to the medical imaging modalities utilized in this work. Significantly more detail can be found in medical imaging and medical physics literature. For additional information on positron emission tomography see [25,26,27,28,29,30], on computed tomography see [26,27,28,29], and on magnetic resonance imaging see [26,27,28,29,31].

1.5.1 Positron Emission Tomography

Positron emission tomography (PET) is a powerful method of tomographic imaging. Radioactive isotopes, known as radiopharmaceuticals, are administered to the patient and the decay of the isotopes is used to image the distribution of the isotope as a function of time. These radioactive isotopes are often called tracers or radiotracers since the movement or trace of them through the body is of interest. The radioactive isotopes can be administered to the patient through inhalation, orally, or by injection.

The radioactive isotopes are often included in chemicals that the body processes in a specific manner. For example, a glucose analog is a radiopharmaceutical that is processed by the body in a manner similar to glucose. By designing the radiopharmaceutical as a glucose analog it can be used to observe how the body would process glucose.

Positron emission tomography takes advantage of isotopes that decay primarily by positron emission. Positrons are small particles similar to electrons only with a positive charge. The positron is ejected from the decaying atom and loses its kinetic energy through coulomb interactions with the surrounding matter. Since electrons and positrons have the same mass these interactions cause significant changes in the trajectory of the positron and cause it to follow a chaotic path. Eventually the positron will come to rest near an electron and form an orbiting pair known as positronium. Positronium has a lifetime of approximately 10^{-10} seconds.

The electron and positron will then combine causing their annihilation. Their mass is converted into energy and is given off as two photons leaving the site of annihilation. From Einstein's mass energy relationship, Equation 1.1, it can be seen that the mass of the positron and electron ($2\times0.00912\times10^{-27}$ kg) is equivalent to approximately 1023 keV of energy. This energy is divided up evenly between the two photons resulting in gamma photons of approximately 511 keV.

$$E = mc^2 \tag{1.1}$$

Since momentum needs to be conserved the photons need to leave the site in approximately opposite directions. The two photons are said to be collinear because they both traverse the same line in space, in opposite directions.

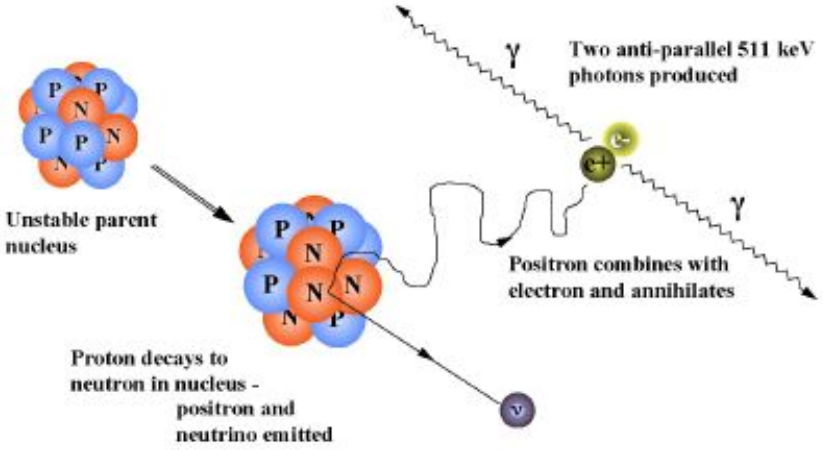

Figure 1.2[B] Schematic showing production of gamma rays from the decay of a radioactive isotope (F-18).

A ring of detectors placed around the object being imaged can detect the created photons. Since the photons are collinear there is a high probability that the decay occurred in the object along a line drawn between the two locations within the detector that the photons were observed. Given a large number of decay events, this collected information can be used to create an estimation map of the distribution of the radiotracer within the body.

The glucose analog used throughout this work is 2-fluoro-2-deoxy-D-glucose, which can be abbreviated as FDG. The fluorine molecule is replaced with the isotope fluorine-18 to create F-18-FDG which will be treated by the body in a manner similar to glucose and has the properties necessary for distribution imaging using PET scanners. As demonstrated by Figure 1.3, the glucose

[B] Figure from [30], used with permission.

analog is taken up by areas in the body which require higher amounts of glucose such as the brain and many cancer cells. In this way it provides information on metabolic activity.

Figure 1.3[C] Example positron emission tomography image showing a coronal slice of the human body. Higher levels of activity can be seen in the brain and renal system including the kidneys and bladder. The heart, liver, and spleen show lower levels of activity.

1.5.2 X-Ray Computed Tomography

X-ray computed tomography imaging (CT) is a transmission imaging technique. X-rays are transmitted into the object being imaged and detectors on

[C] Figure from [32], used with permission.

the opposite side record the quantity of x-rays that successfully pass through the object (Figure 1.4). The quantity of observed x-rays will depend on the composition of material through which the x-rays are required to pass providing a spatially varying signal containing information on the matter between the x-ray source and the detector.

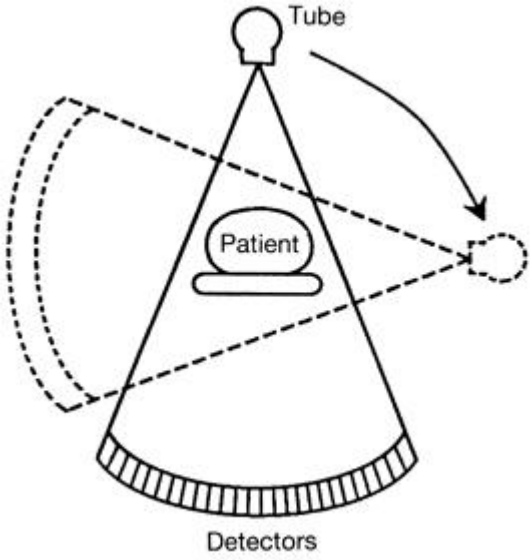

Figure 1.4[D] CT data acquisition procedure.

The attenuation of x-rays will occur as they pass through the object primarily due to the photoelectric effect, and Compton and Rayleigh scattering. The attenuation is dependent on the tissue the x-ray is passing through, for example more attenuation will occur in bone than in soft tissue. In this way the attenuation that occurs can be described by a line integral given by Equation 1.2, where N_i is the x-ray beam intensity at the source, N_0 is the x-ray beam intensity at the detector, $\mu(x)$ is the linear attenuation coefficient at location x in the object, and the integral is over the path of the x-ray beam.

[D] Image courtesy of Hans-Jørgen Smith. Used with permission.

$$\frac{N_i}{N_o} = e^{\int u(x)dx} \qquad (1.2)$$

Additional information on x-ray attenuation by the object can be obtained by transmitting the x-rays through the source at different angles, as shown by the arrows in Figure 1.4. Techniques developed by Radon forms the basis of reconstruction procedures that can be used to recover a detailed image of attenuation at each location within the object from the attenuation collected by transmitting x-rays through the object at a large number of angles. This attenuation image, see for example Figure 1.5, provides high resolution anatomical information.

Figure 1.5[E] Example computed tomography image, showing an axial slice through human head.

[E] Figure from [33], distributed under the Creative Commons Attribution ShareAlike 2.0 License.

1.5.3 Magnetic Resonance Imaging

Magnetic resonance imaging (MRI) is a technique used to create high resolution images of the inside of an object. It utilizes magnetic fields to create a spatially varying response to radio frequency (RF) energy, in particular variations in the phase and frequency of the absorbed and emitted energy are used to isolate the signal from a location within the object.

A particle within a magnetic field can absorb a photon of a frequency dependent on the strength of the magnetic field and the particle's gyromagnetic ratio. This behavior is described by Equation 1.3, where ν is the frequency, γ is the gyromagnetic ratio, and β is the strength of the magnetic field. When performing MRI the particle of interest is usually the nucleus of the hydrogen atom (the proton) due to the large concentration of the element in tissue. The gyromagnetic ratio of hydrogen is approximately 42.58 MHz/T. Energy absorption causes excitation of the particles and subsequent relaxation resulting in the emission of the RF energy, which can be detected using RF coils.

$$\nu = \gamma\beta \tag{1.3}$$

By varying the magnetic field strength across the object being imaged, the location within the object that will absorb an RF pulse of a particular frequency can be controlled, along with the frequency and phase of the RF energy as it is emitted. The absorption and subsequent emission of the RF energy depends on the density of the protons within the tissue and the surrounding molecular structure, giving properties which govern the matter-energy interaction. Specifically, spin density, spin lattice relaxation time, and spin spin relaxation

time. The detected RF energy being emitted from the tissue can be used to create images, usually by using Fourier techniques.

Different protocols (RF signals, magnetic field gradients, and timings) are used to elicit different responses from tissue. In particular, they are designed to maximize the difference in signal (contrast) from tissues of interest. This is demonstrated by Figure 1.6 which shows several images of a slice through a brain with different contrasts. Contrast agents, such as gadolinium, can be used to modify the tissue properties at locations within the object being imaged, aiding in maximizing the contrast. They also provide a means for acquiring function information, such as the uptake and release of the contrast agent. MRI provides a powerful and robust imaging tool with advanced techniques for tasks such as measuring blood flow and water diffusion.

TI (ms)	TR=1000 ms	TR =2000 ms
50	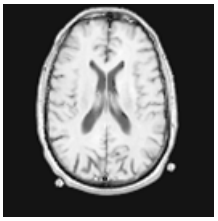	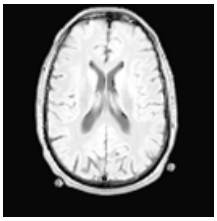
100	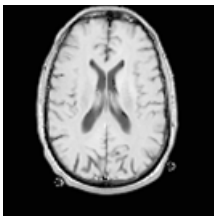	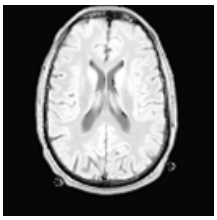
250	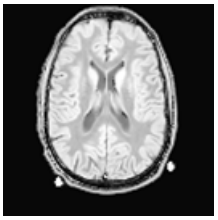	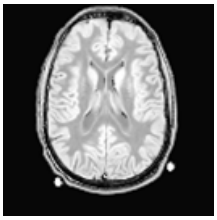
500	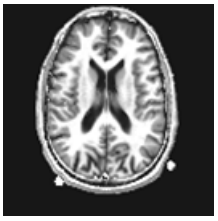	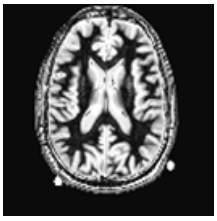
750	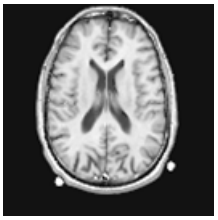	
TI (ms)	TR=1000 ms	TR=2000 ms

Figure 1.6[F] Sample MRI images acquired using an inversion recovery protocol. The different contrasts are due to changes in the timing used, specifically repetition time (TR) and inversion time (TI).

[F] Images from [34], courtesy of Interactive Learning Software. Used with permission.

1.5.4 Ultrasound

Any discussion of breast imaging needs to mention ultrasound. Ultrasound creates images by examining the scattering (reflection) of high frequency sound waves from the tissue being imaged. These waves are generated and detected using transducers. The acquired image can provide information on structure and flow (e.g., blood motion). Ultrasound is generally considered the safest modality since it uses low levels of mechanical energy as opposed to electromagnetic radiation. Since an ultrasound image generally only requires the recorded scatter from a very brief period of time, images can in general be acquired faster than with the other modalities. This allows real-time imaging.

Ultrasound is not discussed further in this work because our focus is on combining metabolic and anatomical information. Metabolic information is unavailable in ultrasound images, and the PET images which provide this information are generally more easily combined with MRI images than ultrasound images. MRI systems have a similar design as PET systems allowing similar imaging procedures, while ultrasound systems require contact to be made between the transducer array and the patient causing additional tissue deformation.

1.6 Physiology of the Breast

Prior to designing a phantom one needs to be knowledgeable about the structures that will be modeled in the phantom. This section provides a brief discussion of breast anatomy and the tissues included in the model. Figure 1.7 and Figure 1.8 support this discussion.

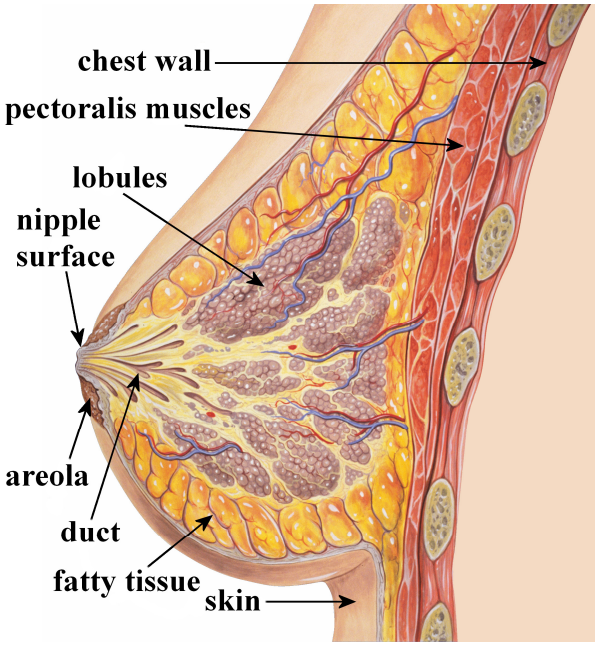

Figure 1.7[G] Breast anatomy.

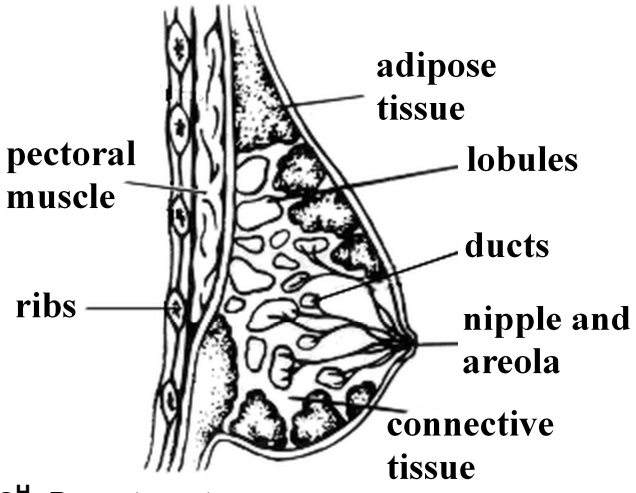

Figure 1.8[H] Breast anatomy.

The back of the breast is well defined by the pectoral muscles (major and minor), supported by the ribs and chest wall. The remaining boundary of the breast is defined by the breast envelope (skin). Like skin throughout the rest of the body the skin on the breast is backed by a layer of adipose (fat) tissue. This layer however can be considerably thicker on the breasts than other areas of the

[G] Figure remixed from [35], distributed under the Creative Commons Attribution 3.0 Unported License.
[H] Figure from [36], used with permission.

body. The remainder of the breast is composed mostly of glandular tissue and connective tissue.

Lobes of glandular tissue, composed of smaller lobules, are responsible for milk production. The lobes (approximately 15) are connected via an intricate system of ducts. These ducts are responsible for storing milk as well as transporting it to the nipple for nourishing young. As a consequence the ducts tend to have a tree like structure branching out from the areola (darkened tissue around the nipple).

The area around the lobules and ducts are filled with supportive connective tissue (stroma), ligaments, and adipose tissue. Fibrous semi-elastic tissues, known as Cooper's ligaments, provide support by connecting the chest wall to the dermis of the skin.

Like every other part of the body, oxygen and nutrients are distributed throughout the breast tissue by a complex network of arteries and veins, usually largest near the back of the breast. The lymphatic system is also present as a series of ducts. Additional information on anatomy can be found by consulting appropriate references.[37,38,39,40,41]

Chapter 2 Registration

2.1 Overview of Registration Techniques

Registration is the process of bringing two or more images into spatial alignment:[42] the "determination of a one-to-one mapping between the coordinates in one space and those in another such that points in the two spaces that correspond to the same anatomical point are mapped to each other."[43] This process typically involves two steps. First, the spatial relationships between the images need to be identified and a mapping between the points in each of the images needs to be found. Second, the mapping needs to be used to transform or warp the images so that a pixel or voxel at the same location in each of the images represents the same physical location.

This difficult task, which has been traditionally performed mentally by the physician, establishes relationships between images and corresponding structures. As medical images began to play a larger role in healthcare, the importance of more objective, and consistent registration methods was realized and significant time and effort has since been devoted to developing techniques for this task. In particular, registration allows images to be superimposed, maximizing the benefit that can be found by utilizing complementary information.[43] The most classic example of this is the display of functional images (such as PET, SPECT, or fMRI) which can provide information on the metabolism, but may lack the necessary anatomical information for accurate localization, with anatomical modalities (such as CT, MRI, or US) providing accurate localization. Of particular interest to breast cancer research is the

benefit to detection and diagnosis of malignant lesions that can come from using multimodal registration techniques.[44,45]

The information required to calculate displacements between images can either come from features visible in both images, or by controlling the environment and calibrating the devices used during image acquisition. Features commonly used to register images include corresponding points (either intrinsic or extrinsic),[46,47,48,49,50,51] corresponding surfaces, curves, or edges,[52,53,54] or similarity measures between the grayscale values of the images.[55,56,57,58,59] Stereotactic frame systems[60,61,62] which mechanically fix the location of the imaging device in relation to the object being imaged is an example of using information on patient and device position during image acquisition for registration. The simplest registration schemes are applied globally and have only a small number of degrees of freedom (ex. rigid registration that supports translation, rotation, and scaling). More complex schemes take into account local deformations and can have thousands of degrees of freedom. For a review of registration techniques see [42,43,63,64,65].

2.2 Breast Registration History

Compared with other areas, such as brain imaging, relatively little effort has been expended developing registration algorithms for breast images. This is most likely due to the complexity of the problem. The breast is composed of soft, highly deformable tissue, without any stationary structures (ex. bone). Some effort has been spent developing intramodality registration algorithms for mammography,[66,67,68,69] ultrasound,[70,71,72,73] and MRI.[74,75,76,77,78,79] Less effort

has been exerted developing intermodality registration. Specifically, work has been done on MRI and mammography registration,[80,81] mostly utilizing MRI to improve mammographic registration.

PET/MRI registration is particularly difficult because we are essentially imaging two different things (metabolic activity vs. anatomy) and as a result there are few if any corresponding features (including the breast surface which is often heavily relied upon by breast registration algorithms). All of the breast registration procedures presented in the previously mentioned publications rely heavily on pixel data and/or corresponding features. This prevents their application to MRI/PET registration. To the author's knowledge, as a result of this issue, there have been no successful attempts at applying classic registration procedure to PET/MRI breast images.

2.3 Deformable Models

Recently individuals within the medical community have devoted efforts to designing biomechanical models in order to predict the deformation of breast tissue.[80,81,82,83,84,85,86,87,88] The application of these models for registration is obvious and they have been directly applied to mammography/MRI registration,[80,81] MRI/MRI registration,[82,83] and as a source of validation data for registration algorithms.[86]

In general these models crudely segment (usually using thresholds) the high resolution MRI images into fatty tissue, adipose tissue, and background. The segmented data is then used to form a discrete geometrical model of the breast. Previously measured elastic properties describing tissue deformation and

compression, such as Young's modulus, stress, and strain are assigned. A skin model might be included. Solid mechanics principles can then be applied to predict how the model will deform under different external forces.

Difficulties exist with these models that can hinder their use in a clinical environment. In particular the accuracy of the geometric models is limited by the segmentation process. The accuracy of automated segmentation is limited, and key features that strongly influence deformation, such as the support provided by Cooper's ligaments,[88] compartmentalization of adipose tissue,[82] and flex of pectoral muscles are difficult to model due to limitations in the segmentation.

Further, the patient specific mechanical properties necessary to predict precise deformations are unavailable, and in fact vary over time due to aging and menstrual phase.[89] Only a few experiments have been performed to measure the mechanical properties of breast tissues, and they have been performed ex-vivo on small samples of tissue.[90,91,92,93] These measurements, which show significant variation,[87] ignore supporting structures and are probably considerably different after excision.[88]

In addition, the boundary conditions, external and internal forces on the breast due to gravity, positioning, compression, and muscle tension, are unknown and need to be estimated. This is particularly true in functional images where the external surface of the breast is not visible. These limitations prevent accurate application of the previously developed physically-based deformable breast models for registration of PET/MRI images.

To address the limitations of current registration procedures and deformable models a novel imaging and registration procedure was designed and implemented. This procedure is based on the finite element method, and supported by controlling boundary conditions and introducing corresponding information in the different modalities. An analogy of the tissue deformation to heat transfer allows this registration procedure to utilize existing methods and software. After providing a background on the finite element method, this procedure will be discussed along with supporting validation studies.

2.4 Finite Element Method

The finite element method is a technique that provides approximate solutions to problems defined in a geometrical space and governed by differential solutions. The geometrical domain is divided up into a number of smaller regions and known functions are used to approximate the variable of interest over these regions. Each of these smaller regions is known as a finite element and is defined by a set of geometric locations known as nodes. Figure 2.1 shows a circle divided into triangle shaped elements. Each triangle is a finite element that can be defined by the location of three nodes located at the corners of the triangle. The elements are connected via the nodes and a connected collection of elements are known as a mesh. The mesh approximates a continuous domain in a piecewise manner and can greatly simplify the solutions to problems within the defined domain.

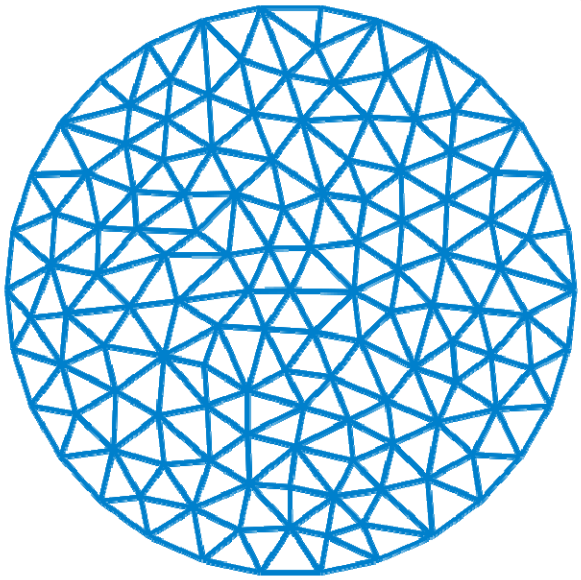

Figure 2.1[I] Example finite element model of a continuous domain.

The finite element method consists of several steps. First, the domain of the problem needs to be approximated using finite elements. Second, interpolation functions need to be defined which determine the variation of the variable of interest through a finite element in terms of the values of the variable at the nodes and the position of the nodes. Third, a stiffness matrix is defined which determines the variation of the variable of interest through the nodes in the mesh. The stiffness matrix combined with appropriate boundary conditions can then be used to estimate the variable of interest at the node locations and the interpolation functions can be used to estimate the variable of interest at other locations within the mesh. This process will be covered in detail throughout the rest of this chapter.

[I] Figure from[94], used with permission.

2.4.1 Steady-State Heat Transfer in Solids

Of particular interest to us is the application of the finite element method for modeling the conduction of heat in solids. Later on, an analogy between the displacement between two images and temperature distribution will be presented.

Heat conduction in solids is described by Fourier's Law, Equation 2.1. This instance of the equation describes heat transfer in the x-direction. Here q is the heat transfer rate, k is the thermal conductivity of the material, A is the cross-sectional area of the material perpendicular to the x-axis, and $\frac{\partial T}{\partial x}$ is the temperature change along the x-direction.

$$q = -kA\frac{\partial T}{\partial x} \tag{2.1}$$

In a steady state situation the heat transfer rate is a constant giving us Equation 2.2. This equation is often referred to as the Laplacian or Laplace's equation.

$$0 = \frac{\partial^2 T}{\partial x^2} \tag{2.2}$$

Further analysis of Equation 2.2 shows it represents linear interpolation. $\partial T_j / \partial x$ and $\partial T_{j+1} / \partial x$ are the derivatives of the temperature at two points located a small distance, c, apart along the x-axis. a and b are small distances along the x-axis and T_i represents the temperature at location i. Specifically, a is the distance between points with temperatures T_{i+1} and T_i and b is the distance between the points with temperatures T_i and T_{i-1}.

$$0 = \frac{\partial^2 T}{\partial x^2} = \frac{\dfrac{\partial T_{j+1}}{\partial x} - \dfrac{\partial T_j}{\partial x}}{c}$$

$$0 = \frac{\partial T_{j+1}}{\partial x} - \frac{\partial T_j}{\partial x} = \frac{T_{i+1} - T_i}{a} - \frac{T_i - T_{i-1}}{b} = bT_{i+1} - bT_i - aT_i + aT_{i-1} \qquad (2.3)$$

$$T_i = \frac{bT_{i+1} + aT_{i-1}}{a+b}$$

When considering heat conduction in multiple dimensions in an isotropic solid Equation 2.2 becomes Equation 2.4 and Equation 2.5, for two and three dimensions respectively.

$$0 = \frac{\partial^2 T}{\partial x^2} + \frac{\partial^2 T}{\partial y^2} \qquad (2.4)$$

$$0 = \frac{\partial^2 T}{\partial x^2} + \frac{\partial^2 T}{\partial y^2} + \frac{\partial^2 T}{\partial z^2} \qquad (2.5)$$

2.4.2 One-Dimensional Heat Transfer Example

The basic element in one-dimensional finite element analysis is a bar element consisting of two nodes connected by an edge of a specified length. Consider the mesh shown in Figure 2.2. The mesh consists of three bar elements defined by four nodes.

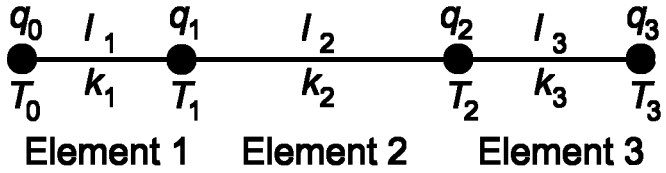

Figure 2.2 Example one-dimensional heat transfer mesh.

The direct approach for the finite element method, which is based upon matrix analysis of structures, will be used in this example. We will first consider Element 1. For a single element, the heat entering the element must equal the heat exiting the element in a steady state situation. The transfer rates at the two nodes of the element come from Fourier's Law (Equation 2.1) and are given by

Equations 2.6 and 2.7. The heat transfer rate and temperature at the first node of the element are given by q_0 and T_0, the conductivity is given by k_1, the length by l_1, and the cross-sectional area by A_1.

$$q_0 = -k_1 A_1 \frac{T_1 - T_0}{l_1} \tag{2.6}$$

$$q_1 = -k_1 A_1 \frac{T_1 - T_0}{l_1} \tag{2.7}$$

We can modify Equation 2.6 creating Equation 2.8 and combine Equations 2.7 and 2.8 into Equation 2.9. This equation has the form shown in Equation 2.10 where $[F]$ is known as the load matrix, $[K]$ is known as the stiffness matrix, and $[u]$ is known as the displacement matrix. The stiffness matrix represents the material properties of the element.

$$-q_0 = -k_1 A_1 \frac{(T_0 - T_1)}{l_1} \tag{2.8}$$

$$\begin{bmatrix} -q_0 \\ q_1 \end{bmatrix} = \frac{-k_1 A_1}{l_1} \begin{bmatrix} 1 & -1 \\ -1 & 1 \end{bmatrix} \begin{bmatrix} T_0 \\ T_1 \end{bmatrix} \tag{2.9}$$

$$[F] = [K][u] \tag{2.10}$$

The equations for a single element, often referred to as local, can be expanded into a global form providing the contribution from the local element to all nodes in the mesh. The global form of Equation 2.9 is given as Equation 2.11.

$$\begin{bmatrix} -q_0 \\ q_1 \\ 0 \\ 0 \end{bmatrix} = \begin{bmatrix} \frac{-k_1 A_1}{l_1} & \frac{k_1 A_1}{l_1} & 0 & 0 \\ \frac{k_1 A_1}{l_1} & \frac{-k_1 A_1}{l_1} & 0 & 0 \\ 0 & 0 & 0 & 0 \\ 0 & 0 & 0 & 0 \end{bmatrix} \begin{bmatrix} T_0 \\ T_1 \\ 0 \\ 0 \end{bmatrix} \tag{2.11}$$

Similar equations can be constructed for the other two elements. These equations are given by Equations 2.12 and 2.13.

$$\begin{bmatrix} 0 \\ -q_1 \\ q_2 \\ 0 \end{bmatrix} = \begin{bmatrix} 0 & 0 & 0 & 0 \\ 0 & \frac{-k_2 A_2}{l_2} & \frac{k_2 A_2}{l_2} & 0 \\ 0 & \frac{k_2 A_2}{l_2} & \frac{-k_2 A_2}{l_2} & 0 \\ 0 & 0 & 0 & 0 \end{bmatrix} \begin{bmatrix} 0 \\ T_1 \\ T_2 \\ 0 \end{bmatrix} \tag{2.12}$$

$$\begin{bmatrix} 0 \\ 0 \\ -q_2 \\ q_3 \end{bmatrix} = \begin{bmatrix} 0 & 0 & 0 & 0 \\ 0 & 0 & 0 & 0 \\ 0 & 0 & \frac{-k_3 A_3}{l_3} & \frac{k_3 A_3}{l_3} \\ 0 & 0 & \frac{k_3 A_3}{l_3} & \frac{-k_3 A_3}{l_3} \end{bmatrix} \begin{bmatrix} 0 \\ 0 \\ T_2 \\ T_3 \end{bmatrix} \tag{2.13}$$

The equations for each of the elements, Equations 2.11, 2.12, and 2.13, can be combined giving us a single system of equations. This task is accomplished by adding together the local stiffness matrices and correctly adjusting the load and displacement matrices to represent the same system. This matrix equation, Equation 2.14, represents the behavior of the entire mesh.

$$\begin{bmatrix} -q_0 \\ 0 \\ 0 \\ q_3 \end{bmatrix} = \begin{bmatrix} \frac{-k_1 A_1}{l_1} & \frac{k_1 A_1}{l_1} & 0 & 0 \\ \frac{k_1 A_1}{l_1} & \frac{-k_1 A_1}{l_1} + \frac{-k_2 A_2}{l_2} & \frac{k_2 A_2}{l_2} & 0 \\ 0 & \frac{k_2 A_2}{l_2} & \frac{-k_2 A_2}{l_2} + \frac{-k_3 A_3}{l_3} & \frac{k_3 A_3}{l_3} \\ 0 & 0 & \frac{k_3 A_3}{l_3} & \frac{-k_3 A_3}{l_3} \end{bmatrix} \begin{bmatrix} T_0 \\ T_1 \\ T_2 \\ T_3 \end{bmatrix} \tag{2.14}$$

By examining Equation 2.14 we can understand the boundary conditions required by the problem. We have a system of four equations, six unknowns and the boundary conditions need to be selected so that the system can be reduced to a system with the same number of equations and unknowns.

In this simple one-dimensional heat transfer example, the boundary conditions are usually specified as the temperatures at the endpoints. Assuming

T_0 and T_3 are known, we can simplify the system by replacing the equations containing these temperatures with simpler ones, giving us Equation 2.15. Since these equations no longer contain any unknowns we can algebraically reduce the size of the system of equation, resulting in Equation 2.16, which can be easily be solved for the remaining unknown temperatures.

$$\begin{bmatrix} T_0 \\ 0 \\ 0 \\ T_3 \end{bmatrix} = \begin{bmatrix} 1 & 0 & 0 & 0 \\ \frac{k_1 A_1}{l_1} & \frac{-k_1 A_1}{l_1} + \frac{-k_2 A_2}{l_2} & \frac{k_2 A_2}{l_2} & 0 \\ 0 & \frac{k_2 A_2}{l_2} & \frac{-k_2 A_2}{l_2} + \frac{-k_3 A_3}{l_3} & \frac{k_3 A_3}{l_3} \\ 0 & 0 & 0 & 1 \end{bmatrix} \begin{bmatrix} T_0 \\ T_1 \\ T_2 \\ T_3 \end{bmatrix} \quad (2.15)$$

$$\begin{bmatrix} -T_0 \frac{k_1 A_1}{l_1} \\ -T_3 \frac{k_3 A_3}{l_3} \end{bmatrix} = \begin{bmatrix} \frac{-k_1 A_1}{l_1} + \frac{-k_2 A_2}{l_2} & \frac{k_2 A_2}{l_2} \\ \frac{k_2 A_2}{l_2} & \frac{-k_2 A_2}{l_2} + \frac{-k_3 A_3}{l_3} \end{bmatrix} \begin{bmatrix} T_1 \\ T_2 \end{bmatrix} \quad (2.16)$$

Using this approach a continuous domain can be approximated by a discrete domain. As the size of the domain increases, the dimensionality increases, and the accuracy of the approximation increases. Equation 2.10 can grow rapidly in size. However, since it represents a system of linear equations it can still be quickly solved using techniques such as Gaussian elimination.[95]

2.4.3 Two-Dimensional Triangle Element

The most basic two-dimensional element is a triangle with a linear variation in temperature through its area (Figure 2.3). The triangle consists of three nodes, each defined by its x- and y-coordinates. As a convention, the coordinates are usually numbered in a counter-clockwise direction.

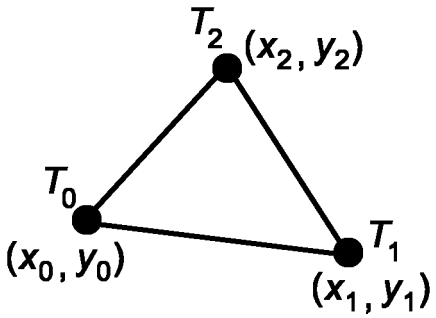

Figure 2.3 Two-dimensional triangle finite element.

2.4.3.1 Interpolation Function

The interpolation for a triangle element is most easily defined using area coordinates (sometimes referred to as natural coordinates or homogeneous barycentric coordinates). Area coordinates define a location inside of a triangle in terms of the locations of its nodes. Consider the triangle shown in Figure 2.4. We would like to represent the interior point, located at (x, y), using area coordinates. Using the interior point the triangle can be divided up into three triangles with areas A_0, A_1, and A_2 as shown in Figure 2.4.

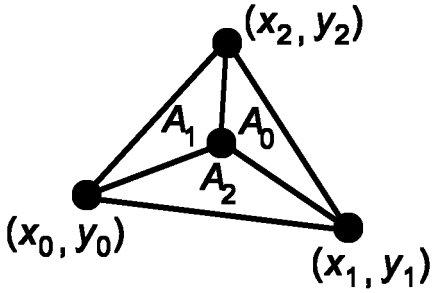

Figure 2.4 Triangle area coordinates.

The area coordinates, L_0, L_1, L_2, of the triangle are defined as simply the ratio of the area of each region to the area of the entire triangle as shown in Equation 2.17. A_i corresponds to the area opposite node (x_i, y_i). The L_i axis

runs perpendicular to the side opposite the node (x_i, y_i), and lines of constant L_i run parallel with that side. Because L_i is defined as a ratio of the areas it is clear that it varies from zero at the side opposite the node (x_i, y_i) to one at node (x_i, y_i). L_0, L_1, and L_2 uniquely define a location within the triangle and by definition clearly add to unity.

$$\begin{aligned} L_0 &= \frac{A_0}{A} \\ L_1 &= \frac{A_1}{A} \\ L_2 &= \frac{A_2}{A} \end{aligned} \tag{2.17}$$

Using Equation 2.18 for the area of a triangle, where the line brackets represent the determinant of the enclosed matrix, we can find the relationship between the area coordinates and the Cartesian coordinates of the triangle and the interior point as given by Equation 2.19.

$$A = \frac{1}{2}\begin{vmatrix} 1 & x_0 & y_0 \\ 1 & x_1 & y_1 \\ 1 & x_2 & y_2 \end{vmatrix} \tag{2.18}$$

$$\begin{aligned} L_0 &= \frac{A_0}{A} = \frac{1}{2A}\begin{vmatrix} 1 & x_1 & y_1 \\ 1 & x_2 & y_2 \\ 1 & x & y \end{vmatrix} = \frac{(x_1 y_2 - x_2 y_1) + x(y_1 - y_2) + y(x_2 - x_1)}{2A} \\ L_1 &= \frac{A_1}{A} = \frac{1}{2A}\begin{vmatrix} 1 & x_2 & y_2 \\ 1 & x_0 & y_0 \\ 1 & x & y \end{vmatrix} = \frac{(x_2 y_0 - x_0 y_2) + x(y_2 - y_0) + y(x_0 - x_2)}{2A} \\ L_2 &= \frac{A_2}{A} = \frac{1}{2A}\begin{vmatrix} 1 & x_0 & y_0 \\ 1 & x_1 & y_1 \\ 1 & x & y \end{vmatrix} = \frac{(x_0 y_1 - x_1 y_0) + x(y_0 - y_1) + y(x_1 - x_0)}{2A} \end{aligned} \tag{2.19}$$

The function, $T(x, y)$, shown in Equation 2.20 meets the requirements for our interpolation function. In particular, the boundary conditions hold in that the

interpolated temperature at a node equals the actual temperature at the node, the coefficients of the function range from having a value of one at its associated node to having a value of zero at the other two nodes, and the function is smoothly varying with a constant gradient.

$$T(x,y) = L_0T_0 + L_1T_1 + L_2T_2 = \begin{bmatrix} L_0 & L_1 & L_2 \end{bmatrix} \begin{bmatrix} T_0 \\ T_1 \\ T_2 \end{bmatrix} \tag{2.20}$$

The coefficients of the interpolation function are referred to as the shape functions. Using the values of L_i provided by Equation 2.19, we can write Equation 2.20 as Equation 2.21.

$$T(x,y) = \frac{1}{2A} \begin{bmatrix} 1 & x & y \end{bmatrix} \begin{bmatrix} x_1y_2 - x_2y_1 & x_2y_0 - x_0y_2 & x_0y_1 - x_1y_0 \\ y_1 - y_2 & y_2 - y_0 & y_0 - y_1 \\ x_2 - x_1 & x_0 - x_2 & x_1 - x_0 \end{bmatrix} \begin{bmatrix} T_0 \\ T_1 \\ T_2 \end{bmatrix} \tag{2.21}$$

2.4.3.2 Stiffness Matrix

It is well known that the stiffness matrix for heat transfer is of the form shown in Equation 2.22. The derivation of this stiffness matrix is discussed in further detail in Appendix A.

$$[K] = \int_A [N]^T [L]^T [k][L][N] t dx dy \tag{2.22}$$

$[N]$ represents the shape functions and $[L]$ is the partial derivative operator, whose application to $[N]$ for the two-dimensional triangle element is shown by Equation 2.23. $[k]$ is the thermal conductivity matrix given by Equation 2.24, where the thermal conductivity along the x and y direction are equivalent for our problem. The integration is carried out over the area of the element and t is the element thickness.

$$[L][N]=\begin{bmatrix}\partial/\partial x\\ \partial/\partial y\end{bmatrix}\begin{bmatrix}L_0 & L_1 & L_2\end{bmatrix}=\begin{bmatrix}\partial L_0/\partial x & \partial L_1/\partial x & \partial L_2/\partial x\\ \partial L_0/\partial y & \partial L_1/\partial y & \partial L_2/\partial y\end{bmatrix} \quad (2.23)$$

$$[k]=\begin{bmatrix}k_x & 0\\ 0 & k_y\end{bmatrix}=\begin{bmatrix}k & 0\\ 0 & k\end{bmatrix} \quad (2.24)$$

Simplifying Equation 2.23 shows that [L][N] is a constant (Equation 2.25) depending only on the nodal locations, and Equation 2.22 can be rewritten as Equation 2.26 where the value of the integral is the area of the triangle.

$$\begin{aligned}[L][N]&=\begin{bmatrix}\partial/\partial x\\ \partial/\partial y\end{bmatrix}\begin{bmatrix}L_0 & L_1 & L_2\end{bmatrix}\\ &=\begin{bmatrix}\partial/\partial x\\ \partial/\partial y\end{bmatrix}\frac{1}{2A}\begin{bmatrix}1 & x & y\end{bmatrix}\begin{bmatrix}x_1y_2-x_2y_1 & x_2y_0-x_0y_2 & x_0y_1-x_1y_0\\ y_1-y_2 & y_2-y_0 & y_0-y_1\\ x_2-x_1 & x_0-x_2 & x_1-x_0\end{bmatrix}\\ &=\frac{1}{2A}\begin{bmatrix}0 & 1 & 0\\ 0 & 0 & 1\end{bmatrix}\begin{bmatrix}x_1y_2-x_2y_1 & x_2y_0-x_0y_2 & x_0y_1-x_1y_0\\ y_1-y_2 & y_2-y_0 & y_0-y_1\\ x_2-x_1 & x_0-x_2 & x_1-x_0\end{bmatrix}\end{aligned} \quad (2.25)$$

$$[K]=[N]^T[L]^T[k][L][N]t\int_A dxdy=[N]^T[L]^T[k][L][N]tA \quad (2.26)$$

Substituting in values and reducing Equation 2.26 gives us Equation 2.27, the local stiffness matrix for a two-dimensional triangular element. Just like in the 1D case, the local stiffness matricies can be expanded into a global form and combined to create a system of linear equations that can be quickly solved.

$$[K]=\begin{bmatrix}(y_1-y_2)^2+(x_2-x_1)^2 & (y_1-y_2)(y_2-y_0)+(x_2-x_1)(x_0-x_2) & (y_1-y_2)(y_0-y_1)+(x_2-x_1)(x_1-x_0)\\ (y_1-y_2)(y_2-y_0)+(x_2-x_1)(x_0-x_2) & (y_2-y_0)^2+(x_0-x_2)^2 & (y_2-y_0)(y_0-y_1)+(x_0-x_2)(x_1-x_0)\\ (y_1-y_2)(y_0-y_1)+(x_2-x_1)(x_1-x_0) & (y_2-y_0)(y_0-y_1)+(x_0-x_2)(x_1-x_0) & (y_0-y_1)^2+(x_1-x_0)^2\end{bmatrix}\frac{kt}{4A} \quad (2.27)$$

A similar process can be followed for other element shapes and higher dimensional elements, such as the 3D tetrahedron. For additional information on the finite element method see [96,97,98,99,100,101,102], for information on heat conduction see [103,104,105,106].

2.5 The Registration Process

The proposed registration procedure overcomes the difficulties previously discussed with regards to classic registration procedures and deformable models. In particular it provides corresponding information in both modalities, provides more exact boundary conditions, and does not require information on patient-specific breast morphology and elastic tissue properties.

To accomplish this, a small number of non-invasive fiducial skin markers visible in PET and MRI are placed on the surface of the examined breast, and identical patient support and positioning systems are used while acquiring images in both modalities. Identical patient positioning is achieved by imaging in the prone position (lying on front with face down) using a replica MRI coil during PET data acquisition. In this situation the breasts are suspended and the only load on them is due to gravity.

As a result, the stress conditions within the breast are nearly identical between PET and MRI. In this situation, intermodality displacements are predominantly due to small positioning errors and underlying biological and physical differences in the imaging process, particularly spatial distortions due to scanners, resolution differences, noise, and biological processes within the patient.[107,108] Since these differences are small we can accurately describe them in a piecewise linear manner. This approach can only be applied in situations where similar stress conditions exist.

A deformable model of the breast is created by using the geometry obtained from the MRI scan. The displacement vectors for each pair of fiducial skin

markers are found and applied to the deformable model. These displacements are first distributed linearly along the surface of the breast (due to skin being orders of magnitude stiffer than adipose or glandular tissue[109]) and then throughout the interior of the breast, providing a geometrical mapping between the two modalities.

To facilitate this, an analogy was made between the displacements and the temperature in a steady state temperature distribution problem. The problems are analogous because the primary variables (temperature and displacement in a single direction), are both linearly distributed over the domain of the problem. Since the displacements along the x-, y-, and z-axes are orthogonal and breast tissue can be considered isotropic,[91] the problem can be treated as three identical steady state temperature distribution problems, each providing the displacements along a different orthogonal direction.

The advantage of this analogy is that standard finite element software exists for quickly and easily solving temperature distribution problems.[110,111] Since the problems are linear and the software has been highly optimized the displacements can be calculated within seconds. This is important if the approach is going to be implemented in a clinical setting.

2.5.1 Image Acquisition

The data were acquired under an approved SUNY Upstate Medical University Institutional Review Board protocol #4493: “Comparative Study of the Diagnostic Accuracy of Scintimammography (Technetium 99m-Sestamibi and Fluorine 18–FDG PET Scintigraphic Imaging) and Magnetic Resonance Imaging

in Identifying Malignant Breast Lesions, in Subjects with Breast Abnormalities." Each subject was required to read and sign the Informed Consent Form prior to participating in the study.

The images were acquired by clinicians during the regular course of their duties. The procedures followed during imaging are outlined here.

2.5.1.1 MRI Image Acquisition

Prior to imaging, the fiducial marker locations are decided and marked on the breast using a felt tipped permanent marker. Initially the fiducial skin markers used during MRI were made from 2 mm diameter, 4 mm length, polyethylene tubes filled with diluted Magnevist (manufactured by Bayer Schering Pharma AG, Berlin, Germany). Magnevist is a complex of gadolinium with a chelating agent (diethylenetriamine penta-acetic acid).[112] In later studies vitamin E capsules were used. These markers were taped to the breast surface at the locations previously marked.

Figure 2.5[J] Philips Intera MRI system.

Figure 2.6[K] Philips 1.5 T breast coil.

[J] Image courtesy of Philips Medical Systems. Used with permission.
[K] Image courtesy of Block Imaging International, Inc. Used with permission.

Figure 2.7[L] Patient positioned prone with breasts suspended in the Philips 1.5 T breast coil.

The MRI images were collected using a Philips Intera 1.5 T system (Figure 2.5) with a standard Phillips breast coil (Figure 2.6). The patient was positioned prone with both breasts suspended into the single well of the breast coil (Figure 2.7). High resolution fast field echo images were collected for use in the registration process. A resolution of 320×256×120 was used with a TR of 14 ms, a TE of 2.9784 ms, slice spacing of 1.12 mm and a flip angle of 20 degrees. The data were reconstructed using Fourier transforms to a 512×512×120 matrix with a resolution 0.7×0.7×1.12 mm. Appendix B contains the DICOM header from a subject scan, additional information on image acquisition can be found there. Other images used for clinical purposes, but not during this work, were also acquired, but are not discussed here.

[L] Image courtesy of Philips Medical Systems. Used with permission.

2.5.1.2 PET Image Acquisition

A procedure similar to that followed during the MRI was followed during the PET data acquisition. Prior to imaging with markers, necessary clinical procedures were performed. During the course of these procedures 10 μCi of F-18 FDG was injected in the medial antecubital vein (located on the inner surface of the forearm) on the side opposite to the breast with the suspicious lesion.

The markers were first placed on the breast at the locations previously marked during the MRI scan. The markers used were created by placing a 1 mL (0.5 μCi) drop of F-18 FDG on a 3 mm diameter blotting paper disk. The disk was then encased using two pieces of medical tape.

The PET images were collected using either a GE Advance NXi (Figure 2.8) or GE Discovery ST (Figure 2.9) system. The patient was positioned prone with breasts suspended into the single well of a breast coil replica (Figure 2.10). The replica was constructed out of plastic with low attenuation for 511 keV photons.

Figure 2.8[M] GE Advance NXi PET system.

Figure 2.9[N] GE Discovery ST PET/CT system.

[M] Figure from [113], used with permission.
[N] Figure from [114], used with permission.

Figure 2.10 MRI breast coil replica for use during PET imaging.

The images were acquired in 2D mode (with septa) for 10 minutes approximately 60 minutes after the administration of the F-18 FDG. The delay in acquisition is due to the experimental images with the markers being obtained after the diagnostic images.

Images were reconstructed using ordered subset expectation maximization.[115] When using the Advance system, images were reconstructed to a 128×128×35 matrix with a 4.30×4.30×4.25 mm resolution, and when using the Discovery system images were reconstructed to a 128×128×91 matrix with a resolution of 4.69×4.69×3.27 mm. Appendix B contains the DICOM header from a subject scan using both systems, additional information on image acquisition and reconstruction can be found there. Other images used for clinical purposes, but not during this work, were also acquired, but are not discussed here.

2.5.2 Registration Procedure

The registration procedure can be performed using the following steps: contrast correction, image orientation adjustment, upsampling, rigid registration, contour extraction, fiducial marker extraction, model generation, displacement propogation, and image transformation.

2.5.2.1 Contrast Correction

This step is necessary as we will be working with the images as a volume, and eventually transforming the images in such a way the voxels may move between slices. DICOM images utilize a slope/intercept relationship to optimize the use of grey values supported by 16-bit data sets. This relationship is shown as Equation 2.28, where stored value (SV) is the stored pixel value in the DICOM image and pixel value unit (U) is the corrected pixel value.[116] The meaning and units of the pixel value units will vary depending on scanner settings and image processing procedures. For example, with PET images the pixel value units might provide the standard uptake value (g/ml) or radioactive concentration (Bq/ml). Each slice of the DICOM image may have its slope and intercept assigned independently of the other slices.

$$U = SV * \text{slope} + \text{intercept} \tag{2.28}$$

To correct for this, the slices in the image volumes need to be normalized. Doing this based on the histogram might provide visually acceptable results, but for accuracy, the contrast of each of the slices in a volume should be modified so that the slope and intercept are constant throughout the volume.

In the case of MRI images, which generally only have a 12-bit dynamic range, each slice usually shares the same intercept and slope and therefore no

correction needs to be applied. In the case of PET images, which have the full 16-bit dynamic range, this correction is always necessary.

2.5.2.2 Image Orientation Adjustment

Even though the patient is positioned the same way in all modalities the different scanners will provide the images oriented differently. Both PET and MRI usually provide images sliced in the transverse direction, however our MRI slices are generally ordered from inferior to superior (foot to head) and our PET slices are generally ordered from superior to inferior (head to foot). In addition, the slices may be oriented in different directions. Usually our MRI images have the patient facing up while the PET images have the patient facing down. To correct for these orientation issues the slices of one modality need to be reordered, and a simple 180 degree rotation is applied. This task can be accomplished by simple reordering of the pixel data.

Modifying the MRI and PET images to have the same orientation allows the x-, y-, and z-axes through each of the images to correspond to the same physical directions through the patient's body. Having the same orientation of the patient in the image from both modalities is essential when reporting fiducial marker locations and comparing locations within the images. The coronal direction is usually chosen as the slicing direction, since images in this direction allow easy extraction of the breast contours.

2.5.2.3 Upsampling

In order to simplify the process, coordinates are expressed in terms of the voxel location along the x-, y-, and z-axes. This causes issues due to resolution

differences in MRI and PET, as well as anisotropic voxels in both modalities. In addition, when it comes time to jointly display the two images, having the images at the same resolution simplifies the process.

During this stage all images are changed to have the same resolution and isotropic voxel. The resolution is chosen based on the smallest voxel dimension within the data set, usually given by the pixel spacing (in slice resolution) in the MRI image. This change in resolution is usually accomplished using simple cubic spline interpolation.

2.5.2.4 Rigid Registration

This is an optional stage that can help the operator visualize the data and the process. During this stage rigid registration (rotation, translation) can be performed to aid the operator when finding corresponding markers between the images. This task has been manually performed by the operator, but could be automated.

Geometric transformations of the pixel data are used to translate and rotate the images.[117] A transformation is accomplished via a matrix multiplication using Equation 2.29, where Q is the transformed location and P is the original location, both given as homogenous coordinates.

$$Q = \begin{bmatrix} Q_x \\ Q_y \\ Q_z \\ 1 \end{bmatrix} = M \begin{bmatrix} P_x \\ P_y \\ P_z \\ 1 \end{bmatrix} = MP \qquad (2.29)$$

M is the transformation matrix. A translation is equivalent to a shift along each of the three primary axes. For a translation, M is given as Equation 2.30, where T_x, T_y, and T_z represent the shift along each axis.

$$\begin{bmatrix} 1 & 0 & 0 & T_x \\ 0 & 1 & 0 & T_y \\ 0 & 0 & 1 & T_z \\ 0 & 0 & 0 & 1 \end{bmatrix} \tag{2.30}$$

Transformation matrices which perform a counter clockwise rotation around the x-, y-, and z-axes are given by Equations 2.31, 2.32, and 2.33, respectively. θ is the angle of rotation.

$$\begin{bmatrix} 1 & 0 & 0 & 0 \\ 0 & \cos(\theta) & -\sin(\theta) & 0 \\ 0 & \sin(\theta) & \cos(\theta) & 0 \\ 0 & 0 & 0 & 1 \end{bmatrix} \tag{2.31}$$

$$\begin{bmatrix} \cos(\theta) & 0 & \sin(\theta) & 0 \\ 0 & 1 & 0 & 0 \\ -\sin(\theta) & 0 & \cos(\theta) & 0 \\ 0 & 0 & 0 & 1 \end{bmatrix} \tag{2.32}$$

$$\begin{bmatrix} \cos(\theta) & -\sin(\theta) & 0 & 0 \\ \sin(\theta) & \cos(\theta) & 0 & 0 \\ 0 & 0 & 1 & 0 \\ 0 & 0 & 0 & 1 \end{bmatrix} \tag{2.33}$$

In general, when done manually, the images will first be shifted to have the same origin and then rotated around one or more axis. This process can be represented as a single transformation by combining the transformation matricies through multiplication. For example if we wanted to first translate the image and then rotate it around the z-axis we could combine Equations 2.30 and 2.33 as

shown in Equation 2.34. Note that the order of the matrices in the multiplication is reversed.

$$\begin{bmatrix} \cos(\theta) & -\sin(\theta) & 0 & 0 \\ \sin(\theta) & \cos(\theta) & 0 & 0 \\ 0 & 0 & 1 & 0 \\ 0 & 0 & 0 & 1 \end{bmatrix} \begin{bmatrix} 1 & 0 & 0 & T_x \\ 0 & 1 & 0 & T_y \\ 0 & 0 & 1 & T_z \\ 0 & 0 & 0 & 1 \end{bmatrix} = \begin{bmatrix} \cos(\theta) & -\sin(\theta) & 0 & T_x\cos(\theta) - T_y\sin(\theta) \\ \sin(\theta) & \cos(\theta) & 0 & T_x\sin(\theta) + T_y\cos(\theta) \\ 0 & 0 & 1 & T_z \\ 0 & 0 & 0 & 1 \end{bmatrix} \quad (2.34)$$

This step can be considered optional, because any rigid displacements are automatically corrected in later stages of the registration procedure.

2.5.2.5 Contour Extraction

During this stage the contours of the breast are extracted from coronal slices of the MRI volume. If possible these contours are selected from the slices containing fiducial markers. The contours can be extracted in a number of different ways, such as using thresholding,[118] morphological operators,[118] active contours[119] such as level sets,[120,121] or even manually. For example, a threshold can be applied to segment the image from the background. The thresholded region could then be dilated and subtracted from the original thresholded region to obtain the contour around the breast.

Figure 2.11 shows a coronal breast slice, an active contour technique[120] was used to obtain the breast boundary (Figure 2.12).

Figure 2.11 Example coronal breast slice.

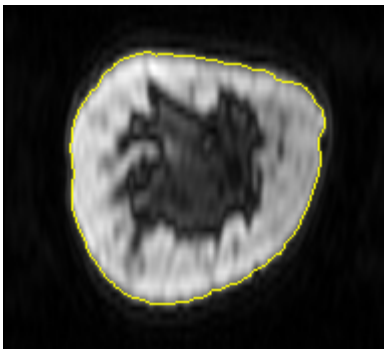

Figure 2.12 Example coronal breast slice with contour. Contour obtained with [122].

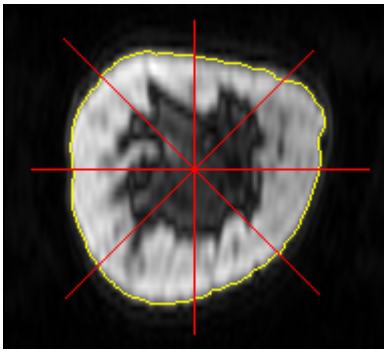

Figure 2.13 Example coronal breast slice with sampled contour. The points located at the intersections of the yellow curve with the red lines define the contour.

The contours are defined as a set of points with an approximately equal angular spacing around the contour. This is demonstrated by Figure 2.13. The red lines are drawn at a 45 degree spacing around the manually selected center of the breast. The points of intersection between the red lines and the yellow contour are selected to define the contour. In this case we have 8 points, however a larger number can be used to more accurately represent the contour. The angular spacing of these points do not need to be exact, however they should provide an accurate description of the shape.

2.5.2.6 Fiducial Marker Extraction

The locations of the markers in each of the modalities need to be found, so that the difference in location between pairs of corresponding markers can be

used to deform our model. The centroid of the markers in both MRI and PET are manually selected and their locations recorded. After a marker in the MRI image and a marker in the PET image are realized as being located at the same physical location of the breast, the difference in their locations along the x-, y-, and z-axes are recorded.

2.5.2.7 Model Generation

During model generation recorded contours are used to generate a discrete model of the breast geometry. Version 5.7 of the ANSYS[110] FEM software package, made by ANSYS, Inc., was used to define the model. See the phantom and patient experiments for details on their associated model design, Section 2.6.2 and Section 2.7.2, respectively.

2.5.2.8 Displacement Propagation

During this step the differences of location between corresponding markers in the PET and MRI images are applied as loads on the breast model. The models were designed to have a node located at each marker location, so loads are assigned as temperature values at the associated nodes.

The model is then analyzed using ANSYS.[110] This is done three times, each run corresponding to the displacement in one of the three orthogonal directions, with the assigned nodal loads corresponding to the change in marker location along that direction. Due to the higher conductivity assigned to the surface the displacements are in effect first distributed along the skin, and then propagated throughout the rest of the breast tissue. The result of the FEM analysis is the estimated displacement along the primary axes for each node within the model.

2.5.2.9 Image Transformation

The displacements found at the nodal positions, can be used to estimate the deformation at each point within the volume and a deformed (warped) volume can be created. The MRI image is transformed to bring it into spatial registration with the PET image. This process is relatively simple since interpolation functions (see Section 2.4) define the relationships between the nodes and any point in the element's interior. A backward approach achieves the best results, however a forward approach will first be described since it is more intuitive, and can aid in understanding the backward approach.

In the forward approach we examine each voxel in the original image and calculate its position in the deformed image. We first find the voxel's location within the model. More, specifically we need to find the element that contains the voxel. To do this we can calculate the coefficients of the interpolation function for each element (for example see Equation 2.19). As mentioned earlier, the voxel is located within the element if and only if the sum of the absolute values of the coefficients is one.

$$\sum_i |L_i| = 1 \qquad (2.35)$$

Once the element containing the voxel has been identified, the interpolation function can be used to find the displacement at that voxel location. The estimated displacements at the nodes of the element, provided by the finite element analysis, are plugged into the interpolation function providing the displacement for the voxel (for example see Equation 2.21). Since the new location of the voxel most likely does not fall exactly at a voxel location in the

deformed image, some method needs to be defined to determine how the voxel contributes to the surrounding voxels in the deformed image.

The biggest problem with the forward approach arises from the fact that, depending on the deformation, none of the voxels in the original image may get mapped to a given voxel in the deformed image. As a result the deformed image might have holes (empty voxels). Because of smoothly varying deformations in our problem, this is only a minor issue.

The backward approach avoids this problem. Here we start with a voxel in the deformed image and find the voxels in the original image that contribute to it. By approaching the problem this way, every voxel in the deformed image will get a value assigned to it. For a given voxel in the deformed image, we find the associated element of the deformed model in the same manner as the forward case. The interpolation function can then be used with the negated displacements (displacements necessary to change the deformed model to the original one) to find the voxel location in the original image. Again the voxel in the deformed image is unlikely to map exactly to a voxel in the original image, but the assigned value can be easily decided by interpolation of the surrounding voxels.

2.5.3 Error Measures

In order to determine success/failure or accuracy of the registration algorithm metrics are needed. This section describes three metrics that will be used to evaluate the registration procedure.

2.5.3.1 Fiducial Registration Error (FRE)

Evaluating the registration between different modalities can be difficult, especially when registering a functional image with an anatomic image, since in general the images provide a significant amount of complementary information and relatively little redundant information. Fiducial skin markers are used during the registration procedure to provide known displacements between the modalities. Due to the difficulty in indentifying exact relationships between internal features, it is only natural that we utilize the corresponding information provided by the fiducial markers.

We can consider the error of the registration procedure when predicting the displacements of the fiducial markers between the MRI and PET image. Since this is a physical movement the error can simply be represented as the Euclidean distance between the known displacement of the marker and the displacement estimated by the model. This is shown as Equation 2.36 where (e_x, e_y, e_z) is the estimated displacement provided by the deformable model and (m_x, m_y, m_z) is the actual measured displacement. Obviously this error metric can only be used to evaluate the error for markers not used for the registration process, since the marker displacement used to drive the registration procedure will always be accurately predicted by the model.

$$FRE = \sqrt{(e_x - m_x)^2 + (e_y - m_y)^2 + (e_z - m_z)^2} \qquad (2.36)$$

2.5.3.2 Target Registration Error

A similar error measure can be used if there are corresponding points in all modalities that can be accurately localized, for example a lesion. Although not

generally the case for PET and MRI images, our phantom (Section 2.6) has several lesions that are visible in both modalities. The metric can be calculated using Equation 2.37. This metric can more easily be applied to intramodality registration.

$$TRE = \sqrt{(e_x - m_x)^2 + (e_y - m_y)^2 + (e_z - m_z)^2} \qquad (2.37)$$

2.5.3.3 Normalized Mutual Information

Since the other metrics discussed here only consider the registration accuracy of distinct points in the images, we would like to consider one other metric which utilizes the full image content. The selected metric, known as normalized mutual information, was presented in [123].

The normalized mutual information metric builds on earlier work in information (communication) theory. The amount of information provided by a series of events (in our case pixel values) is represented by its entropy.[124] Entropy can be calculated using Equation 2.38 where X is a random variable, and $P(x_i)$ is the probability of the random variable having the value x_i.

$$H(X) = -\sum_i P(x_i) \log P(x_i) \qquad (2.38)$$

Entropy represents the average amount of information we get from observing one instance of the random variable. This can be understood by considering the entropy of two random variables. Let the first random variable be a constant. There is only one possible value for x_i which has a probability of one. We see from Equation 2.38 that we would have zero entropy for this random variable. Because the random variable is a constant we already know what the value of the next instance will be, and we gain no information by observing it.

On the other hand, if we have a uniform random variable where we have an equal probability of observing each value of the random variable, entropy will be maximized. This is because the next instance of the random variable could be any allowed value. We have no way of providing a prediction for the random variable that will be any more accurate than a random guess. As a result we will obtain a significant amount of information by observing the next value of the random variable.

Joint entropy, Equation 2.39, describes the average information from observing a pair of values, such as the MRI and PET intensity values at the same physical location, from a joint probability distribution. If we consider two registered images of the same object, the structures in the images will line up providing many similar pairs of values giving us small joint entropy. If we consider two unregistered images we will in general have a greater variety of pairs due to a single structure in one image overlapping multiple structures in the other image, resulting in a larger joint entropy.

$$H(X,Y) = -\sum_{i,j} P(x_i, y_j) \log P(x_i, y_j) \qquad (2.39)$$

Although joint entropy can be used as a metric to measure registration accuracy, it has difficulties due to changes in the overlap of the images during registration. As a result, mutual information and, later, normalized mutual information were proposed as alternate metrics.[123] Normalized mutual information is based on entropy and can be calculated using Equation 2.40.

$$Y(X;Y) = \frac{H(X) + H(Y)}{H(X,Y)} \qquad (2.40)$$

Due to joint entropy being located in the denominator, normalized mutual information increases as registration improves. The marginal entropies in the numerator scale the normalized mutual information to account for variations in the marginal entropies which result from changes in the overlap of the two images. See Appendix C for more information and justification for using normalized mutual information as a similarity measure.

It should be noted that the value of normalized mutual information as a registration metric depends directly on the similarity between the modalities of the images being registered. It provides a reliable metric for intramodality registration where the same structures are visible in both images, but is less consistent for intermodality registration. This is especially true when registering a functional and an anatomical image, where different structures are present, or are represented differently. For example, in PET and MRI we are in essence imaging two different things, the distribution of a radioisotope verse the signal from hydrogen atoms in the body. Other difficulties arise due to differences in resolution, sensitivity, and noise. Because of these issues, the displacements that maximize the normalized mutual information metric are most likely not the same as the actual displacements. This needs to be kept in mind when using information content based metrics.

2.6 Phantom Study

A proof of concept study was performed using a custom made breast phantom. The phantom, manufactured by CIRS, Inc., Norfolk, VA, consisted of a medium stiffness gel (vinyl based hydropolymer with a low concentration of nickel

chloride) surrounded by a skin made of thin urethane foil (Figure 2.14). The phantom had a radius of approximately 50 mm and extended 120 mm from the base. Simulated lesions were injected into the phantom and it was imaged using both MRI and PET with associated markers. A finite element model of the phantom was generated and used to distribute the marker displacements throughout the phantom. Fiducial registration errors and target registration error were calculated to evaluate the accuracy of the registration method.

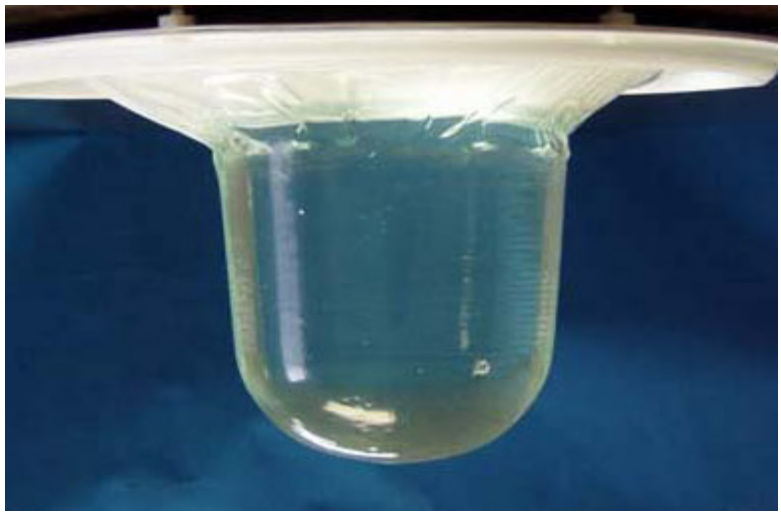

Figure 2.14 Deformable breast phantom. The phantom had a radius of approximately 50 mm and extended 120 mm from the base.

2.6.1 Data Acquisition

During MRI acquision the phantom was positioned in the coil to simulate a patient being imaged in the prone position. The thirty-three polyethylene tube markers were placed on the breast in the configuration shown in Figure 2.15. Eight markers were placed on each of the four meridians with one additional marker placed at the apex (nipple region).

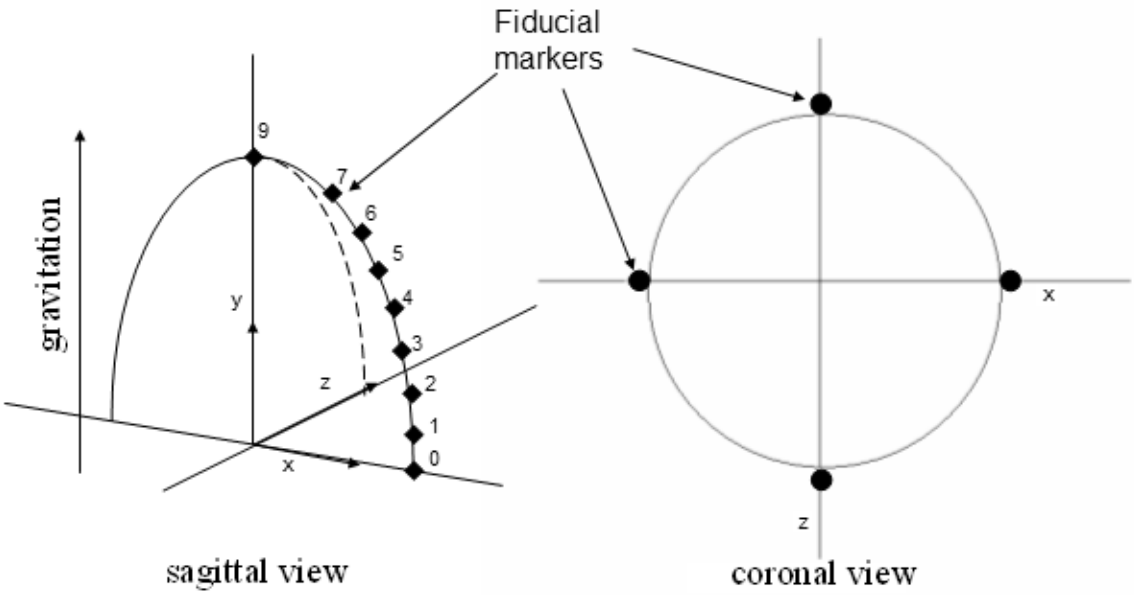

Figure 2.15 Maker placement on the deformable phantom.

Lesions were simulated in the phantom by injecting it with a drop of mineral oil (Johnson & Johnson, New Brunswick, NJ) which would not diffuse into the gel, containing organic azo dyes. The dyes made the lesion locations clearly visible to the human eye. The placement of the lesions is shown in Figure 2.16. Images were collected using the protocol previously described in Section 2.5.1.1. Figure 2.17 and Figure 2.18 which are examples of the images collected, show the markers and lesions.

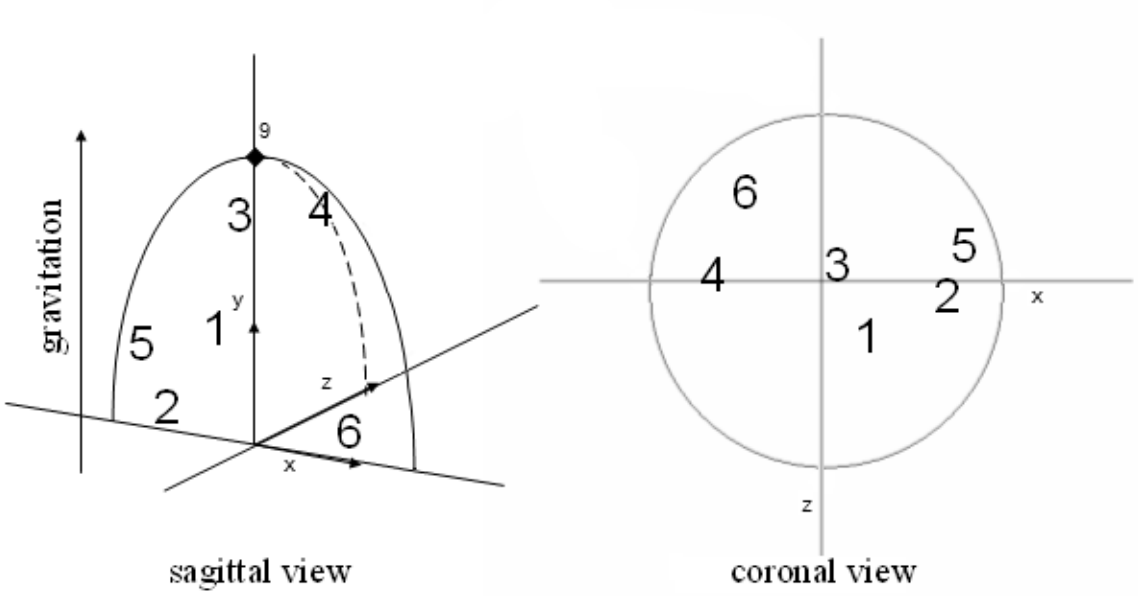

Figure 2.16 Lesion placement in the deformable phantom.

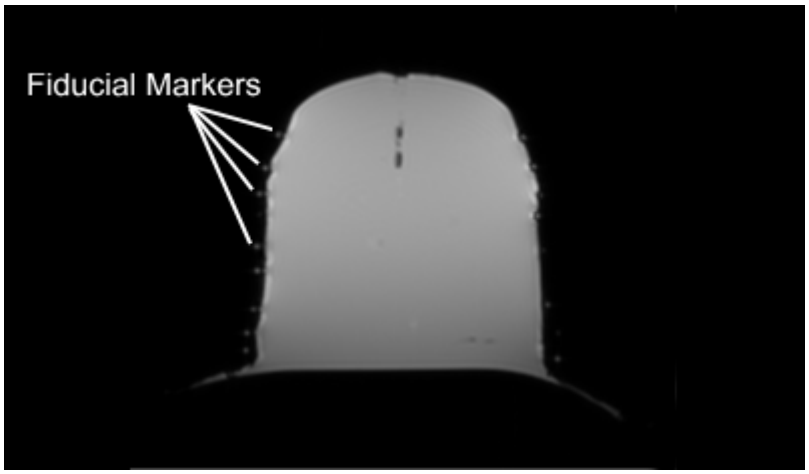

Figure 2.17 Sagittal cross section through the MRI image of the phantom showing the fiducial markers. The position corresponds with xy-plane of Figure 2.15.

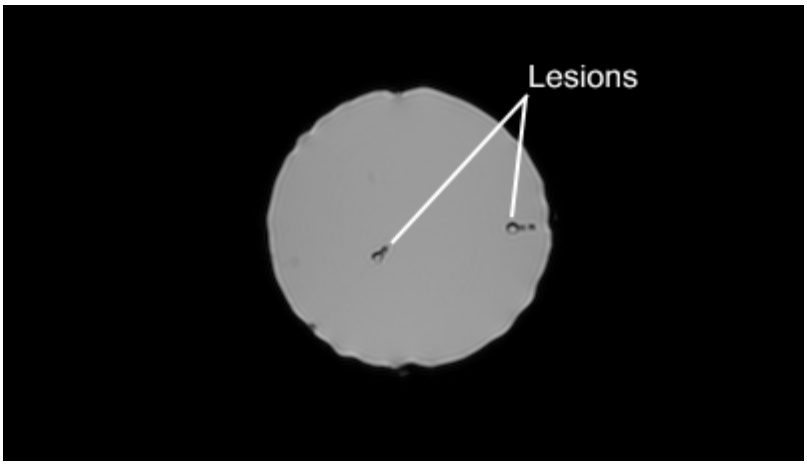

Figure 2.18 Coronal cross section through the MRI image of the phantom showing the simulated lesions.

PET images were collected with the GE Advance NXi system. The PET fiducial markers were placed in the identical location of their MRI counterparts. Simulation of lesions for PET was accomplished by diluting F-18 FDG with water-soluble gelatin and organic dyes. The lesions were injected as closely as possible to the lesions added for MRI. The phantom was positioned as similarly as possible to its position during the MRI data collection. Data were collected and reconstructed as described in Section 2.5.1.2. A cross section through the PET image volume showing markers and lesions is shown as Figure 2.19.

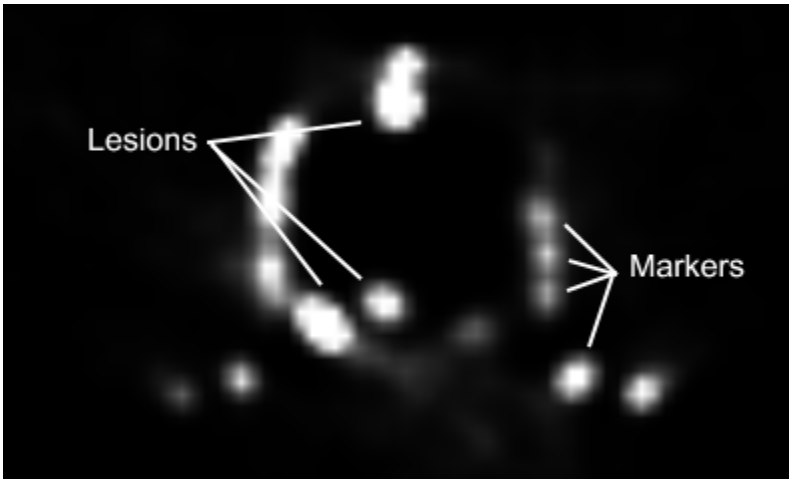

Figure 2.19 Sagittal cross section through the PET image of the phantom showing the simulated lesions and fiducial skin markers.

2.6.2 Mesh Creation

After imaging the registration procedure presented in Section 2.5.2 was followed. Six corresponding lesions were identified in both PET and MRI along with 27 of the fiducial markers. The remaining markers were not usable due to motion from poor adhesion during image acquisition, or due to difficulties identifying them in the acquired images.

The geometry of the phantom was modeled using brick (Figure 2.20), tetrahedral (Figure 2.21), and shell (Figure 2.22) elements. The bulk of it was modeled using brick elements with the tetrahedral used for areas of higher curvature (ex. apex region). The shell elements were placed as a layer around the surface of the phantom to represent the skin. The shell elements were assigned a much greater conductivity transforming the displacements from a set of points (markers) to a surface. The model which consisted of 15,636 nodes can be seen in Figure 2.23 and Figure 2.24.

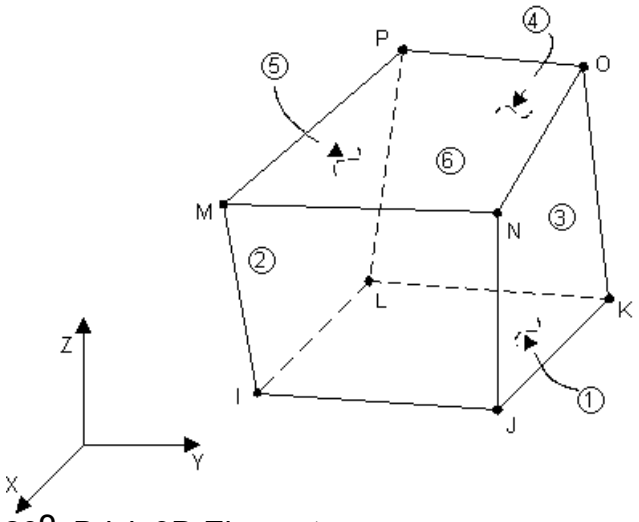

Figure 2.20[O] Brick 3D Element.

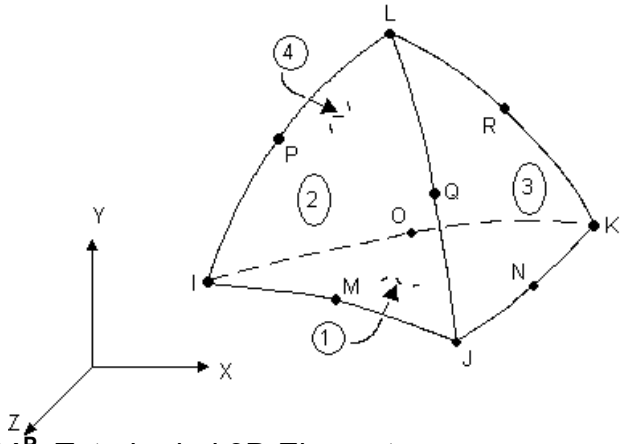

Figure 2.21[P] Tetrahedral 3D Element.

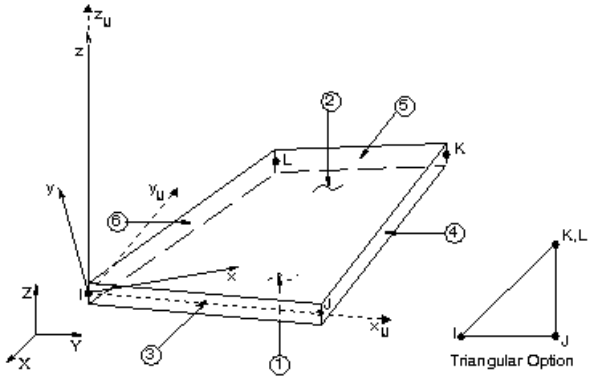

Figure 2.22[Q] Shell 2D Element with triangular option.

[O] Image from [125], courtesy of ANSYS, Inc.
[P] Image from [126], courtesy of ANSYS, Inc.
[Q] Image from [127], courtesy of ANSYS, Inc.

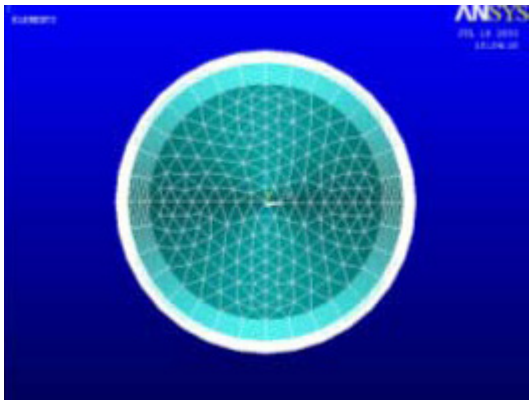

Figure 2.23 Top view of model of breast phantom. 2D surface shell elements are visible.

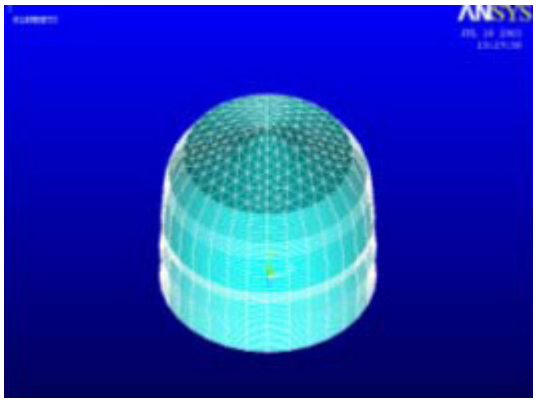

Figure 2.24 Side view of model of breast phantom. 2D surface shell elements are visible.

2.6.3 Results

The results of the registration procedure were evaluated using fiducial registration error and target registration error metrics. First, a small subset of the markers was used to estimate the location of the other markers. This was done twice, the first time using the eight markers available at locations 0, 3, and 9 and then again using the thirteen markers available at locations 0, 3, 6, and 9 (see Figure 2.15 for marker locations). The errors, which were found to be approximately the size of one PET voxel (4.3 mm), are presented in Table 2-I.

Table 2-I Fiducial registration errors.

No. of markers used to drive model	Mean Error (mm)	Standard Deviation of Error (mm)
8	4.27	2.16
13	4.06	1.55

The target registration error was estimated using the six artificial lesions visible in both modalities. Table 2-II shows the target registration error for each lesion. The lesion numbers correspond to the positions shown in Figure 2.16. The accuracy was found to be within approximately 5 mm.

Table 2-II Target registration errors.

Lesion	Target Registration Error (mm)
1	4.92
2	4.58
3	3.57
4	4.55
5	0.34
6	2.54

Smaller subsets of fiducial markers were also used to estimate the lesion locations. Figure 2.25 shows the relationship between the target registration error and the number of fiducial markers used. As expected, as the number of fiducial markers increases, the error asymptotically approaches a value close to the resolution of the PET images.

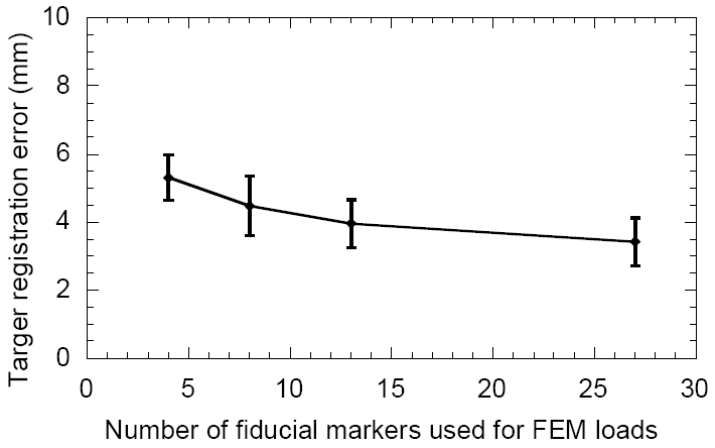

Figure 2.25 Relationship between target registration error and number of fiducial markers used. The standard error bars are based on the six lesions.

The phantom study demonstrated the feasibility of this registration approach and justified subject trials. Since the positioning could be accurately controlled and a large number of markers could be used this experiment represents a best case scenario. Registration accuracy was limited by the resolution of the PET image and the reader's ability to accurately localize the fiducial marker locations.

2.7 Initial Patient Studies

Additional validation of the registration procedure was performed using patients who volunteered for the study. An example patient study will be presented here and evaluated using the normalized mutual information metric.

2.7.1 Data Acquisition

The patient was imaged in PET and MRI as described in Section 2.5.1. PET imaging was done using the GE Discovery ST system and the vitamin E capsules were used as the MRI fiducial markers. Figure 2.26 contains a MRI image with a visible marker and Figure 2.27 contains a PET image with visible markers.

Five fiducial markers were used for the study, four distributed around the exterior of the breast and one on the apex. The actual placement of the markers was determined by the clinician during imaging. The placement of the markers can be seen by examining Figure 2.28. The locations of the markers are shown by projecting them onto a transaxial and coronal view of the breast.

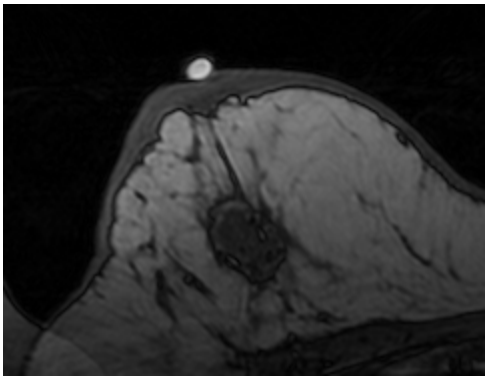

Figure 2.26 Transaxial view from the MRI image of the patient's breast showing fiducial marker located at nipple.

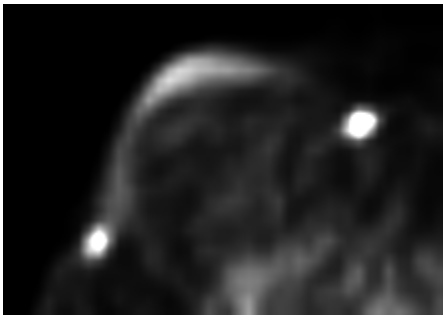

Figure 2.27 Transaxial view from the PET image of the patient's breast showing two fiducial markers.

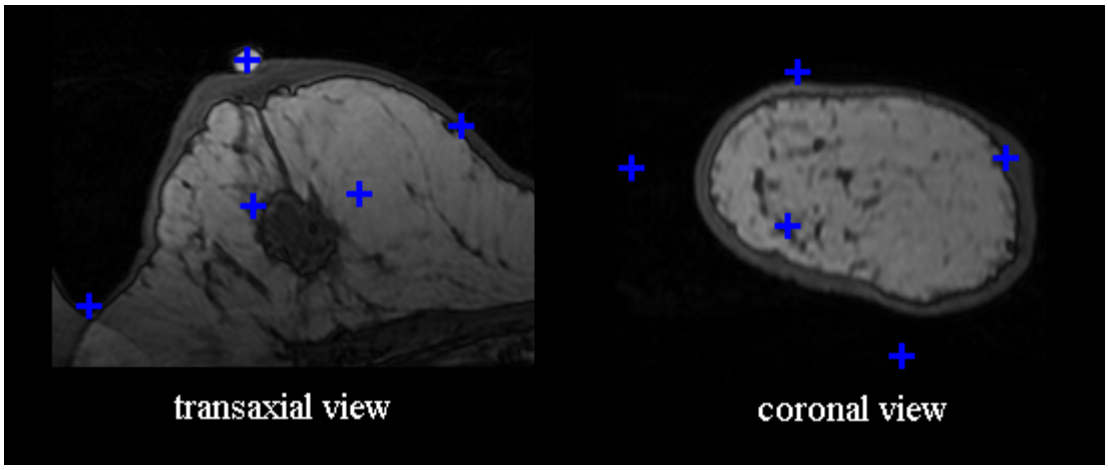

Figure 2.28 Transaxial and coronal MRI views through middle of breast. Blue marks indicate fiducial marker locations projected onto the slices.

2.7.2 Mesh Creation

The geometry of the mesh was constructed based on the MRI image. An example ANSYS[110] script is provided as Appendix D. Points along the contours were extracted as discussed in Section 2.5.2.5. Twenty four points were identified along fifty different contours parallel to the breast bone (coronal slices as demonstrated by Figure 2.13). The points were selected in such a way that one of them corresponded with the location of each fiducial marker.

The contours were first reconstructed from the extracted points by interpolating them with B-splines. B-splines are piecewise cubic curves that exhibit local control (moving one control point affects only a portion of the curve) and C^2 continuity (the second derivatives on both sides of the point where two segments of the curve meet are equal).

Like many piecewise cubic curves, the curve segments can be given by Equation 2.41, where S_i is the i^{th} curve segment, G_i are the geometrical constraints, and B represents the blending functions. The blending functions

can be defined by a matrix, M, representing the coefficients, and $T(t)$ the powers of the parameter value t. With a B-spline the geometric constraints are the locations of four surrounding control points, giving us Equation 2.42.

$$S_i = G_i B \tag{2.41}$$

$$S_i = \begin{bmatrix} P_{i-1} & P_i & P_{i+1} & P_{i+2} \end{bmatrix} M \begin{bmatrix} 1 \\ t \\ t^2 \\ t^3 \end{bmatrix} \tag{2.42}$$

The components of M can be found by imposing the C^2 constraints at the intersection, x, between segments, Equation 2.43, Equation 2.44, and Equation 2.45. An additional constraint, that the blending function sum to unity at $t = 0$, is necessary to give us an equal number of equations and unknowns. Solving the system of equations gives us M, Equation 2.46.[96]

$$S_i(x) = S_{i+1}(x) \tag{2.43}$$

$$S'_i(x) = S'_{i+1}(x) \tag{2.44}$$

$$S''_i(x) = S''_{i+1}(x) \tag{2.45}$$

$$M = \frac{1}{6} \begin{bmatrix} 1 & -3 & 3 & 1 \\ 4 & 0 & -6 & 3 \\ 1 & 3 & 3 & -3 \\ 0 & 0 & 0 & 1 \end{bmatrix} \tag{2.46}$$

The resulting blending functions are shown in Figure 2.29. These functions represent the contribution of each control point at each location, t, along the segment. In general, B-splines do not pass through the control points because more than one blending function is not equal to zero at each of the endpoints. The control points defining the contours of the breast are selected so that the curve passes through the points along the contour extracted from the MRI image.[128]

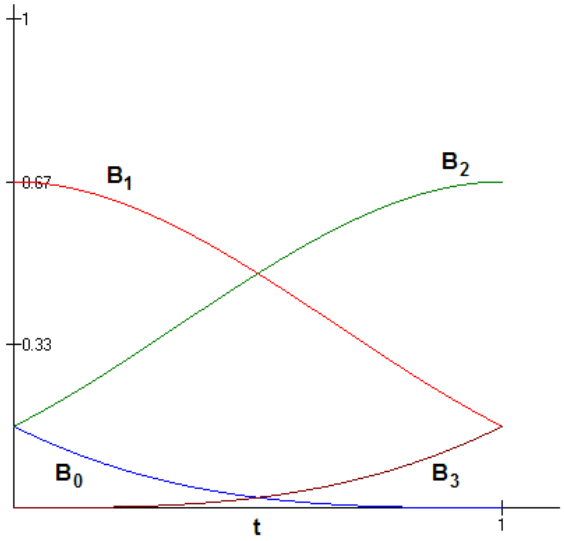

Figure 2.29 Blending functions for B-spine.

Initial volumes are defined by a small range of corresponding points on two neighboring cross-sections and the midpoints of the two cross-sections. Points are inserted along the lines composing the volume and used as the starting point to mesh the breast volume using tetrahedral elements (Figure 2.21). ANSYS[110] uses the GHS3D tetrahedral mesh generator[129,130] from INRIA[131] and Distene[132]. GHS3D is a Delaunay technique mesher which refines the mesh to a higher resolution finding a Delaunay triangulation.

The Delaunay triangulation of a set of points in n-dimensional space is a triangulation such that no point in the set is inside the circum-hypersphere (the unique hypershere which passes through each of the simplex's vertices) of any simplex (n-dimensional triangle analog) in the triangulation.[133,134] For a two-dimensional example see Figure 2.30 and Figure 2.31. Figure 2.30 does not satisfy the required properties because the red vertex is located inside the circumcircle of a triangle. On the other hand, Figure 2.31 satisfies the requirements for a Delaunay triangulation since there are no vertices located

within the circumcircles of the triangles. A Delaunay triangulation maximizes the minimum angle in the triangulation, increasing the chance of avoiding narrow elements that can decrease the accuracy of the finite element method.

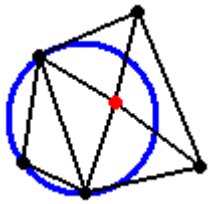

Figure 2.30 The red vertex violates the Delaunay triangulation criteria because it lies within the circumcircle of one of the triangles.

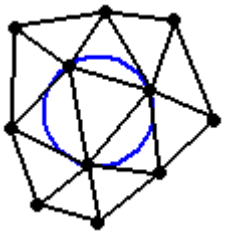

Figure 2.31 A Delaunay triangulation.

After the interior of the breast has been modeled, the final step in the construction of the geometry is the addition of the skin. The skin is formed by meshing the vertices defining the surface of the breast volume with triangular shell elements (Figure 2.22). Since the underlying volume is already defined by a well formed mesh, the skin can be extruded from the underlying mesh. Two views of the resulting breast model for the patient are shown in Figure 2.32 and Figure 2.33. The model consists of approximately 32,000 nodes, 20,000 tetrahedral elements, and 4,000 triangular surface elements.

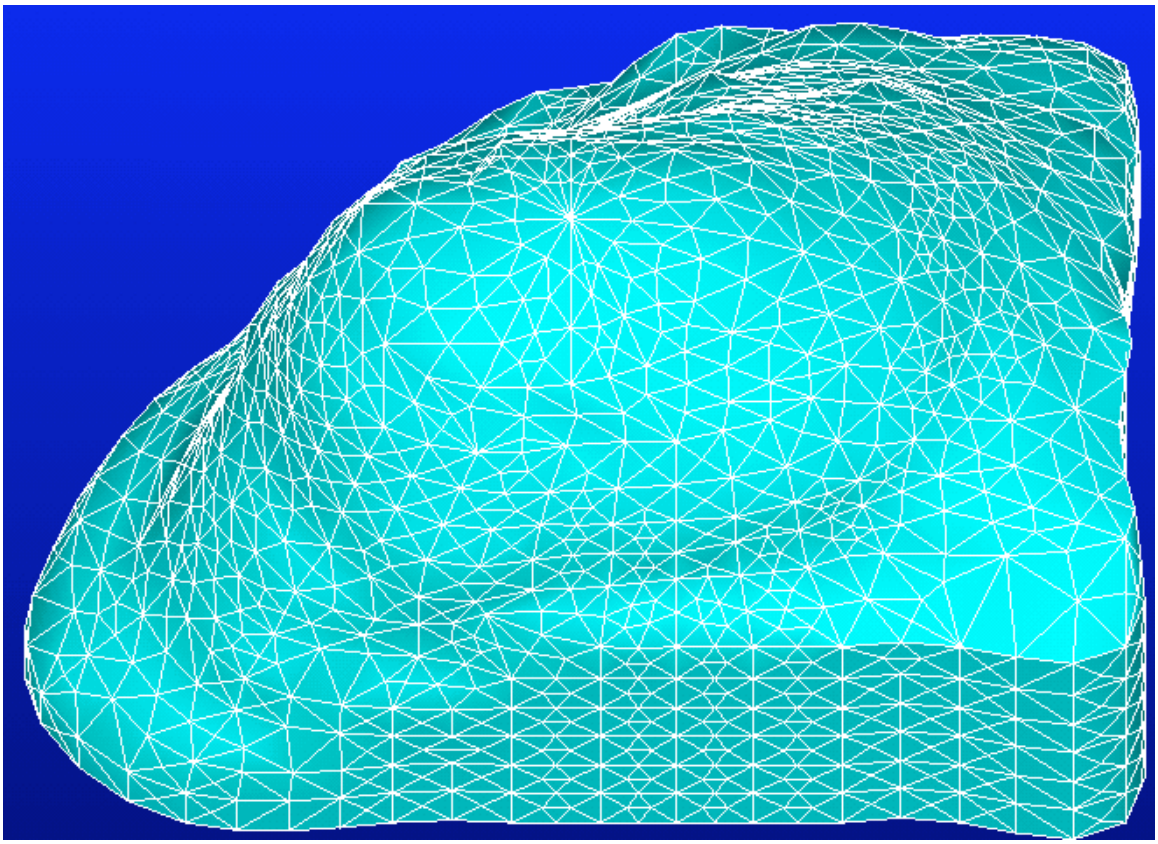

Figure 2.32 Patient breast model. Right breast as viewed from the anterior inferior side.

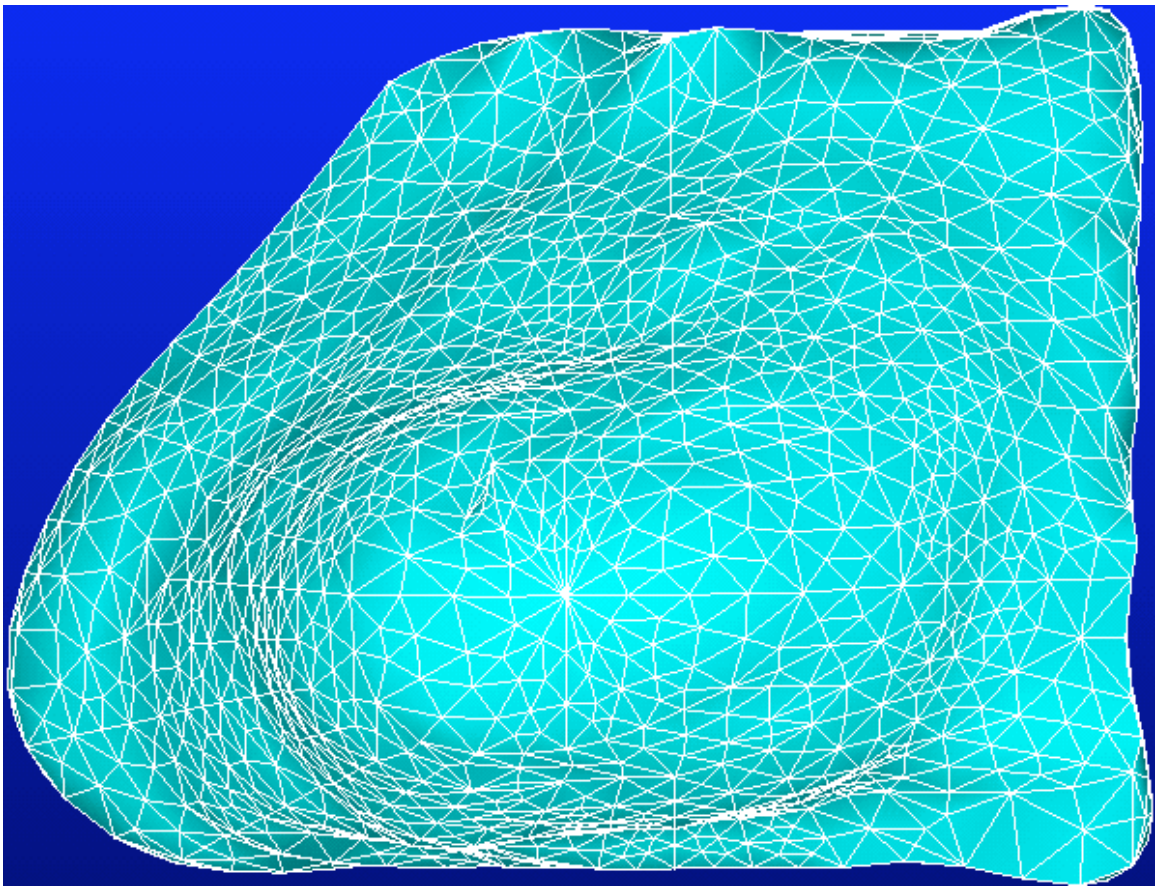

Figure 2.33 Patient breast model. Right breast as viewed from the anterior, patient's head would be at the top.

The resulting model is image and patient specific. A similar model will need to be generated for other image series and patients.

2.7.3 Results

The displacements at the fiducial markers were distributed throughout the rest of the volume using the ANSYS[110] software package. The displacements were used to warp the MRI image to the PET image as discussed in Section 2.5.2.9.

The improvement in registration of the FEM procedure over standard rigid registration is demonstrated in Figure 2.34, Figure 2.35, and Figure 2.36. Each figure shows a slice of the PET image and the corresponding slice of the MRI

image after rigid registration and after FEM registration. The images were converted from 16-bit to 8-bit using a mild histogram equalization technique.[135] In order to simplify examining the results, fused PET/MRI images are also shown. The PET image was first colored with a blue lookup table (Figure 2.37) from ImageJ[136] and then the fused images were created by averaging the voxel colors in the pseudo colored PET image with the MRI images. The fused image intensities were then scaled by 1.3 to account for decreases in contrast due to averaging. This fusion, while not useful for clinical image analysis, helps us to identify misregistrations. The blue lookup table and color averaging make the areas of high activity clearly visible on the grayscale MRI background. The fusion was performed using the Fusion Viewer software package (see Section 3.5) and the resulting two-dimensional color table is shown in Figure 2.38. Clear improvements can be seen when examining the areas of higher metabolic activity within the breast and along the skin surface.

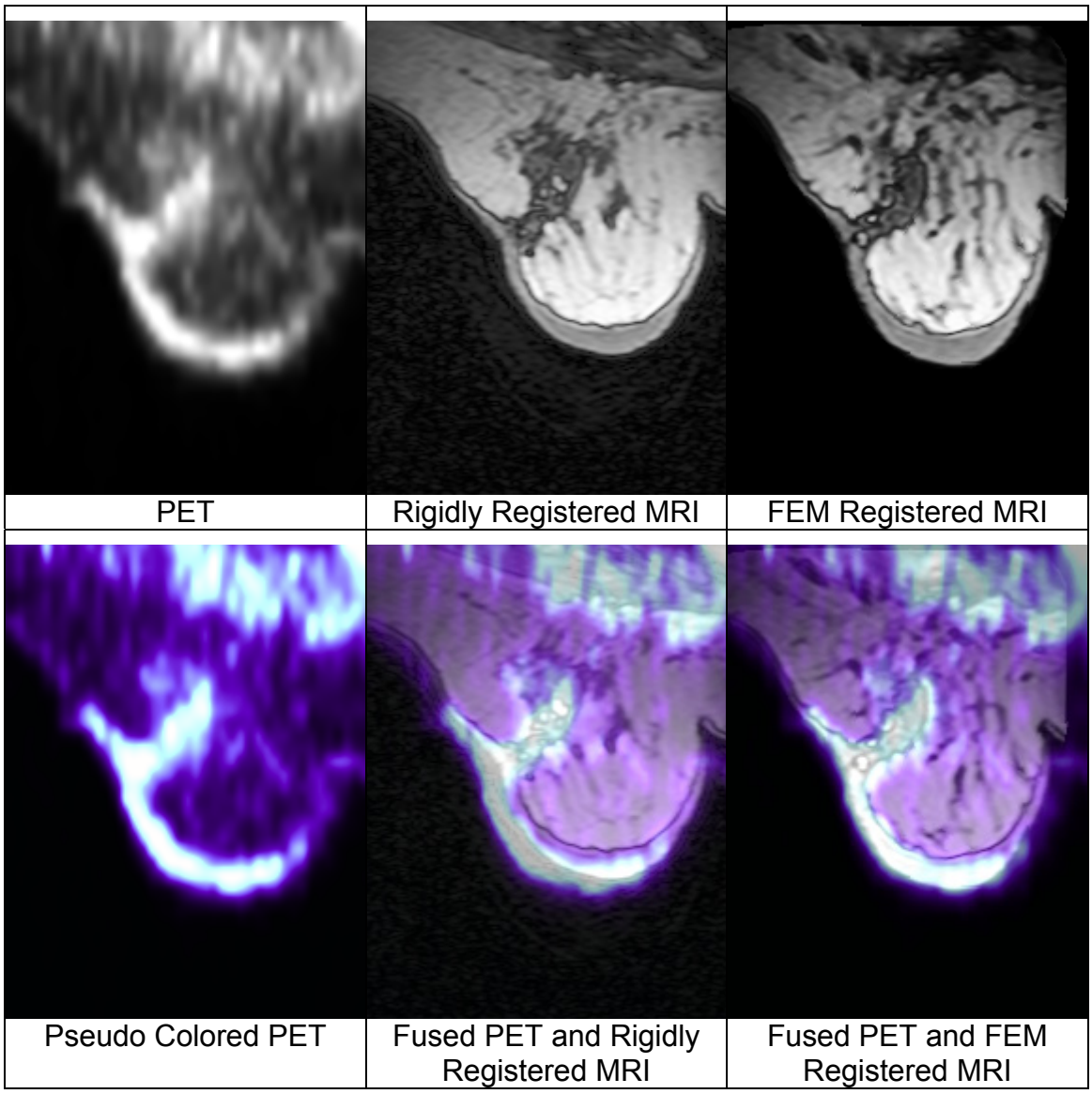

Figure 2.34 Example demonstrating the improvement of FEM registration over rigid registration. Original PET image (top left), MRI image after rigid registration (top middle), MRI image after FEM registration (top right), pseudo colored PET image (bottom left), fused pseudo color PET image and MRI image after rigid registration (bottom middle), and fused pseudo color PET image and MRI image after FEM registration (bottom right). Improvements in registration can be seen along the skin surface and at the areas of higher activity within the body of the breast. Look up tables used to pseudo color PET image and fuse MRI and PET images are shown in Figure 2.37 and Figure 2.38, respectively.

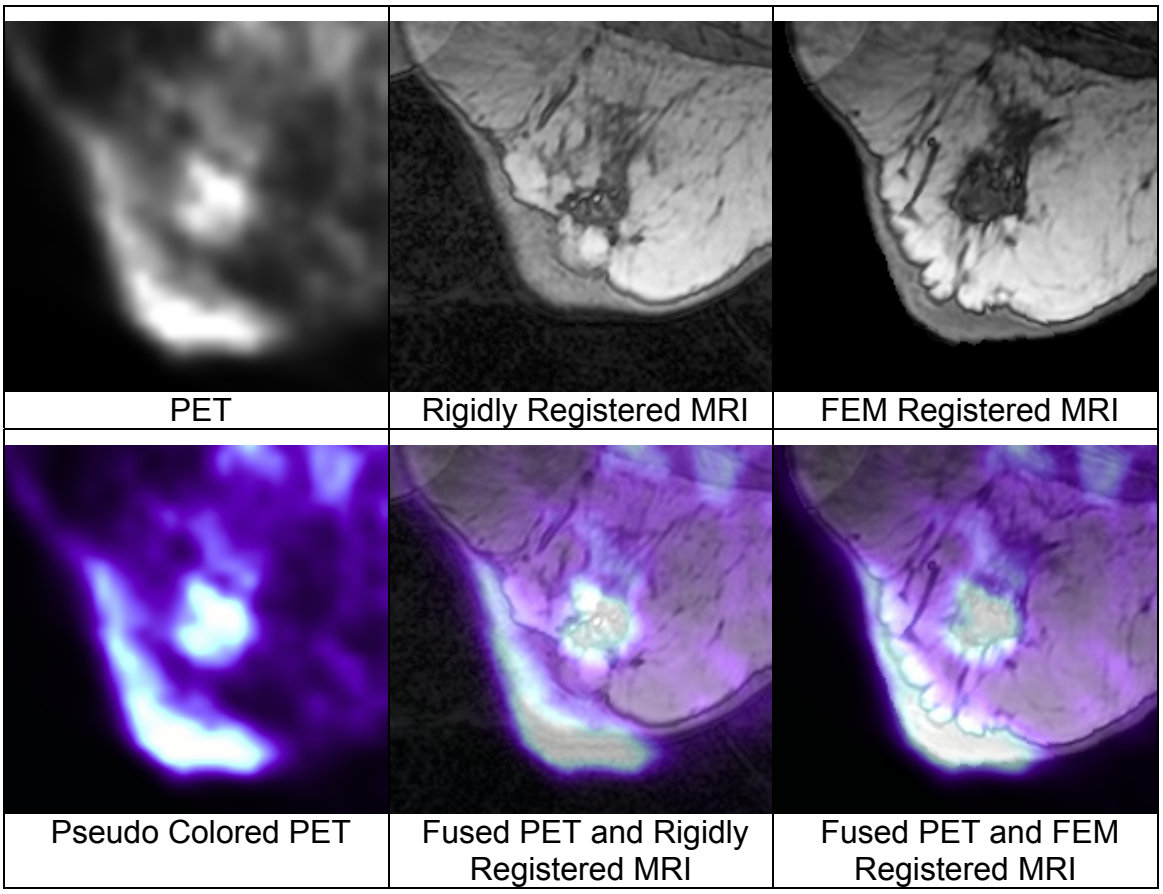

Figure 2.35 Second example demonstrating the improvement of FEM registration over rigid registration. Original PET image (top left), MRI image after rigid registration (top middle), MRI image after FEM registration (top right), pseudo colored PET image (bottom left), fused pseudo color PET image and MRI image after rigid registration (bottom middle), and fused pseudo color PET image and MRI image after FEM registration (bottom right). Improvements in registration can be seen along the skin surface and at the areas of higher activity within the body of the breast. Look up tables used to pseudo color PET image and fuse MRI and PET images are shown in Figure 2.37 and Figure 2.38, respectively.

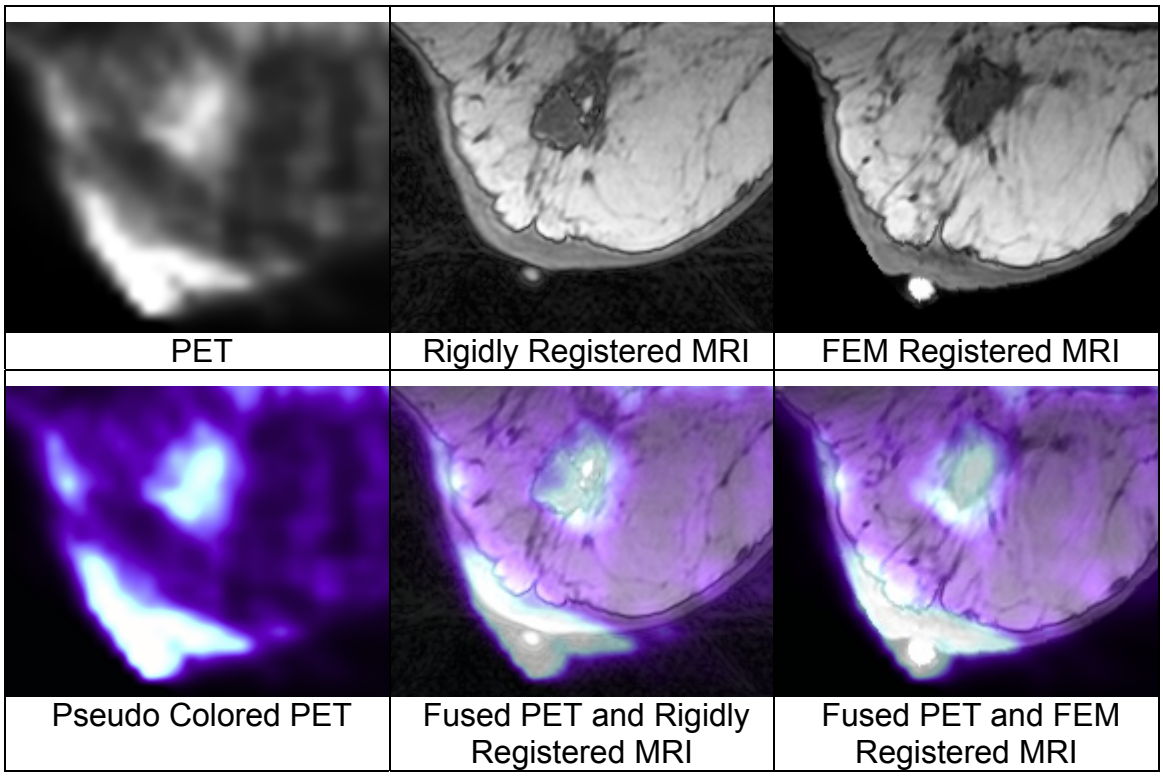

Figure 2.36 Third example demonstrating the improvement of FEM registration over rigid registration. Original PET image (top left), MRI image after rigid registration (top middle), MRI image after FEM registration (top right), pseudo colored PET image (bottom left), fused pseudo color PET image and MRI image after rigid registration (bottom middle), and fused pseudo color PET image and MRI image after FEM registration (bottom right). Improvements in registration can be seen along the skin surface and at the areas of higher activity within the body of the breast. Look up tables used to pseudo color PET image and fuse MRI and PET images are shown in Figure 2.37 and Figure 2.38, respectively.

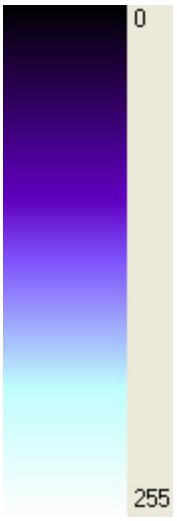

Figure 2.37 Blue look up table used to pseudo color PET image in Figure 2.34, Figure 2.35, and Figure 2.36.

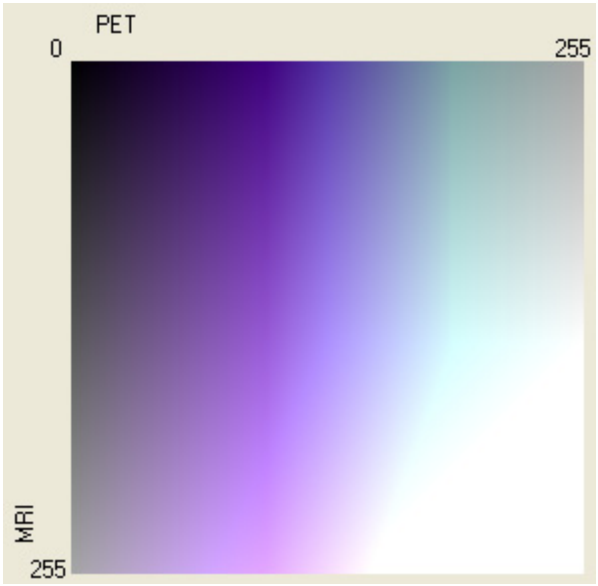

Figure 2.38 Resulting two-dimensional look up table from fusion scheme used to create the joint MRI/PET images shown in Figure 2.34, Figure 2.35, and Figure 2.36.

The quality of the image registration was also evaluated using the image content based normalized mutual information metric (Section 2.5.3.3). For this particular patient the metric value was 1.07 after rigid registration and increased to 1.33 after FEM registration. This is a significant improvement in normalized

mutual information which for any given distributions will typically have a maximum less than two. Similar results were achieved with the other patients.

A procedure for estimating and correcting deformation of the breast tissue that occurs during imaging was developed and testing. This procedure provides a method for the registration of PET and MRI images which, if implemented properly, could be used in a clinical setting.

2.8 Continued Work and Future Directions

Effort on the registration procedure has been expended by others. The registration procedure has been evaluated for registration of images with dynamic PET/MRI series. Figure 2.39 shows differential MRI images created by subtracting an image acquired after administration of Magnevist with that previously acquired. Due to remaining misregistration, structures are difficult to identify in the rigidly registered differential images, however after application of the FEM registration technique the lesions can clearly be identified.

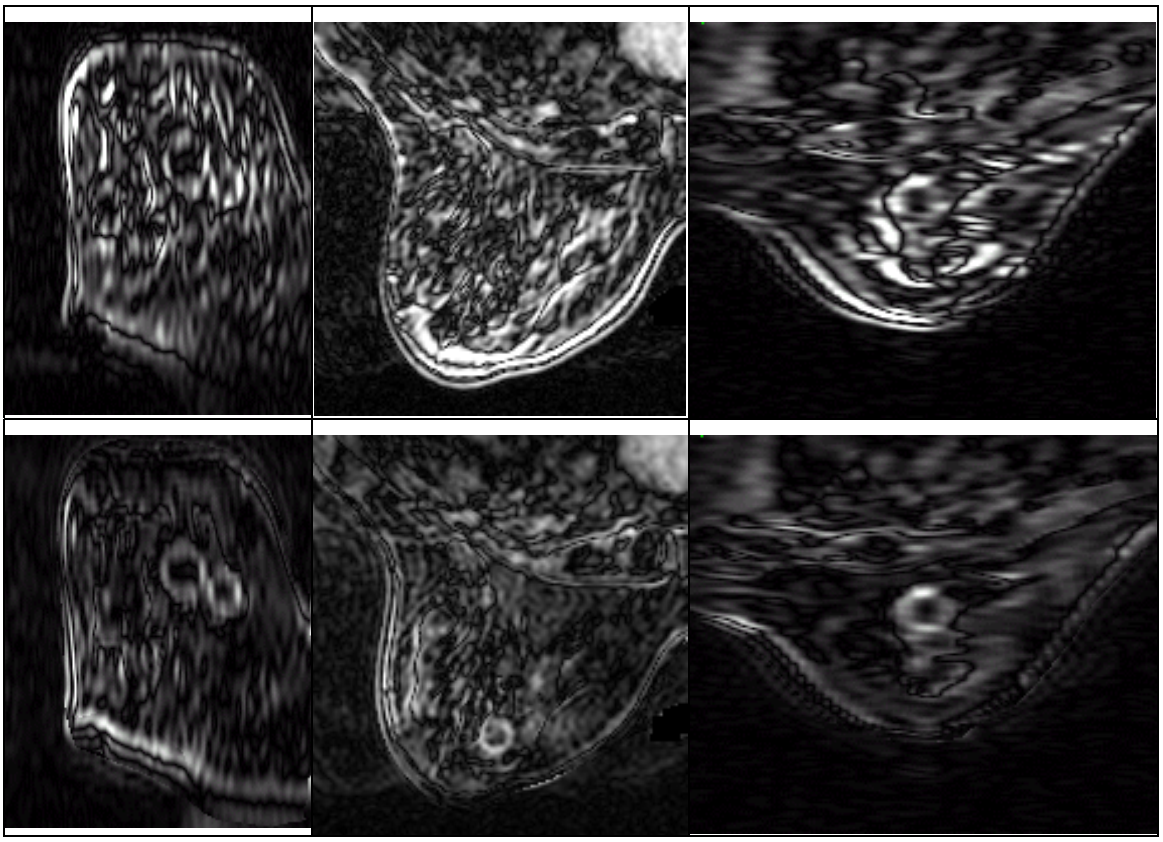

Figure 2.39 MRI differential images top row from left to right: coronal, transaxial, and sagittal views after rigid registration. Botttom row from left to right: coronal, transaxial, and sagittal views after FEM registration. Lesions which are difficult to identify after rigid registration are clearly visible after FEM registration.

Work on developing the registration procedure has continued and a second surface matching phase has been implemented. Surface matching was previously not possible because the external surface of the breast is not clearly defined in PET images. With the invention of PET/CT machines such as the GE Discovery ST which provide registered PET/CT data sets the surface of the CT image can be extracted and matched to the surface of the MRI image. Points believed to be corresponding on the two surfaces are identified and their differences in location are used to deform the breast model a second time.

Future efforts need to address the limitations of the registration procedure which prevent its use in a clinical environment, particularly automation of the process. The entire process needs to be wrapped into a single package and tasks such as extraction of contours and fiducial markers, and generation of the ANSYS scripts need to be automated. Automatic fiducial marker identification using simple three dimensional match filters should be possible since they have a consistent known shape. Automatic identification of points along the breast surface, to define the contours, should be a relatively simple task. Software engineering techniques can be used to connect the different software packages involved and create a streamlined process with a unified user interface.

Rather than manipulating both the PET and MRI image to have isotropic high resolution voxels, real world locations can be used throughout the registration procedure. Doing so would only require image manipulation to be performed during the final image transformation stage of the registration procedure. This minimizes the number of image manipulations and may reduce resulting errors, while decreasing the time required for registration.

Chapter 3 Fusion

3.1 Background

There has been a significant amount of effort spent registering images from different modalities. There has however, been significantly less effort spent on finding the best way to utilize the registered information. This includes efforts on image fusion, which is the process of taking multiple images and combining them into a single image, and work on interfaces for analyzing multiple medical images simultaneously. The lack of effort is partially due to the fact that the registration problem needs to first be solved prior to image fusion, and partially because, due to costs and insurance reimbursements, images from multiple modalities were rarely acquired before the development of commercially available joint PET/CT scanners in 2001.[137]

The advantage of a fused image comes from the inability to visually judge spatial relationships between images when they are viewed side by side. Depending on background shades and colors, identical shapes and lines may appear to be different sizes.[138] This can be demonstrated with simple illusions. The Ebbinghaus Illusion is shown as Figure 3.1. The two center circles are exactly the same size, however because they have different backgrounds they appear to be different sizes. Figure 3.2 is known as the Hering Illusion. The two horizontal lines are perfectly straight. The background pattern causes the two lines to appear slightly curved.

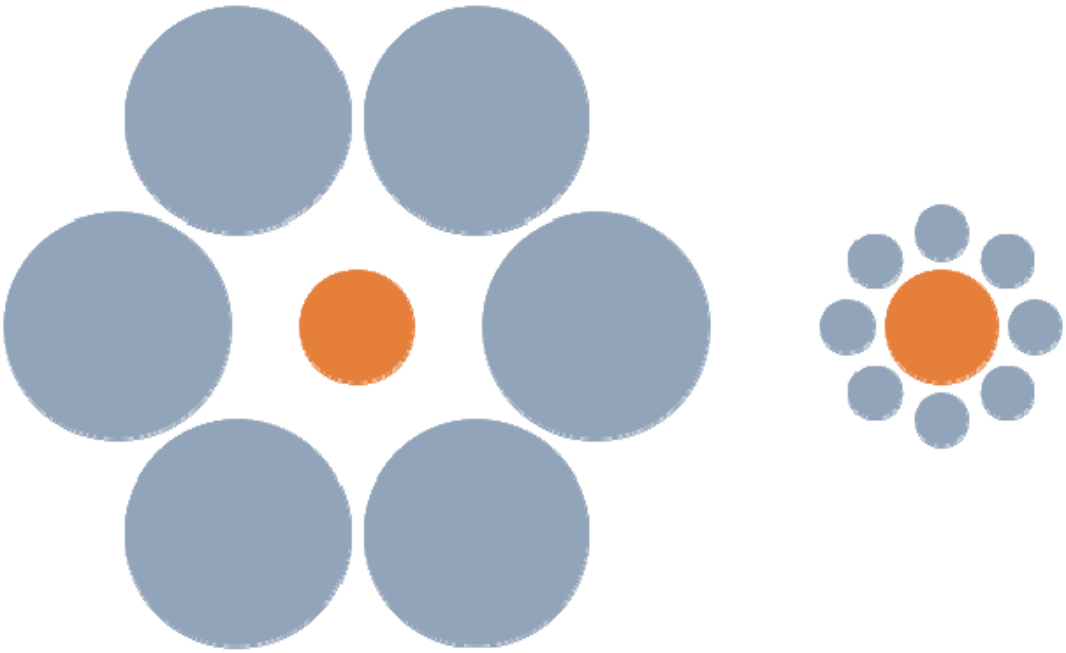

Figure 3.1[R] Ebbinghaus Illusion.

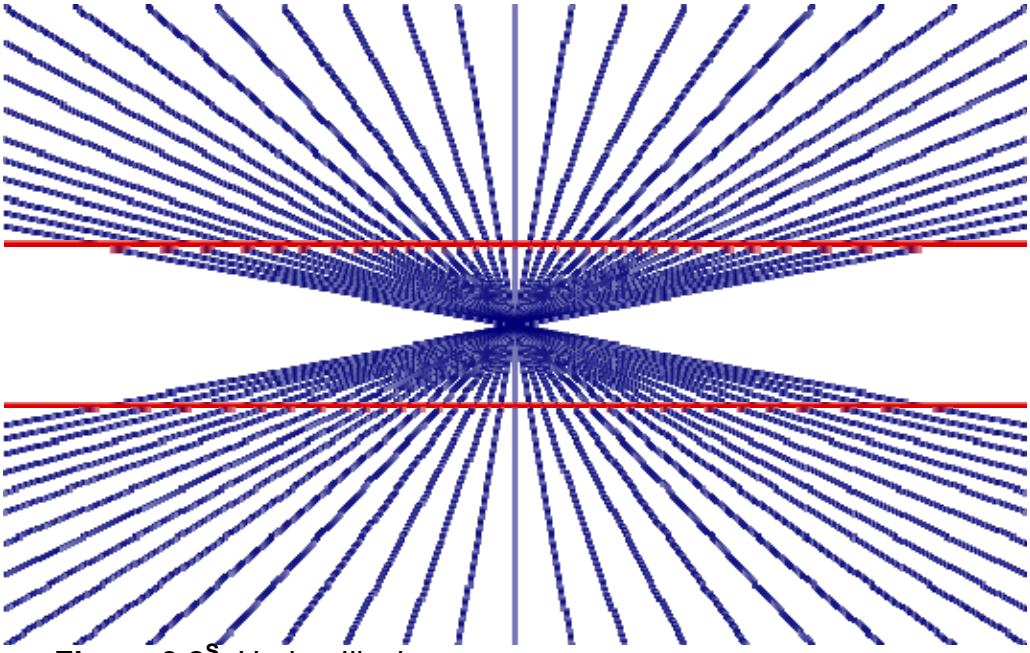

Figure 3.2[S] Hering Illusion.

[R] Figure from [139], used with permission.
[S] Figure from [140], used with permission under the GFDL (GNU Free Documentation License).

The most obvious application is to combine a functional image that identifies a region of interest, but lacks structural information necessary for localization, with an anatomical image providing this information.

This section will begin by discussing factors that need to be considered when fusing images. After a review of the fusion techniques available in the literature, a novel algorithm that automatically generates color tables for image fusion will be presented. The section will conclude with a study in which radiologists were evaluated performing tasks with a number of different fusion techniques.

3.2 Selection of a Fusion for Visualization Technique

Several factors need to be considered when choosing a visualization technique. These include information content, observer interaction, ease of use, and observer understanding. From an information point of view it is desirable to maximize the amount of information present in the fused image. Ideally, the registered images would be viewed as a single image that contains all of the information provided by both the MRI image and the PET image. Limitations in the dynamic range and colors visible on current display devices, as well as limitations in the human visual system make this nearly impossible.

This loss of information can be partially compensated for by making the fused display interactive. Some sort of control over the fusion technique can be provided which allows the observer to change the information that is visible in the fused display. The design of this control is an important part of the fusion process. How simple is it to use the control? How much training is required? Do

the display options offered by the control aid the observer or just complicate the observation process? How responsive is the control?

Perhaps the most important factor relates to the observer's understanding of the fused volume. For example, radiologists understand what they are looking at when they examine a grayscale MRI image, or PET image, i.e. variations in intensity and texture have a meaning. In the ideal case the knowledge and experience the observer has in examining the individual modalities would be directly applicable to the fused images.

It should be kept in mind that the choice of a fusion for visualization technique should be both application and observer dependent. It is well known that various vision deficiencies, such as deuteranomaly, influence how individuals perceive color. This means that in general there will not be a fusion technique that is ideal for everyone. Even among those without any documented vision deficiencies, the choice of the optimal colors will vary with factors such as experience and training. On the other hand, standard consistent fusion techniques are easier to support, aid in training, and can encourage collaborations and consults.

It is also necessary to consider environmental factors that affect how observers will perceive the displayed colors. This includes conditions such as the lighting in the room, the color of the background, and the gamma and black offset of the display device.

A useful tool for describing static techniques for fusing two sources is a two-dimensional color table or look-up-table. Just like a one-dimensional color table

which assigns a color to each value (usually grayscale intensity) in the image, a two dimensional color table assigns a color for a pair of values. The grayscale values of the two source images for a given pixel serve as indices in the color map. Looking up the indices in the color map gives the color that the same pixel in the fused image should have.

For an example see Figure 3.3 of a 3×3 color table. The vertical numbering represents intensity values in the first source image, while the horizontal numbers represent intensity values in the second source image. If the first source image is given by Figure 3.4 and the second source by Figure 3.5, then using this color table to fuse the two images will result in Figure 3.6.

Figure 3.3 Sample two-dimensional color table.

Figure 3.4 First source image.

Figure 3.5 Second source image.

Figure 3.6 Images shown in Figure 3.4 and Figure 3.5 fused using two-dimensional color table shown in Figure 3.3.

3.3 Overview of Fusion for Visualization Techniques

Much research has been devoted to discovering new and optimum ways to take two images and display them as a single image. These techniques include color overlay, color mixing, techniques based directly on color spaces, and spatial and temporal interlacing. To demonstrate each of these techniques, the

MRI image shown in Figure 3.7 and the PET image shown in Figure 3.8 will be used.

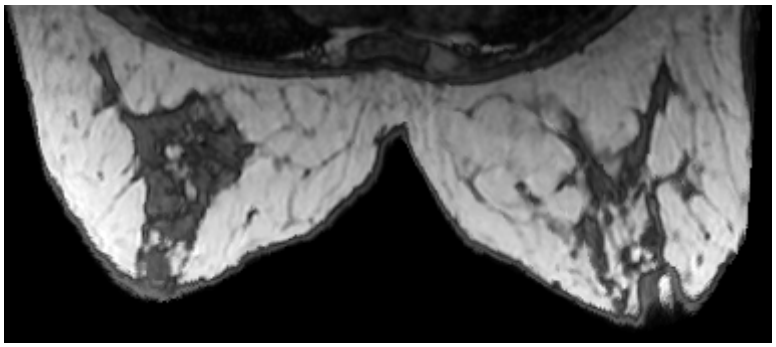

Figure 3.7 Example grayscale MRI image.

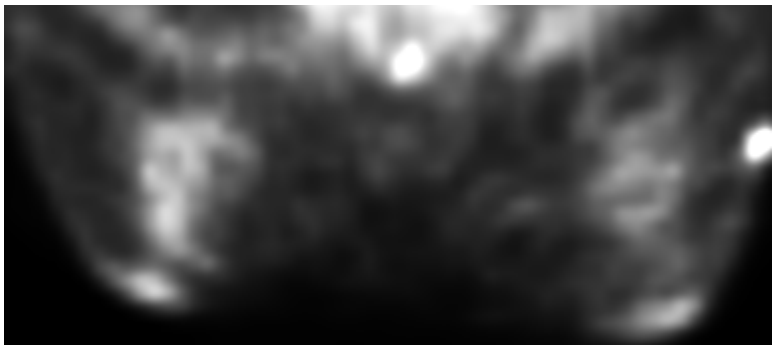

Figure 3.8 Example grayscale PET image.

3.3.1 Color Overlay

One of the most common techniques used for the fusion of two images is the color overlay technique.[141,142] In this technique one image is displayed semi-transparently on top of the other image. This can be implemented in many ways such as the addition of images, implementation of a 2D color table, or use of the alpha channel.

In this work, it is performed by a weighted averaging of the source images. Color tables are used to convert the grayscale MRI image and grayscale PET image to color images. A weighting is set, and the intensity of the fused image can be adjusted. Averaging causes a loss in contrast and a decrease in overall

intensity, so the ability to scale the intensity of the fused image may be necessary. Weighting can be easily implemented and adjusted via a scroll bar. When the slider is on one side of the scroll bar the PET image is shown, when it is on the other the MRI is shown. When the slider is set in between these extremes an image that is a linear combination of the PET and MRI is shown. For example, if the scroll bar is set to 76% PET image and 24% MRI image, the displayed image can be calculated by multiplying the brightness adjustment by the weighted average of the source images (0.76*PET+0.24*MRI). This equation would be used three times, once for each channel in the displayed image (ex. red, green, blue), using the associated channel in each of the source images.

An example of an image fused using color overlay is Figure 3.9. The MRI image is displayed using a grayscale color table and the PET using a yellow color table. The images are given equal weight and the resulting intensity is not being adjusted. The resulting color table is shown in Figure 3.10.

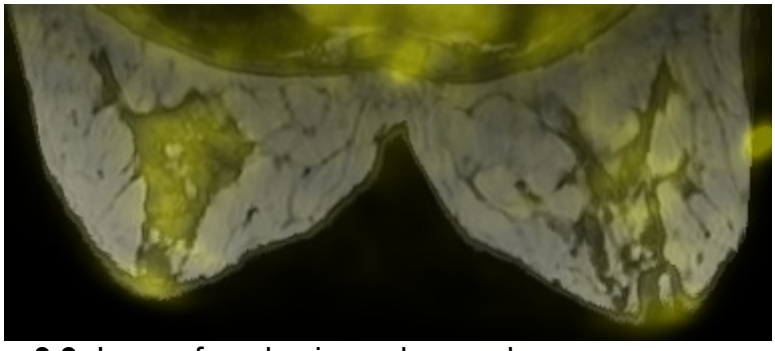

Figure 3.9 Image fused using color overlay.

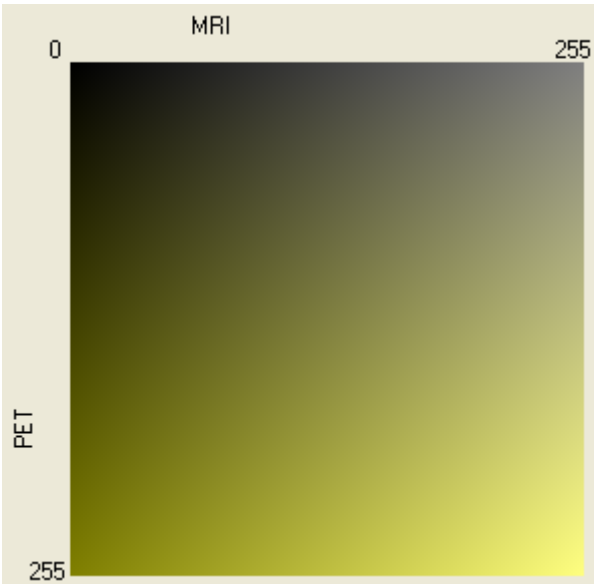

Figure 3.10 Color table used to create image shown in Figure 3.9.

Other common color tables used include grayscale/fire (Figure 3.11), and red/green (Figure 3.12). Study of the human visual system suggests that intensity should be used for the higher resolution image while color should be used for the lower resolution image. This is because the human eye is more sensitive to changes in intensity than changes in color.[143,144,145] The optimum color table is operator dependent, and care should be taken to select a color table that conveys the original intent of the image.

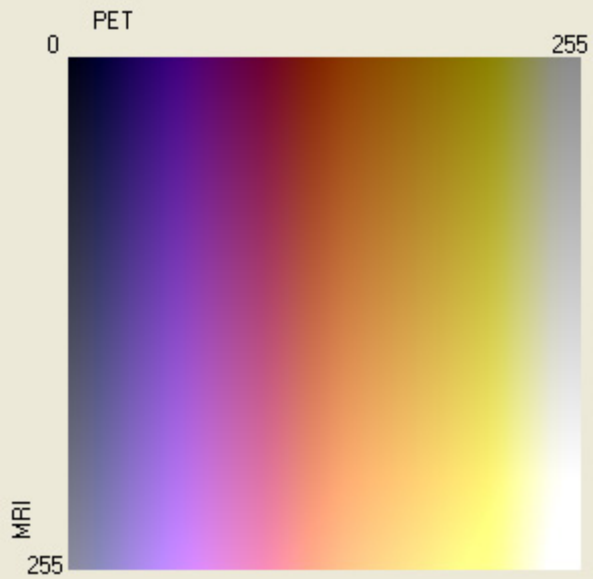

Figure 3.11 Grayscale/fire (hot-cold) color table.

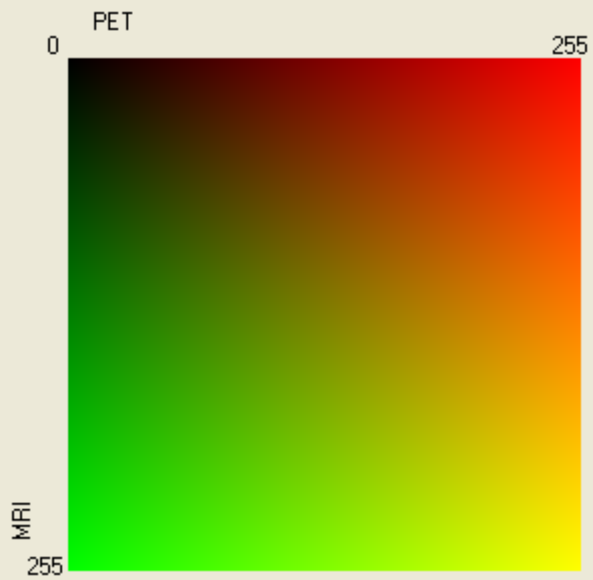

Figure 3.12 Red/green color table.

Color overlay is probably the most common technique used due to its simplicity. The controls are intuitive, and require little or no training or mathematical background. Depending on the choice of color it may be easy to visually pick out the contribution from each of the source images in the resulting image, and convey the original meaning of those images to the user.

3.3.2 Color Mixing

Color mixing is a technique that can be used to take any number of one channel images, N, and create a fused color image, typically defined in RGB (red, green, blue). Channel mixing is performed using Equation 3.1. Here R, G, B represent the red, green, and blue channels in the displayed image respectively, S_i represents the intensity in the i^{th} source image, R_i, G_i, B_i are the weighting factors for the red channel, green channel, and blue channel. They determine the contribution of source i to each of the output channels.

$$\begin{bmatrix} S_1 & S_2 & \dots & S_N \end{bmatrix} \begin{bmatrix} R_1 & G_1 & B_1 \\ R_2 & G_2 & B_2 \\ \cdot & \cdot & \cdot \\ \cdot & \cdot & \cdot \\ \cdot & \cdot & \cdot \\ R_N & G_N & B_N \end{bmatrix} = \begin{bmatrix} R & G & B \end{bmatrix} \qquad (3.1)$$

Let the source intensities be normalized from zero to one. Applying Equation 3.1 is then equivalent to taking the intensity axis of source *i* and lying it along the line segment formed by connecting $(0,0,0)$ to (R_i, G_i, B_i) in the RGB color space. The output image is then formed by summing the projections of each of these onto the red, green, and blue axes.

When using color mixing to combine PET and MRI images, there would be two sources (Figure 3.7 and Figure 3.8) and six weights. The observer can adjust the weighting to create a variety of fused images. Allowing the adjustment of weights during viewing can make the fusion technique interactive. Even though this is a powerful technique that provides a nearly infinite set of possible

fused images, it is not suitable for clinical use, since it may be difficult to predict how changing weights affects the fused image.

The best implementation of this method in clinical settings would involve a radiologist spending the time to select a small set of weighting matrices that produce useful fused images. Then, in a normal clinical setting, the observer could be presented a list describing these matrices and the capability to easily switch between them, via a drop down list or similar control.

For the most responsive implementation, RGB Mixing can be implemented as a 2D look up table (LUT) once the weights have been selected. Figure 3.13 is an example of an image produced this way, and Figure 3.14 is the corresponding 2D LUT.

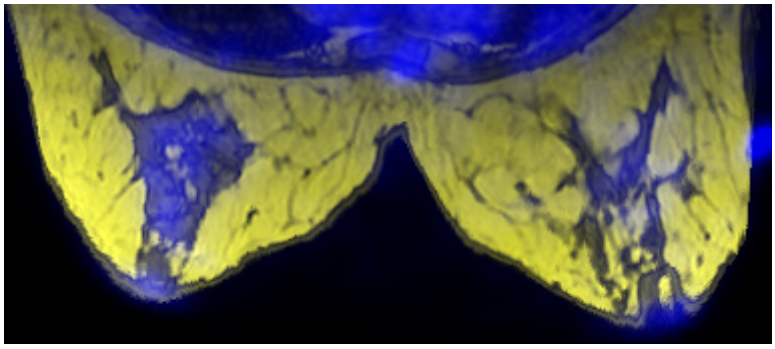

Figure 3.13 Image fused using color mixing.

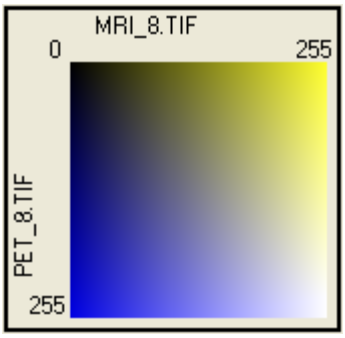

Figure 3.14 Color table used to create image shown in Figure 3.13.

The technique can be extended by allowing the vectors (R_i, G_i, B_i) to point in any direction. For example, as the source intensity increases the red in the fused image decreases. The technique can also be extended by using an offset so that the vectors, (R_i, G_i, B_i), do not need to be located at the origin. After making this modification the color mixing technique can be represented by Equation 3.2, where O_{xi} represents the offset from the origin along the x-axis for the contribution from source i.

$$(R, G, B) = (\sum_{i=1}^{N}(S_i R_i + O_{Ri}), \sum_{i=1}^{N}(S_i G_i + O_{Gi}), \sum_{i=1}^{N}(S_i B_i + O_{Bi})) \qquad (3.2)$$

3.3.3 Use of Other Color Spaces

A powerful, yet more complex technique for the creation of fused images involves the use of different color spaces.[143,144,145] A few examples include CIE XYZ, CIE L*a*b*, HSV, and HSL. Each source grayscale image can be used as a channel in the color space. The resulting color image can then be converted to the RGB color space for display. For example if registered PET, CT, and MRI images are available, MRI can be used as the lightness, CT as the saturation, and PET as the hue (Figure 3.15).

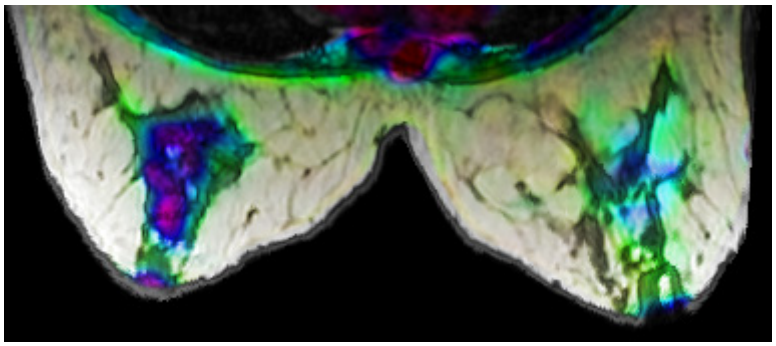

Figure 3.15 Image created using the HSL (hue, saturation, lightness) color space. Hue=PET, Saturation=CT, Lightness=MRI.

This technique is perhaps more intuitively applied for the fusion of three sources, but none the less can be used for the fusion of two. It can be done by using a source for more than one channel, by setting the third channel to a constant (Figure 3.16), or by mapping one of the sources to a combination of the two available channels.

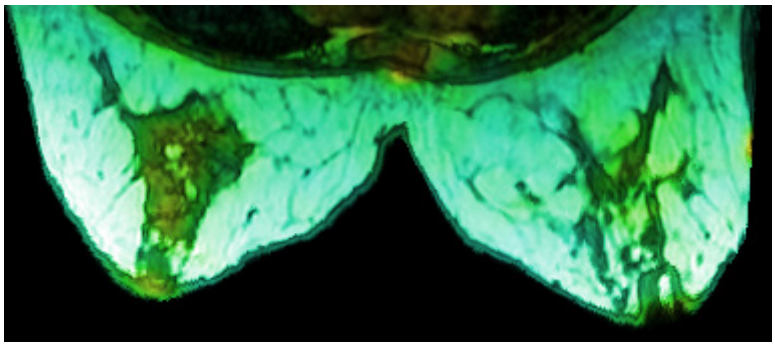

Figure 3.16 Image created using the HSL (hue, saturation, lightness) color space. Hue=PET, Saturation=constant, Lightness=MRI. Hue values are allowed to vary from cyan to green to yellow.

Care needs to be taken with selection of a color space and its implementation details. For example, when mapping a source to the hue channel, it is has been advised to map the source intensities to a small range of angles. Mapping to all 360 degrees will result in drastic color changes, distorting or hiding the intensity changes in the channel, and creating false segmentation. It has been suggested that varying hue from cyan to green to yellow (Figure 3.16) gives good results, while using the red, purple, and blue hues gave false impressions of lower intensity values.[144]

Of the fusion techniques presented here, the use of other color spaces is the least intuitive. In particular, the conversion from other color spaces to RGB often

fuses the sources in a complex, difficult to understand manner. As a result training will most likely be needed before implementation in a clinical setting.

3.3.4 Interlacing

Interlacing is a very common image fusion technique.[138,142,146] A simple implementation is to interleave the pixels in the source images. Fused images are created by taking alternating pixel from each of the source images. For example, the odd pixels in the fused image are taken from odd pixels in the first source image while the even pixels are taken from even pixels in the second source image. In other words, the first pixel of the fused image will be the first pixel of the first source image, the second pixel of the fused image will be the second pixel of the second source image, and so on (Figure 3.17). Independent color tables can be applied to the source images, and the observer should be given control of the source intensities. By adjusting the intensities of the source images the observer can bring each of the source images out of the fused image as necessary.

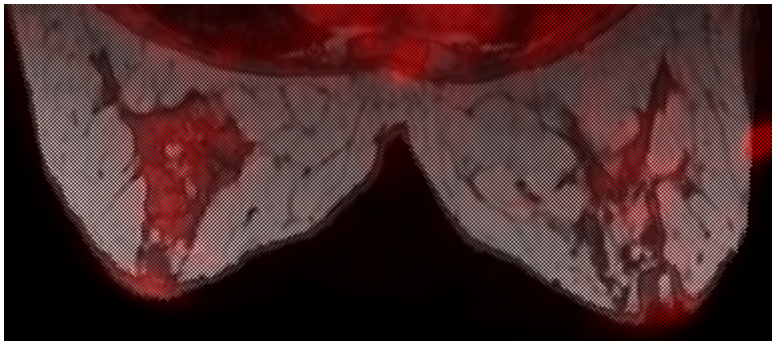

Figure 3.17 Image created by interlacing PET and MRI data. PET image data is displayed using a red color table and MRI with a grayscale**.**

Other interlacing options include interleaving the rows, or columns of the source images. Adjusting the ratio of pixels given to the two modalities is

another option for making one of the sources more prevalent. For example, have two MRI rows followed by one PET row.

One of the largest drawbacks of an interlacing approach is the loss of spatial resolution. Discarding every other row or pixel, causes the contribution to the fused volume to have half of the resolution of the source. In the case of PET, which is magnified to be the same resolution as the MRI prior to fusion, this is a minor issue. However, the effect of this approach on the high resolution MRI should be considered.

This lose of resolution could be compensated for by doubling the size of the source images. This however is not always convenient. This issue has been addressed by performing the interlacing temporally rather than spatially. Rapidly alternating the images allows fusion to be performed within the eye, via residual images on the retina. Adjusting the intensity of the images, or their allotted display times will adjust their contribution to the fused image.[146]

3.4 Genetically Generated Color Tables

As noted above, the majority of the fusion techniques discussed can be implemented using two-dimensional color tables. This facilitates an alternative approach to discovering the best visualization technique. Rather than trying out each visualization technique and determining optimum parameters, a difficult and time consuming task, in this section we focus on finding the best two-dimensional color map.

This is not a new approach and a lot of effort has been expended on studying the design of color tables, how various properties of them affect the perception of

the displayed images, and the role the images that the color table is being applied to play.[147,148,149] In this section a new genetic algorithm which automatically generates color tables with desired properties is discussed.

3.4.1 Drawbacks of the Color Table Approach

Color tables are often created by hand, and are usually evaluated by humans. The biggest drawbacks of this approach are that the color tables tend to be large, and that it is only feasible to evaluate a small number of them.

The size of the color map depends on the number of discrete values in the sources to be displayed, and the number of colors the display device has access to. For example if there are two 8-bit sources, there will be 256*256 entries in the color map. Assuming an 8-bit display, each entry can be one of 256*256*256 colors. Considering every color for each entry is a nearly impossible task for a human. This problem is usually avoided by selecting and using one of the previously mentioned fusion for visualization techniques (Section 3.3). The problem with taking one of these approaches is that only a small set of the possible color tables are considered. To address this issue a new genetic algorithm based color table creation method is proposed. This method will search through the space containing all possible color tables in order to produce one that best represents a set of criteria.

Evaluation of the color tables is usually done directly by humans, and unless vast human resources exist, only a small number of color tables are considered for a particular task. A simple technique for automatic evaluation of color tables that is used by the genetic algorithm will be discussed. While this technique is

not meant to replace human evaluation, it can be used to pre-evaluate a large set of color tables, guiding the genetic algorithm in selecting a small set for human review.

3.4.2 Automatic Evaluation of Color Tables

3.4.2.1 Color Difference Definition

Before an algorithm which generates color tables can be created, there needs to be a way to quantitatively define guidelines or requirements to be used when generating the color tables. The result of evaluating a color table with these guidelines will be the fitness factor used to determine the reproduction of the color tables within the genetic algorithm.

To aid in defining these guidelines a method for determining the difference between two colors is first introduced. Traditionally this difference is defined as the Euclidean distance between the two colors in the CIE L*a*b* space (Equation 3.3) or the CIE L*u*v* space (Equation 3.4).

$$\Delta E = \sqrt{(\Delta L^*)^2 + (\Delta a^*)^2 + (\Delta b^*)^2} \quad (3.3)$$

$$\Delta E = \sqrt{(\Delta L^*)^2 + (\Delta u^*)^2 + (\Delta v^*)^2} \quad (3.4)$$

The validity of Equation 3.3 and Equation 3.4 comes from the assumption that the color spaces are perceptually uniform and orthogonal. In order for the Euclidean distance to apply, the basis channels used to define colors within the space need to be orthogonal, this is true for both CIE L*a*b* and CIE L*u*v*. In order for the color space to be perceptually uniform the Euclidean distance between two colors within the space need to be directly related to the perceived closeness of the colors. It has been shown that this assumption is not quite true

for either CIE L*a*b* or CIE L*u*v*.[150] In particular, each of these give unacceptable errors for certain regions of the color gamut.[151] For this reason and for explicit definition in the RGB color space, which is required for display on current hardware, we choose to use the more recently developed computationally efficient measurement, shown as Equation 3.5, used by CompuPhase in their PaletteMaker application.[151,152]

$$\begin{aligned}
\bar{r} &= \frac{C_{1,R} - C_{2,R}}{2} \\
\Delta R &= C_{1,R} - C_{2,R} \\
\Delta G &= C_{1,G} - C_{2,G} \\
\Delta B &= C_{1,B} - C_{2,B} \\
\Delta C &= \sqrt{(2 + \frac{\bar{r}}{256}) * (\Delta R)^2 + 4 * (\Delta G)^2 + (2 + \frac{255 - \bar{r}}{256}) * (\Delta B)^2}
\end{aligned} \tag{3.5}$$

Here ΔC is the perceived difference between the two colors defined in non-linear RGB space (sRGB) as $(C_{1,R}, C_{1,G}, C_{1,B})$ and $(C_{2,R}, C_{2,G}, C_{2,B})$, where $C_{X,Y}$ is the value for the Y^{th} channel for the X^{th} color, and has values from 0 to 255. This color difference equation assumes display on a standard computer monitor (CRT, LCD) with a gamma of approximately 2.5 in a typical office viewing environment. For further discussion of this metric see [152]. Color difference equations aid in defining requirements and evaluation procedures for color tables.

3.4.2.2 RGB Color Space

It was decided that the color tables produced need to be defined in the 8-bit per channel RGB color space supported by most applications. This is a non-linear gamma correct RGB color space, so that colors will appear properly on a typical CRT or LCD display. This is required in order to facilitate easy use and

guaranteed compatibility of the color tables produced. This was taken into consideration when selecting the formula for color differences.

3.4.2.3 Order Principle

Trumbo defines several desirable properties of color tables.[153] One of these is the order principle. Basically, if a color table satisfies the order principle, then the colors chosen to represent the data values should be perceived as ordered in the same order as the data values. Spectral color tables where large variations of hue occur do not satisfy this principle. This is important because the pixel values in the original medical data represent physical quantities, such as the concentration of F-18 decay in the PET images. This is the information radiologists need to have. If one pixel is shown as blue and another red, the radiologists will be unable to determine which pixel has a higher concentration without referring to the color table. While the color table will not be a secret from the radiologist evaluating the fused data, the less they need to refer to the color table the more efficiently they can examine the data.

In addition, a side effect of a color table not satisfying the order principle is that the color table often creates false segmentation when applied to the image. The color contours created in the image emphasize particular pixel values.

To guarantee that the order principle is satisfied, a representation of the color table based on the extended color mixing technique (Equation 3.2) is used by the algorithm. The linearity imposed by the color mixing model ensures that the order principle will be satisfied.

3.4.2.4 Rows and Columns Principle

The rows and columns principle is also defined by Trumbo.[153] It states that the colors in the color table should be chosen so that the two source images do not obscure one another.

This is particularly important when viewing medical images. Each of the input images and their gray levels mean something to the radiologist. This meaning must be preserved in the fused images. The radiologist needs to be able to identify the intensity of each of the source images by examining the fused image.

This is ensured by making the colors used for the first source's one dimensional color table as different as possible from the colors used for the second source's one dimensional color table. In other words, the first row of the color table should consist of colors as different as possible from the first column. This can quantitatively be measured by maximizing ΔC in Equation 3.5, for the average color in the first row of the table and the average color for the first column in the table. This color difference will be referred to as $\Delta C_{sources}$. Due to the linear model of the color mixing technique, this property will then be distributed throughout the rest of the color table.

3.4.2.5 Perceivably Uniform

The ideal color table should be perceivably uniform. The ΔC between neighboring entries in the color table should be constant throughout the table. This can be measured by finding ΔC for all neighbors and then examining its

variance. The smaller the variance the better. We will refer to this variance as $\mathrm{var}(\Delta C_{table})$.

This is an important factor because it minimizes the reliance on the color table, due to the fact that the radiologist's intuition about the location of the color in the color table is more likely to be correct.

3.4.2.6 Maximized Contrast

The contribution from each source should have as much contrast as possible. As contrast increases for a source, it gets easier to see the variations in the fused image due to that source. Due to using the color mixing model we need only to examine the endpoints of the first row and column of the color table to know the range of colors available for each of the sources to use.

Maximizing ΔC between the first entry in the first column and the last entry in the first column of the color table will maximize the contrast for the first source. Similarly, maximizing ΔC between the first entry in the first row and the last entry in the first row of the color table will maximize the contrast for the second source.

In additional, to ensure good contrast throughout the color table it is desirable to have the contrast along the diagonal of the color table maximized. This is done by maximizing ΔC for the first entry in the first row and column of the color table and the last entry in the last row and column of the color table. Contrast throughout the remainder of the color table is also evaluated by maximizing the mean ΔC for all neighboring pixels in the color table.

In summary we will evaluate contrast using by four factors: the contrast for the first source (ΔC_{s1}), the contrast for the second source (ΔC_{s2}), the contrast along the diagonal (ΔC_{diag}), and the mean contrast between neighboring pixels ($\overline{\Delta C_{table}}$).

3.4.2.7 Desirable Properties Not Considered

It should be noted that in the current implementation the algorithm does not consider all of the desired properties of a color table. For example, no preference is given to any particular color. Humans may find some colors easier to look at and examine for long periods of time than others.

Simultaneous contrast and chromatic contrast effects, as described in [148], are not considered. These effects describe how the appearance of a particular color may change based on the surrounding colors in the image.

Another, often neglected, effect that the human visual system has on images is how the color of an object influences its perceived size.[154,155] For example, if we color a lesion red-purple it would appear larger than if it had been colored green.

3.4.3 The Algorithm

A relatively simple and standard genetic algorithm is used for the generation of the color tables. Each color table is defined by 12 real numbers that have a range from -1 to 1. These numbers represent the following variables from Equation 3.2: R_1, O_{R1}, G_1, O_{G1}, B_1, O_{B1}, R_2, O_{R2}, G_2, O_{R2}, B_2, O_{B2}. These

coefficients when used with the color mixing equation completely define a color table.

To start, an initial population of color tables is randomly generated. An iterative loop is then entered. Each member of the population is then evaluated and ranked based on the requirements of the desired color table. A new population is then generated, where the contribution from each member of the previous generation to the new generation is based upon its ranking. This process is repeated for a large number of iterations.

To evaluate a population of color tables, they are tested for each requirement as previously described. The numeric results of the evaluation of a given color table can then be weighted and summed to give the fitness score for that member of the population. This process is shown as Equation 3.6. Each of the three desirable properties included in the fitness factor are given equal weight. Prior to creating the fitness factors each term is normalized by the mean value of that term for the entire population and threshold to a maximum absolute value of 2. This prevents any single term from dominating and insures improvements in any term can influence the fitness factor.

$$fitness\_factor = \Delta C_{sources} - \mathrm{var}(\Delta C_{table}) + \frac{\Delta C_{table}}{4} + \frac{\Delta C_{s1}}{4} + \frac{\Delta C_{s2}}{4} + \frac{\Delta C_{diag}}{4} \quad (3.6)$$

The members of the current generation with the highest fitness scores are automatically included in the next generation. The rest of the members in the next generation are created by splicing or mutating the members in the current population.

When creating a population member by mutation, a member of the previous generation is chosen randomly with a probability proportional to its fitness score. The new population member is then created from the old one by making one or two random changes to its defining coefficients.

When creating a population member by splicing, two members of the previous generation are chosen at random with a probability proportional to their fitness scores. The new population member is generated by taking the first X coefficients of it from the first chosen member and remaining 12-X coefficients from the second member. The point of splicing, X, which determines the amount of each of the chosen color tables that gets transferred to the new color table, is chosen at random.

For the stopping criteria the algorithm can be halted when the member with the highest fitness score does not change for a number of generations. There is no fear of running the algorithm for too many generations due to the nature of the problem.

After the algorithm has finished executing, the member of the final population with the highest fitness score represents the 'best' color table that the algorithm could come up with. The algorithm can either be run several times or the top members of the final population can be considered, providing a set of color tables that can then be evaluated by human observers. The algorithm was written in MATLAB[156] and the code is available in Appendix E.

3.4.4 Results

The genetic algorithm was run twice. An initial population of 100 color tables was randomly created. When creating a new generation the highest ranked member of the current generation, along with 29 other members were selected for replication. The remaining 70 members of the new generation were created by splicing and mutation, with probabilities of 30% and 70%, respectively. A single iteration of the algorithm took an average of 0.17 sec on an Intel Core 2 Duo E6420, with only minor changes in the member with the highest fitness score occurring after approximately 300 iterations. The results are shown as Figure 3.18 and Figure 3.19. Images fused using these color tables are shown as Figure 3.20 and Figure 3.21, original PET and MRI images used are shown as Figure 3.22 and Figure 3.23. Differences in the optimized color table are due to a different random initial population, and a different sequence of random mutations, splicing, and selection.

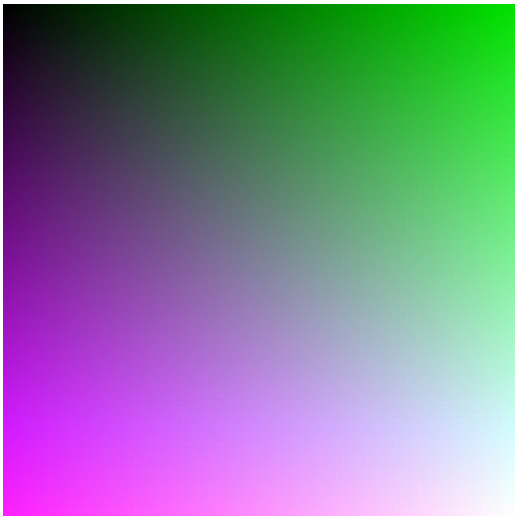

Figure 3.18 Sample color table generated using genetic algorithm.

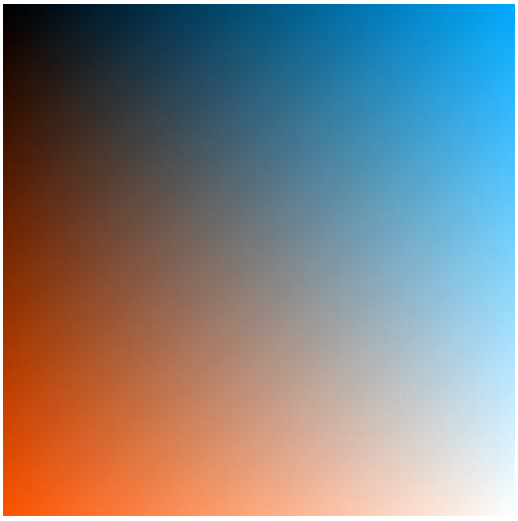

Figure 3.19 Sample color table generated using genetic algorithm.

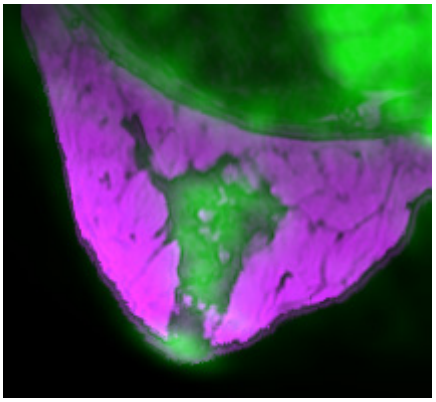

Figure 3.20 Fused image of Figure 3.22 and Figure 3.23 created using the color table shown in Figure 3.18.

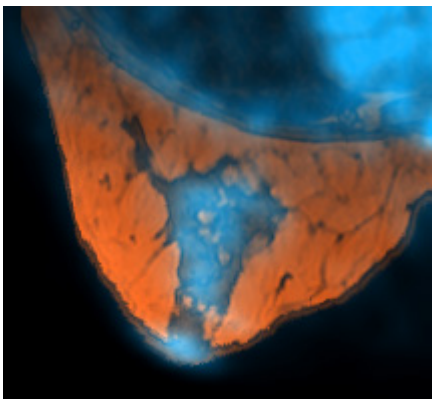

Figure 3.21 Fused image of Figure 3.22 and Figure 3.23 created using the color table shown in Figure 3.19.

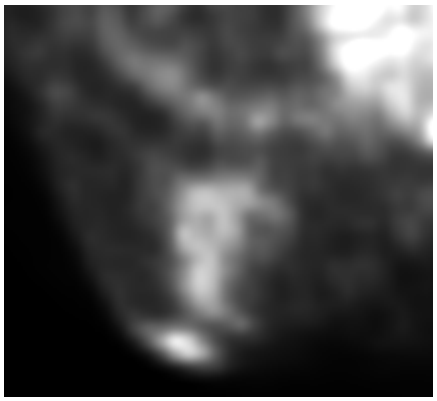

Figure 3.22 Original PET Image.

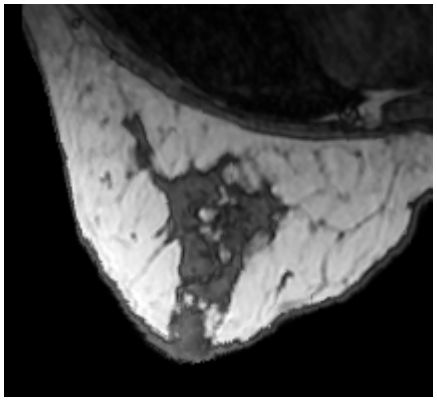

Figure 3.23 Original MRI Image.

These results can better be understood by plotting the color tables in a color space which is known to be relatively perceptually uniform. The CIE L*a*b* was used for this purpose. Figure 3.24, Figure 3.25, Figure 3.26, and Figure 3.27 provide different views of the color table shown in Figure 3.18 plotted within this color space. Figure 3.28, Figure 3.29, Figure 3.30, and Figure 3.31 provide different views of the color table shown in Figure 3.19 in this color space.

The results have similarities to color tables proposed in earlier works. It has been proposed to generate color tables as planes, portions of cylinders, or cones within a uniform color space.[153,157] Recent results show that best observer performance was achieved when using a plane.[157] Small gamut sizes and the rectangular shape of the color tables however limit the range of colors and

amount of contrast available when the color table is created as a plane through a uniform color space. The cone or cylinder shaped color tables can increase contrast and the range of colors used for encoding.

The color tables generated by the genetic algorithm appear to strike a compromise between the planar and curved surfaces. In general a planar shape is followed with the addition of slight curvature that provides a significant increase in the range of colors and contrast within the color table. As shown by the visualization study conducted in Section 3.6 this compromise was preferred by observers. The slight contours of these color tables when plotted in a perceivably uniform color space differentiates them from previous efforts.

Through modification of the way color tables are evaluated by the algorithm, color tables that may meet specific requirements and needs can be generated. The color tables created from the runs, presented here, provide a new way to fuse multimodal medical data sets for presentation to radiologists.

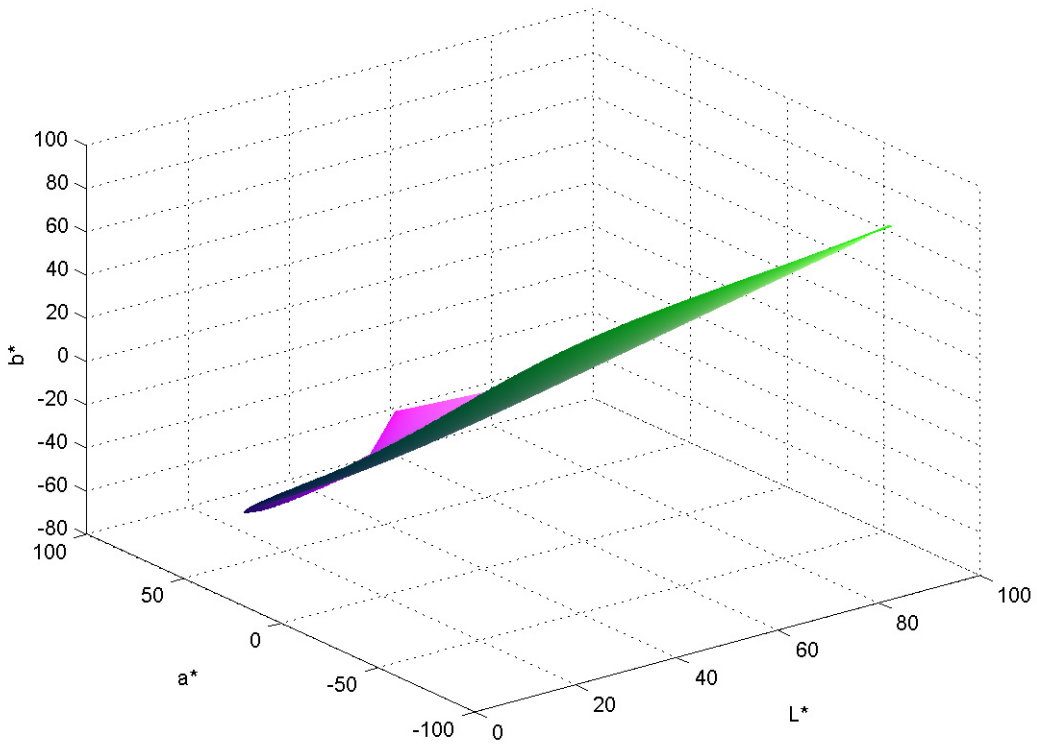

Figure 3.24 Color table shown in Figure 3.18 plotted in the CIE L*a*b* color space. The nearly planar structure of the color table is clearly visible.

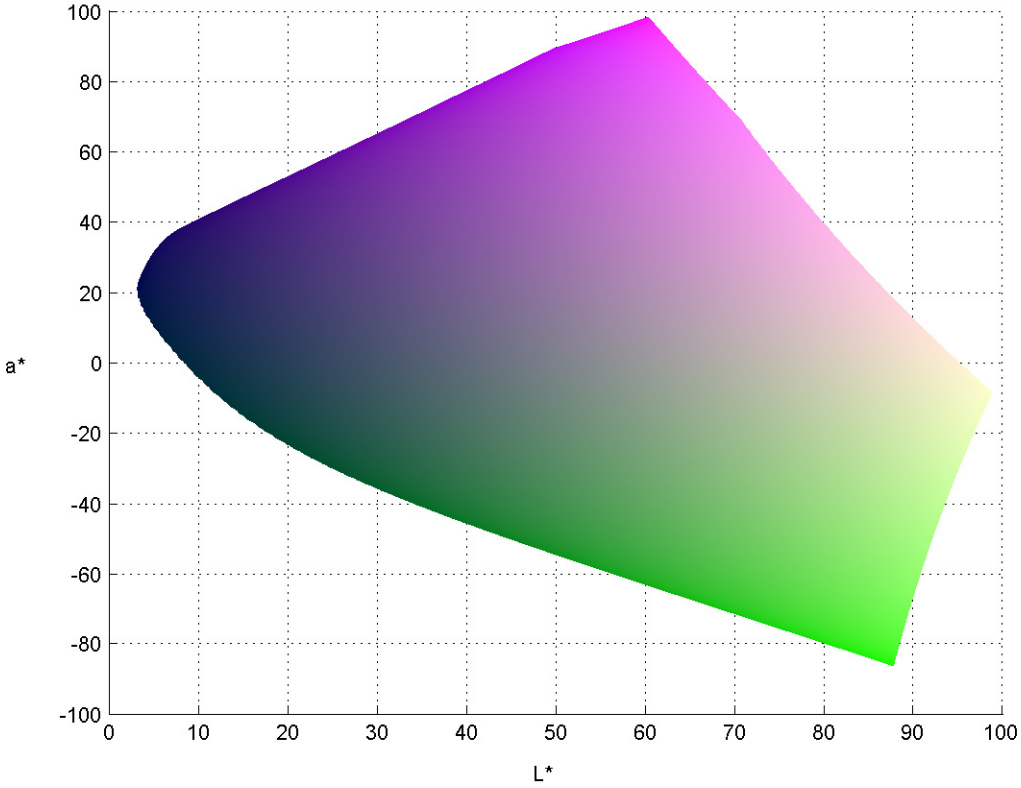

Figure 3.25 Color table shown in Figure 3.18 projected onto the L*a*-plane in the CIE L*a*b* color space.

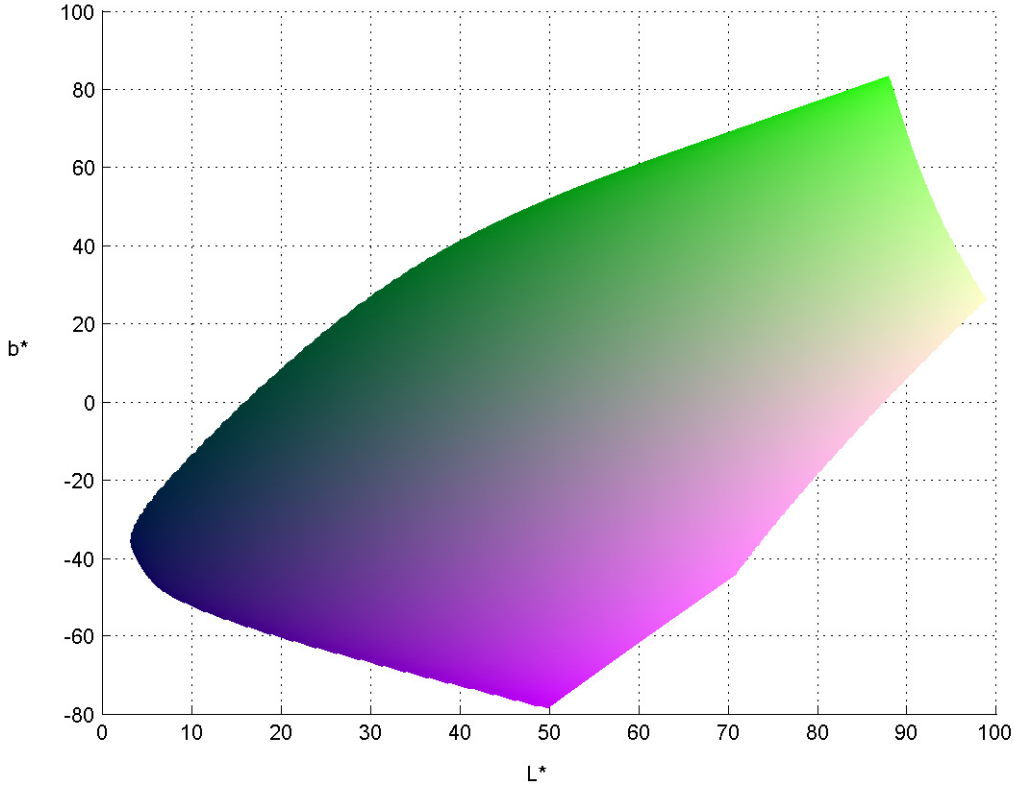

Figure 3.26 Color table shown in Figure 3.18 projected onto the L*b*-plane in the CIE L*a*b* color space.

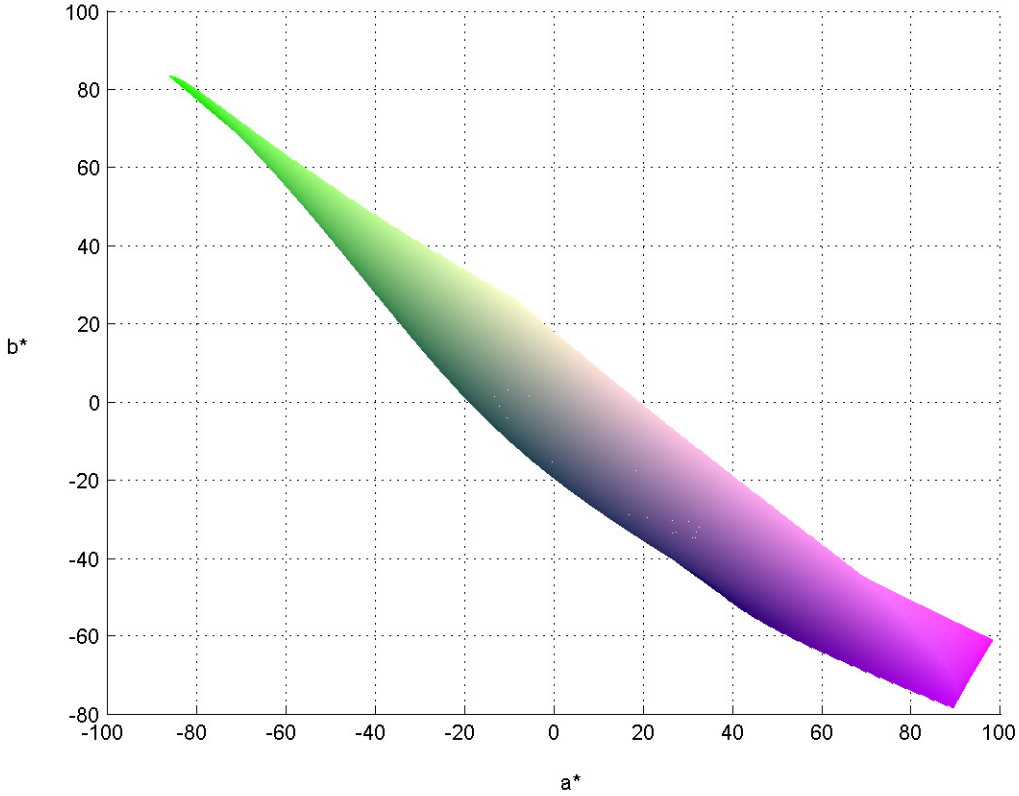

Figure 3.27 Color table shown in Figure 3.18 projected onto the a*b*-plane in the CIE L*a*b* color space.

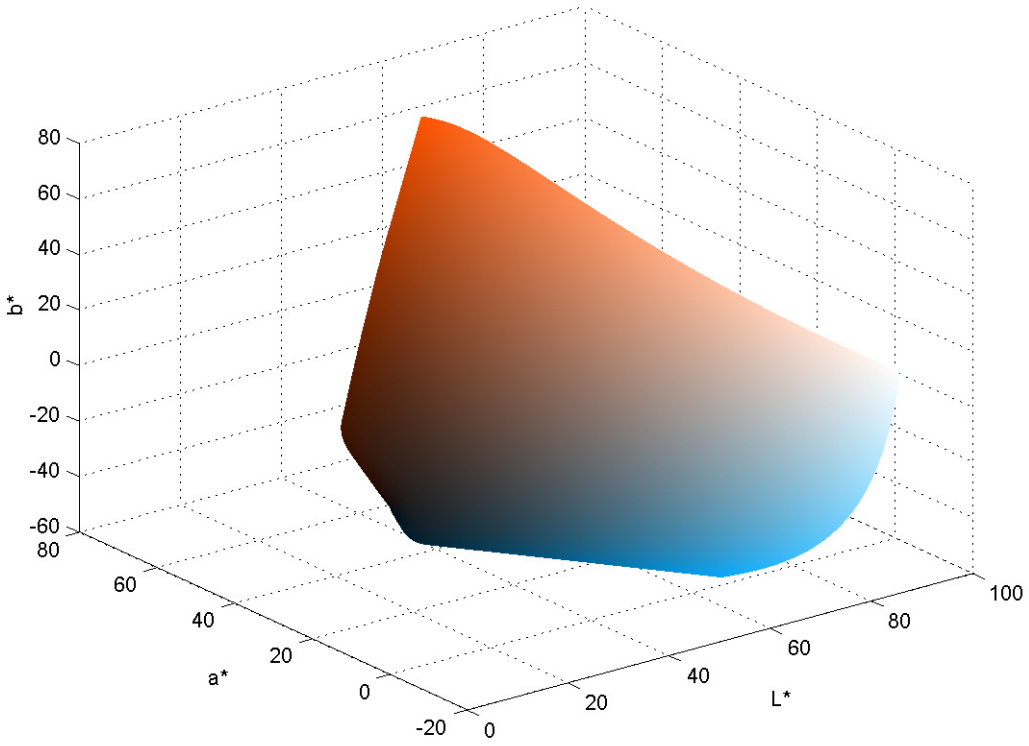

Figure 3.28 Color table shown in Figure 3.19 plotted in the CIE L*a*b* color space.

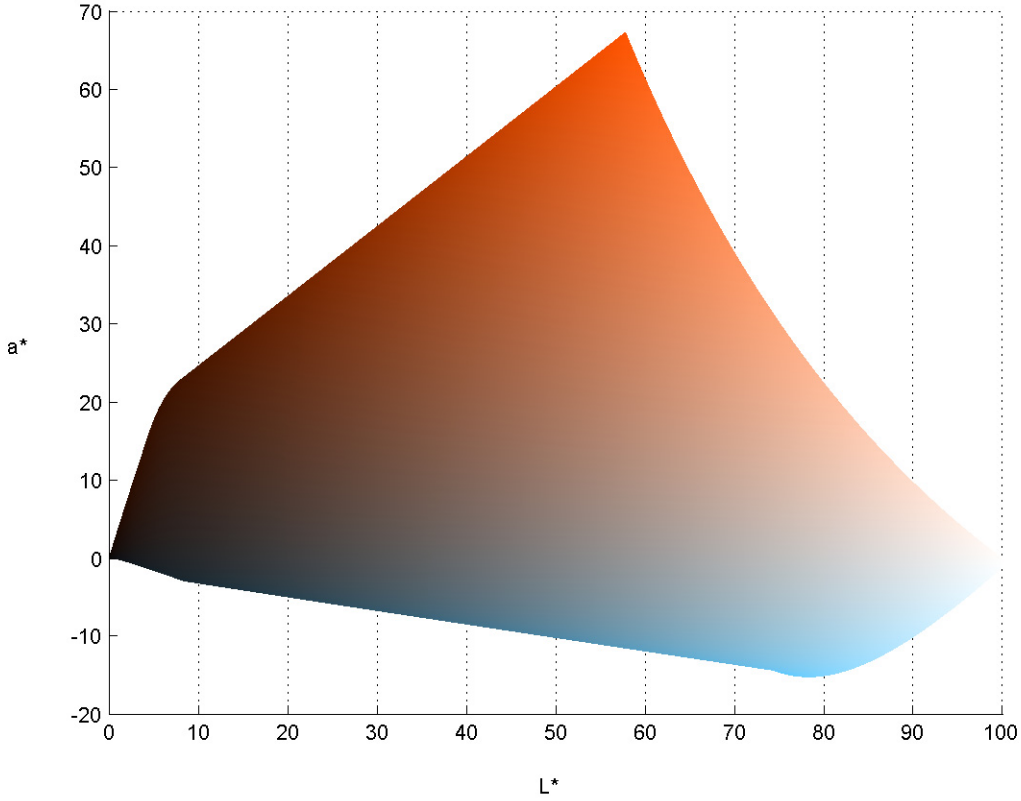

Figure 3.29 Color table shown in Figure 3.19 projected onto the L*a*-plane in the CIE L*a*b* color space.

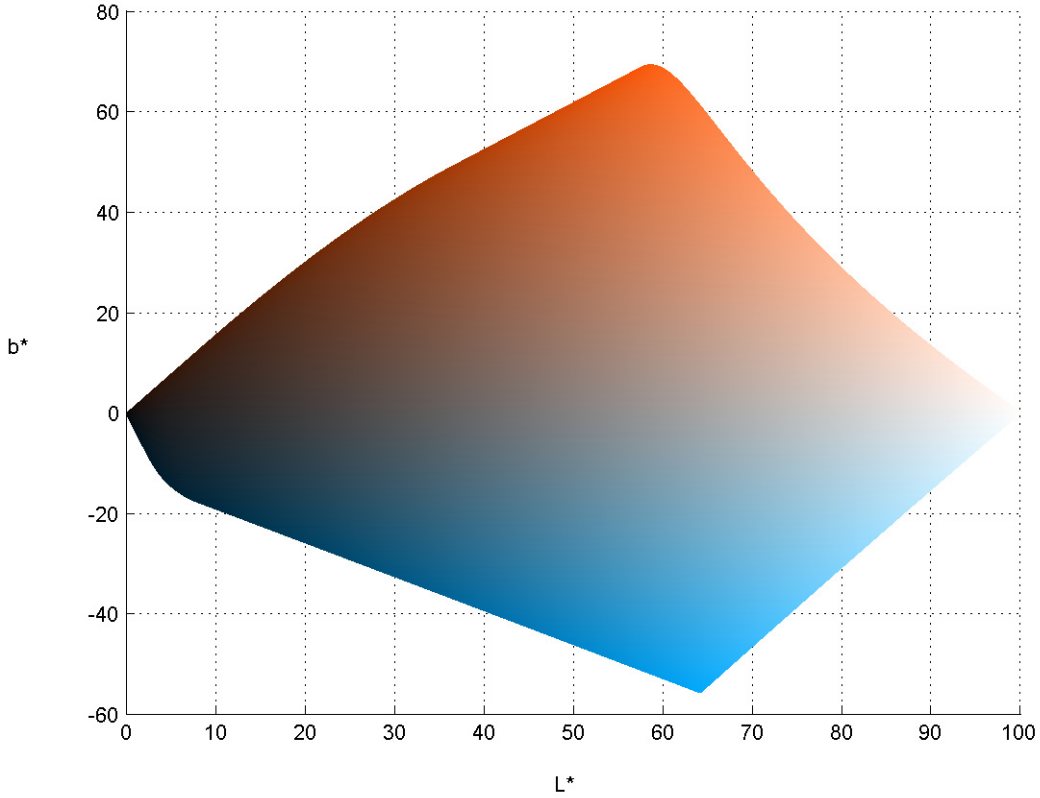

Figure 3.30 Color table shown in Figure 3.19 projected onto the L*b*-plane in the CIE L*a*b* color space.

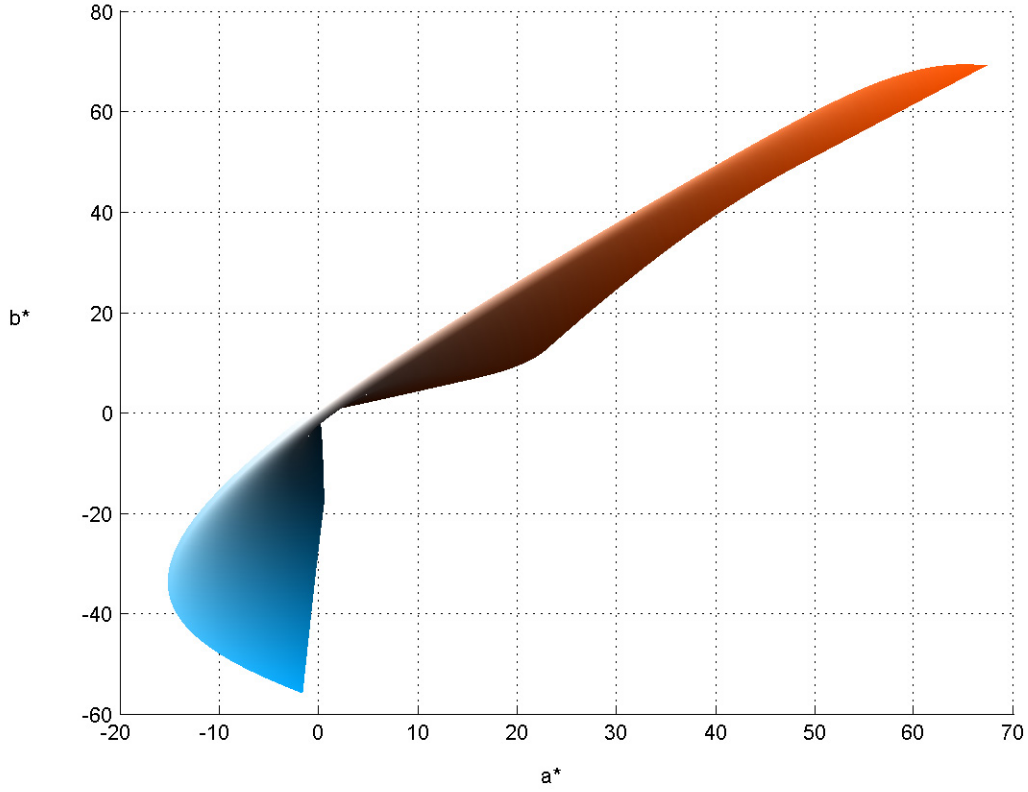

Figure 3.31 Color table shown in Figure 3.19 projected onto the a*b*-plane in the CIE L*a*b* color space.

3.5 Fusion Viewer

To the author's knowledge, there is not a readily available tool for use by the medical research community which is designed for studying multimodal or multi-image data sets. In order to facilitate research on image fusion, particularly rapid implementation and easy evaluation of novel fusion techniques a new application, Fusion Viewer, was created. It is designed to allow easy side-by-side evaluation of multiple data sets, and provides tools for studying fusion techniques and the volumetric display of fused data sets. The remainder of this section covers the design and capabilities of the Fusion Viewer application.

3.5.1 Application Design

The application, Fusion Viewer, was designed and implemented with a modular object oriented design. It was decided that the application should be implemented on the .NET platform, in its language of choice, C#. This insures that the application can be widely used due to the unique capability of a .NET application to be both operating system, and machine architecture independent. The growing popularity of the .NET platform ensures that the application will be supported for the foreseeable future.

C# was selected for its rapid development tools and large, well documented, supporting framework (library). Unlike traditional C++, and similar to Java, it provides a managed setting (i.e., garbage collection, exception handling, enhanced security). Unlike Java however, C# makes access to the operating system and native code easy through the runtime marshalling infrastructure. The direct memory access feature (i.e., pointers), while not currently used, is considered a necessity by many programmers developing image processing applications.

Novel fusion techniques, both of the raw image data and of projection data, can be quickly and easily implemented as plug-ins for the Fusion Viewer. The plug-ins simply need to be placed in the program directory and no recompilation of the application source code is necessary. Due to the language independent nature of the .NET platform, implementers of plug-ins can work in the programming language of their choice.[158]

Fusion Viewer is designed to process data on an “as-needed” basis. By only processing the portions of the image volume that are currently visible to the user, the images can be resized, converted to 8-bit (dynamic range adjusted), undergo contrast and brightness adjustments, have color tables applied, and be fused with other images in real time. By processing on an “as-needed” basis a highly interactive environment is available to the user.

Difficult installation of research tools often limits their acceptance by the biomedical research community. The .NET platform makes the distribution of the Fusion Viewer software trivial. The application only needs to be compiled (to Microsoft Intermediate Language) once, after which it can be run on any computer with the .NET framework installed. This means it can simply be downloaded and run. The user does not need to perform a complicated compilation process.

In addition to fusing capabilities, several options are provided for mapping 16-bit data sets onto an 8-bit display, including windowing, automatically and dynamically defined tone transfer functions, and histogram based techniques. Also, both traditional Maximum Intensity Projections (MIP) and MIPs of fused volumes are supported.

3.5.2 Importing and Exporting Data

The ‘File’ menu of Fusion Viewer provides access to the import and export features of the application. While Fusion Viewer supports two-dimensional images, it is designed specifically for three-dimensional data sets. The read and write capabilities of the software are provided by the FreeImage library.[159,160]

FreeImage is a cross-platform library designed to allow popular graphics image formats to be easily used in other applications. This means that with little effort the Fusion Viewer application can be modified to read and write any of the more than 20 image formats supported by FreeImage.

Currently only the capability for importing multi-page Tagged Image File Format (TIFF) files is included in the release version of the software, but work on supporting other formats such as DICOM is underway. When exporting images from Fusion Viewer you have the choice of exporting the entire volume as you have manipulated it for display, or just the currently visible portion of the volume (e.g., a slice from a stack view, or the current projection from a projection view).

3.5.3 Displaying a Volumetric Data Set

By default, when a volume is first opened it is displayed using the conventional orthogonal cross-section views. Figure 3.32 is a screenshot that shows volumes being displayed using this method. Each displayed volume is shown as three images, each representing a cross-section through the volume, axial, sagittal, and coronal. The three images shown are selected in such a way that they pass orthogonally through a focus point in the volume. The cross-hairs shown on each image indicate the point of focus, and the two lines of each cross-hair represent the locations of the other two displayed slices.

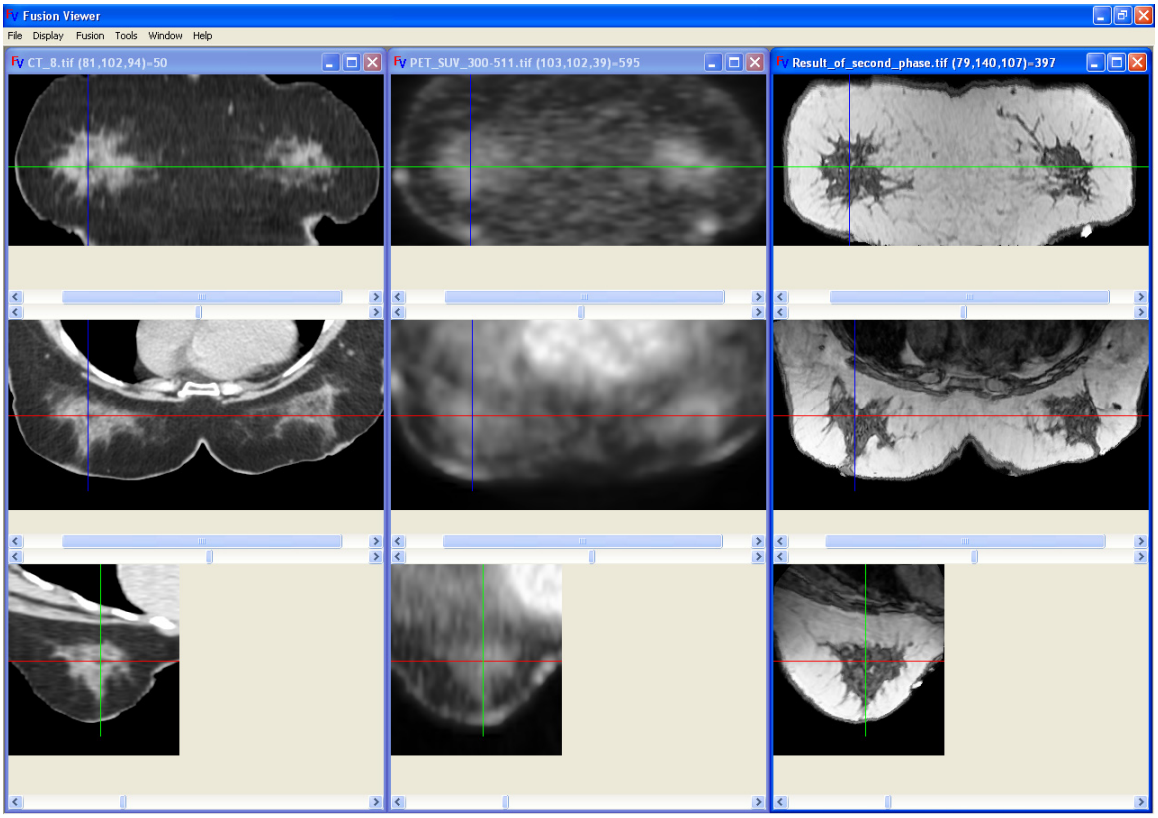

Figure 3.32 Volumes displayed as orthogonal cross-sections. The top images are coronal slices, the middle are axial slices, and the bottom are sagittal slices. From left to right a CT data set, a PET data set, and a MRI data set are shown.

The focus can be changed by either manually entering a coordinate or by clicking on one of the three orthogonal views. Clicking on a view will move the cross-hair to the point clicked, and will change the other two views so that they represent the slices at the new location of the cross-hair. The cross-hairs can be made invisible so that they are not a distraction when reading the images. Lastly, a scroll bar located under each of the views allows the location of the slice shown along the associated axis to be changed. For example, scrolling the scroll bar under the coronal view will result in the neighboring coronal slices being shown.

A three orthogonal cross section view allows a volumetric data set to be easily navigated while being presented in full detail. Every voxel can be independently examined and easily located. This is not always the case with other volumetric views such as projections or surface renderings.

Other views can be found on the 'Display' menu. A standard stack view is available, where the volumetric data is presented as a stack of images with different locations along the coronal, the sagittal, or the axial axis. Currently, the only other way to view a volume data set in the current version of Fusion Viewer is by using projections.

3.5.4 Image Adjustments for Improved Display

Most medical images, as acquired, are not ready to be examined using the previously discussed display options. A few simple steps can be taken to prepare the data for analysis. All of the options discussed here are available from the 'Display' menu of the Fusion Viewer program. The first issue that needs to be addressed is the image resolution. Typically the voxels of a medical data set are not isotropic. Most modalities produce a volume with a higher in-plane resolution than a between plane resolution. If such a volume is treated as though it had isotropic voxels it would appear as if it was being compressed along the axis orthogonal to the acquired planes. To correct this, a scale factor can be set. The scale factor along each axis indicates the amount a voxel needs to be stretched in each direction in order to make it isotropic. Setting the scale factor will allow Fusion Viewer to display the images correctly. The scale factor can also be used for zooming in and out of the image. For example to display a

volume one quarter of its size multiply the scale factor of each axis by 0.25, to display the volume twice its size multiply each of the scale factors by 2.

Another important issue that needs to be dealt with is the dynamic range of the volume. Most modalities provide 16-bit data sets. This allows 65536 unique intensities for each voxel. Even though most of the modalities do not use this full range, they do use more than the 256 supported by standard CRT or LCD displays. Finding the best options for mapping 16-bit data sets to an 8-bit display is an active area of research. Fusion Viewer provides the traditional tools to do this as well as some more advanced and novel techniques.

When a global operator is used to map the 16-bit data to 8-bits this mapping can be described by a function known as the tone transfer function (TTF). Figure 3.33 shows the TTF that was used for displaying the MRI images shown in Figure 3.32. The values on the horizontal axis correspond to the 1439 intensities found in the original MRI data set, and the values on the vertical axis correspond to the 256 intensities that can be shown on the display. To map a voxel's intensity from the MRI volume to its displayed intensity, move vertically on the TTF plot from the appropriate value. After intersecting the TTF, move horizontally until the vertical axis has been crossed. The point at which the vertical axis is crossed represents the intensity that the voxel will be assigned for display.

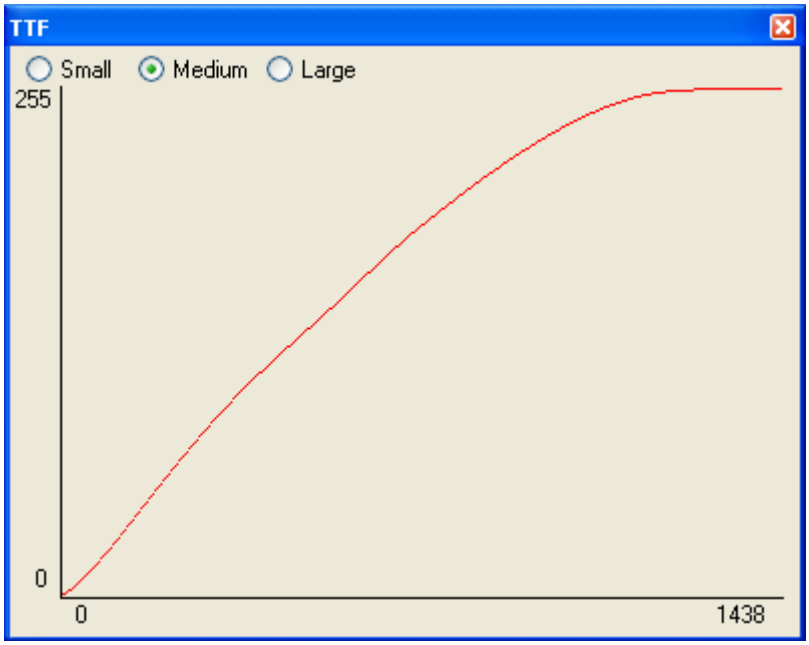

Figure 3.33 The tone transfer function used to map the original 1439 intensities in the MRI data set shown in Figure 1 to the 256 intensities that can be shown by a standard CRT or LCD monitor.

The traditional linear mapping of 16-bit data sets to 8-bits used in medical applications is supported. The range of the intensities in the original data set to be mapped linearly to the display can be either selected by setting a minimum and maximum or a window and level. More advanced histogram based techniques[118] are supported as well as two novel spline based techniques. The histogram techniques are good for maximizing the contrast shown in the displayed images, or displaying images where an appropriate window and level are not known. The spline based techniques are designed to be an alternative to the traditional linear windowing. The advantage of the spline based windowing techniques over traditional windowing techniques is their ability to retain a relatively high contrast in the intensity range of interest, while not totally discarding the intensity information that does not fall in this range. Using this

technique, what may be important, contextual information is not totally lost. This technique is discussed in detail in Section 3.5.5. The plug-in interface for Fusion Viewer allows alternative dynamic range techniques, such as the spline based techniques, to be easily implemented.

A few other options for fine tuning the display exist. These include the ability to linearly scale the brightness of the image and the option to set voxels whose intensities exceed the maximum value being displayed to black instead of the usual white. This setting may make reading the images easier on the eye, and takes the natural emphasis off of these voxels that are outside of the range of intensities that are of interest.

The option to present a grayscale image in color is present. Through the use of color tables, also known as look up tables or color tables, the 256 display intensities can be assigned colors. For compatibility Fusion Viewer adopted the color table definition used by the popular ImageJ[136] software package. Twenty-two such color tables are included, but any other one can also be loaded and applied to a grayscale image. The PET data set in Figure 3.34 is an example of the Fire color table applied to a grayscale image.

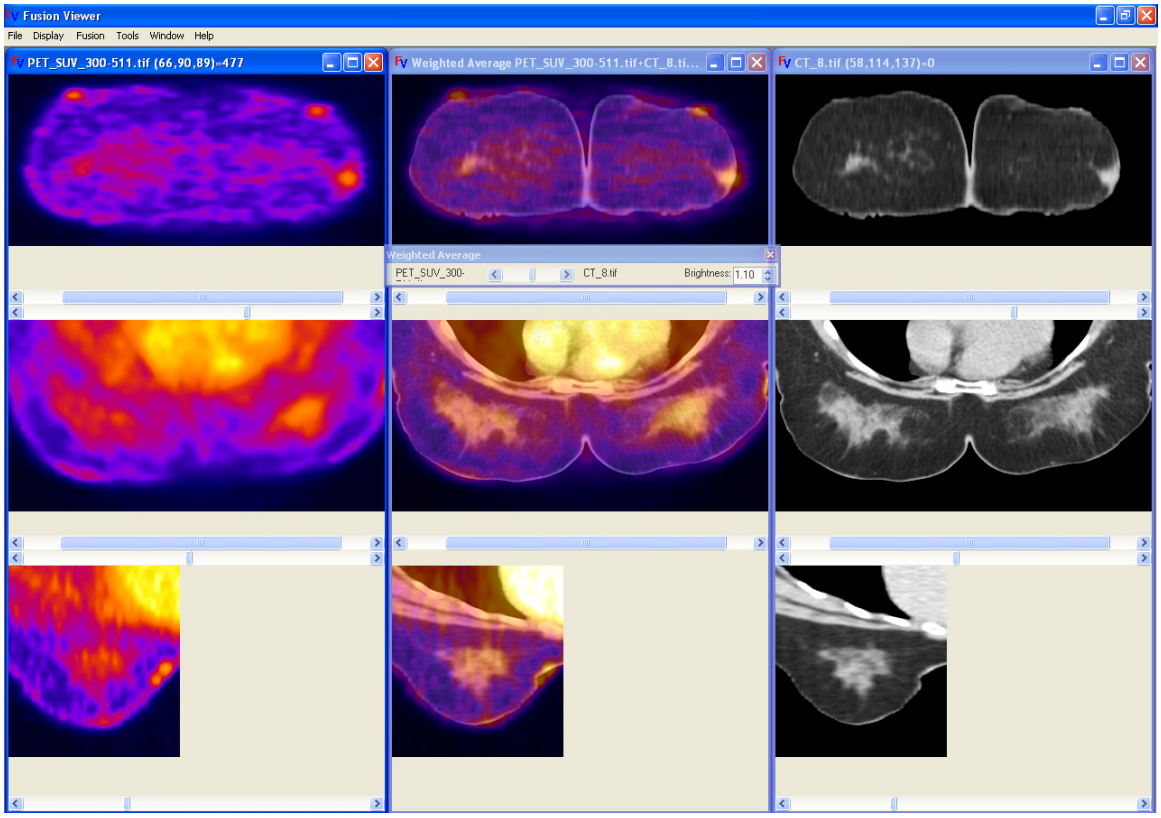

Figure 3.34 A screenshot of a fused data set created using the Fusion Viewer software. The three orthogonal images on the left are from the PET data set after the application of the Fire color table, the three orthogonal images on the right are from the CT data set. The three orthogonal images in the center are from fusing the PET and CT images using the weighted average fusion plug-in. In essence the coloring of the CT image is based on the PET intensity values. Not only can we see the anatomical structure, but we can also see the metabolic activity for each structure.

3.5.5 Spline Based Dynamic Range Techniques

Linear window dynamic range techniques remain the most popular, even after significant research into more advanced techniques (e.g., adaptive histogram equalization[161,162]), due to their simplicity and easy application to any data set.[163] The most significant drawback of the linear approach is the complete loss of intensity information outside of the defined window. For example, see the TTF shown in Figure 3.35. The intensities that fall outside the lower bound of the

window are completely discarded, while the intensities that fall outside of the upper bound are saturated.

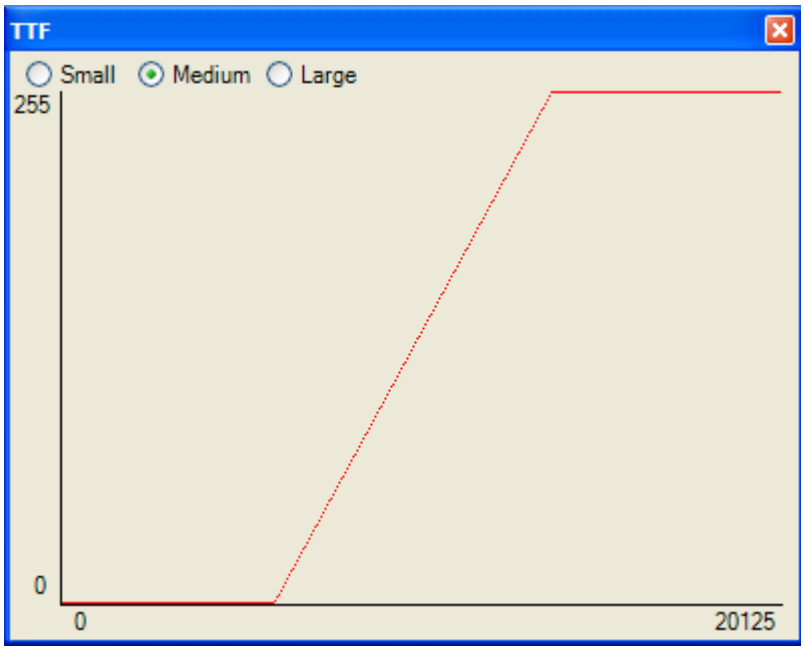

Figure 3.35 Example of a linear window tone transfer function.

While this windowing can result in an appropriate level of contrast within the intensity range of interest, supporting contextual information is often lost. Discussion with the radiologists at SUNY Upstate Medical University suggested that a method to compress rather than completely remove the intensities outside of the window of interest may in some cases significantly aid in image interpretation.

A function often relied upon to accomplish this task is the sigmoid curve shown as Equation 3.7. Other related curves such as the cumulative normal function, shown as Equation 3.8 and in Figure 3.36, where μ is the mean and σ is the standard deviation, provide slightly more robust alternatives. While these curves have been shown to work well with pictorial images, are simple to use

with optimum parameters that can be automatically calculated,[164] they lack the precision and robustness necessary for medical imagery. To address this need, spline based techniques that provide the necessary control using a similar interface as the linear windows were developed.

$$f(i) = \frac{1}{1+e^{-i}} \tag{3.7}$$

$$f(i) = \frac{1}{\sigma\sqrt{2\pi}} \int_{-\infty}^{i} e^{-\frac{(t-\mu)^2}{2\sigma^2}} dt \tag{3.8}$$

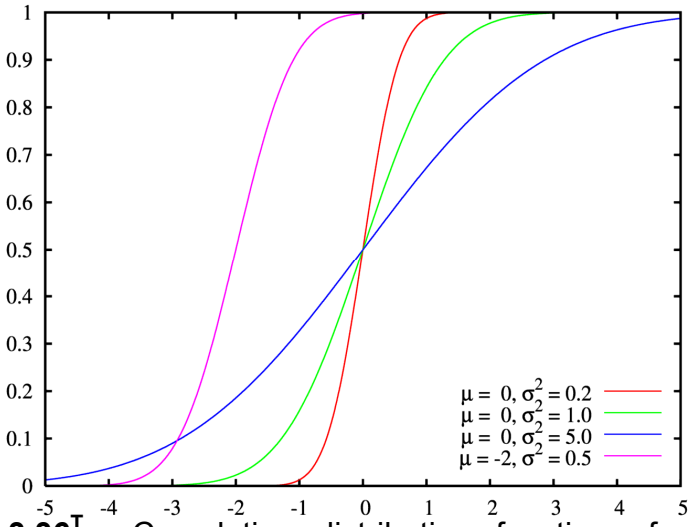

Figure 3.36[T] Cumulative distribution functions for normal distributions with varying means and variances.

Splines are piecewise polynomials of degree n that have the advantage of being simple functions with a very flexible global behavior. They are used as interpolators preserving the monotonicity and convexity of the data. These polynomials are joined together at the break points with n-1 continuous derivatives. These properties render themselves very useful for generating a piecewise Tone Transfer Function.

[T] Figure from [165], used with permission under the GFDL (GNU Free Documentation License).

The TTF is divided into four regions as shown in Figure 3.37, with breakpoints set at $(I_{\min}, O_{\min})$, $(W_{\min}, D_{\min})$, $(W_{\mathrm{mid}}, D_{\mathrm{mid}})$, $(W_{\max}, D_{\max})$ and $(I_{\max}, O_{\max})$. The horizontal axis shows the 1624 different intensities in the input MRI data set and how these are mapped into 256 gray level values for a common 8-bit display.

The minimum and maximum gray level values that are to be retained from the input image, $I_{\min}$ and $I_{\max}$, are found and these are mapped to the output minimum and maximum intensity values, $O_{\min}$ and $O_{\max}$, respectively.

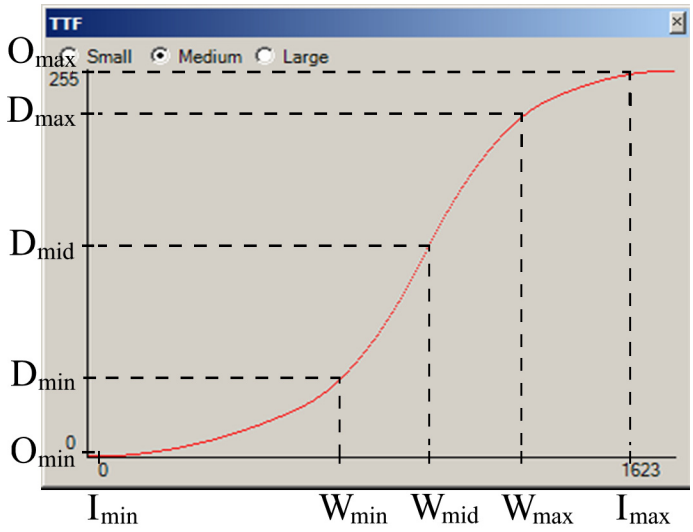

Figure 3.37 Example spline based TTF.

$W_{\min}$, W_{mid} and $W_{\max}$ are determined by the user using standard window/level adjustment controls. W_{mid} is the level and $W_{\min}$ and $W_{\max}$ are the upper and lower range of the window respectively. W_{mid} is halfway between $W_{\min}$ and $W_{\max}$ and serves as a point of inflection. The goal is to maximize the contrast of intensities that reside in the window while not completely removing the other intensities.

The parameters that define this window are selected using a slider tool that allows real-time visualization of both the image and the TTF.

The output window size is specified by the observer and is related to the points on the vertical axis according to Equation 3.9.

$$W_{\text{size}} = \frac{D_{\max} - D_{\min}}{O_{\max} - O_{\min}} \tag{3.9}$$

The value of W_{size} ranges from 0 to 1. The location of D_{mid} is determined from the location of W_{mid} using Equation 3.10.

$$D_{\text{mid}} = (O_{\max} - O_{\min}) * \left(\frac{W_{\text{mid}} - I_{\min}}{I_{\max} - I_{\min}} \right) + O_{\min} \tag{3.10}$$

$D_{\max}$ and $D_{\min}$ are determined from D_{mid} and W_{size} utilizing Equation 3.11 and Equation 3.12.

$$D_{\max} = D_{\text{mid}} + \frac{W_{\text{size}}}{2} * (O_{\max} - O_{\min}) \tag{3.11}$$

$$D_{\min} = D_{\text{mid}} - \frac{W_{\text{size}}}{2} * (O_{\max} - O_{\min}) \tag{3.12}$$

Due to saturation the slope of the TTF to the left of $I_{\min}$ and the right of $I_{\max}$ is assumed to be zero and these values are used along with the breakpoint locations to start the interpolation process.

Values within the window specified by the user are mapped to a percentage, W_{size}, of the display's intensity range and the values outside of the window are compressed significantly to the remaining portions of the display's intensity range. For example, intensities of interest from 600 to 1000 are mapped to 80% of the display's intensity range, and the remaining intensities are compressed significantly more and mapped onto the remaining 20% of the display's intensity

range. Figure 3.38 shows an MRI image created by using a linear window. The window and level settings were selected to maximize the detail in the glandular tissue region. The same image windowed using the quadratic spline tone transfer function, with identical window and level settings, is shown as Figure 3.39. While a similar level of detail is available within the glandular tissue, more details are made visible within the surrounding fatty tissue when using the quadratic spline tone transfer function. Figure 3.40 and Figure 3.41 provide another example.

Figure 3.38 Axial MRI image through middle of breast with contrast adjusted using a linear window to maximize detail of the glandular tissue.

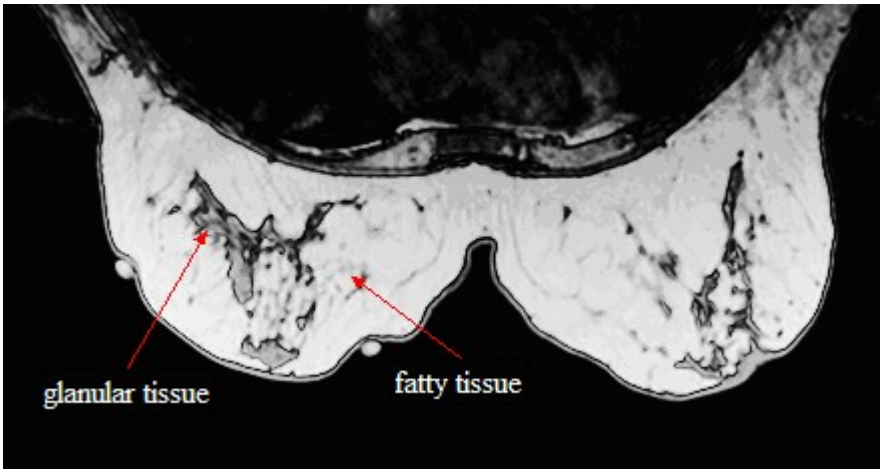

Figure 3.39 Same image as Figure 3.38 only with contrast adjusted using a quadratic spline tone transfer function.

Figure 3.40 Axial MRI image through middle of breast with contrast adjusted using a linear window to maximize detail of the glandular tissue.

Figure 3.41 Same image as Figure 3.40 only with contrast adjusted using a quadratic spline tone transfer function.

The advantage of the spline based windowing techniques over traditional windowing techniques is their ability to retain a relatively high contrast in the intensity range of interest, while not totally discarding the intensity information that does not fall in this range. The familiar window/level user interaction makes adoption of the spline based dynamic range techniques much simpler than other dynamic range options. Two spline options have been implemented: quadratic splines, and quadratic-cubic splines. The first of these options is self

explanatory. When choosing the second option, the interpolators between $(I_{\min}, O_{\min})$ and $(W_{\min}, D_{\min})$, and $(W_{\max}, D_{\max})$ and $(I_{\max}, O_{\max})$ are quadratic splines and the interpolators between $(W_{\min}, D_{\min})$ and $(W_{\text{mid}}, D_{\text{mid}})$, and $(W_{\text{mid}}, D_{\text{mid}})$ and $(W_{\max}, D_{\max})$ are cubic splines.

3.5.6 Viewing Multiple Data Sets

While Fusion Viewer provides a nice tool for examining stand alone medical images, the real strength of the application lies in its ability to simultaneously examine multiple registered data sets. The simplest example of this is when multiple images are open such as in Figure 3.32. Unless otherwise specified by the user, Fusion Viewer will keep the view of all of the opened volumes synchronized. In other words, changing the point of focus for the PET volume will also change the point of focus for the MRI and CT volumes. Similarly, if projections are shown for multiple volumes, changing the angle of projection for one volume will change the angle of the projection shown for all of the other volumes. This allows a registered view of multiple data sets to be maintained as they are examined side by side.

In addition to allowing multiple volumes to be viewed side by side, they can also be combined (fused) and viewed as a single volume. The currently supported fusion techniques are listed under the 'Fusion' menu, but as will be shown later, new fusion techniques can be easily implemented using Fusion Viewer's plug-in interface. Upon selecting a fusion technique from the 'Fusion' menu, a dialog is displayed. This simple dialog is used to select the volumes to fuse and the role they will play in the fused image. For example, when selecting

the hue, saturation, lightness plug-in, this dialog box allows you to choose which volume should be used for the hue value, which should be used for the saturation value, and which should be used for the lightness value.

Figure 3.34 provides an example of fusing a CT image with an FDG-PET image. Here the weighted average fusion plug-in was used. When using this plug-in the colors of the CT image are averaged with the colors from the PET image using a weighting based on the position of the scroll bar in the window titled 'Weighted Average'. By moving this scrollbar all of the way to the right we see the original CT image, all the way to the left we see the original PET image. Anywhere in between we see a weighted average of the two.

Figure 3.42 shows a subset of the fusion capabilities provided by the current plug-ins. For more information on fusion techniques see Section 3.3. In addition to fusing images from multiple modalities, combined images from dynamic (time) series data sets can also be presented. For example, the plug-in interface could be used to present a volume representing the peak SUV for each voxel.

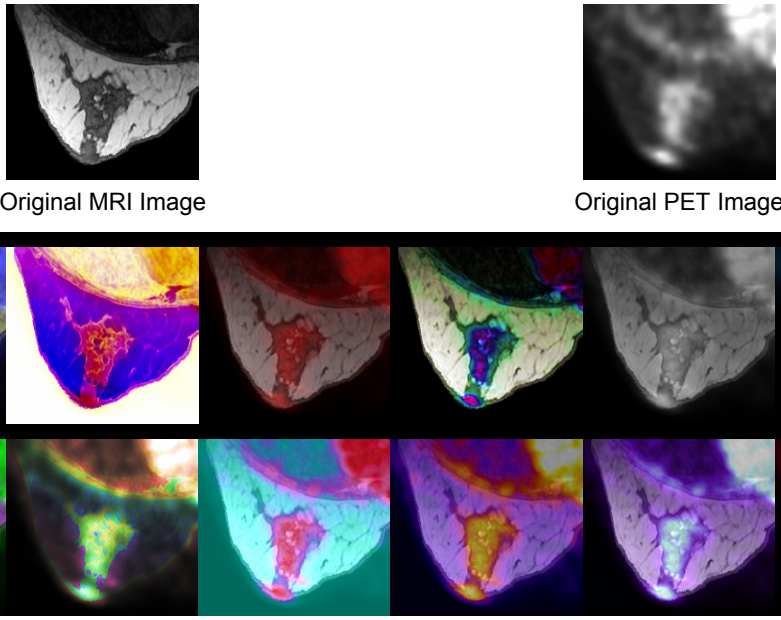

Figure 3.42 An assortment of fused images created by fusing the original MRI and PET image shown at the top of the figure. All images were created using fusion plug-ins supplied with Fusion Viewer.

3.5.7 Implementing a New Fusion Plug-in

In this section the required code for a plug-in will be covered. The discussion will pertain to the code shown in Figure 3.43. This code was written in C#, for a good introduction to C# see [166]. As mentioned before, a programmer should be able to write their plug-in in the language of their choice supported by the .NET framework. The sample plug-in discussed here takes two input image volumes and creates a fused color image by assigning one input image to the monitor's red channel, and the other to the monitor's blue channel. Each plug-in will be contained within its own class. References need to exist to System.dll, System.Windows.Forms.dll that are included with the .NET framework, and to FusionViewerResources.dll that is provided as part of the Fusion Viewer software package. When discussing the code, the current line of interest will be identified by its line number. The line numbers are shown in red in Figure 3.43.

```
1.  namespace MyPlugin
2.  {
3.      public class MyPlugin :
            FusionViewer.OrthogonalViewFormFused,FusionViewer.IPlugin
4.      {
5.          public int NumberOfSources
6.          {
7.              get { return 2; }
8.          }

9.          public string SourceSelectionMessage
10.         {
11.             get { return "Select 2 source volumes with the same dimension."
                    + "  The first source selected will be used for the"
                    + " red channel, the second for the blue."; }
12.         }

13.         public System.Type SourceType
14.         {
15.             get { return typeof(FusionViewer.OrthogonalViewFormGreyscale);}
16.         }

17.         public override byte[] RawSliceData(
                FusionViewer.SliceDirection sliceDirection,
                FusionViewer.Point3D focus)
18.         {
19.             byte[] source1 = sources[0].RawSliceData(sliceDirection,focus);
20.             byte[] source2 = sources[1].RawSliceData(sliceDirection,focus);
21.             byte[] buffer = new byte[4 * source1.Length];
22.             for (int i = 0; i < source1.Length; i++)
23.             {
24.                 buffer[4 * i] = source2[i];
25.                 buffer[4 * i + 1] = 0;
26.                 buffer[4 * i + 2] = source1[i];
27.             }
28.             return buffer;
29.         }

30.         protected override void Initialize()
31.         {
32.             this.Title = "My Plugin " + " Red: " + sources[0].Title
                    + " Blue: " + sources[1].Title;
33.             this.Text = this.Title;
34.         }
35.     }
36. }
```

Figure 3.43 The code for a basic fusion plug-in.

The code begins with the standard namespace and class definition on line 1 and 3 respectively. The class is required to inherit from FusionViewer.OrthogonalViewFormFused, and implement the FusionViewer.IPlugin interface. The class needs to have several properties that tell the Fusion Viewer application and the user what the required input images to the plug-in should be. The first property, NumberOfSources, gives the number of

images the plug-in fuses. The property can be found on line 5. It usually returns a value of two or three, but plug-ins can work with a much larger number of input images as well. For example, a plug-in that takes a dynamic PET series and returns a volume representing the peak SUV for each voxel might require a much higher number of input images. The number of input images is only limited by the system memory. The example plug-in requires two input images.

The second required property, located on line 9, returns an instructional message to plug-in users. This property must be called SourceSelectionMessage and in our case returns a string telling the user that the first image they select will be used for the red channel and the second for the blue channel.

The last property is SourceType located on line 13. This property is used to identify the types of images that the plug-in works with. In this case we specify FusionViewer.OrthogonalViewFormGreyscale, which means our plug-in can use any grayscale image as its input. These images can either be a volume loaded into the program or a projection volume created by the program. Additional options for the source image types include color images created by other plug-ins or user defined image types.

One of the two functions, RawSliceData on line 17, is where the plug-in does its work. This function always receives as input the orientation of the slice currently being viewed, and the focus point. When working with projection volumes the orientation of the slice will be a constant. The plug-in programmer

usually does not need to worry about what these parameters represent, since in most cases they will just be passed on.

In this function as well as throughout the rest of the class the plug-in will have access to an array of source images. These are the images that were provided by the user to the plug-in. In lines 19, and 20 we reference the sources images in order to obtain the portions of the images that are currently being viewed by the user. The RawSliceData function of each source image provides this data when you pass it the slice orientation and the focus. By simply passing the sliceDirection and focus arguments to the RawSliceData function for each source, the plug-in will have access to the data that it needs for generating the fused data for display. By only processing the data currently being displayed most plug-ins can perform image fusion in real-time.

On line 21 we define an array of bytes called buffer that will be used to store the fused image data. The RawSliceData function of the plug-in will return buffer and not have to worry about preparing the data for display or actually displaying it.

In lines 22 through 27 we enter a FOR loop. In the FOR loop a color is assigned to each voxel of the fused image that is currently visible to the user. Four bytes are used to represent each color voxel, the first represents the blue value, and the second and third represent the green and red respectively. The fourth byte is reserved for the alpha channel and in general should be left filled with zero. For the example plug-in we assign the voxel intensity of the first

source to the red channel, the voxel intensity of the second source to the blue channel, and set the green channel to zero.

The final function of the class is not required, but can be used to place appropriate text in the title bar of windows that are using the plug-in. This function is named Initialize and can be found on line 30.

After a successful build, the plug-in assembly (DLL) must be placed in the 'plugins' folder found in the Fusion Viewer application directory. After restarting the Fusion Viewer application the new plug-in will show up as an option under the 'Fusion' menu. The option will share the same name as the assembly containing the plug-in.

A screenshot taken after running Fusion Viewer and providing the sample plug-in a MRI and PET image can be seen in Figure 3.44.

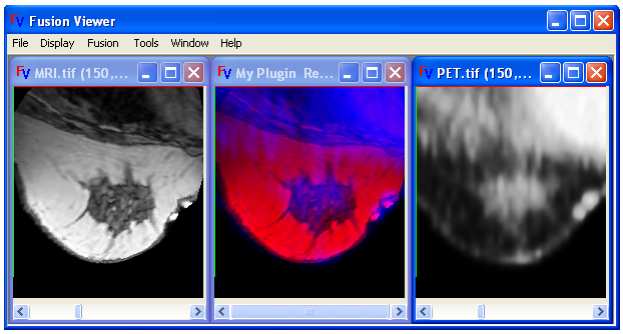

Figure 3.44 Screenshot taken of the plug-in defined by the code in Figure 3.43. The setting to only show the sagittal view was selected from the 'Display' menu.

3.5.8 Projection Displays

When using projections a new volume is created which consists of projections of the current volume acquired from different directions. These projections are created using standard ray tracing techniques.[117] Successively showing different projections give the appearance of a rotating three-dimensional

volume. Projection techniques can be used to create what looks like a three-dimensional image on a two dimensional display.

The interface for setting the projection options is shown in Figure 3.45. The first option is the axis with which to have the projections revolve around. A series of projections will be taken at different angles around this axis. Unlike most projection programs, Fusion Viewer can create the projections along any arbitrary axis. The second option is the size of the projected volume. Typically this is set to a size greater than the extent of the volume when rotated around the selected axis.

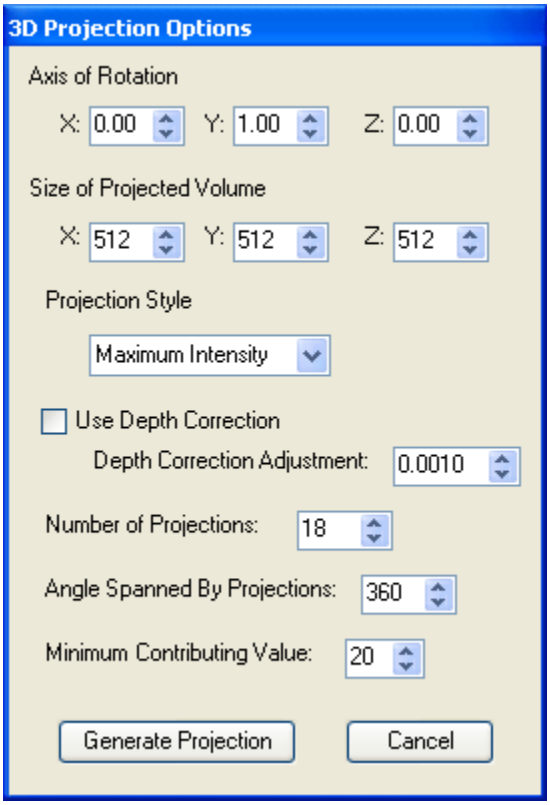

Figure 3.45 Dialog that allows the user to change the volume projection options.

The projection style allows the property that we are projecting to be selected. Currently either the maximum intensity or the mean intensity can be projected.

The maximum intensity projection (MIP) is the most widely used volume visualization technique in medical imaging.[167] The method finds the maximum value of the signal in the way of parallel rays traced from the view plane to the plane of projection. It provides a very good understanding of the structures defined by high signal intensities. Figure 3.46 shows an example image created in this manner. The mean intensity projection is an alternative for denser imaging modalities, such as MRI, that may give poor results when using a maximum intensity projection. The algorithms were implemented in such a way that very little new code needs to be written in order to implement other projection styles.

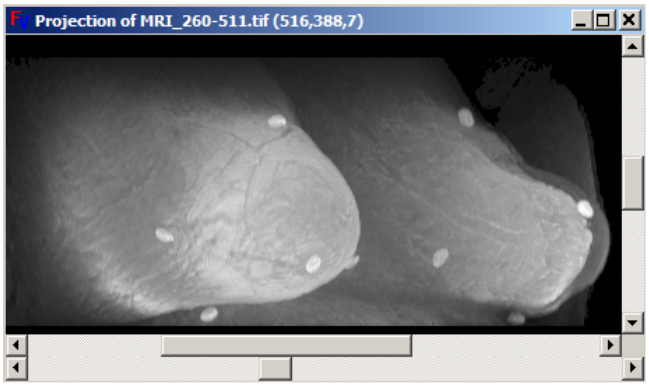

Figure 3.46 MIP formed from MRI. Projection performed at an angle of 40 degrees (rays traced from right, anterior). Bright spots correspond to fiducial markers placed on patient's skin for image registration.

Advanced features such as depth adjustment and noise suppression are supported. The depth correction option can be used to increase the three-dimensional feel of the projections. When using depth correction voxels closer to the source of the traced rays are given more weight than voxels further from the ray source. In other words, the voxels at the front of the volume when viewed at the current angle are weighted more than the voxels at the back of the volume.

The difference in weight is determined by the depth correction adjustment option. The minimum contributing value can be used to ignore voxels with low signal. This can often be used to prevent noise in the background from contributing to the projections. Other options include the number of projections to take, and the total angle to be covered by the projections.

Color projections have also been implemented for creating fused projection volumes. An example using PET/MRI data is shown in Figure 3.47. Fusion was created by performing a weighted average of the two volumes and selecting a gray scale look-up-table for the MRI set and a red look-up-table for the PET set. In this case the intensity was used to determine the projection, but other properties, for example, the redness, could be used. Projection of other properties is supported using the plug-in interface. Options exist for both fusing projection volumes and creating projections of fused volumes.

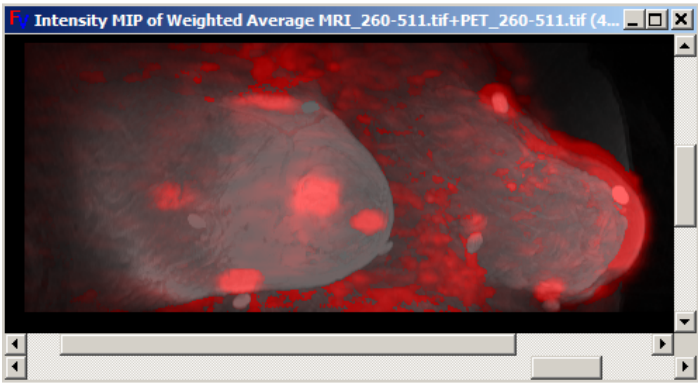

Figure 3.47 Color MIP from fused PET/MRI. Projection performed at an angle of 40 degrees (rays traced from right, anterior). Areas of higher activity (red) are visible along the breast surface. These correspond to the nipple region and the fiducial markers used during PET imaging.

3.5.9 Summary

Fusion Viewer, a new application for visualizing and examining three-dimensional medical data sets, was designed and implemented. The most significant advantage of Fusion Viewer over previous applications is its capability to examine multiple data sets simultaneously. Not only does Fusion Viewer keep multiple data sets synchronized, but it also provides tools for displaying them as a single color data set. Several fusion options are already provided as plug-ins, and a simple interface exists for experimenting with new fusion schemes.

In addition to these capabilities Fusion Viewer provides interfaces to evaluate various projection techniques, such as the popular maximum intensity projection (MIP). Specifically of interest are its capabilities to fuse projected data sets, and create projections of fused data sets. Fusion Viewer has capabilities for dealing with the dynamic range of medical images. Specifically, novel spline based techniques are available, and an interface exists for experimenting with new dynamic range techniques.

Fusion Viewer was implemented on the .NET framework for easy distribution, installation, and compatibility with current and future platforms. The interfaces and plug-in design allows expansion through new fusion techniques, projection techniques, and dynamic range techniques with a minimal amount of effort and very little new code. Its design for only processing the data currently being presented to the user makes it an ideal tool for real-time fusion and evaluation of large data sets.

Fusion Viewer serves as a software framework for visualization of multimodal data sets. It provides an environment that can be used to implement and evaluate new fusion operators.

3.6 Visualization Study

A study was conducted during which radiologists were asked to evaluate images created using different fusion-for-visualization techniques. The aim was to determine which fusion techniques are most useful for enhanced diagnostic performance. Specifically, the radiologist's preference, ease of use, understanding, efficiency, and accuracy when reading the images were evaluated. This section discusses the study, the techniques selected for evaluation, and the results.

3.6.1 Study Objectives

The study was designed to answer the following questions:

1. Are the spatial relationships between images better conveyed when viewed side-by-side or as a fused image?
2. Which fusion techniques do the radiologists prefer?
3. Which fusion techniques do the radiologists think they can use the best?
4. Which fusion techniques are easiest for the radiologists to use?
5. Which fusion techniques most accurately allow the original MRI and PET information to be recovered by the radiologist?

3.6.2 Participants

Four radiologists from SUNY Upstate Medical University and University Hospital, located in Syracuse, NY, participated in the study. The radiologists had normal or corrected to normal vision. The qualifications of each participant are listed below. Please note that there is no correspondence between the order listed here and the observer numbers used to identify the study results corresponding to each observer.

Michele Lisi
Certification/Degrees: MD, ABR certified in diagnostic radiology and nuclear radiology
Clinical Experience: 4 years (in Nuclear Medicine)
Position Title: Assistant Professor of Radiology

Daniel Tam
Certification/Degrees: MD
Clinical Experience: 1 year (in Nuclear Medicine)
Position Title: Fellow in Nuclear Medicine

Mary McGrath
Certification/Degrees: MD, ABNM certified
Clinical Experience: 8 years (in Nuclear Medicine)
Position Title: Assistant Professor of Radiology

Mehr Khan
Certification/Degrees: MD
Clinical Experience: 1 year (in Nuclear Medicine)
Position Title: Clinical Assistant Professor of Medicine

3.6.3 Walkthrough of Study

The study consisted of the following tasks:

1. On a PET monochrome image click on the region of maximum metabolic activity (glandular tissue).
2. On a gray scale LUT select the gray level, on the PET image, that corresponds to the gray level value of the region of maximum activity.

3. On an MRI image click on the morphological region that corresponds to the gray level value of the region of maximum metabolic activity (the same location clicked on the PET image).

4. On a gray scale LUT select the gray level, on the MRI image, that corresponds to the gray level value of the region of maximum activity.

5. Trace the region of maximum metabolic activity on both the PET and MRI images.

6. On a fused image click on the region of maximum metabolic activity.

7. Click on the corresponding color on the LUT to identify the associated PET and MRI values.

8. Trace the region of maximum metabolic activity on the fused image.

9. Evaluate degree of difficulty while performing the task.

10. Evaluate understanding of the fusion technique used.

11. Indicate preference for the fusion technique.

These tasks, and the interfaces used while performing them, are now discussed in more detail. The instructions provided to the study administrator and the observers are provided as Appendix F.

The observer was presented with a series of screens. On each screen they were instructed to read and follow the directions. After entering in their name and selecting a file to write the study results to, the observers were presented with the screen shown in Figure 3.48. The observer was instructed to click on

the most metabolically active region on the PET image. Upon doing so, the point that the observer clicked on was recorded. The time it took for the observer to click on the active region was also recorded. The observers were unaware that they were being timed. Upon completion of this task the observer clicked on the next button to move to the next step.

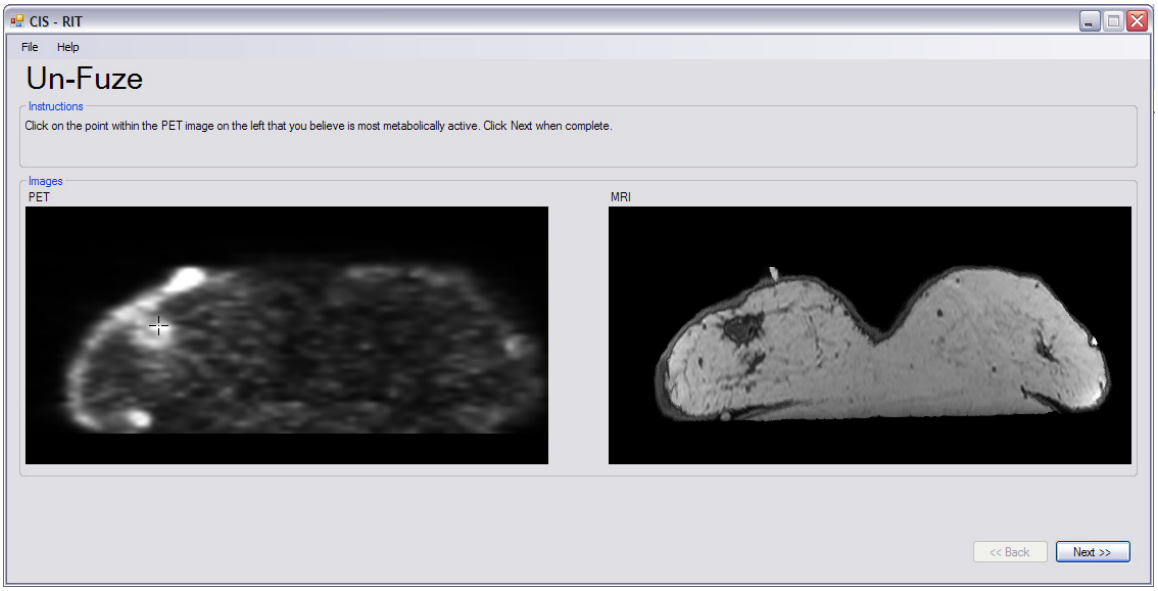

Figure 3.48 Screenshot from study. Observer was asked to click on the point of highest metabolic activity on the PET image.

The next step was for the observer to select a color on the color table corresponding to the color at the point selected previously on the PET image. This was performed using the screen shown as Figure 3.49. The intensity at the point that the observer clicked on was recorded and could be compared with the intensity the observer had previously selected on the PET image.

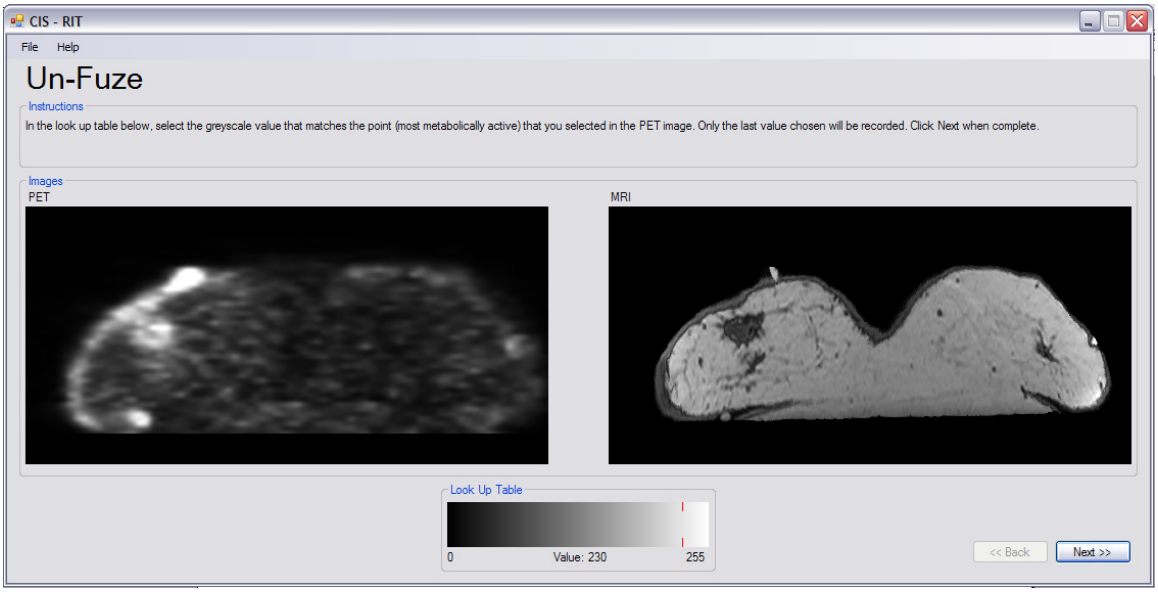

Figure 3.49 Screenshot from study. Observer was asked to click the color on the color table corresponding to the location they previously selected on the PET image.

The observer was then asked to trace around the outline of the metabolically active region in the PET. The trace was recorded as a set of points. An example trace can be seen in Figure 3.50.

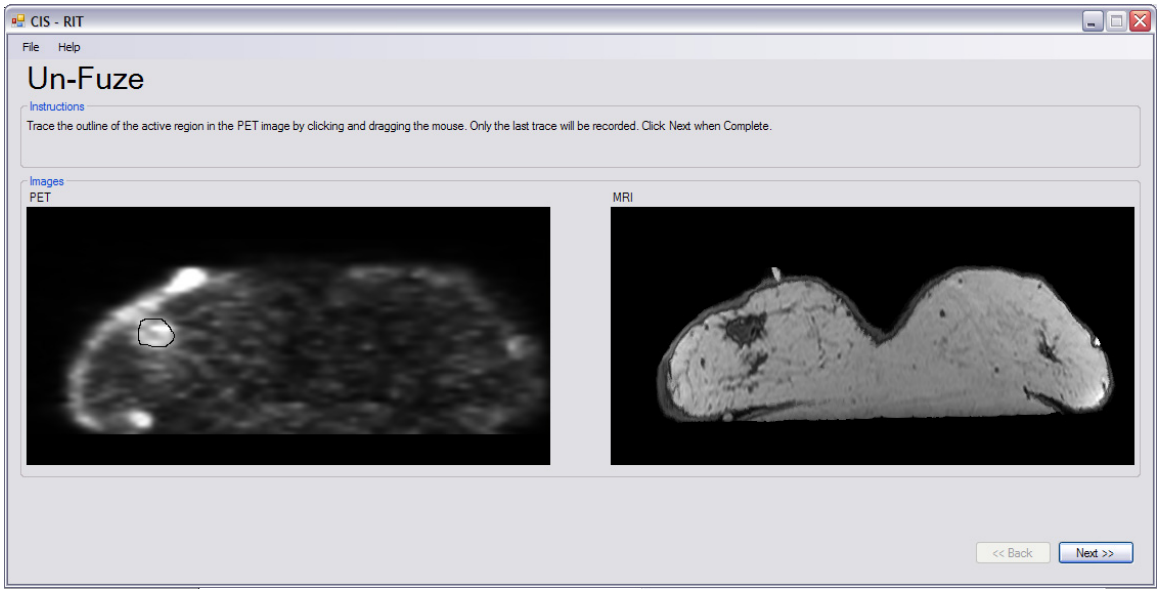

Figure 3.50 Screenshot from study. Observer was asked to trace (using the mouse) the region of highest metabolic activity on the PET image.

The observer was then asked to repeat these steps on the MRI image. The observer was instructed to click on the most metabolically active region in the MRI. Upon doing so, the point that the observer clicked on was recorded, along with the time it took for the observers to click on the active region. The observer identified the intensity at the location they had previously clicked by selecting the intensity from a grayscale color table, and then traced the outline of the active region on the MRI image. This procedure was repeated for each of the MRI/PET image pairs used in the study.

After several days had passed the observer was then asked to perform similar tasks using fused images. Again the observer was asked to read and

follow the instructions presented at the top of each screen. They began by entering their name, selecting an output file, and selecting a fusion technique. They were then presented with a screen (Figure 3.51) which provided a little background on the fusion technique.

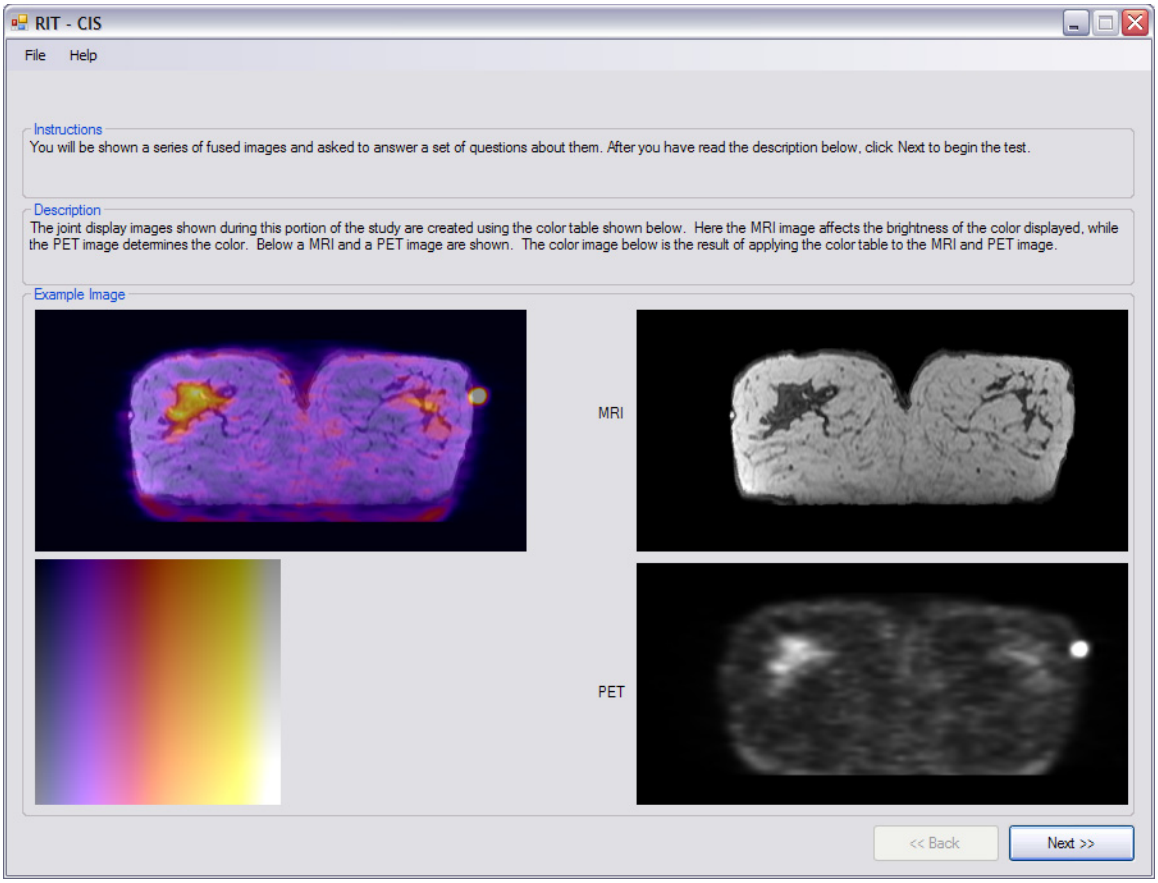

Figure 3.51 Screenshot from study. The observer is being presented with an introduction to the fusion technique they will be using for the remainder of the session.

On the next screen, the observer was instructed to click on the most metabolically active region. This was done on the screen shown in Figure 3.52. The location clicked by the observer and the time it took for the observer to click on the location were recorded.

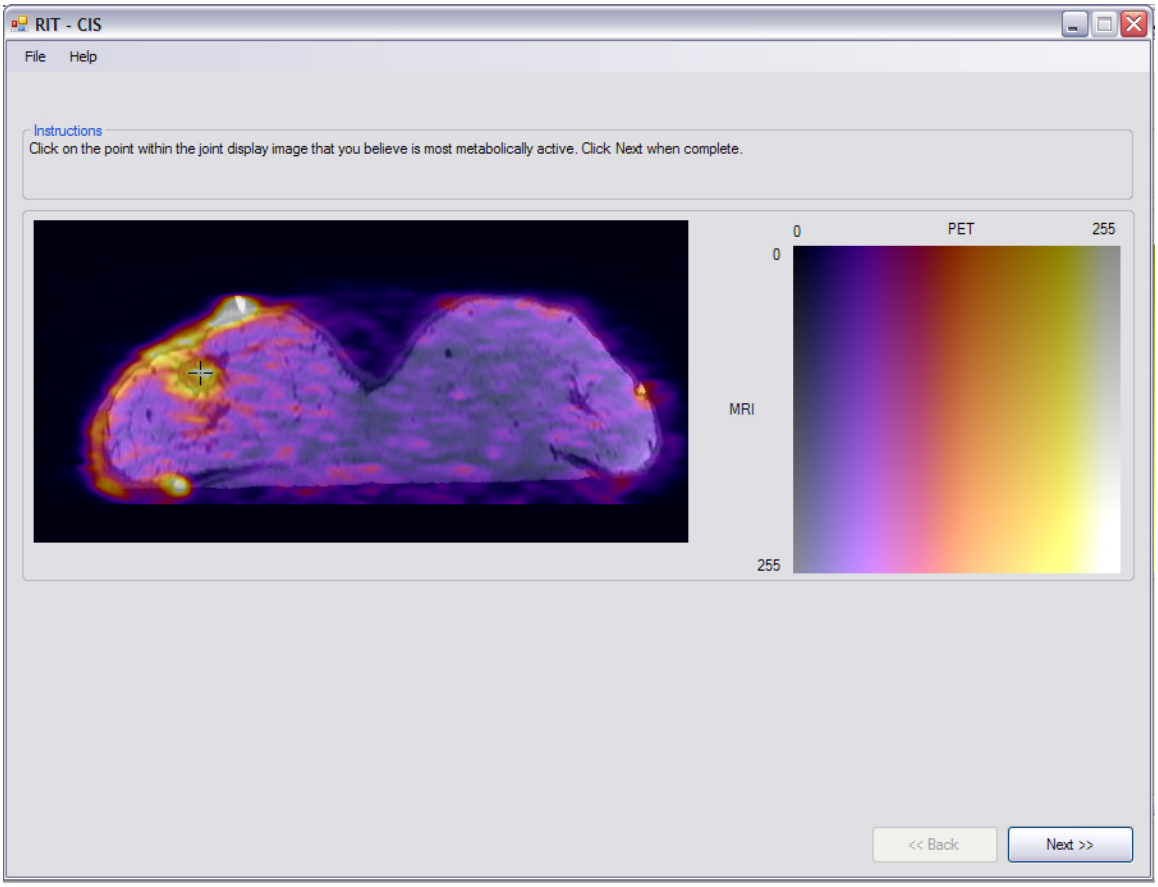

Figure 3.52 Screenshot from study. The observer is asked to click on the most metabolically active location in the image.

The observer was then asked to identify the color for the location they previously selected from the color table used to perform the fusion. This was done using the screen shown in Figure 3.53. The location that the observer clicked on the color table was stored. Both the Euclidean and color difference between the color selected and the actual color could be calculated.

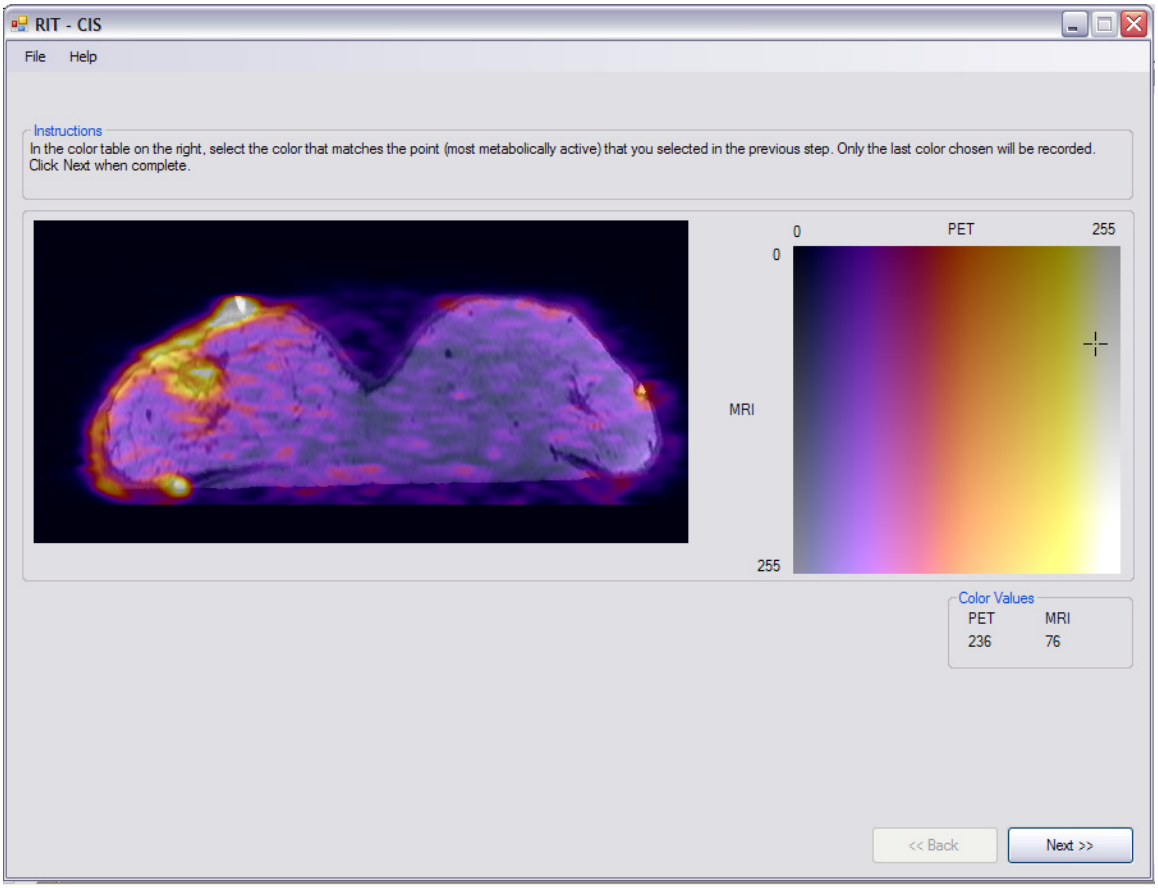

Figure 3.53 Screenshot from study. The observer is asked to click the color on the color table corresponding to the location they previously selected on the fused image.

The observer was then instructed to trace an outline of the metabolically active region in the image. They were instructed to consider both the PET and MRI information while dragging the mouse to trace the region. The trace was stored as a set of points. An example trace can be seen in Figure 3.54.

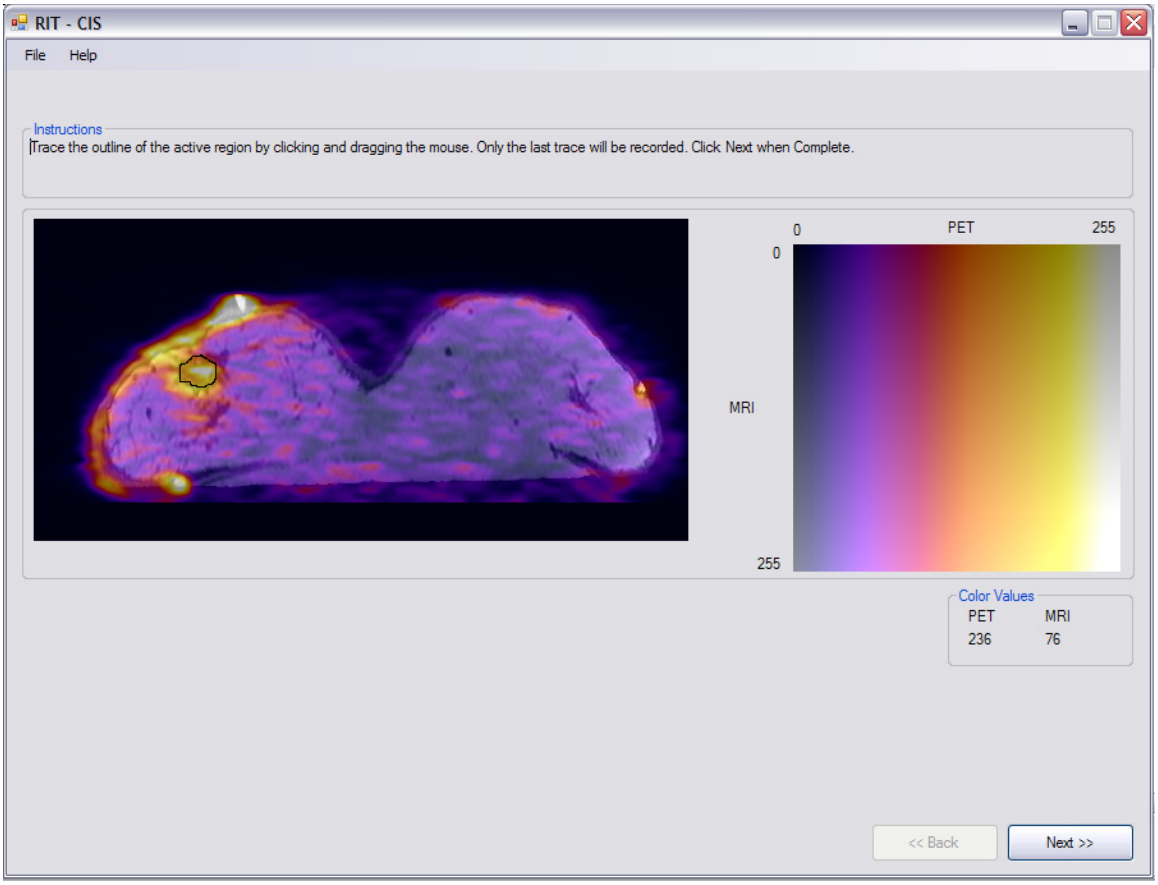

Figure 3.54 Screenshot from study. The observer is asked to trace the region of highest metabolic activity in the fused image.

Each time the observers completed this series of tasks using a fusion technique, they were asked to rate how difficult it was for them. This was done using radio buttons as shown in Figure 3.55. A rating of three was used as a starting point. The assigned ratings were recorded.

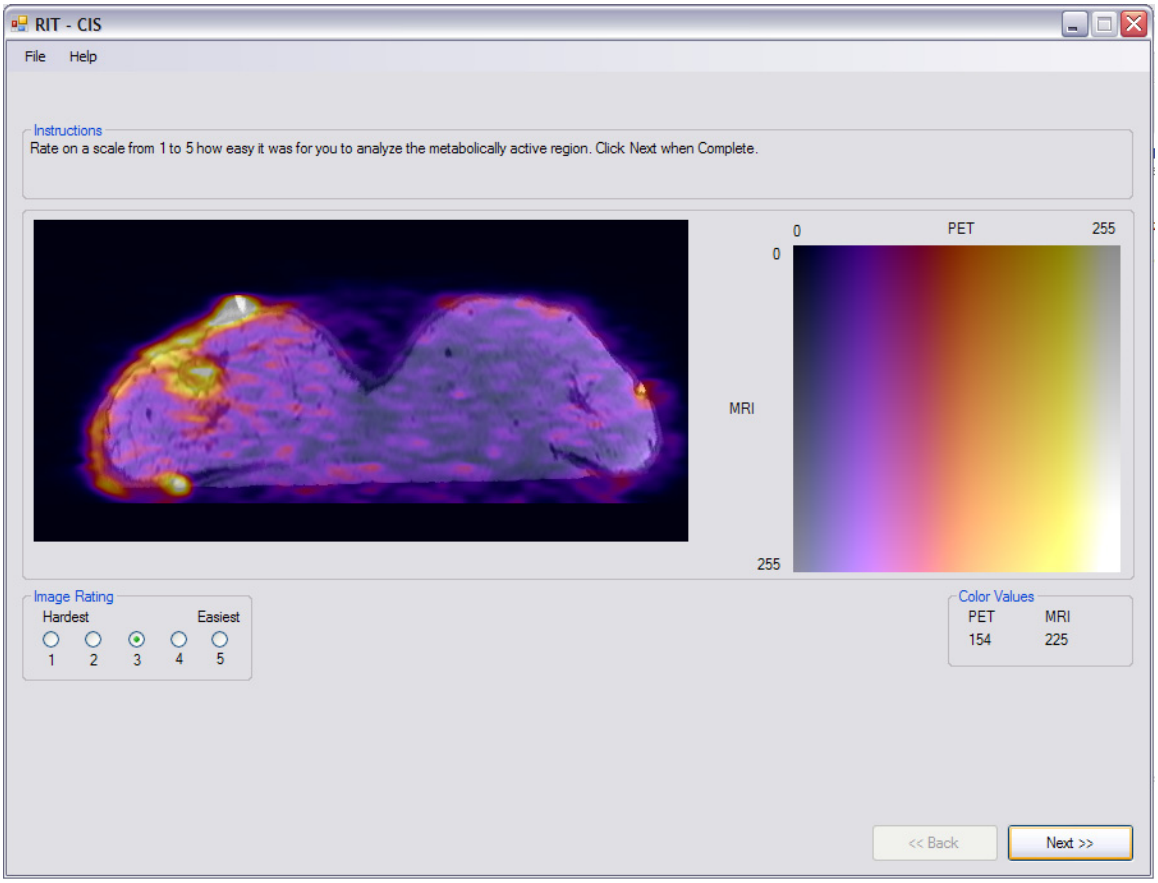

Figure 3.55 Screenshot from study. The observer is asked to rate how difficult it was to perform the previous tasks.

This process was repeated using the same fusion technique for each of the MRI/PET image pairs. Upon completion the observers were asked to rate their ability to use each technique, and to rate the technique according to preference. The opportunity to provide additional feedback was also given. This was done using the screen shown in Figure 3.56. The results were recorded. The entire process for a single fusion technique took from five to ten minutes.

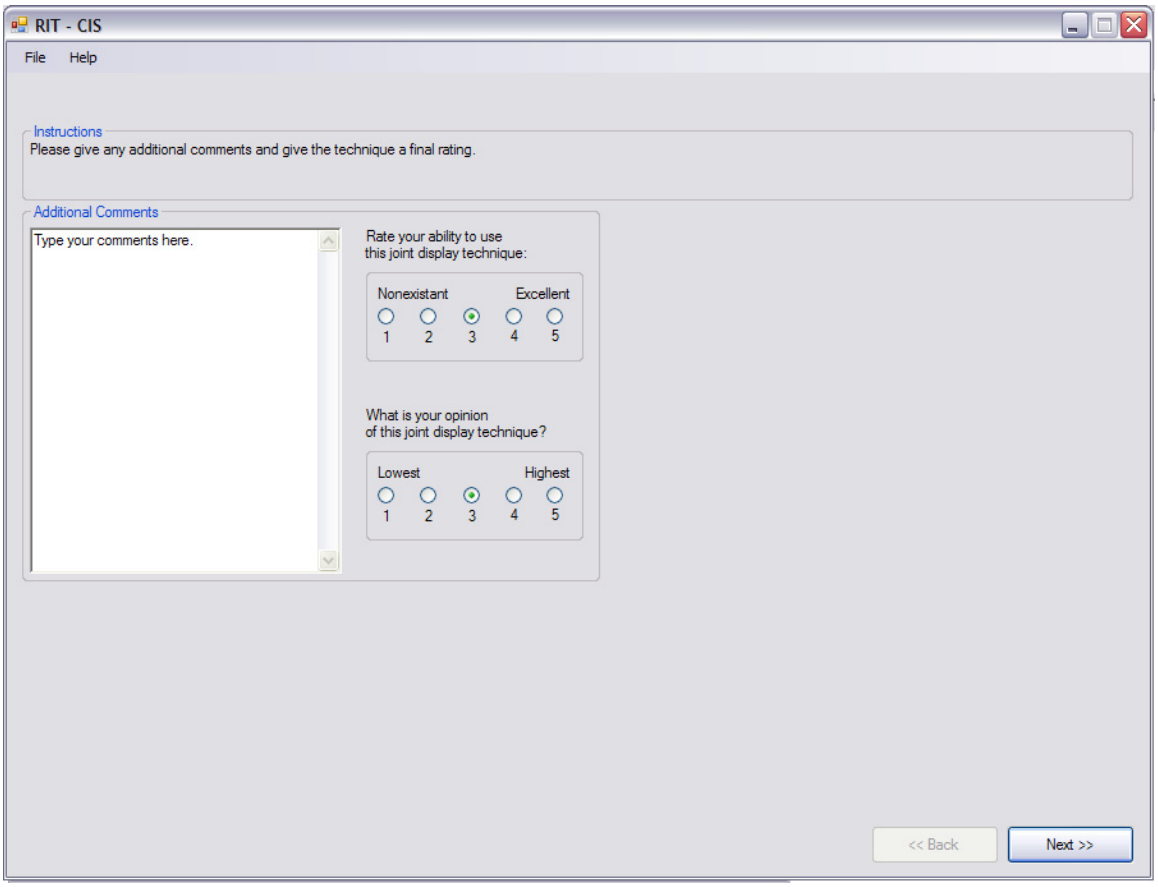

Figure 3.56 Screenshot from study. The observer is asked to rate their ability to use each technique, give an opinion of the technique and provide any additional comments.

This entire process was repeated as a separate session for each of the other fusion techniques. For each observer the fusion techniques were presented in a random order.

There was a several day period between each session to help prevent the radiologists from remembering the images. Due to the large volume of images investigated by the radiologists daily, this period was assumed sufficient. To reduce variations in perceived colors the radiologists were asked to perform every session from the same computer with the same lighting. The entire study took 3 months to complete.

3.6.4 Application for Study Administration

Since the study took place over an extended period of time and at the location and convenience of the participating radiologists, it was necessary to have the study administration as automated as possible for consistency. To accomplish this, three applications were developed. The first was responsible for managing the study for each observer. In particular, it determined the order that the different fusion techniques would be presented to each observer. The other two applications 'Fuze' and 'Un-Fuze' took the observer through the fused display and side-by-side display of the study, respectively. Specific instructions were provided to the study administrator who was responsible for running each application. To maintain consistency all instructions to the observer were presented in writing. The instructions to the administrator and observers can be found in Appendix F. The applications managed the study results, storing the collected data in XML (Extensible Markup Language) files. These files provided formatted data that could be analyzed at a later date.

3.6.5 Data Used

Images from three patients were acquired and registered as discussed in Section 2.5 and Section 2.7. For this study it was assumed that the registration procedure provided accurate results. This implies that the difference, in voxels, between locations in two registered images accurately represents the real distance between those two locations within the patient.

After registration, three orthogonal slices (axial, coronal, and sagittal) through a region of interest were selected from each data set for use in the study. The slices were extracted using the Fusion Viewer application and correspond to the standard views: coronal, sagittal, and axial. The regions of interest were selected to be regions containing above average metabolic activity. For subject 1 the slices were taken through a point in the upper right quadrant of the subject's right breast, for subject 2 the slices were taken through a point in the upper right quadrant of the subject's right breast, and for subject 3 the slices were taken through a point in the center of the subject's left breast. Random variations in window and level were applied to the PET images to cause small changes in the grayscale values at the regions of high metabolic activity and to cause variation of contrasts. The fused images were then created using the Fusion Viewer application and previously created color tables corresponding to each of the fusion techniques being studied.

3.6.6 Techniques Studied

Eight promising fusion for visualization techniques were selected for the study. The techniques were either selected for their psychophysical properties or

because of their use in other medical imaging research projects. Each of these techniques is shown and identified with a number in Figure 3.57. Sample fused images created using each technique are shown in Figure 3.58. Each technique, and the reason it was selected for the study, will now be discussed in detail.

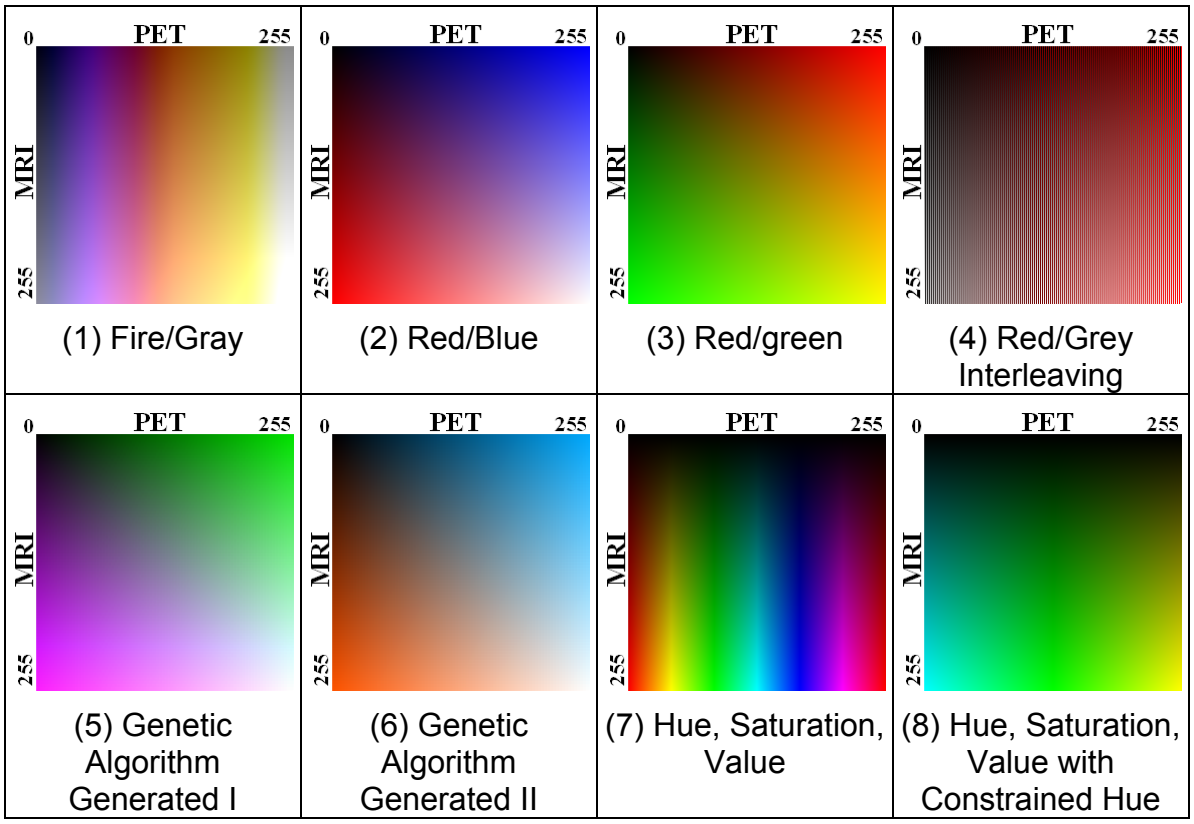

Figure 3.57 Color tables for the different fusion techniques investigated in the study.

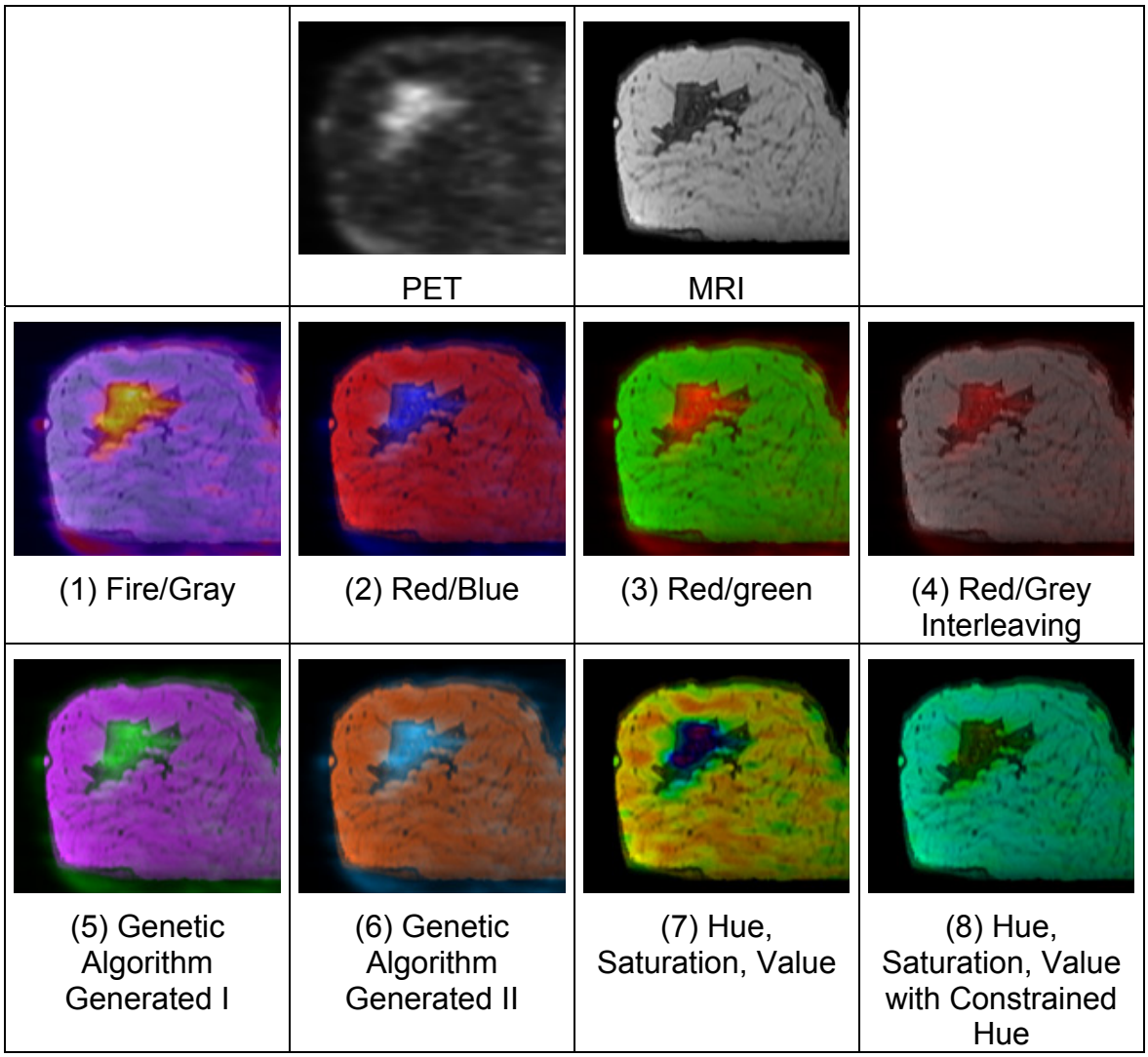

Figure 3.58 Fused images created using each technique. The PET and MRI source images used are shown in the top row.

3.6.6.1 Fire/Gray

This technique was created using color overlay (Section 3.3.1). The fire (hot-cold) color table (Figure 3.59) from ImageJ[136] was applied to the PET image and a grayscale color table to the MRI image. Color was used for PET and variations in intensity for MRI, since MRI is a higher resolution modality, and as previously discussed the human visual system is more sensitive to small changes in intensity than to small changes in color. The technique was selected for study

due to its use in the other research projects currently being conducted at SUNY Upstate.

Figure 3.59 Fire color table.[136]

3.6.6.2 Red/Blue

This technique is based on opponent color theory first proposed by Hering in 1872.[168] The theory states that although the human retina has three distinct cones, sensitive to short (roughly blue), medium (roughly green), and long (roughly red) wavelengths of light, color information is passed to the brain using two chromatic channels.

The information encoded in these channels is the result of the signals from the ganglion cells which are responsible for conveying the information about light to the brain in the form of electrical signals. Certain ganglion cells will increase their fired signals when receiving messages from the long cones and will decrease their signal when receiving signals from medium cones. Other ganglion cells do the opposite. The signal from these ganglion travel the same pathway in essence creating a channel that responds to red and green light. Due

to the nature of this relationship only one message, green or red, can be transmitted at a time.

The other channel is the result of ganglion cells which fire when the signal from the short cone is increased and will reduce firing when receiving signals from the medium and long cones. Again there are other cells that do the opposite. This results in a channel that goes from blue to yellow (green + red = yellow). These opponent colors are graphically shown in Figure 3.60.

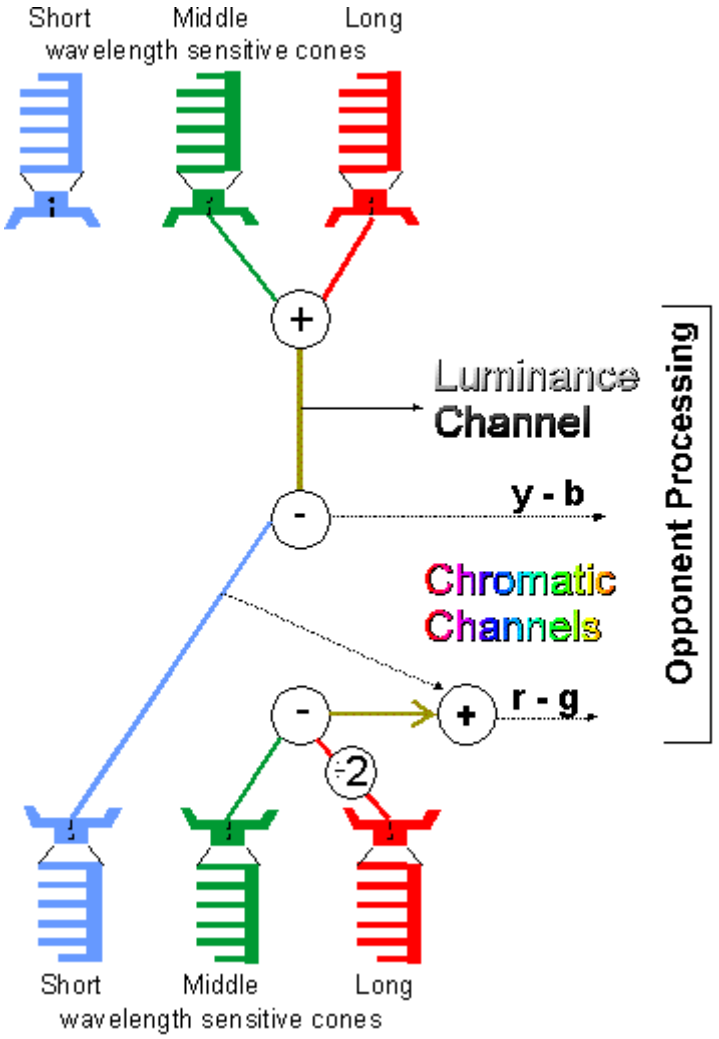

Figure 3.60[U] Simplified diagram of opponent color theory.

[U] Figure from [169], used with permission.

Opponent color theory explains why we perceive certain colors but not others. In particular we can see colors that result from a mixture of the two channels, but not colors that result from a mixture along a single channel. For example, we can see red + yellow = orange or red + blue = magenta, but not blue + yellow = bluish - yellow or red + green = reddish - green.[170]

Trying to leverage the results of this theory a two dimensional color table was created by assigning shades of blue to the PET image and shades of red to the MRI image. Since these colors are transmitted on separate channels according to opponent color theory changing the MRI value (amount of blue) should have little impact on the perceived PET value (amount of red) and vice versa. This is as opposed to our next fusion technique which uses red for one source and green for the other, where changing the amount of red should change the perceived amount of red.

3.6.6.3 Red/Green

This is another color overlay technique. A red color table is applied to the PET image and a green color table to the MRI image. It was selected for inclusion in the study because of its use in the Mayo Clinic's Analyze[171] software package.

3.6.6.4 Gray/Red Interlace

This fusion technique is based on spatial interlacing. Fused images were created by taking alternating columns from each of the source images. For example, the odd columns in the fused image are taken from odd columns in the PET image while the even columns are taken from even columns in the MRI

image. The PET image was first pseudo colored using a red color table. This technique was selected for the study because of its popularity in the research literature.[138,142,146]

3.6.6.5 Genetic Algorithm I and II

These two fusion techniques selected for the study are the result of running the previously discussed genetic algorithm (Section 3.4). These results were presented in Section 3.4.4.

3.6.6.6 Hue, Saturation, Value

The hue, saturation, value (HSV) color space is a model designed to describe how humans perceive color. Hue is the color, saturation is the amount of the color, and value is the intensity of the color. A visual representation of this color space is shown in Figure 3.61. For this technique hue was used to present the PET image and value was used to present the MRI image. The saturation was kept constant. Like the Fire/Gray technique the MRI was used for the intensity, because of the human visual system's higher sensitivity to changes in intensity over changes in color. This color table was selected because of its popularity throughout the literature. It is assumed that because colors are naturally described using hue, saturation, and value that observers will be able to identify changes in one of these amounts independent of the other two.

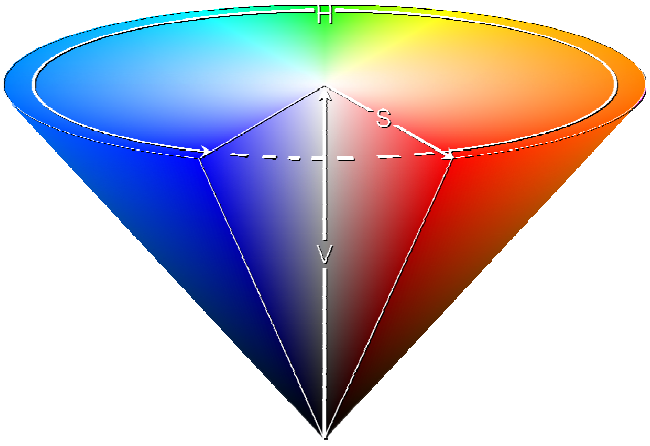

Figure 3.61[V] Conical representation of the HSV color space.

3.6.6.7 HSV, Constrained Hue

This technique is similar to the previously discussed hue, saturation, value technique except that it uses a constrained hue angle. Instead of allowing the color to vary over the entire spectrum, it was only allowed to vary within the cyan to green to yellow region.[144] Constraining the hue angle helps prevent false segmentation due to changes in color, and provides colors that appear to have a natural ordering to a human observer.

3.6.7 Data Analysis

Data resulting from the participants performing the tasks using each of the selected fusion techniques were collected. This data, stored in XML, was analyzed using a series of IDL[173] programs. These programs present the data in a number of different ways, however only the plots that contain the information from all observers, viewing all images with all techniques are presented in the next section.

[V] Figure from [172], used with permission under the GFDL (GNU Free Documentation License).

3.6.8 Results and Conclusions

To aid in interpreting the results the techniques are listed again in Table 3-I.

Table 3-I Techniques investigated by the study.

Technique Number	Technique Name
1	Fire/Gray
2	Red/Blue
3	Red/Green
4	Gray/Red Interlace
5	Genetic Algorithm 1
6	Genetic Algorithm 2
7	Hue, Saturation, Value
8	HSV, Constrained Hue

Figure 3.62 shows a plot of the average distance, in pixels, over all participants, between the location of the area of maximum metabolic activity selected on the MRI and the PET gray scale images when viewed side-by-side. One pixel corresponds to 0.7 mm by 0.7 mm. All error bars shown here represent the standard error. It can be seen that the average distance, over all images, is approximately 10.7 pixels, in other words, there is up to approximately a 1 cm difference between the two regions selected when viewing PET and MRI images side by side. This discrepancy increases the risk of performing a biopsy in the wrong location, misdiagnosis, and justifies the need for a fused display.

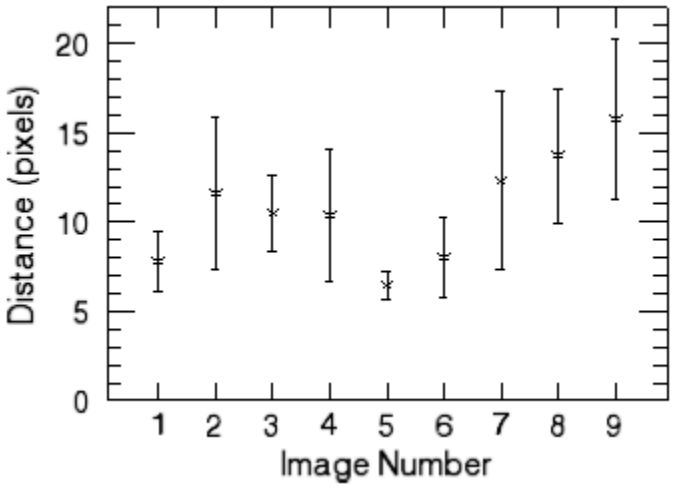

Figure 3.62 Distance in pixels between corresponding location chosen on PET and MRI image when viewed side-by-side.

Figure 3.63, on the other hand, shows the average distance, over all observers and images for each technique, in pixels between the location of the area of maximum metabolic activity selected on the fused image and the corresponding location selected on the gray scale PET image. It can be seen that the average distance is reduced particularly with techniques 5 and 6, which correspond to the two color tables generated by the genetic algorithm. Performance is worst with technique 8, possibly because as the range of colors gets smaller they become increasingly difficult to differentiate.

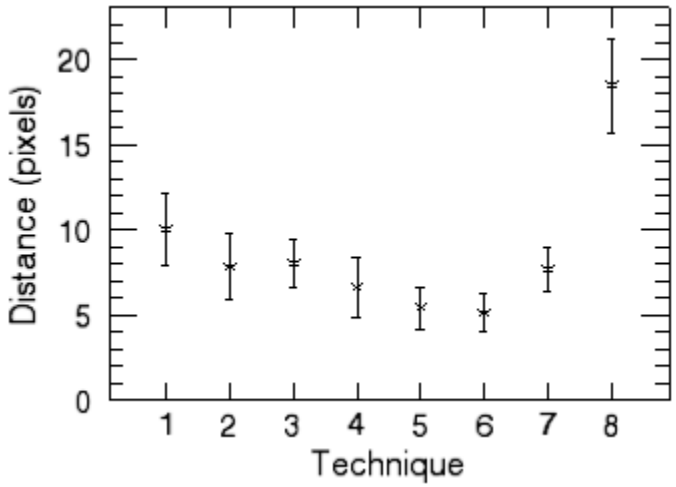

Figure 3.63 Distance in pixels between corresponding locations chosen on PET and fused image.

Figure 3.64 shows results of the difficulty rating assigned by the observer when performing the tasks with each technique, where 5 represents easiest and 1 represents hardest. It can be seen that techniques 5 and 6 are ranked the easiest to use. Techniques 1 and 3 also have high rankings, which may reflect past experience using those techniques.

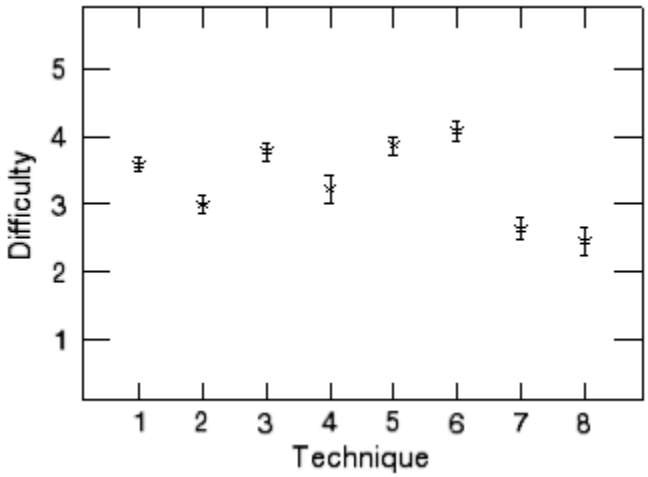

Figure 3.64 Difficulty ratings assigned when performing tasks for each technique. One corresponds to hardest and five to easiest.

In hindsight, it is obvious that telling the observers to rate the difficulty they had performing the tasks can be interpreted in different ways. The responses might reflect other areas not directly related to the fusion technique such as using the user interface. The same is true to a lesser extent of the other subjective questions asked. It is believed however, that since the observers were aware of the study goals and informed about the research being performed, that they answered the questions as intended.

Figure 3.65 shows the level of ability each observer believes he or she has for using each of the techniques, where one means they do not think they are capable of using it and five means they believe they are an expert at using the technique. The rankings are fairly even with techniques 3 and 4 having the highest and techniques 7 and 8 the lowest. It is not surprising that 7 and 8 rank the lowest, as it is unlikely that radiologists have significant experience describing colors using HSV color space.

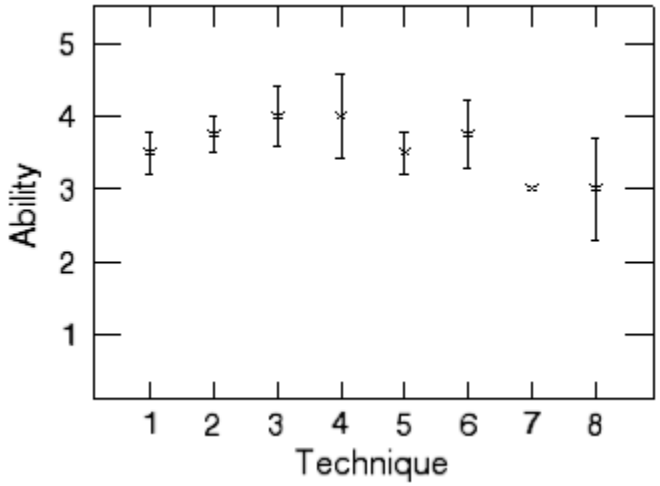

Figure 3.65 Ability level assigned by observers for each technique. One means they do not think they are capable of using it and five means they believe they are an expert at using the technique.

Figure 3.66 shows the preferences assigned to each technique by the observers. No technique is given significantly higher preference than any other. The higher preferences are assigned to techniques 1, 3, 4, and 6. It is interesting to note that the techniques the observers claimed to prefer and understand the best were not necessarily the ones with which they were best able to complete the tasks. This suggests that thorough testing should be performed before selecting a fusion technique rather than choosing the technique most radiologists seem to prefer.

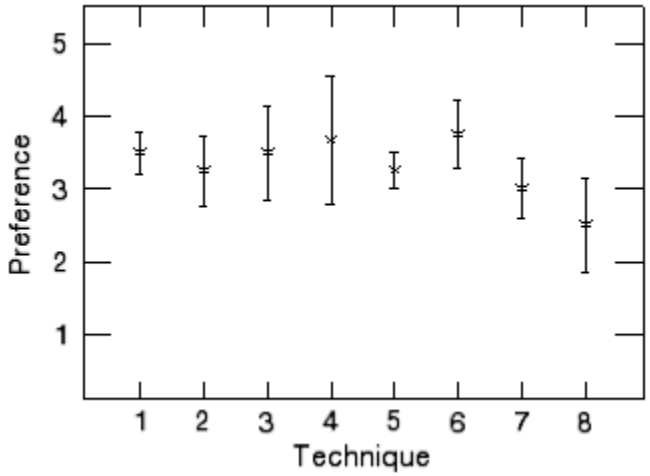

Figure 3.66 Preference level assigned by observers for each technique. One corresponds to no preference and five corresponds to a preferred technique.

Figure 3.67 shows the distance on the color tables between the color at a point selected in the fused images and that color as identified on the color table by the observer. This distance represents the observer's ability to decode the coloring used for the fusion. In other words, the ability of the observer to recover the original MRI and PET value at a given point in the image. Observers achieved the smallest distances with techniques 1, 3, and 5. Technique 4 could not be evaluated with this metric since colors could appear at more than one location in the color table.

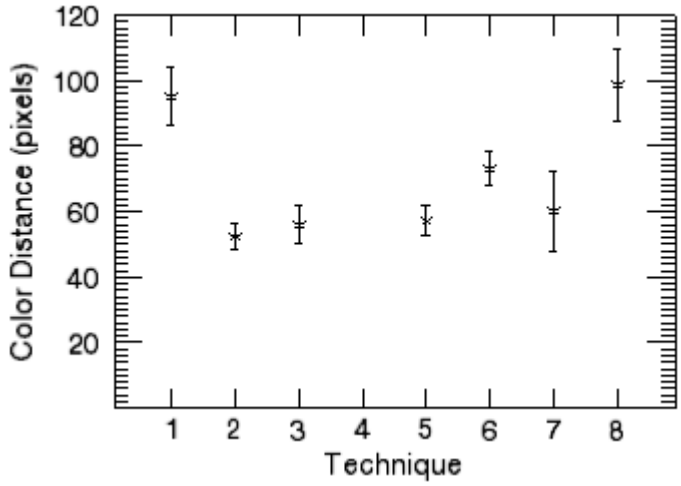

Figure 3.67 Distance in pixels on the color table between the color observers thought they chose from the fused image and color they actually chose. Maximum distance is approximately 362 pixels.

Another way to look at the color accuracy is in terms of the color difference between the color the observer chose from the color table and the one they should have chosen. While this metric does not tell us how far off their perception of the MRI and PET values were, it does give us information on the observer's ability to compare specific colors. This metric, defined as the distance in the CIE L*a*b* color apace between the color they observer selected on the color table and the one they should have selected, is shown in Figure 3.68.

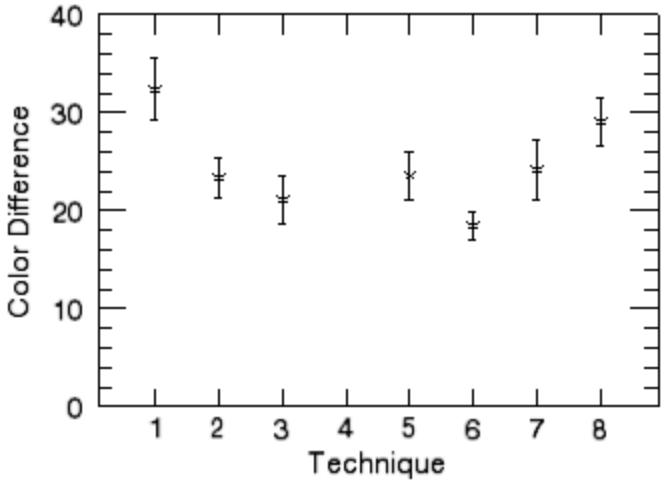

Figure 3.68 Distance in CIE L*a*b* color space between the color the observer chose from the fused image and the color they chose on the color table.

Unfortunately the times recorded from the study provided no additional information. In an attempt not to influence reading times, the radiologists were not informed that they were being timed. The sometimes excessively long reading times indicate that the radiologists were distracted and interrupted during the study (probably by their regular duties). It is hoped that this situation can be avoided in future studies by informing participants about the timing.

The study clearly demonstrates the need and benefit of a joint display because of the inaccuracy when using a side-by-side display. In many cases the differences between the techniques are qualitatively significant. The study suggests that the color tables generated by the genetic algorithm, particularly technique 5, are good choices for fusing MRI and PET images. This is best demonstrated in Figure 3.63 which demonstrates the spatial accuracy of the technique. This property is hardest to obtain through other tools, as compared, for example, to the MRI and PET values for a point in the image, which are usually accessible to the observer through other means.

It is interesting to note that popular techniques such as the Fire/Grey and techniques based on the HSV color space, which are prevalent in the literature, appear to give poorer performance. This might be because false assumptions were made in designing these techniques. One common misconception is that a larger range of colors will allow smaller variations to be seen, when in reality sharp changes in color might attract the focus making variations within the individual colors difficult to discern. Also, radiologists do not necessarily have the same skills at interpreting colors and identifying specific characteristics (e.g., hue and intensity) as artists or color specialists might have.

The study suggests that more extensive studies should be used to determine which fusion technique to use in a clinical setting. This is supported by Figure 3.65 and Figure 3.66 where the fusion techniques the radiologists prefer and believe they are most capable of using are not necessarily the ones that provide the best results.

Further details on the study, including the tools used, data used, and data collected can be found in “Multimodal Display Techniques with Application to Breast Imaging,” available through Rochester Institute of Technology’s Digital Media Library.[174]

3.7 Future Directions

The genetic algorithm was shown to be a promising way to generate color tables. Continued efforts should refine the algorithm to consider additional desired properties (Section 3.4.2.7). Results can be compared using additional underlying models, including those representing interactive fusion operators.

It is clear that a larger study including additional radiologists needs to be performed to confirm and support the results of this study. Of particular interest would be a study comparing interactive versions of select fusion techniques. The most appropriate technique will most likely depend on the specific tasks and future studies should focus on evaluating the radiologist while performing clinical duties.

One area the study was designed to investigate, but provided no useful results, was reading efficiency (how much time is needed to read each image). Future studies might address this issue using an eye tracking device. The recorded fixations might provide a more accurate result than recorded time. Using eye fixations will exclude effects due to the user interface and other distractions, which a recorded time cannot. In addition, it might provide insight into how radiologists read images.

The study does make clear the need for fused displays and encourages fusion capabilities to be introduced into PACS systems. It stresses the need for manufacturers of multimodal systems, such as PET/CT systems, to investigate ways to improve the presentation of the acquired data.

Chapter 4 Digital Phantom for Image Synthesis

Obtaining “ground-truth” data in medical imaging is an almost impossible quest when pathology reports are not available. One way to circumvent this limitation is by creating digital synthetic phantoms with the appropriate physical properties and characteristics that can be imaged using digital simulators.

Digital simulators can be used to study system design, acquisition protocols, reconstruction techniques, and evaluate image processing algorithms. Specifically in this work, simulated images can aid in the evaluation of the registration procedure, and provide data for studies accessing the ability of radiologists to use specific visualization techniques. In addition to providing a precise ground truth, they can be used to save significant time and money compared to finding volunteers, and arranging and paying for scanner time. The simulators selected for this work are SimSET for PET and SIMRI for MRI.

The work discussed focuses on the design and simulation of breast phantoms. A new specification for multi-component geometric phantoms is proposed, along with a novel relational descriptive language that defines the relationships between the components. The designed phantoms are unique in that they are geometric based and contain dynamic information.

A breast phantom has been implemented in this new format. The assignment of appropriate physical properties for simulated positron emission tomography imaging of the phantom will be discussed. A simulated system and results of the simulated imaging of this phantom are presented.

4.1 Simulation Software

The University of Washington has developed a PET/SPECT simulator based on Monte Carlo techniques that models the physical processes and instrumentation used in emission imaging. SimSET,[175,176,177,178,179] which can be used to model both single photon emission computed tomography (SPECT) and PET, models the important physical phenomena including photoelectric absorption, Compton's scattering, coherent scattering, photon non-colinearity, and positron range. It supports a variety of collimator and detector designs, and already includes the attenuation properties for many common materials. If the attenuation and activity properties are known for each voxel the gamma signal can be generated. SimSET and its source code can be downloaded from [180]. The code is written in a modular format, see Figure 4.1.

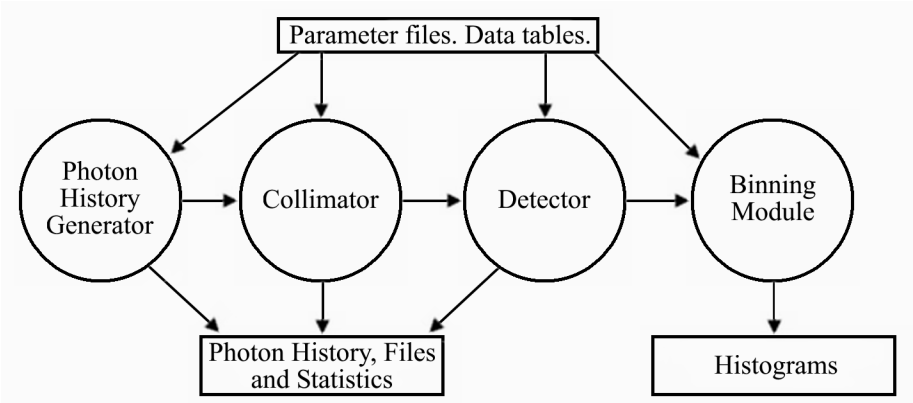

Figure 4.1[W] Block diagram of SimSET modules.

Even at this preliminary stage it was realized that the computational complexity of the simulator may be a limitation for its utility due to the extremely long time required to run realistic simulations. To overcome this difficulty, we have proposed and accomplished a parallel implementation based on the

[W] Adapted from [181].

Condor[182,183] distributed computing environment. This implementation which is beyond the scope of this dissertation was presented as “Distributed Wrapper for SimSET Monte Carlo PET/SPECT Simulator” in volume 20, supplement 1, of the *Journal of Digital Imaging*.

SIMRI is a 3D MRI simulator based on the Bloch equation developed in CREATIS, Lyons, France.[184,185] The source code is downloadable from [186]. It includes a few pulse sequences, and the framework allows for the implementation of *ad hoc* sequences. It supports static field inhomogeneities due to improper shimming and tissue susceptibility, features efficient modeling of intravoxel inhomogeneities, and properly models the main artifacts such as susceptibility, wrap around, chemical shift, and partial volume effects. The design of SIMRI is shown in Figure 4.2. SIMRI is already implemented on a grid architecture.

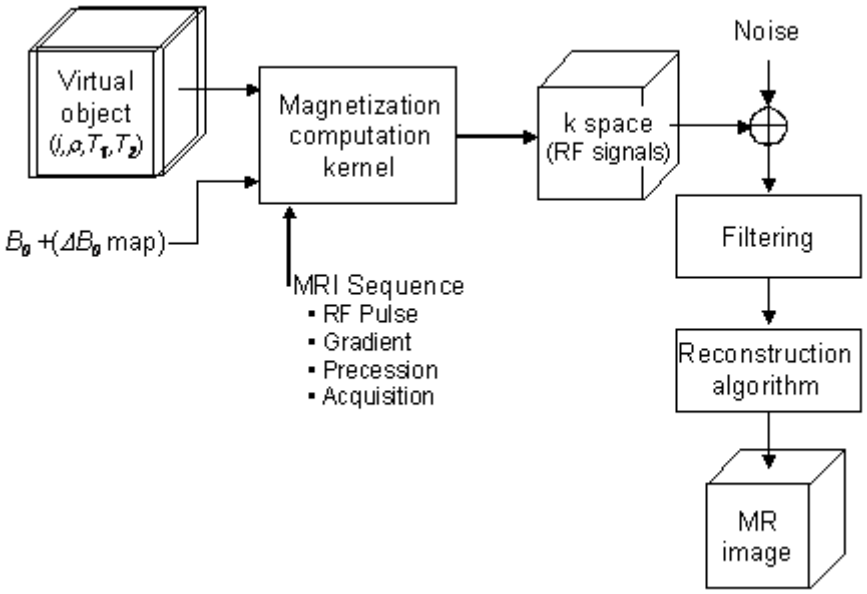

Figure 4.2[X] Block diagram of SIMRI simulator.

If the fractional tissue components of each voxel are known, the magnetic resonance signal can be generated. The magnetic resonance signal will vary for each pulse sequence that is used to acquire images. In general, the signal is a function of the spin-lattice relaxation time (T_{1i}), the spin-spin relaxation time (T_{2i}), and spin density (ρ_i) of the *i* tissues, and the acquisition parameters prescribed by the operator. The acquisition parameters depend on the pulse sequence. Some examples include the repetition time (TR), the echo time (TE), the flip angle (θ), and the inversion time (TI).

4.2 Digital Phantom Design

The quality and realism of the simulated images is currently limited by the quality of the digital phantoms used for the simulations. The transition from simple raster (voxel) based phantoms to more detailed geometric (mesh) based

[X] Figure from [184], used with permission.

phantoms has the potential to increase the usefulness of simulated data. By defining each tissue component separately and utilizing geometric transformations (i.e., scaling, rotation, translation, skewing), a single phantom can be used to model a population of individuals or a single individual being imaged in different positions. Individual tissues can be manipulated independently or even added and removed. Since the phantoms are defined in a continuous space, with a proper interpolation function, they can be used to perform simulations at any resolution. Performing these tasks on raster phantoms is challenging, often requiring redesign of the phantom from the ground up.

The phantoms can be either designed to the desired level of realism by medical illustrators, or created by segmenting previously acquired medical data sets. A time dimension can provide the dynamic properties of the tissue and can be utilized in the simulation of dynamic studies. The geometric phantoms used here are defined as a set of enclosed surfaces in 3D space. The surfaces define the boundary of a tissue and anything within the area is identified as containing that tissue. The surfaces are defined as a series of adjacent triangle elements as shown in Figure 4.3.

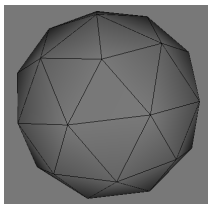

Figure 4.3 Example surface of a geometric phantom.

Each component of the phantom is defined as a separate surface that can be individually manipulated using geometric transformations or more complex displacement fields. The nature of the phantoms makes them robust and easy to modify.

4.2.1 Phantom Design

A breast phantom was designed and created using MilkShape 3D,[187] a graphics model creation package by chUmbaLum sOft. The phantom is designed to support current and future projects on breast imaging. The phantom, when combined with appropriate physical properties, can be used with SIMRI, SimSET, or another simulator. The phantom contains ten different tissues including adipose tissue, areola, blood, bone (rib), ductal tissue, Cooper's ligament, lobule, muscle (pectoral), skin, and stroma connective tissue. Many of these components, such as the blood and lobules, are comprised of many discrete parts that can be further divided as desired.

Each component is defined by a series of connected triangles that define an orientable manifold (closed surface with a defined interior and exterior). The ordering of the triangle vertices is used to specify the front or back face of the triangle. This can be done using standard culling techniques. If the normal of the triangle is pointed towards an observer they are looking at the front face of the triangle, and if the normal points away from the observer they are looking at the back of the triangle. The normal of the triangle can be found using Equation 4.1, where P_0, P_1, and P_2 are three element vectors representing the location of

the vertices of the triangle labeled in a counter-clockwise order.[95] The vector cross product operator is represented by $\times$.

$$N = (P_1 - P_0) \times (P_2 - P_0) \qquad (4.1)$$

Figure 4.4 shows the interface of MilkShape 3D used for creating the phantom. The model for one of the lobes is displayed. This model consists of 1,442 triangles. Similar models were created for the other tissue components providing an 83,278 triangle model.

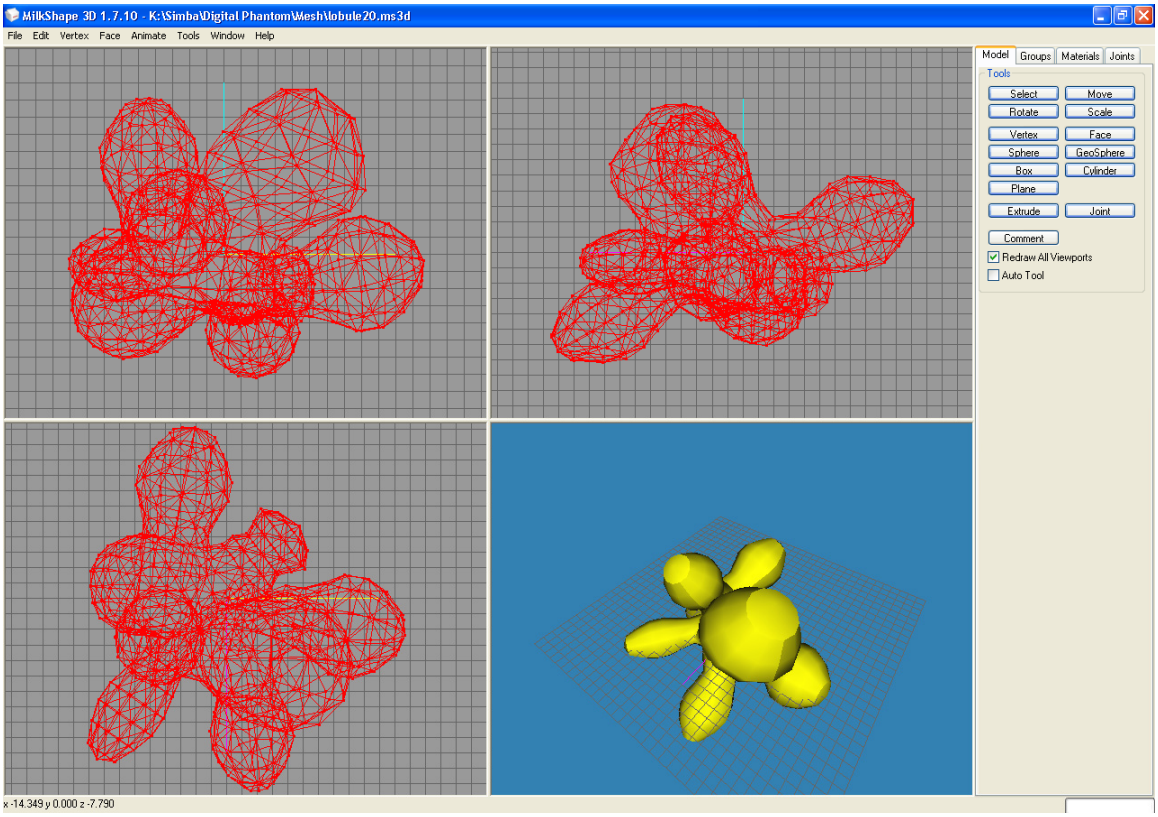

Figure 4.4 Screen shot of MilkShape 3D. A lobe shown as three orthogonal projections and a 3D rendering (bottom right).

The interior of the breast model is shown in Figure 4.5. Five tissues are visible in the image including: skin, areola, lobule, ductal, and blood. Additional information on the design can be obtained by displaying the phantom as a wire

frame (Figure 4.6). The wire frame shows the vertices and edges used to define the model.

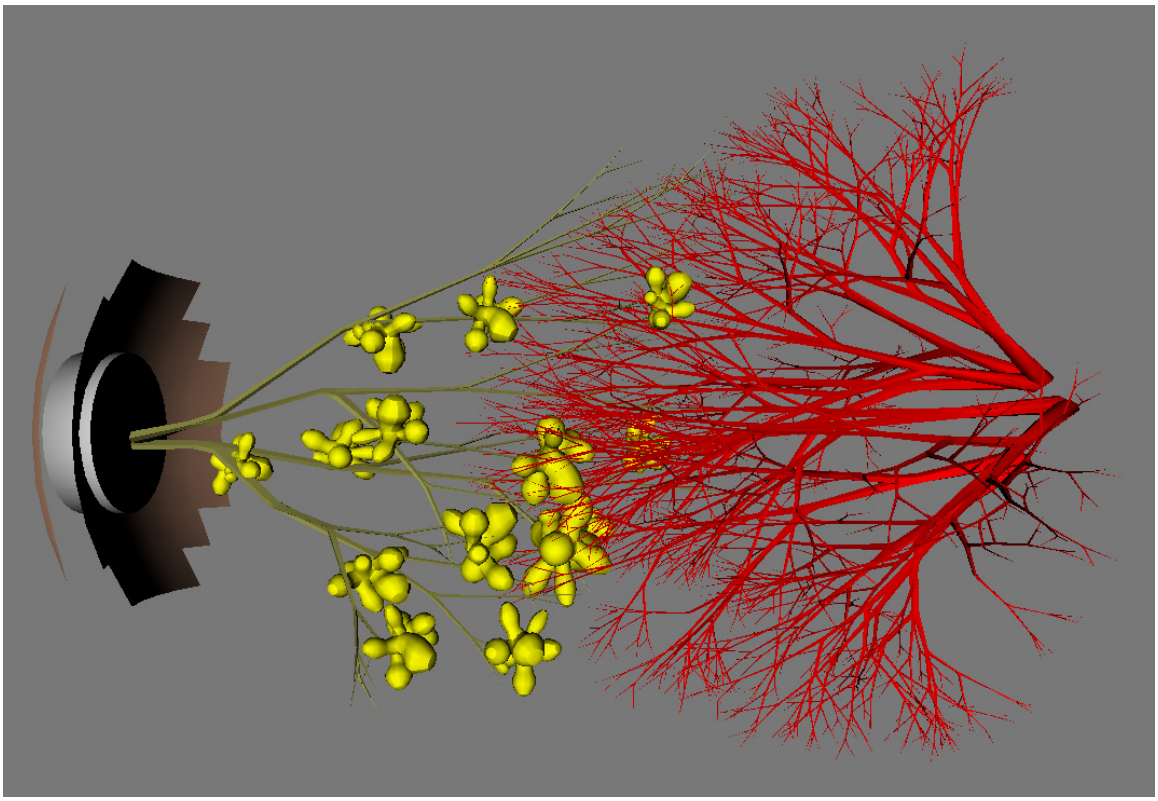

Figure 4.5 Interior of breast phantom shown using surface rendering techniques. Tissues present include skin, areola, lobule, ductal, and blood.

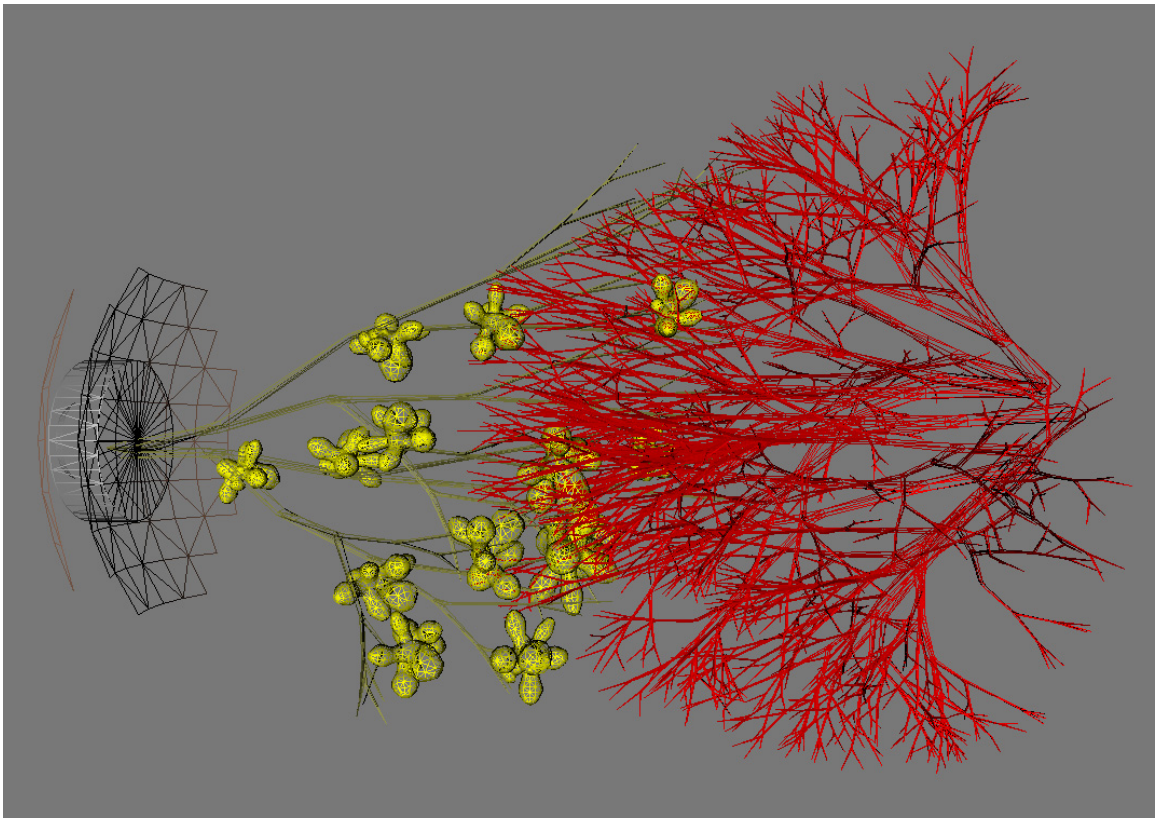

Figure 4.6 Portions of phantom shown in Figure 4.5 displayed as a wire frame.

The exterior of the phantom is shown as a wire frame in Figure 4.7. The phantom is bounded by a layer of skin at the front, and by pectoral muscle at the back. As can be seen from Figure 4.7 the skin consists of two mesh layers that meet and form a closed surface at the base of the breast. The areola tissue overlaps the skin and occupies a region at the apex of the phantom. The pectoral muscle is a layer covering the back of the breast along with the ribs.

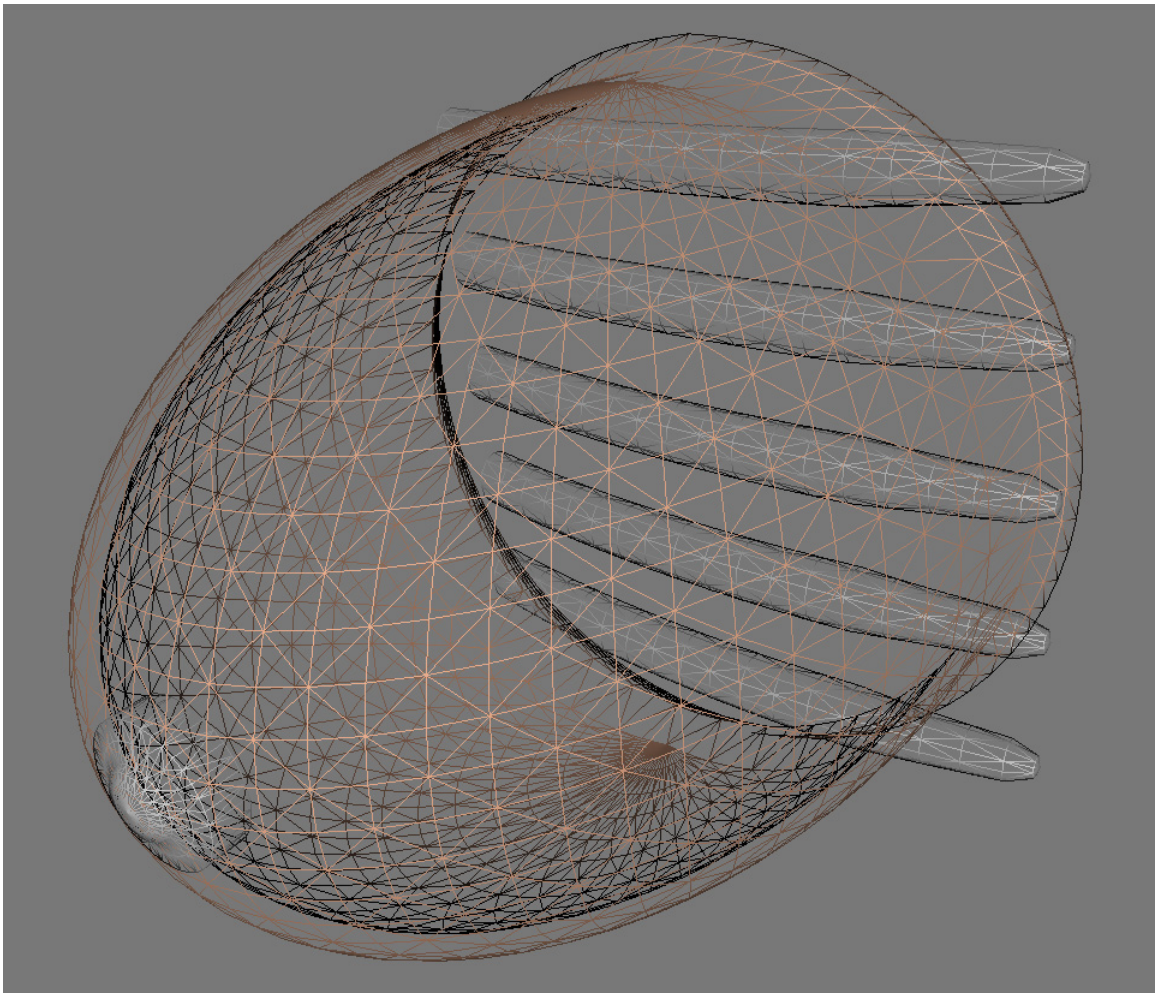

Figure 4.7 Exterior of breast phantom shown as a wire frame. Tissues present include skin, areola, and ribs.

The interior consists of a layer of adipose tissue which is similar to, but thicker than, the layer of skin. The center of the phantom is filled with connective tissue. The Cooper's ligaments run from the skin through the adipose tissue to the connective tissue. Ductal tissue branches out of the areola with lobule tissue located along it. Veins and arteries enter and spread out from the posterior, narrowing and tapering off as they head toward the apex.

The phantom, while robust for simulation, is still a simplification of the actual breast. For example, human tissue has a more complex vascular structure than

the phantom. Some simplifications were made because they have potential benefits. One example is the limited extent of the blood vessels. In the phantom they only extend approximately two-thirds of the way throughout the breast (a geometric transform of the vascular component could make them extend throughout the entire breast). This leaves a portion of the simulated images unaffected by the activity from the blood, and will provide a simpler area to test segmentation or classification algorithms.

4.2.2 Relationships Between Components

A new relational descriptive language which indicates the relationship between the component meshes was developed. For example, if a point in space is contained in both the blood component mesh and the adipose tissue component mesh then the point should be considered blood. Using a descriptive language will allow for special behavior for different combinations of tissues, as well as simplifying mesh design since the mesh author will not be required to have all of the component meshes fit together perfectly like a puzzle. In our previous example, the potential user was not required to modify the adipose tissue mesh to have openings for the veins. This simplifies mesh design, permitting modification of tissue components or allowing additional ones to be added later, without requiring modification of the other components. This will allow for more complex phantoms and faster phantom development.

The tissue located at a point is determined by comparing the signature at the point to a series of mask pairs. The first mask pair matched determines the tissue properties for that point. The signature is the binary string representing

the components the point is contained within. For the breast phantom this string is [adipose, areola, blood, bone, Cooper's, ductal, lobule, pectoral, skin, connective]. If a point is located within the Cooper's ligament component and the adipose component it will have the signature [1000100000].

The first mask in each mask pair determines the components the mask is interested in, it is referred to as the interest mask. The second identifies the requirements for those components, and is called the relation mask. For example, to require a point to be located in the adipose component but not the blood component we would use the mask pairs ([1010000000], [1000000000]). Here the first mask identifies the components we are interested in (the first and third), and the second mask determines the values required in the signature for those components (contained within the first component but not the third). The values located in the other bits of the second mask are ignored.

Simple binary operators are used to determine if a signature matches a mask pair. Equation 4.2 shows this operation. Here $\oplus$ is the binary exclusive or operation, $\vee$ is the binary inclusive or operation, and $\neg$ is the binary negation operation. If Match_Value evaluates to the binary string composed entirely of ones than the signature matched the mask pair.

$$\begin{array}{r} \text{Signature} \\ \oplus \neg \text{Relation\_Mask} \\ \vee \neg \text{Interest\_Mask} \\ \hline \text{Match\_Value} \end{array} \qquad (4.2)$$

As an example we will consider the mask given above for a point contained within the adipose and Cooper's ligament components. Comparison of this mask to the previously given mask pair for a point located in the adipose, but not the

blood component, is given by Equation 4.3. As expected, since the signature represents a point located within the adipose, but not the blood component, the result of the comparison is a binary string of ones indicating the signature matched the mask pair.

$$\begin{aligned}
&\text{Match_Value} = (\text{Signature} \oplus \neg\,\text{Relation_Mask}) \vee \neg\,\text{Interest_Mask} \\
&= ([1000100000] \oplus \neg[1000000000] \vee \neg[1010000000] \\
&= ([1000100000] \oplus [0111111111]) \vee [0101111111] \\
&= [1111011111] \vee [0101111111] \\
&= [1111111111]
\end{aligned} \tag{4.3}$$

The signature is compared to each mask pair in a predetermined order. The first mask pair matched determines the physical properties that are assigned to that location. Table 4-I lists the masks that are used for the breast phantom in the order that they are applied.

Table 4-I Masks for tissue assignment of breast phantom.

Interest Mask	Relation Mask	Assigned Tissue
0010000000	0010000000	Blood
0001000000	0001000000	Bone
1100000000	0100000000	Areola
1000100001	1000100000	Cooper's Ligament
0000000110	0000000010	Skin
0000000100	0000000100	Pectoral
0000001000	0000001000	Lobule
0000010000	0000010000	Ductal
0000000001	0000000001	Connective
1000000000	1000000000	Adipose
0000000000	0000000000	Air

This signature and mask pairs format was selected due to its simplicity. Implementation of the operations is trivial and can easily be included in any application that works with digital phantoms. Conversion of a set of mask pairs

into an if-then-else format is easily performed at run-time. This new language is extremely robust permitting a large number of relational situations.

4.2.3 Phantom Sampling

The majority of medical image simulators, including SimSET and SIMRI, require raster phantoms. Until simulator software evolves, mesh based phantoms will need to be converted into raster data for use with the simulators. To address this shortcoming a software package that samples (finds phantom values at evenly spaced location) was designed to convert mesh phantoms into raster phantoms. The algorithm used by the software will be the focus of this section.

The application was written in C++ leveraging the computational advantages of threading. It provides a generic mesh class for compatibly with a large number of mesh types, such as those provided by Autodesk's 3ds Max (3D Studio MAX),[188] Autodesk's AutoCAD,[189] Microsoft's Direct X,[190] and NewTek's Lightwave 3D.[191] Input parameters provide the necessary inputs such as mesh files, relational masks, dimensions, and sampling resolution.

The sampling uses a standard intersection of a ray and a triangle algorithm, similar to the one provided by Lengyel,[95] and the "odd parity" rule introduced by Sutherland and Hodgman[192,193] in order to perform point location. The "odd parity" rule states that to determine the location of a point with respect to a polygon, a ray from the point can be drawn in any direction to infinity. If the ray intersects the polygon an odd number of times the point is located within the polygon, otherwise it is located outside of the polygon.

For each sampling point a ray is traced in an arbitrary direction. The number of times the ray intersects each component is counted, providing the location of the point with regards to the components. The intersection of the ray with each component is determined by counting the number of triangles defining the component that the ray intersects.

The normal of each triangle is first found using Equation 4.1. The plane containing the triangle is defined by the normal and a signed distance of the plane from the origin calculated using Equation 4.4, where $\bullet$ is the dot product.

$$D = -N \bullet P_0 \tag{4.4}$$

Note that the signed distance is negative and scaled by the length of N. The plane containing the triangle can then be defined as Equation 4.5, where P is any point on the plane.

$$N \bullet P + D = 0 \tag{4.5}$$

Letting P_S be the point that is being sampled and V be the ray direction, the ray extending from point P_S to infinity is defined by Equation 4.6.

$$R(t) = P_S + tV \tag{4.6}$$

The intersection of the ray with the plane of the triangle is first confirmed. If the dot product of N and V do not equal zero (Equation 4.7) then the ray and plane are not parallel and must meet at some point.

$$N \bullet V \neq 0 \tag{4.7}$$

The intersection of the plane and ray can then be found by substituting Equation 4.6 into Equation 4.5 and solving for t (Equation 4.8).

$$
\begin{aligned}
&N \bullet R(t) + D = 0 \\
&N \bullet \left(P_S + tV\right) + D = 0 \\
&t = \frac{-\left(N \bullet P_S\right) - D}{N \bullet V}
\end{aligned}
\tag{4.8}
$$

The point of intersection is then given by Equation 4.9.

$$
R(t) = P_S + \left(\frac{-\left(N \bullet P_S\right) - D}{N \bullet V} \right) V \tag{4.9}
$$

Area coordinates (Section 2.4.3.1) can then be used to determine if the point of intersection lies within the bounds of the triangle. After the location of each sampling point is found with regards to each of the components, the relational descriptive language and the masks are used to determine the value at that point within the raster phantom.

4.2.4 Assignment of Properties

Prior to generating simulated images of the phantom appropriate imaging properties need to be assigned for each tissue type. Specifically, radiotracer concentration and attenuation coefficients need to be provided.

4.2.4.1 Activity

Radiotracer concentrations were assigned based on manual selection of regions of interest corresponding to specific tissues from a dynamic pet series acquired using a GE Advance NXi, as described in Section 2.5.1.2.

Figure 4.8 and Figure 4.9 indicate the regions selected. The clearly visible vertebra was selected to provide the activity values for bone which were assigned to the ribs. The higher activity region in the center of the breast consisting of connective and glandular tissue was selected to represent the connective tissue (Cooper's ligament and stroma). The glandular tissue (ductal

and lobule) which is also located throughout this region and is generally more active, was assigned activity values one standard deviation higher than that of connective tissue. The areola was assigned the same value, due to the large concentration of ducts and increased blood flow. The activity for pectoral muscle was assigned from the area of higher activity along the chest wall. The adipose tissue was assigned values from the lower activity region between the surface of the breast and connective tissue because of the relatively thick layer of fatty tissue that backs the skin. Blood, which in general influences the entire image, was measured in the left ventricle of the heart which is easily identified due to the distinctive shape of the myocardium.[194] Skin which is generally not visible in PET images was assigned a very low level of activity.

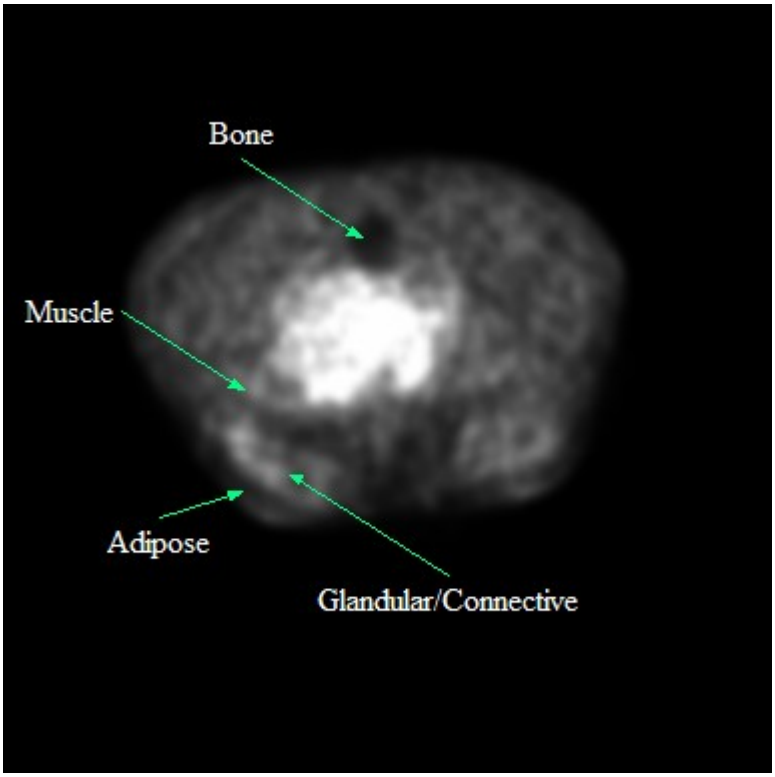

Figure 4.8 Regions selected to provide radiotracer concentrations for breast phantom.

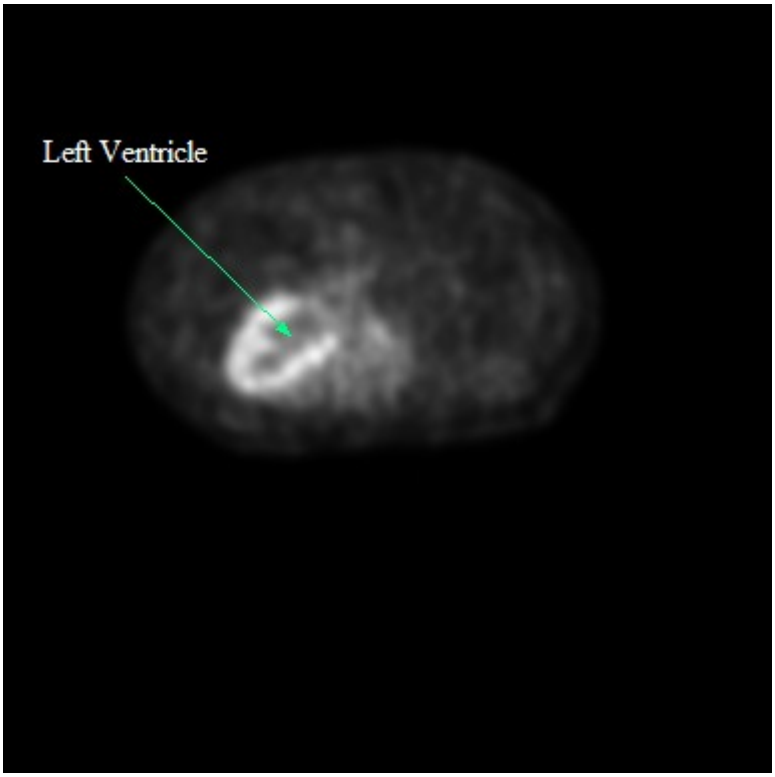

Figure 4.9 Regions selected to provide radiotracer concentrations for breast phantom.

The concentrations were recorded for each of the six volumes of the dynamic series providing concentrations at 9.3, 20.4, 30.8, 41.7, 52.3, and 69.7 minutes after administration of the radiopharmaceutical. The measured values are shown in Table 4-II. These values should be considered approximate and relative. They do not take into account effects like spill over (e.g., between myocardium and left ventricle) due to the low resolution of PET.

Table 4-II Relative radiotracer concentrations (Bq/ml).

Time (minutes)	9.3	20.4	30.8	41.7	52.3	69.7
Adipose	3206	2504	2391	2261	1998	580
Air	0	0	0	0	0	0
Bone	1840	2246	2607	2504	1829	1779
Connective (Cooper's Ligament, Stroma)	8065	9689	9390	9047	6446	6014
Glandular (Ductal, Lobule, Areola)	9050	10408	10424	9807	7214	6616
Left Ventrical (Blood)	19231	13522	12745	11568	10472	8631
Muscle (Petoral)	7011	8324	6388	5407	4958	3895
Skin	360	400	360	320	280	280

As shown in Figure 4.10 the time activity curves follow expected uptake and washout trends.

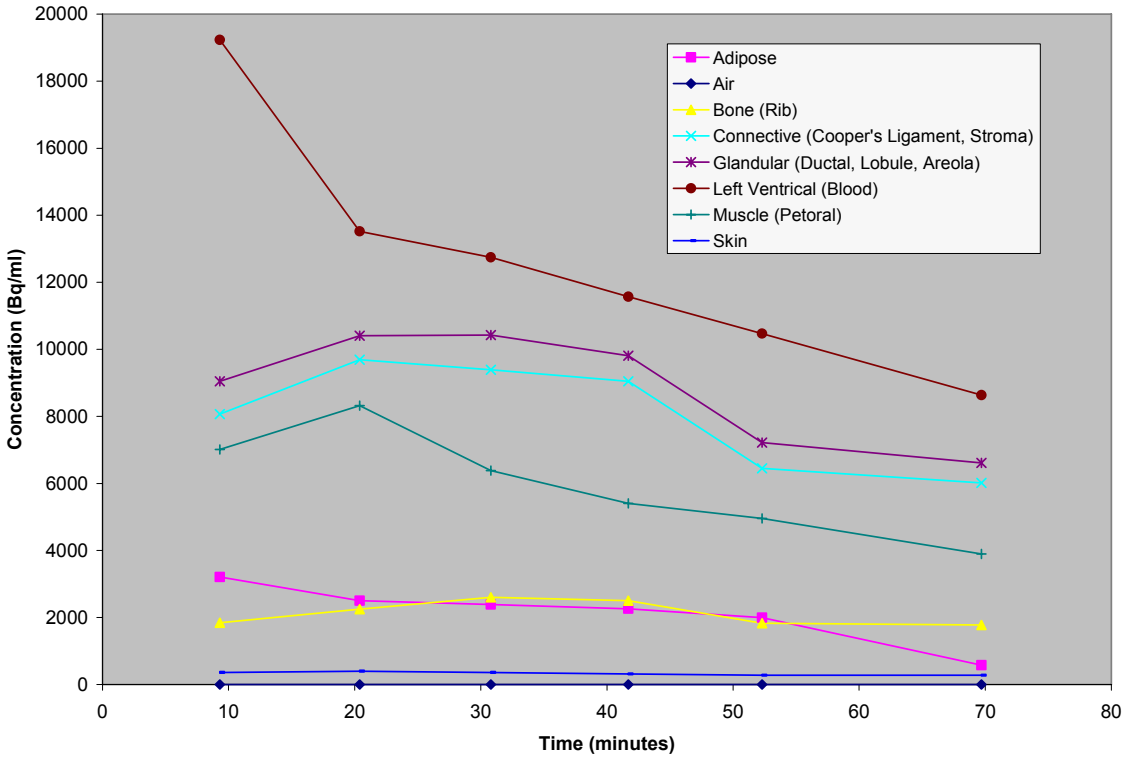

Figure 4.10 Relative time activity curves for breast phantom.

4.2.4.2 Attenuation

The attenuation in SimSET is based upon the linear attenuation coefficient and probability of photoelectric absorption, Compton, and coherent scattering. Known elemental compositions and densities of selected tissues have been used to calculate these values for photons from 5 to 1000 keV from a database of photon interaction behaviors for elements with atomic numbers from 1 to 100.[179]

Attenuation properties were assigned to the phantom by matching them with the tissues already supported in SimSET as shown in Table 4-III. Refer to the SimSET attenuation files for details on the attenuation properties for each tissue type.[180]

Table 4-III Tissue attenuation properties for breast phantom.

Phantom Tissue Type	SimSET Tissue Type
Adipose	Fat
Air	Air
Bone	Bone
Connective (Cooper's Ligament, Stroma)	Connective Tissue
Glandular (Ductal, Lobule, Areola)	Connective Tissue
Left Ventrical (Blood)	Blood
Muscle (Petoral)	Muscle
Skin	Fat

4.3 Simulation Setup

A standard 3D mode system geometry was selected for the simulations. The system consists of a ring of detectors positioned around the object being imaged. End shields are used to reduce the number of random coincidences. This geometry is shown in Figure 4.11.

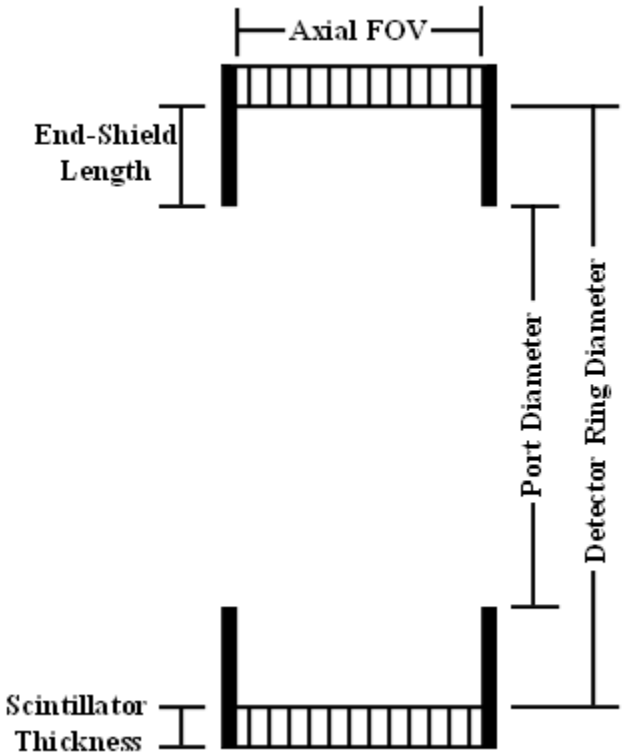

Figure 4.11 Simulated PET system geometry.

The port diameter was set to 70 cm and the axial field of view (FOV) to 60 cm. Modeling of decays and photon tracking within the object and port was modeled using the Photon History Generator. The Collimator Module was used to track the photons from the port to the detector ring. Lead end-shields, 11 cm in length, were used to limit the field of view. No septa were modeled during the simulation as a fully 3D PET system was being modeled.

The Detector Module was used to track the photons from the detector ring inner diameter until energy deposition or photon escape. The detector was a scintillator array consisting of 2.5 cm thick LSO (lutetium oxyorthosilicate) crystals. The Binning Module was used to record the location of energy deposition. 20 bins were used along the axial dimension and 175 along the

transaxial. 256 azimuthal angles spanning 180 degrees were used. This allows reconstruction to an in-plane resolution of 4.29×4.29 mm.

The object to be imaged was placed analogous to a patient positioned prone at the center of the field of view. The phantom was scaled to 14.4 $cm^{3,}$ with a distance of approximately 12.3 cm from apex to chest wall and a width of 12.7 cm at the chest wall.

4.4 Attenuation Correction

Prior to image reconstruction the raw data were attenuation corrected. A transmission scan of the phantom using a rotating gamma ray source was simulated. Since each line of response (LOR) has a finite width, each LOR was sub-sampled into 64 LOR.

For each sub-sample a photon was tracked along the LOR and the encountered attenuation calculated using Equation 4.10, where μ is the linear attenuation coefficient of the LOR, x_i is the distance traveled by the photon through the i^{th} tissue, μ_i is the linear attenuation coefficient for the i^{th} tissue, and i varies through each tissue encountered along the LOR.

$$\mu = \sum_i x_i \mu_i \qquad (4.10)$$

The mean linear attenuation coefficient for each detector pair, $\overline{\mu}$, is then used to scale the signal from that detector pair, correcting for the attenuation that occurred during image acquisition. This is performed according to Equation 4.11, where N is the number of observed coincidence pairs and N_0 is the number of coincidence pairs after attenuation correction.

$$N_0 = Ne^{\bar{\mu}} \tag{4.11}$$

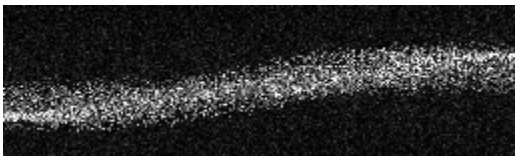

Figure 4.12 Example sinogram before attenuation correction.

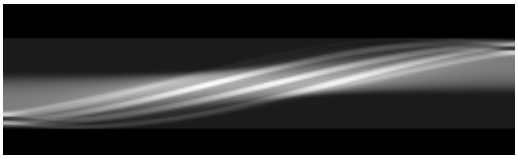

Figure 4.13 Measured scaling due to attenuation, $e^{\bar{\mu}}$, for sinogram shown in Figure 4.12.

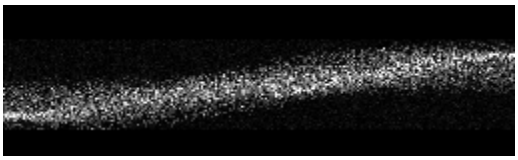

Figure 4.14 Sinogram shown in Figure 4.12 after attenuation correction using sinogram shown in Figure 4.13.

4.5 Reconstruction

Image reconstruction was performed using STIR (Software for Tomographic Image Reconstruction).[195,196] STIR is an open source software package maintained by Kris Thielemans. The 3D reconstruction algorithm 3DRP (Three-Dimensional Reprojection), developed by Kinahan and Rogers, was selected to reconstruct the simulated data.[197,198] This algorithm was selected due to its wide acceptance. In general, it serves as a gold standard and was the first fully 3D reconstruction algorithm supported by clinical scanners.

The algorithm is outlined in Figure 4.15 and described here. During the first step standard two-dimensional filtered back projection is performed using the direct projections to provide an first estimate of the object being imaged. Other

projections that are nearly orthogonal to the scanner axis may be used to improve this initial estimate using rebinning techniques.

A second step is performed in which projections of the initial estimate are taken in order to obtain values for lines of response which had low efficiency or were truncated due to the limited axial field of view of the scanner. These estimated lines of response are then merged with the measured lines of response in step three. This provides a complete set of projections for all detector ring pairs.

The estimated projections provide no additional data, but prepare the projections for filtering, in particular correcting spatial variance. The complete set of projections is then used to perform three-dimensional filtered back projection.

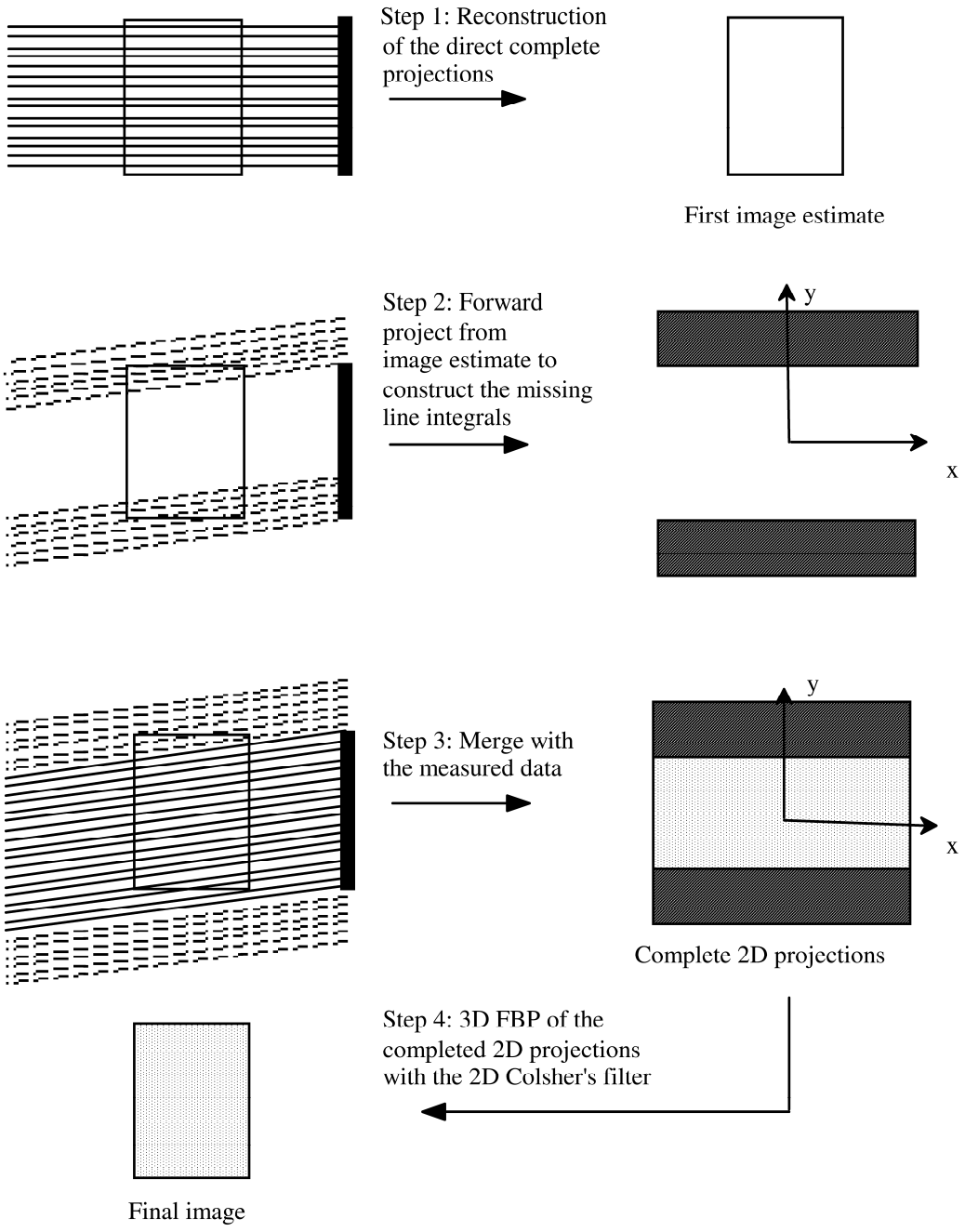

Figure 4.15[Y] 3DRP reconstruction algorithm.

4.6 Simulation Results

The simulation took approximately 82 hours on a SunBlade 1500 (1.503Ghz) workstation. The simulation would have provided comparable results and taken

[Y] Figure from [199], used with permission.

a fraction of the time using the previously mentioned parallel implementation. The parallel implementation was not used since it was under development at the time of this work. Photon histories were recorded corresponding to 2×10^8 decays which provided 1.2×10^8 detected coincidences. Figure 4.16, Figure 4.17, and Figure 4.18 provide images from the simulation.

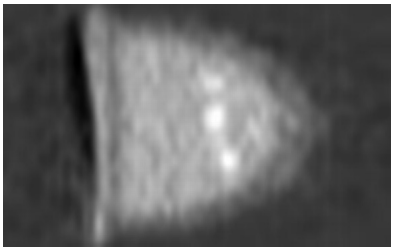

Figure 4.16 Axial view of simulated phantom.

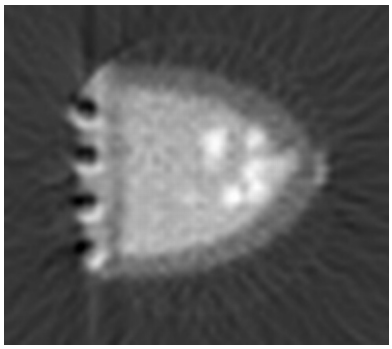

Figure 4.17 Sagital view of simulated phantom.

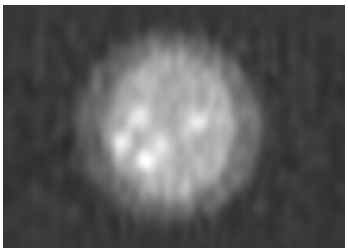

Figure 4.18 Coronal view of simulated phantom.

Desired characteristics are present in the simulated images. These features are identified in Figure 4.19. Specifically: 1) an area of higher activity is visible at the rear of the breast marking the chest wall (due to pectoral muscle), 2) area of lower activity surrounding exterior of breast (due to skin and adipose tissue), 3)

an area of higher activity within the center of the breast (due to connective and glandular tissue), and 4) variation in intensity of the high activity region of the breast due to different tissues (connective vs. glandular).

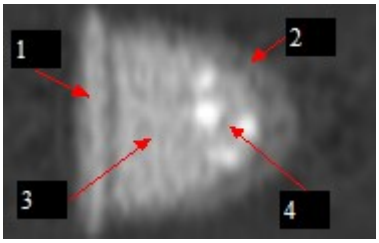

Figure 4.19 Simulated phantom with discussed characteristics labeled.

This proof of concept showed how a geometric phantom could be created and used with the SimSET simulator. The phantom and simulator provide images with a known ground truth. These images can aid in the development of image processing algorithms. For example, segmentation and classification algorithms can be quantitatively evaluated, a task which is difficult on real images. The dynamic properties of the phantom, and the availability of both PET and MRI simulators, provide tools which can support multimodal imaging research.

4.7 Future Directions

There are many directions this work can take. The tissue properties necessary for imaging the breast phantom with the MRI simulator, discussed in Section 4.1, need to be found. Similar phantoms can be created for other areas of anatomy such as the thorax. More realistic phantoms can be created by segmenting images or by medical illustrators.

On the software side, tools for manipulating the phantoms need to be developed, as well as enhancements made to available simulators to increase their utility. For example, support for tissue deformation and flow during image acquisition, such as would occur if imaging the heart.

There is also room for technological advancements such as integration of simulators to provide a single environment for multimodal simulation. In particular, closer integration with other software packages for phantom creation and manipulation or image processing and reconstruction would increase simulator utility. The need for improving simulator efficiency by taking advantage of recent computational advancements such as distributed computing, threading, and short vector architectures exists to ensure the ability to perform realistic simulations.

Chapter 5 Summary of Contributions

This chapter is devoted to providing a brief review of this dissertation, highlighting the contributions.

A novel registration algorithm for intermodal and intramodal breast images was presented. Careful patient positioning is utilized to control the extent of the deformations. The procedure uses a deformable model and a finite element model to distribute displacements at known locations (fiducial skin markers) throughout the entire volume of the breast. The registration was evaluated using a breast phantom and examining registration errors for fiducial markers and artificial lesions. The registration of patient images was evaluated qualitatively and with the use of normalized mutual information. This effort addressed our first aim, providing a method to estimate and correct the tissue deformation that occurring during imaging.

Work on the joint display or fusion of PET and MRI images was presented. This work goes beyond that which is currently presented in the literature. Current techniques are discussed. A technique for automatically evaluating two dimensional color tables was presented and this technique was used along with a genetic optimization algorithm to generate new color tables.

A study was conducted in which radiologists were asked to perform a series of tasks using images presented side-by-side and images fused with a number of pre-selected techniques. This study reinforced the need for joint displays and indicated that the new color tables may be the best choice for joint display of PET and MRI images.

In order to support future research on image fusion a software package was developed for displaying multiple medical data sets simultaneously using a synchronized interface. This software provides interfaces for rapid implementation and evaluation of new fusion techniques, dynamic range techniques, and projection based volumetric displays. In addition to providing a large number of fusion options for medical data sets, this package is perhaps the first available which supports fused projection images. Novel spline based dynamic range techniques designed to address concerns of radiologists are also included as part of this software.

These efforts on image fusion address our second aim. A tool that can be used to implement and develop new fusion techniques was developed, a new fusion operator was presented, and a study was performed evaluating the new fusion operator along with operators proposed by others.

Available medical image simulation packages were investigated and a new format for geometric digital phantoms was presented. This allows a single phantom to be used for simulating images of populations or individuals at different times or in different positions. A breast phantom was designed with the appropriate properties for simulated imaging of the phantom in a PET system. These efforts on image simulation address our third aim. They allow creation of synthetic breast images with a known ground truth and will support future multimodal imaging work.

The importance of developing algorithms, tools, and procedures for multimodal imaging can not be overstated. With the growing use of medical

imaging and the desire to utilize all collected and available information, more effort will be dedicated to optimizing the use of each individual modality and finding ways to use the complementary information provided from multiple sources.

Bibliography

[1] American Cancer Society: "Cancer Facts and Figures 2007." Available at http://www.cancer.org/downloads/STT/CAFF2007PWSecured.pdf. Accessed 19 September 2007.

[2] Bombardieri E, Crippa F: "PET Imaging In Breast Cancer." *The Quarterly Journal of Nuclear Medicine*, 45:245-256, 2001.

[3] Whal WR: "Current Status of PET in Breast Cancer Imaging, Staging, and Therapy." *Seminars in Roentgenology*, 36:250-259, 2001.

[4] Palmedo H, Hensel J, Reinhardt M, Von Mallek D, Matthies A, Biersack HJ: "Breast Cancer Imaging with PET and SPECT Agents: An In Vivo Comparison." *Nuclear Medicine and Biology*, 29(8):809-815, 2002.

[5] Scheidhauer K, Walter C, Seemann MD: "FDG PET and Other Imaging Modalities in the Primary Diagnosis of Suspicious Breast Lesions." *European Journal of Nuclear Medicine and Molecular Imaging*, 31(supplement 1):S70-S79, 2004.

[6] Heiba SI, Bernik S, Raphael B, Sandella N, Cholewinski W, Klein P: "The Distinctive Role of Positron Emission Tomography/Computed Tomography in Breast Carcinoma with Brown Adipose Tissue 2-Flouro-2-Deoxy-D-Glucose Uptake." *The Breast Journal*, 11(6):457-461, 2005.

[7] Benard F, Turcotte E: "Imaging in Breast Cancer: Single-Photon Computed Tomography and Positron-Emission Tomography." *Breast Cancer Research*, 7:153-162, 2005.

[8] Eliat PA, Dedieu V, Bertino C, Boute V, Lacroix J, Constans JM, de Korvin B, Vincent C, Bailly C, Joffre F, de Certaines J, Vincensini D." *Magnetic Resonance Imaging*, 22(4):475-481, 2004.

[9] Gibbs P, Liney GP, Lowry M, Kneeshaw PJ, Turnball LW: "Differentiation of Benign and Malignant Sub-1 cm Breast Lesions Using Dynamic Contrast Enhanced MRI, *Breast*, 13(2):115-121, 2004.

[10] Kvistad KA, Rydland J, Vainio J, Smethurst HB, Lundgren S, Fjosne HE, Haraldseth O: "Breast Lesions: Evaluation with Dynamic Contrast-Enhanced T1-Weighted MR Imaging and with T2*-Weighted First-Pass Perfusion MR Imaging." *Radiology*, 216:545-553, 2000.

[11] Schnall MD, "Application of Magnetic Resonance Imaging to Early Detection of Breast Cancer." Breast Cancer Research, 3:17-21, 2001.

[12] Lehman CD, Schnall MD: "Imaging in Breast Cancer: Magnetic Resonance Imaging." *Breast Cancer Research*, 7:215-219, 2005.

[13] Hathaway PB, Mankoff DA, Maravilla KR, Austin-Seymour MM, Ellis GK, Gralow JR, Cortese AA, Hayes CE, Moe RE: "Value of Combined FDG PET and MR Imaging in the Evaluation of Suspected Recurrent Local-Regional Breast Cancer: Preliminary Experience." *Radiology*, 210:807-814, 1999.

[14] Chen X, Moore MO, Lehman CD, Mankoff DA, Lawton TJ, Peacock S, Schubert EK, Livingston RB: "Combined Use of MRI and PET to Monitor Response and Assess Residual Disease for Locally Advanced Breast Cancer Treated With Neoadjuvant Chemotherapy." *Academic Radiology*, 11:1115-1124, 2004.

[15] Shapiro S, Venet W, Venet L, Strax P, Roeser R: "Ten to Fourteen Year Effect of Screening on Breast Cancer Mortality." *Journal of the National Cancer Institute*, 69(2):349-355, 1982.

[16] Tabar L, Fagerberg G, Gad A, Baldetorp L, Holmberg L, Grontoft O, Ljungquist, Lundstrom B, Manson J, Eklund G: "Reduction in Mortality from Breast Cancer After Mass Screening with

Mammography: Randomized Trial from the Breast Cancer Screening Working Group of the Swedish National Board of Health and Welfare." *The Lancet*, 345:829-832, 1995.

[17] Tabar L, Fagerberg G, Chen H, Duffy SW, Smart CR, Gad A, Smith RA: "Efficacy of Breast Cancer Screening by Age. New Results from the Swedish Two-County Trial." *Cancer*, 75(10):2507-2517,1995.

[18] Bloomstone M, D'Angelo P, Galliano D, Butler J, Jr, Dean R, Rosemurgy AS: "One Hundred Consecutive Advanced Breast Biopsy Instrumentation Procedures: Complications, Costs, and Outcome." *Annals of Surgical Oncology*, 6:195-199, 1999.

[19] Burkhardt JH, Sunshine JH: "Core-Needle and Surgical Breast Biopsy: Comparison of Three Methods of Assessing Cost." *Radiology*, 212:181-188, 1999.

[20] Philpotes LE, Hooley RJ, Lee CH, "Comparison of Automated Versus Vacuum-Assisted Biopsy Methods for Sonographically Guided Core Biopsy of the Breast." *American Journal of Roentgenology*, 180:347-351, 2002.

[21] Howard B: "Brave New Breast Tests: How Techniques Make Disease Detection Easier and Keep You Safer Than Ever." New Woman, 28, Oct. 1999.

[22] Oncology Channel: "Breast Biopsy." Available at http://www.oncologychannel.com/breastcancer/breastbiopsy/index.shtml. Accessed 19 September 2007.

[23] National Cancer Institute: "Breast Cancer (Screening and Early Detection)." Available at http://cra.nci.nih.gov/3_types_cancer/breast_screening.htm.orig. Accessed 6 April 2005.

[24] National Cancer Institute: "Planes of the Body." Available at http://training.seer.cancer.gov/module_anatomy/unit1_3_terminology2_planes.html. Accessed 9 January 2008.

[25] Cherry SR, Sorenson JA, Phelps ME: *Physics in Nuclear Medicine*, third edition. Philadelphia: Saunders, 2003.

[26] Sprawls P, Jr.: *Physical Principles of Medical Imaging*, second edition. Gaithersburg, MD: Aspen Publishers, Inc., 1993.

[27] Farr RF, Allisy-Roberts PJ: *Physics for Medical Imaging*. Bridgend, Mid Glamorgan: Saunders, 1997.

[28] Bushberg JT, Seibert JA, Leidholdt EM, Jr., Boone JM: *The Essential Physics of Medical Imaging*. Baltimory, MD: Williams & Wilkins, 1994.

[29] Kak AV, Slaney M: *Principles of Computerized Tomographic Imaging*. New York, NY: IEEE Press, 1988.

[30] Badawi R: "Introduction to PET Physics." Available at http://depts.washington.edu/nucmed/IRL/pet_intro/. Accessed 29 November 2007.

[31] Hornak JP: The Basics of MRI. Available at http://www.cis.rit.edu/htbooks/mri/. Accessed 29 November 2007.

[32] Lynch T: "Imaging." *Oncology News*, 1(1):22-25, 2006.

[33] Ciscel A: "Image:Head CT scan.jpg.". Available at http://en.wikipedia.org/wiki/Computed_tomography. Accessed 7 January 2008.

[34] Interactive Learning Software, Henrietta, NY: "The Basics of MRI." Available at http://www.cis.rit.edu/htbooks/mri/. Accessed 7 January 2008.

[35] Lynch PJ: “Image:Breast anatomy normal scheme.png.” Available at http://commons.wikimedia.org/wiki/Image:Breast_anatomy_normal_scheme.png. Accessed 7 January 2008.

[36] National Institutes of Health: “Anatomy of the Breast.” Available at http://mammary.nih.gov/reviews/development/Human-breast001/index.html. Accessed 7 January 2008.

[37] Zimmerman BT: *Understanding Breast Cancer Genetics*. Jackson, MS: University Press of Mississippi, 2004.

[38] Agur AMR, Lee MJ: *Grant’s Atlas of Anatomy*, ninth edition. Baltimore, MD: Williams & Wilkins, 1991.

[39] Leonard RJ: *Human Gross Anatomy*. New York, NY: Oxford University Press, 1995.

[40] Beth Israel Health Care System: “Anatomy of the Breast.” Available at http://mammary.nih.gov/reviews/development/Human-breast001/index.html. Accessed 30 November 2007. New York, NY.

[41] Newimage.com – Online Cosmetic Plastic Surgery Network: “Anatomy of the Female Breast.” Available at http://www.breastimplants4you.com/breast_anatomy.htm. Accessed 30 November 2007.

[42] Maintz JBA, Viergever MA: “An Overview of Medical Image Registration.” Imaging Science Department, Imaging Center Utrecht, 1996.

[43] Maurer CR Jr., Fitzpatrick JM: “A Review of Medical Image Registration.” In *Interactive Image-Guided Neurosurgery*, Editor Maciunas RJ. Park Ridge, IL: American Association of Neurological Surgeons (AANS), 17-44, 1993.

[44] Somer EJ, Marsden PK, Benatar NA, Goodey J, O’Doherty MJ, Smith MA: “PET-MR Image Fusion in Soft Tissue Sarcoma: Accuracy, Reliability and Practicality of Interactive Point-Based and Automated Mutual Information Techniques.” *European Journal of Nuclear Medicine and Molecular Imaging*, 30:54-62, 2003.

[45] Sailer SL, Rosenman JG, Soltys M, Cullip TJ, Chen J: “Improving Treatment Planning Accuracy Through Multimodality Imaging.” *International Journal of Radiation Oncology*, 35:117-124, 1996.

[46] Gall KP, Verhey LJ: “Computer-Assisted Positioning of Radiotherapy Patients Using Implanted Radioopaque Fiducials.” *Medical Physics*, 20(4):1152-1159, 1993.

[47] Ellis RE, Toksvig-Larsen S, Marcacci M, Caramella D, Fadda M, “Use of a Biocompatible Fiducial Marker in Evaluating the Accuracy of CT Image Registration , *Investigative Radiology*, 31(10):658-667, 1996.

[48] Maurer CR, McCrory JJ, Fitzpatrick JM: “Estimation of Accuracy in Localizing Externally Attached Markers in Multimodal Volume Head Images.” *Proceedings of SPIE Medical Imaging*, 1898:43-54, 1993.

[49] Fright RW, Linney AD: “Registration of 3-D Head Surfaces using Multiple Landmarks. *IEEE Transactions on Medical Imaging*,12(3):515-520, 1993.

[50] Mandava VR, Fitzpatrick JM, Maurer CR Jr., Maciunas RJ, Allen GS: “Registration of Multimodal Volume Head Images via Attached Markers.” *Proceedings of SPIE Medical Imaging*, 1652:271-282,1992.

[51] Hill DLG, Hawkes DJ, Crossman JE, Gleeson MJ, Cox TCS, Bracey ECML, Strong, AJ, Graves P: “Registration of MR and CT Images for Skull Base Surgery using Point-like Anatomical Features.” *British Journal of Radiology*, 64(767):1030-1035, 1991.

[52] Pelizzari CA, Chen GTY, Spelbring DR, Weichselbaum RR, Chen CT: “Accurate Three-Dimensional Registration of CT, PET, and/or MRI Images of the Brain.” *Journal of Computer Assisted Tomography*, 13:20-26, 1989.

[53] Chua CS, Jarvis R: “3D Free-Form Surface Registration and Object Recognition.” *International Journal of Computer Vision*, 17:77-99, 1996.

[54] Moshfeghi M: “Elastic Matching of Multimodality Medical Images, *CVGIP: Graphical Models and Image Processing*, 53:271-282, 1991.

[55] Junck L, Moen JG, Hutchins GD, Brown MB, Kuhl DE: “Correlation Methods for the Centering, Rotation, and Alignment of Functional Brain Images.” *Journal of Nuclear Medicine*, 31:1220-1276, 1990.

[56] Maes F, Collignon A, Vandermeulen D, Marchal G, Suetens P: “Multimodality Image Registration by Maximization of Mutual Information.” *IEEE Transactions on Medical Imaging*, 16(2):187-198, 1997.

[57] Hoh CK, Dahlbom M, Harris G, Choi Y, Hawkins RA, Phelps ME, Maddahi J: Automated Iterative Three-Dimensional Registration of Positron Emission Tomography Images.” *Journal of Nuclear Medicine*, 34:2009-2018, 1993.

[58] Viola P, Wells WM III: “Alignment by Maximization of Mutual Information.” *Proceedings of the Fifth IEEE International Conference on Computer Vision*, 16-23, 1995.

[59] van den Elsen PA, Pol EJD, Sumanaweera TS, Hemler PF, Napel S, Adler JR, “Grey Value Correlation Techniques Used for Automatic Matching of CT and MR Brain and Spine Images. *Proceedings of the SPIE Visualization in Biomedical Computing*, 2359:227-237, 1994.

[60] Clarke RH, Horsley V: “On a Method of Investigating the Deep Ganglia and Tracts of the Central Nervous System (Cerebellum).” *British Medical Journal*, 2:1799-1800, 1906.

[61] Horsley V, Clarke RH: “The Structure and Function of the Cerebellum Examined by a New Method.” *Brain*, 31:45-124, 1908.

[62] Lunsford LD: “Modern Stereotactic Neurosurgery.” Martinus Mijhoff, Boston, MA, 1988.

[63] Hajnal JV, Hill DLG, Hawkes DJ: *Medical Image Registration*. Boca Raton, FL: CRC Press, 2001.

[64] Maintz JBA, Viergever MA: “A Survey of Medical Image Registration.” *Medical Image Analysis*, 2(1):1-37, 1998.

[65] Hill DLG, Batchelor PG, Holden MH, Hawkes DJ: “Medical Image Registration.” *Physics in Medicine and Biology*, 46(1):R1-R45, 2001.

[66] Richard FJP, Bakic PR, Maidment ADA: “Mammogram Registration: A Phantom-Based Evaluation of Compressed Breast Thickness Variation Effects.” *IEEE Transactions on Medical Imaging*, 25(2):188-197, 2006.

[67] Van Engeland S, Snoeren P, Hendriks J, Karssemeijer N: “A Comparison of Methods for Mammogram Registration.” *IEEE Transactions on Medical Imaging*, 22(11):1436-1444, 2003.

[68] Marias K, Behrenbruch C, Parbhoo S, Seifalian A, Brady M: “A Registration Framework for the Comparison of Mammogram Sequences.” *IEEE Transactions on Medical Imaging*, 24(6):782-790, 2005.

[69] Vujovic N, Brzakovic D: “Establishing the Correspondence Between Control Points in Pairs of Mammographic Images.” *IEEE Transactions on Image Processing*, 6(10):1388-1399, 1997.

[70] Moskalik A, Carson PL, Mayer CR, Fowlkes JP, Rubin J, Roubidoux M: “Registration of Three-Dimensional Compound Ultrasound Scans of the Breast for Refraction and Motion Correction.” *Ultrasound in Medicine and Biology*, 21(6):769-778, 1995.

[71] Xiao G, Noble JA, Burcher M, English R, Michael B: “Nonrigid Registration of 3-D Free Hand Ultrasound Images of the Breast.” *IEEE Transactions on Medical Imaging*, 21(4):405-412, 2002.

[72] Meyer CR, Boes L, Kim B, Bland PH, Lecarpentier GL, Fowlkes JB, Roubidoux MA, Carson PL: “Semiautomatic Registration of Volumetric Ultrasound Scans.” *Ultrasound in Medicine and Biology*, 25(3):339-347, 1999.

[73] Krucker JF, LeCarpentier GL, Fowlkes JB, Carson PL: “Rapid Elastic Image Registration for 3-D Ultrasound.” *IEEE Transactions on Medical Imaging*, 21(11):1384-1394, 2002.

[74] Rueckert D, Sonoda LI, Hayes C, Hill DLG, Leach MO, Hawkes DJ: “Nonrigid Registration Using Free-Form Deformations: Application to Breast MR Images.” *IEEE Transactions on Medical Imaging*, 18(8):712-721, 1999.

[75] Rohlfing T, Maurer CR Jr., Bluemke DA, Jacobs MA: “Volume-Preserving Nonrigid Registration of MR Breast Images Using Free-Form Deformation With an Incompressibility Constraint.” *IEEE Transaction on Medical Imaging*, 22(6):730-741, 2003.

[76] Hill A, Mehnert A, Crozier S, Leung C, Wilson S, McMahon K, Kennedy D: “Dynamic Breast MRI: Image Registration and its Impact on Enhancement Curve Estimation.” *Proceedings of the 28th IEEE Engineering in Medicine and Biology Society Annual International Conference, EMBS’06*, 3049-3052, 2006.

[77] Hayton PM, Brady M, Smith SM, Moore N: “Non-rigid Registration Algorithm for Dynamic Breast MR Images.” *Artificial Intelligence*, 114(1-2):125-156, 1999.

[78] Kumar R, Asmuth JC, Hanna K, Bergen J, Hulka C, Kopans DB, Weisskoff R, Moore R: “Application of 3D Registration for Detecting Lesions in Magnetic Resonance Breast Scans.” *Proceedings SPIE Medical Imaging*, 2710:646-656, 1996.

[79] Zuo CS, Jiang A, Buff BL, Mahon TG, Wong TZ: “Automatic Motion Correction for Breast MR Imaging.” *Radiology*, 198:903-906, 1996.

[80] Ruiter NV, Rainer S, Muller TO, Gemmeke H, Reichenbach JR, Kaiser WA: “Model-Based Registration of X-Ray Mammograms and MR Images of the Female Breast.” *IEEE Transactions on Nuclear Science*, 53(1):204-211, 2006.

[81] Zhang Y, Qiu Y, Goldgof DB, Sarkar S, Li H: “3D Finite Element Model of Nonrigid Breast Deformation for Feature Registration in –ray and MR Images.” *Proceedings IEEE Workshop on Applications of Computer Vision, WACV’07*, 4118767, 2007.

[82] Azar FS, Metaxas DN, Schnall MD: “A Deformable Finite Element Model of the Breast for Predicting Mechanical Deformations Under External Perturbations.” *Academic Radiology*, 8:965-975, 2001.

[83] Azar FS, Metaxas DN, Schnall MD: “Methods for Modeling and Predicting Mechanical Deformations of the Breast Under External Perturbations.” *Medical Image Analysis*, 6:1-27, 2002.

[84] Samani A, Bishop J, Yaffe MJ, Plewes DB: “Biomechanical 3-D Finite Element Modeling of the Human Breast Using MRI Data.” *IEEE Transactions on Medical Imaging*, 20(4):271-279, 2001.

[85] Samani A, Bishop J, Plewes DB: “A Constrained Modulus Reconstruction Technique for Breast Cancer Assessment.” *IEEE Transactions on Medical Imaging*, 20(9):877-885, 2001.

[86] Schnabel JA, Tanner C, Castellano-Smith AD, Degenhard A, Leach MO, Hose DR, Hill DLG, Hawkes DJ: “Validation of Nonrigid Image Registration Using Finite-Element Methods: Application to Breast MR Images.” *IEEE Transactions on Medical Imaging*, 22(2):238-247, 2003.

[87] Tanner C, Degenhard A, Schnabel JA, Castellano-Smith A, Hayes C, Sonoda LI, Leach MO, Hose DR, Hill DLG, Hawkes DJ: "A Method for the Comparison of Biomechanical Breast Models." *Proceedings of the IEEE Workshop on Mathematical Methods in Biomedical Image Analysis MMBIA'2001*, 11-18, 2001.

[88] Tanner C, Degenhard A, Schnabel JA, Castellano-Smith A, Hayes C, Sonoda LI, Leach MO, Hose DR, Hill DLG, Hawkes DJ: "Comparison of Biomechanical Breast Models: A Case Study." *Proceedings of SPIE Medical Imaging*, 4684:1807-1818, 2002.

[89] Baines CJ: "Menstrual Cycle Variation in Mammographic Breast Density: So Who Cares?" *Journal of the National Cancer Institute*, 90(12):875-879, 1998.

[90] Wellman PS: *Tactile Imaging*. Ph.D. Thesis, Harvard University, 1999.

[91] Krouskop TA, Wheeler TM, Kallel F, Garra BS, Hall T: "Elastic Moduli of Breast and Prostate Tissues Under Compression." *Ultrasonic Imaging*, 20:260-274, 1998.

[92] Skovoroda AR, Dawson KA, Gusakyan DA, Mayevskii YI, Yermilova VD, Oranskaya GA, Sarvazyan AP: "Quantitative Analysis of the Mechanical Characteristics of Pathologically Changed Soft Biological Tissues." *Biophysics*, 40:1359-1364, 1995.

[93] Lawrence AJ, Rossman PJ, Mahowald JL, Manduca A, Hartmann LC, Ehman RL: "Assessment of Breast Cancer by Magnetic Resonance Elastography." *Proceedings of the Seventh Scientific Meeting of the International Society for Magnetic Resonance in Medicine*, 525, 1999.

[94] Alexandrov O: "Image:Finite element triangulation.svg." Available at http://en.wikipedia.org/wiki/Finite_element_method. Accessed 29 August 2007.

[95] Lengyel E: *Mathematics for 3D Game Programming & Computer Graphics*, second edition. Hingham, MA: Charles River Media, Inc., 2004.

[96] Hughes TJR: *The Finite Element Method: Linear Static and Dynamic Finite Element Analysis*. Mineola, NY: Dover Publications, Inc., 2000.

[97] Akin JE: *Finite Element Analysis for Undergraduates*. Orlando, FL: Academic Press, Inc., 1986.

[98] Pepper DW, Heinrich JC: *The Finite Element Method Basic Concepts and Applications*. Hemisphere Publishing Corporation, 1992.

[99] Reddy JN: *An Introduction to the Finite Element Method*, second edition. New York, NY: McGraw-Hill, Inc., 1993.

[100] Buchanan GR: *Theory and Problems of Finite Element Analysis*. New York, NY: McGraw-Hill, 1995.

[101] Khraishi T: "Introduction to the Finite Element Method (FEM)." Available at http://www.me.unm.edu/~khraishi/ME360_SPRING2005/FEM_intro_Ch1_rev032905.pdf. Accessed 8 March 2006.

[102] Zienkiewicz OC: *The Finite Element Method*, third edition. London, UK: McGraw-Hill Book Compnay Limited, 1977.

[103] Sears FW, Zemansky MW, Young HD: *University Physics*, fifth edition. Reading, MA: Addison-Wesley Publishing Company, 1976.

[104] Halliday D, Resnick R: *Fundamentals of Physics*, revised printing. New York, NY: John Wiley & Sons, Inc., 1974.

[105] University of Phymouth: "Heat Transfer." Available at http://www.tech.plym.ac.uk/sme/THER204B-web/Heatran1.PDF. Accessed 18 September 2007.

[106] University of Phymouth: “2-D Steady State Heat Conduction.” Available at http://www.tech.plym.ac.uk/sme/THER204B-web/Heatran2.PDF. Accessed 18 September 2007.

[107] Jazzard P: “Physical Basis of Spatial Distortion in MRI.” In *Handbook of Medical Imaging*, Editor Bankman IN, San Diego, CA: Academic Press, 2000.

[108] Dahlbom M, Huang C: “Physical and Biological Bases of Spatial Distortion in PET.” In *Handbook of Medical Imaging*, Editor Bankman IN, San Diego, CA: Academic Press, 2000.

[109] Elden HR: Biophysical Properties of Skin. New York, NY: Wiley-Interscience, 1977.

[110] ANSYS, Inc.: “ANSYS” software. Homepage: www.ansys.com, Canonsburg, PA.

[111] SIMULIA brand of Dassault Systemes: “Abaqus” software. Homepage: www.simulia.com, Providence, RI.

[112] “Medical Dictionary Online.” Available at http://www.online-medical-dictionary.org/. Accessed 11 October 2007.

[113] GE Healthcare: “PET/CT – A Premier Whole Body PET Imaging System.” Available at http://www.gehealthcare.com/usen/fun_img/pet/products/nxi.html. Accessed 7 January 2008.

[114] GE Healthcare: “PET/CT – Discovery ST.” Available at http://www.gehealthcare.com/usen/fun_img/pet/products/stover.html. Accessed 7 January 2008.

[115] Hudson HM, Larkin RS: “Accelerated Image Reconstruction using Ordered Subsets of Projection Data.” *IEEE Transactions on Medical Imaging*, 13(4):601-609, 1994.

[116] National Electrical Manufacturers Association: *Digital Imaging and Communications in Medicine (DICOM)*. Rosslyn, VA: National Electrical Manufacturers Association, 2007.

[117] Hill FS Jr: *Computer Graphics Using Open GL*, second edition. Upper Saddle River, NJ: Prentice Hall, 2001.

[118] Gonzalez RC, Woods RE: *Digital Image Processing*, second edition. Upper Saddle River, NJ: Prentice Hall, 2002.

[119] Boudier T: “Developing a Deformation Model for Complex-Shaped Contours.” *Innovation et Technologie en Biologie et Medecine*, 18(1), 1997.

[120] Thevenaz P, Unser M: “The Snakuscule.” *Proceedings of IEEE International Conference on Image Processing*, 1633-1636, 2006.

[121] Baum KG: “Level Set Methods: What are they and what can they be used for?” Internal publication, available on request, 2004.

[122] Boudier T: “Snake” ImageJ plugin. Available at http://imagejdocu.tudor.lu/Members/tboudier/plonearticle.2006-07-12.1260738650/. Accessed 8 October 2007.

[123] Studholme C, Hill DLG, Hawkes DJ: “An Overlap Invariant Entropy Measure of 3D Medical Image Alignment.” *Pattern Recognition*, 32:71-86, 1999.

[124] Shannon CE: “A Mathematical Theory of Communication.” *Bell System Technical Journal*, 27:379-423, 623-656, 1948.

[125] Figure 70.1 of ANSYS Element Reference, Release 8.0, copyright 2003 SAS IP, http: http://www1.ansys.com/customer/content/documentation/80/ansys/Hlp_E_SOLID70.html.

[126] Figure 87.1 of ANSYS Element Reference, Release 8.0, copyright 2003 SAS IP, http: http://www1.ansys.com/customer/content/documentation/80/ansys/Hlp_E_SOLID87.html.

[127] Figure 57.1 of ANSYS Element Reference, Release 8.0, copyright 2003 SAS IP, http: http://www1.ansys.com/customer/content/documentation/80/ansys/Hlp_E_SHELL57.html.

[128] Voehl M: Private Communication. Email, 25 October 2007.

[129] INRIA – Simulog-Technologies: "GHS3D, Tetrahedral Mesh Generator." Le Chesnay Cedex, France.

[130] ANSYS, Inc.: *ANSYS Command Reference, Release 8.0.* Canonsburg, PA: ANSYS, Inc..

[131] INRIA: "GHS3D" software. Homepage: http://www.inria.fr/, Le Chesnay Cedex, France.

[132] Distene: "GHS3D" software. Homepage: http://www.distene.com/en/, Bruyères-le-Chatel, France.

[133] Wikipedia: "Delaunay Triangulation." Available at http://en.wikipedia.org/wiki/Delaunay_triangulation. Accessed 7 January 2008.

[134] Delaunay B: "Sur la sphère vide." *Otdelenie Matematicheskikh i Estestvennykh Nauk*, **7**:793-800, 1934.

[135] Krik R: "ImageJ Source Code for Histogram Equalization." Available at http://rsb.info.nih.gov/ij/index.html. Accessed 7 January 2008.

[136] National Institutes of Health: "ImageJ" software. Homepage: http://rsb.info.nih.gov/ij/index.html, National Institutes of Health, USA.

[137] Townsend DW, Hall NC, Baker DW: "State of the Art in PET/CT." *Imaging Economics*, September 2004.

[138] Rehm K, Strother SC, Anderson JR, Schaper KA, Rottenberg DA, "Display of Merged Multimodality Brain Images using Interleaved Pixels with Independent Color Scales," *Journal of Nuclear Medicine*, 35:1815-1821, 1994.

[139] Wikipedia: "Ebbinghaus Illusion." Available at http://en.wikipedia.org/wiki/Ebbinghaus_illusion. Accessed 15 November 2007.

[140] Wikipedia: "Hering Illusion." Available at http://en.wikipedia.org/wiki/Hering_illusion. Accessed 15 November 2007.

[141] Porter T, Duff T: "Compositing Digital Images." *Proceedings of SIGGRAPH, 11th Annual Conference on Computer Graphics and Interactive Technologies*, 18:253-259, 1984.

[142] Spetsieris PG, Dhawan V, Ishikawa T, Eidelberg D: "Interactive Visualization of Coregistered Tomographic Images." *Biomedical Visualization Conference*, Atlanta, GA, 1995.

[143] Russ JC: *The Image Processing Handbook*, fourth edition. Boca Raton, FL: CRC Press, 2002.

[144] Agoston AT, Daniel BL, Herfkens RJ, Ikeda DM, Birdwell RL, Heiss SG, Sawyer-Glover AM: 'Intensity-Modulated Parametric Mapping for Simultaneous Display of Rapid Dynamic and High-Spatial-Resolution Breast MR Imaging Data." *Radiographics*, 21:217-226, 2001.

[145] Sammi MK, Felder CA, Fowler JS, Lee JH, Levy AV, Li X, Logan J, Palyka I, Rooney WD, Volkow ND, Wany GJ, Springer CS Jr: "Intimate Combination of Low- and High-Resolution Image Data: I. Real-Space PET and H2O MRI, PETAMRI," *Magnetic Resonance in Medicine*, 42:345-360, 1999.

[146] Lee JS, Kim B, Chee Y, Kwark C, Lee MC, Park KS: "Fusion of Coregistered Cross-Modality Images Using a Temporally Alternating Display Method," *Medical and Biological Engineering and Computing*, 38:127-132, 2000.

[147] Rogowitz BE, Treinish LA: "Data Visualization: The End of the Rainbow." *IEEE Spectrum*, 35:52-59, 1998.

[148] Ware C: "Color Sequences for Univariate Maps: Theory, Experiments, and Principles." *IEEE Computer Graphics and Applications*, 8:41-49, 1988.

[149] Montag ED: "The Use of Color in Multidimensional Graphical Information Display." *Proceedings of IS&T/SID's Seventh Color Imaging Conference*, Scottsdale, 222-226, 1999.

[150] Granger EM: "Is CIE L*a*b* Good Enough for Desktop Publishing?" Technical report, Light Source Inc., 1994

[151] Riemersma T: "Colour Metric." Technical report, ITB CompuPhase, 2006.

[152] CompuPhase: "PaletteMaker" software. Homepage: www.compuphase.com, Canonsburg, PA.

[153] Trumbo BE: "Theory for Coloring Bivariate Statistical Maps." *The American Statistician*, 35(4):220-226, 1981.

[154] Tedford WH Jr., Berquist SL, Flynn WE: "The Size-Color Illusion." *The Journal of General Psychology*, 97, 1997.

[155] Rheingans P: "Task-based Color Scale Design." *SPIE Applied Image and Pattern Recognition*, 35-43, 1999.

[156] The MathWorks, Inc.: "MATLAB" software version 6.5.0. Homepage: http://www.mathworks.com/, Natick, Massachusetts.

[157] Zhang H, Montag ED: "Perceptual Color Scales for Univariate and Biavariate Data Display." *30th International Congress of Imaging Science*, Rochester, NY, 2006.

[158] Microsoft Corporation: "Technology Overview." Available at http://msdn2.microsoft.com/en-us/netframework/aa497336.aspx. Accessed 7 January 2008.

[159] Drolon H: "FreeImage" software. Homepage: http://freeimage.sourceforge.net/.

[160] Drolon H: *FreeImage Documentation, Library Version 3.9.2*. Oct. 29, 2006.

[161] Fayad LM, Jin Y, Laine AF, Berkmen YM, Pearson GD, Freedman B, Van Heertum R: "Chest CT Window Settings with Multiscale Adaptive Histogram Equalization: Pilot Study." *Radiology*, 223(3):845-852, 2002.

[162] Jin Y, Fayad LM, Laine AF: "Contrast Enhancement by Multi-scale Adaptive Histogram Equalization." *Proceedings of SPIE Conference on Wavelets: Applications in Signal and Image Processing*, 4478:206-213, 2000.

[163] Barnes JE: "Characteristics and Control of Contrast in CT." *Radiographics*, 12:825-837, 1992.

[164] Braun GJ, Fairchild MD: "Image Lightness Rescaling Using Sigmoidal Contrast Enhancement Functions." *Journal of Electronic Imaging*, 8:380-393, 1999.

[165] Wikipedia: "Normal Distribution." Available at http://en.wikipedia.org/wiki/Normal_distribution. Accessed 27 November 2007.

[166] Sharp J, Jagger J: *Microsoft Visual C# .NET Step by Step*. Redmond, WA: Microsoft Press, 2002.

[167] Beutel J, Kundel HL, Van Metter RL, eds: *Handbook of Medical Image Volume 1: Physics and Psychophysics*. Bellingham, WA: SPIE Press, 2000.

[168] Wikipedia: "Opponent Process." Available at http://en.wikipedia.org/wiki/Opponent_process#_note-2. Accessed 7 January 2008.

[169] Kaiser P: The Joy of Visual Perception. Available at http://www.yorku.ca/eye/. Accessed Nov, 19, 2007.

[170] Murray MA: "Our Sense of Sight: Part 3. Color Vision." Available at http://faculty.washington.edu/chudler/eyecol.html. Accessed 7 January 2008.

[171] Mayo Clinic, "Analyze" software. Homepage: http://www.analyzedirect.com/, Overland Park, KS.

[172] Wikipedia: "HSL Color Space." Available at http://en.wikipedia.org/wiki/HSV_color_space. Accessed Jan. 6, 2008.

[173] ITT: "IDL" software. Homepage: http://www.ittvis.com/idl/, Boulder, CO.

[174] Rafferty K, Baum KG, Schmidt E, Krol A, Helguera M: "Multimodal Display Techniques with Application to Breast Imaging." *RIT Digital Media Library*, http://hdl.handle.net/1850/4648, 2007.

[175] Lewellen TK, Anson CP, Haynor DR, Harrison RL, Bice AN, Schubert SF, Miyaoka RS, Gillispie SB, Zhu J: "Design of a Simulation System for Emission Tomographs." *Journal of Nuclear Medicine*, 29:871, 1988.

[176] Haynor DR, Harrison RL, Lewellen TK, Bice AN, Anson CP, Gillispie SB, Miyaoka RS, Pollard KR, Zhu JB: "Improving the Efficiency of Emission Tomography Simulations using Variance Reduction Techniques." *IEEE Transactions on Nuclear Science*, 37(2):749-753, 1990.

[177] Haynor DR, Harrison RL, Lewellen TK: "The Use of Importance Sampling Techniques to Improve the Efficiency of Photon Tracking in Emission Tomography." *Medical Physics*, 18(5):990-1001, 1991.

[178] Harrison RL, Vannoy SD, Haynor DR, Gillispie SB, Kaplan MS, Lewellen TK: "Preliminary Experience with the Photon History Generator Module of a Public-Domain Simulation System for Emission Tomography." *IEEE Nuclear Science Symposium Conference Record*, 1154-1158, 1993.

[179] Kaplan MS, Harrison RL, Vannoy SD: "Coherent Scatter Implementation for SimSET." *IEEE Transactions on Nuclear Science*, 45(6):3064-3068, 1998.

[180] University of Washington: "SimSET Home Page." Available at http://depts.washington.edu/simset/html/simset_main.html. Accessed 28 June 2007.

[181] University of Washington: "SimSET User Guide." Available at http://depts.washington.edu/simset/html/user_guide/user_guide_index.html. Accessed 28 June 2007.

[182] Thain D, Tannenbaum T, Livny M: "Distributed Computing in Practice: The Condor Experience." *Concurrency and Computation: Practice and Experience*, 17(2-4):323-356, 2005.

[183] University of Wisconsin-Madison: "Condor Project Homepage." Available at http://www.cs.wisc.edu/condor/. Accessed 28 May 2007.

[184] Benoit-Cattin H, Bellet F, Montagnat J, Odet C: "Magnetic Resonance Imaging (MRI) Simulation on a Grid Computing Architecture." *Proceedings of the 3rd IEEE International Symposium on Cluster Computing and the Grid*, 582-587, 2003.

[185] Benoit-Cattin H, Collewet G, Belaroussi B, Saint-Jalmes H, Odet C: "The SIMRI project: a versatile and interactive MRI simulator." *Journal of Magnetic Resonance,* 173:97-115, 2005.

[186] Benoit-Cattin H, Belaroussi B, Bellet F, Odet C: "SIMRI: A Versatile and Interactive 3D MIR Simulation." Availbable at http://www-creatis.insa-lyon.fr/menu/ivolumique/segmentation/simri-hbc/index-us.html Accessed 28 June 2007.

[187] chUmbaLum sOft: “MilkShape 3D” software. Homepage: http://chumbalum.swissquake.ch/index.html, Zurich, Switzerland.

[188] Autodesk: “3ds Max” software. Homepage: http://usa.autodesk.com, Rafael, California.

[189] Autodesk: “AutoCAD” software. Homepage: http://usa.autodesk.com, Rafael, California.

[190] Microsoft: “Direct X” software. Homepage: http://www.microsoft.com, Redmond, WA.

[191] NewTek, Inc.: “Lightwave 3D” software. Homepage: http://www.newtek.com/, San Antonio, TX.

[192] Sutherland IE, Hodgman GW: “Reentrant Polygon Clipping.” *Communications of the ACM*, 17(1):32-42, 1974.

[193] Ghosh S: “On a Fundamental Physical Principle Underlying the Point Location Algorithm in Computer Graphics.” IEEE Transactions on Education, 42(3):200-204, 1999.

[194] Lin KP, Huang SC, Choi Y, Brunken RC, Schelbert HR, Phelps ME: “Correction of Spillover Radioactivities for Estimation of the Blood Time-Activity Curve from the Imaged LV Chamber in Cardiac Dynamic FDG PET Studies.” *Physics in Medicine and Biology*, 40:629-642, 1995.

[195] Thielemans K: “STIR Software for Topographic Image Reconstruction Homepage.” Available at http://stir.sourceforge.net/main.htm. Accessed 7 January 2008.

[196] Thielemans K, Sauge D, Labbe C, Morel C, Jacobson M, Zverovich A: *STIR User’s Guide Version 1.4*. Available at http://stir.sourceforge.net/documentation/STIR-UsersGuide.pdf. Accessed 7 January 2008.

[197] Rogers JG, Harrop R, Kinahan PE: “The Theory of Three-Dimensional Image Reconstruction for PET.” *IEEE Transactions on Medical Imaging*, MI-6(3):239-243, 1987.

[198] Kinahan PE, Rogers JG: “Analytic 3D Image Reconstruction Using All Detected Events.” *IEEE Transactions on Nuclear Science*, 36(1):964-968, 1989.

[199] Labbe C, Zaidi H, Morel C, Thielemans K: “Description of the STIR Implementation of FBP 3DRP.” Available at http://stir.sourceforge.net/documentation/STIR-FBP3DRP.pdf. Accessed 7 January 2008.

The End

Appendix A Stiffness Matrix for Heat Conduction

The derivation found in this section is based upon work found in [1]. The direct approach used to derive the stiffness matrix in our one-dimensional example quickly becomes infeasible as the dimensionality and complexity of the finite elements increases. Use of other advanced techniques, such as the calculus of variations, becomes necessary to find the appropriate relationship of the form shown in Equation 2.10.

The functional associated with heat conduction, with an absence of internal heat generation, is shown as A.1.

$$J(T) = \int_V \left(\frac{1}{2} k \left(\frac{dT}{dx} \right)^2 \right) dV \qquad \text{(A.1)}$$

We will first show that this functional gives us the governing equation, Equation 2.2. For simplicity we will consider a 1D case with a cross-sectional area A and length L. This allows us to rewrite Equation A.1.

$$J(T) = \int_0^L \left(\frac{1}{2} k \left(\frac{dT}{dx} \right)^2 A \right) dx \qquad \text{(A.2)}$$

We find the solution to our problem by minimizing the functional with respect to the unknown function $T(x)$. We will use the variation operator, $\delta(.)$, to simplify notation. We minimize the functional by finding the $T(x)$ which gives us a variation of zero.

$$\delta J(T) = \int_0^L \left(\frac{1}{2} k \delta \left(\left(\frac{dT}{dx} \right)^2 \right) A \right) dx = 0 \qquad \text{(A.3)}$$

We can rewrite the equation by taking advantage of the fact that differentiation and variation can be interchanged.

$$0 = \int_0^L \left(\frac{1}{2} k 2 \frac{dT}{dx} \frac{d\delta T}{dx} A \right) dx = \int_0^L \left(kA \frac{dT}{dx} \frac{d\delta T}{dx} \right) dx \qquad \text{(A.4)}$$

The equation can further be reduced by integration by parts.

$$0 = kA \frac{dT(L)}{dx} \delta T(L) - kA \frac{dT(0)}{dx} \delta T(0) - kA \int_0^L \left(\frac{d^2 T}{dx^2} \delta T \right) dx \qquad \text{(A.5)}$$

In order for the first two terms to equal zero we need $\left[dT(L)/dx = 0 \text{ OR } \delta T(L) = 0 \right] \text{AND} \left[dT(0)/dx = 0 \text{ OR } \delta T(0) = 0 \right]$ to hold, identifies the required boundary conditions for the problem. The fundamental lemma of calculus of variations states that if $\int_a^b M(x) h(x) dx = 0$ for all $h(x)$ with continuous second partial derivatives, then $M(x) = 0$ on the interval from a to b. Since, δT is arbitrary, $\frac{d^2 T}{dx^2} = 0$ in order for the third term to equal zero. This gives us our governing equation 2.2.

We will now derive the stiffness matrix for the two-dimensional triangle element, Equation 2.22, from the associated functional. The two dimensional functional can be found by rewriting Equation A.1.

$$J(T) = \int_V \left(\frac{k_x}{2} \left(\frac{dT}{dx} \right)^2 + \frac{k_y}{2} \left(\frac{dT}{dy} \right)^2 \right) dV \qquad \text{(A.6)}$$

Here k_x, and k_y represent the thermal conductivity along the x and y direction within the triangle. The triangle element will have a constant thickness,

t, allowing us to re-write the integral in terms of the triangular face of the element.

$$J(T) = \int_A \left(\frac{k_x}{2} \left(\frac{dT}{dx} \right)^2 + \frac{k_y}{2} \left(\frac{dT}{dy} \right)^2 \right) t dx dy \qquad \text{(A.7)}$$

The interpolation function defining the temperature distribution within an element was given by Equation 2.20. Using the interpolation function and one-dimensional partial derivative operators, we can write Equation A.7 in matrix form as Equation A.8.

$$J(T) = \int_A \left(\frac{k_x}{2} \left(\left[\frac{\partial}{\partial x} \right] [N][T] \right)^2 + \frac{k_y}{2} \left(\left[\frac{\partial}{\partial y} \right] [N][T] \right)^2 \right) t dx dy \qquad \text{(A.8)}$$

Here $[T]$ is the vector containing the nodal temperatures. We can place the conductivities in a 1×1 matrix and remove the squared terms by using the matrix transpose notation.

$$J(T) = \int_A \left(\frac{1}{2} [T]^T [N]^T \left[\frac{\partial}{\partial x} \right]^T [k_x] \left[\frac{\partial}{\partial x} \right] [N][T] + \frac{1}{2} [T]^T [N]^T \left[\frac{\partial}{\partial y} \right]^T [k_y] \left[\frac{\partial}{\partial y} \right] [N][T] \right) t dx dy \qquad \text{(A.9)}$$

By using the partial derivative operator defined in Equation 2.23 and the conductivity matrix defined in 2.24 we can combine the two terms in the integral.

$$J(T) = \int_A \left(\frac{1}{2} [T]^T [N]^T [L]^T [k][L][N][T] \right) t dx dy \qquad \text{(A.10)}$$

In order to solve Equation A.10 for the unknown temperatures we follow a similar procedure and find the minimum of the functional with respect to the unknown temperatures.

$$0 = \int_A \left([N]^T [L]^T [k][L][N][T] \right) t dx dy \qquad \text{(A.11)}$$

Note that Equation A.11 contains our previously defined stiffness matrix. This allows us to write the equation in the desired form from Equation 2.10.

$$[K] = \int_A [N]^T [L]^T [k][L][N] t\,dx\,dy \tag{A.12}$$

$$[0] = [K][T] \tag{A.13}$$

The steps presented here were independent of the shape functions, and a similar process can be followed to derive the stiffness matrix for other elements.

[1] Buchanan GR: *Theory and Problems of Finite Element Analysis*. New York, NY: McGraw-Hill, 1995.

Appendix B DICOM Headers from Patient Study

The DICOM headers for some of the images used during this work are included below. They have been made anonymous.

B.1 Philips Intera MRI Header

0002,0013 Implementation Version Name: v1.1.3 Windows
0002,0016 Source Application Entity Title: DIGITAL_JACKET
0008,0005 Specific Character Set: ISO_IR 100
0008,0008 Image Type: ORIGINAL\PRIMARY\M_FFE\M\FFE
0008,0060 Modality: MR
0008,0070 Manufacturer: Philips Medical Systems
0008,1090 Manufacturer's Model Name: Gyroscan Intera
0018,0020 Scanning Sequence: GR
0018,0021 Sequence Variant: SP
0018,0022 Scan Options:
0018,0023 MR Acquisition Type: 3D
0018,0050 Slice Thickness: 2.24
0018,0080 Repetition Time: 14
0018,0081 Echo Time: 2.9784
0018,0083 Number of Averages: 1
0018,0084 Imaging Frequency: 63.9002
0018,0085 Imaged Nucleus: 1H
0018,0086 Echo Numbers(s): 1
0018,0087 Magnetic Field Strength: 1.5
0018,0088 Spacing Between Slices: 1.12
0018,0089 Number of Phase Encoding Steps: 320
0018,0091 Echo Train Length: 0
0018,0093 Percent Sampling: 80
0018,0094 Percent Phase Field of View: 100
0018,1020 Software Versions(s): NT 8.1.3\1.3
0018,1030 Protocol Name: HIRES isoAX
0018,1081 Low R-R Value: 0
0018,1082 High R-R Value: 0
0018,1083 Intervals Acquired: 0
0018,1084 Intervals Rejected: 0
0018,1088 Heart Rate: 0
0018,1100 Reconstruction Diameter: 360
0018,1250 Receiving Coil: Breast
0018,1251 Transmitting Coil: B
0018,1312 Phase Encoding Direction: ROW
0018,1314 Flip Angle: 20
0018,5100 Patient Position: HFP
0020,0013 Image Number: 1

0020,0032 Image Position (Patient): -190.884\-128.084\-14.33
0020,0037 Image Orientation (Patient): 1\0\0\0\1\0
0020,0100 Temporal Position Identifier: 1
0020,0105 Number of Temporal Positions: 1
0020,4000 Image Comments:
0028,0002 Samples per Pixel: 1
0028,0004 Photometric Interpretation: MONOCHROME2
0028,0010 Rows: 512
0028,0011 Columns: 512
0028,0030 Pixel Spacing: 0.703125\0.703125
0028,0031 Zoom Factor: 1\1
0028,0032 Zoom Center: 0\0
0028,0034 Pixel Aspect Ratio: 1\1
0028,0100 Bits Allocated: 16
0028,0101 Bits Stored: 12
0028,0102 High Bit: 11
0028,0103 Pixel Representation: 0
0028,1050 Window Center: 551
0028,1051 Window Width: 1101
0028,1052 Rescale Intercept: 0
0028,1053 Rescale Slope: 1.66007
0028,1054 Rescale Type: normalized
0032,4000 Study Comments:
0040,0275 Request Attributes Sequence:
0040,0007 Scheduled Procedure Step Description:
7FE0,0010 Pixel Data: 4762

B.2 GE Advance NXi PET Header

0002,0013 Implementation Version Name: v1.1.3 Windows
0002,0016 Source Application Entity Title: DIGITAL_JACKET
0008,0008 Image Type: ORIGINAL\PRIMARY
0008,0060 Modality: PT
0008,0070 Manufacturer: GEMS
0008,1090 Manufacturer's Model Name: Advance
0018,0050 Slice Thickness: 4.25
0018,0071 Acquisition Termination Condition: TIME
0018,0073 Acquisition Start Condition: MANU
0018,0074 Acquisition Start Condition Data: 0
0018,0075 Acquisition Termination Condition Data: 0
0018,1020 Software Versions(s): 05.10
0018,1063 Frame Time:
0018,1081 Low R-R Value:
0018,1082 High R-R Value:
0018,1083 Intervals Acquired: 0
0018,1084 Intervals Rejected: 0
0018,1100 Reconstruction Diameter: 550

0018,1120 Gantry/Detector Tilt: 0
0018,1147 Field of View Shape: CYLINDRICAL RING
0018,1149 Field of View Dimensions(s): 550\153
0018,1181 Collimator Type: RING
0018,1242 Actual Frame Duration: 180000
0018,5100 Patient Position: HFP
0020,0013 Image Number: 35
0020,0032 Image Position (Patient): 275\275\0
0020,0037 Image Orientation (Patient): -1\0\0\0\-1\-0
0020,1040 Position Reference Indicator: Orbital Meatal Line
0020,1041 Slice Location: 0.00000000000000
0028,0002 Samples per Pixel: 1
0028,0004 Photometric Interpretation: MONOCHROME2
0028,0010 Rows: 128
0028,0011 Columns: 128
0028,0030 Pixel Spacing: 4.296875\4.296875
0028,0051 Corrected Image:
DECY\ATTN\SCAT\DTIM\RAN\RADL\DCAL\SLSENS\NORM\BLANK\NL
OG
0028,0100 Bits Allocated: 16
0028,0101 Bits Stored: 16
0028,0102 High Bit: 15
0028,0103 Pixel Representation: 1
0028,0106 Smallest Image Pixel Value: 0
0028,0107 Largest Image Pixel Value: 32766 0
0028,1050 Window Center: 447.89059448242
0028,1051 Window Width: 895.78118896484
0028,1052 Rescale Intercept: 0
0028,1053 Rescale Slope: 0.000122131
0054,0013 Energy Window Range Sequence:
0054,0016 Radiopharmaceutical Information Sequence:
0018,0031 Radiopharmaceutical: FDG -- fluorodeoxyglucose
0018,1071 Radionuclide Volume: 0
0018,1072 Radionuclide Start Time: 130500.00
0018,1074 Radionuclide Total Dose: 286168736
0018,1075 Radionuclide Half Life: 6588
0018,1076 Radionuclide Positron Fraction: 0.97000002861023
0054,0300 Radionuclide Code Sequence:
0008,0100 Code Value: C-111A1
0008,0102 Coding Scheme Designator: 99SDM
0008,0104 Code Meaning: 18F
0054,0304 Radiopharmaceutical Code Sequence:
0008,0100 Code Value: Y-X1743
0008,0102 Coding Scheme Designator: 99SDM
0008,0104 Code Meaning: FDG -- fluorodeoxyglucose
0054,0081 Number of Slices: 35

0054,0101 Number of Time Slices: 1
0054,0202 Type of Detector Motion: NONE
0054,0410 Patient Orientation Code Sequence:
0054,0414 Patient Gantry Relationship Code Sequence:
0054,1000 Series Type: STATIC\IMAGE
0054,1001 Units: GML
0054,1002 Counts Source: EMISSION
0054,1100 Randoms Correction Method: RTSUB
0054,1102 Decay Correction: START
0054,1103 Reconstruction Method:
0054,1105 Scatter Correction Method: Convolution subtraction
0054,1201 Axial Mash: 3\2
0054,1202 Transverse Mash: 1
0054,1210 Coincidence Window Width: 14
0054,1300 Frame Reference Time: 0
0054,1320 Slice Sensitivity Factor: 2.06845
0054,1321 Decay Factor: 1.0095
0054,1322 Dose Calibration Factor: 359
0054,1330 Image Index: 1
7FE0,0010 Pixel Data: 5332

B.3 GE Discovery ST PET Header

0002,0013 Implementation Version Name: v1.1.3 Windows
0002,0016 Source Application Entity Title: DIGITAL_JACKET
0008,0005 Specific Character Set: ISO_IR 100
0008,0008 Image Type: ORIGINAL\PRIMARY
0008,0060 Modality: PT
0008,0070 Manufacturer: GE MEDICAL SYSTEMS
0008,1090 Manufacturer's Model Name: Discovery ST
0018,0050 Slice Thickness: 3.2699999809265
0018,0071 Acquisition Termination Condition: TIME
0018,0073 Acquisition Start Condition: MANU
0018,0074 Acquisition Start Condition Data: 0
0018,0075 Acquisition Termination Condition Data: 0
0018,1020 Software Versions(s): 26.14
0018,1040 Contrast/Bolus Route:
0018,1083 Intervals Acquired: 0
0018,1084 Intervals Rejected: 0
0018,1100 Reconstruction Diameter: 600
0018,1120 Gantry/Detector Tilt: 0
0018,1130 Table Height: 146.5
0018,1147 Field of View Shape: CYLINDRICAL RING
0018,1149 Field of View Dimensions(s): 700\157
0018,1181 Collimator Type: RING
0018,1242 Actual Frame Duration: 240000
0018,5100 Patient Position: HFP

0020,0013 Image Number: 26
0020,0032 Image Position (Patient): 297.656250000000\297.656250000000\-247.22999572753
0020,0037 Image Orientation (Patient): -1\0\0\0\-1\-0
0020,1040 Position Reference Indicator: Orbital Meatal Line
0020,1041 Slice Location: -247.22999572753
0028,0002 Samples per Pixel: 1
0028,0004 Photometric Interpretation: MONOCHROME2
0028,0010 Rows: 128
0028,0011 Columns: 128
0028,0030 Pixel Spacing: 4.6875\4.6875
0028,0051 Corrected Image: DECY\ATTN\SCAT\DTIM\RAN\RADL\DCAL\SLSENS\NORM
0028,0100 Bits Allocated: 16
0028,0101 Bits Stored: 16
0028,0102 High Bit: 15
0028,0103 Pixel Representation: 1
0028,0106 Smallest Image Pixel Value: 0
0028,0107 Largest Image Pixel Value: 32767
0028,1052 Rescale Intercept: 0
0028,1053 Rescale Slope: 0.223644
0054,0013 Energy Window Range Sequence:
0054,0014 Energy Window Lower Limit: 000000000000375
0054,0015 Energy Window Upper Limit: 000000000000650
0054,0016 Radiopharmaceutical Information Sequence:
0018,0031 Radiopharmaceutical: FDG -- fluorodeoxyglucose
0018,1071 Radionuclide Volume: 0
0018,1072 Radionuclide Start Time: 125700.00
0018,1074 Radionuclide Total Dose: 441096192
0018,1075 Radionuclide Half Life: 6588
0018,1076 Radionuclide Positron Fraction: 0.97000002861023
0054,0300 Radionuclide Code Sequence:
0008,0100 Code Value: C-111A1
0008,0102 Coding Scheme Designator: 99SDM
0008,0104 Code Meaning: 18F
0054,0304 Radiopharmaceutical Code Sequence:
0008,0100 Code Value: Y-X1743
0008,0102 Coding Scheme Designator: 99SDM
0008,0104 Code Meaning: FDG -- fluorodeoxyglucose
0054,0081 Number of Slices: 91
0054,0101 Number of Time Slices: 2
0054,0202 Type of Detector Motion: NONE
0054,0410 Patient Orientation Code Sequence:
0008,0100 Code Value: F-10450
0008,0102 Coding Scheme Designator: 99SDM
0008,0104 Code Meaning: recumbent

0054,0412 Patient Orientation Modifier Code Sequence:
0008,0100 Code Value: F-10310
0008,0102 Coding Scheme Designator: 99SDM
0008,0104 Code Meaning: prone
0054,0414 Patient Gantry Relationship Code Sequence:
0008,0100 Code Value: F-10470
0008,0102 Coding Scheme Designator: 99SDM
0008,0104 Code Meaning: headfirst
0054,1000 Series Type: STATIC\IMAGE
0054,1001 Units: BQML
0054,1002 Counts Source: EMISSION
0054,1100 Randoms Correction Method: SING
0054,1101 Attenuation Correction Method: measured,, 0.096000 cm-1,
0054,1102 Decay Correction: START
0054,1103 Reconstruction Method: OSEM
0054,1105 Scatter Correction Method: Convolution subtraction
0054,1201 Axial Mash: 3\2
0054,1202 Transverse Mash: 2
0054,1210 Coincidence Window Width: 0
0054,1220 Secondary Counts Type: DLYD
0054,1300 Frame Reference Time: 243000
0054,1310 Primary (Prompts) Counts Accumulated: 191727
0054,1311 Secondary Counts Accumulated: 0
0054,1320 Slice Sensitivity Factor: 0.777493
0054,1321 Decay Factor: 1.0389
0054,1322 Dose Calibration Factor: 159
0054,1323 Scatter Fraction Factor: 0.125335
0054,1330 Image Index: 66
7FE0,0010 Pixel Data: 5744

Appendix C Normalized Mutual Information

This section continues the discussion started in Section 2.5.3.3. This discussion is based on work presented in [1,2]. As we have already discussed one approach to evaluating registration is to search for the transformation that minimizes the joint entropy (Equation 2.39). As we evaluate the registration between two images we can have a variation in the overlap between the two images. This is demonstrated in Figure C.1.

Figure C.1[A] Demonstration on how changes in the registration transformation affect the overlap between the registered images.

If we use joint information to evaluate and choose a transformation we run into problems because the content in the regions of the images used to calculate the joint entropy is changing. In searching for the minimum joint entropy we may end up minimizing the marginal entropy of one or both images.

In an attempt to address this problem it was suggested that mutual information, shown as Equation C.1, be used as the metric.[3] Mutual information contains marginal entropy terms that reflect changes in the overlap. A short experiment however can demonstrate that the placement of the marginal entropies in mutual information does not correctly adjust for the changes in overlap.

[A] Image courtesy of Colin Studhome, Ph.D., Associate Professor, Department of Radiology, University of California, San Francisco. Used with permission.

Figure C.2 shows image M and image N which are to be registered. Both images are of a semicircle. Image M has infinite bounds in the horizontal direction, while image N has a side of variable length, F_{OV}. The experiment will investigate the affect of F_{OV} and the alignment angle (θ) of the two images on the various registration metrics. The images will be registered with the proper translation and so the only registration error will come from the alignment angle. Clearly it is hoped that the registration metrics will be maximized at $\theta = 0$.

$$I(X;Y) = H(X) + H(Y) - H(X,Y) \qquad \text{(C.1)}$$

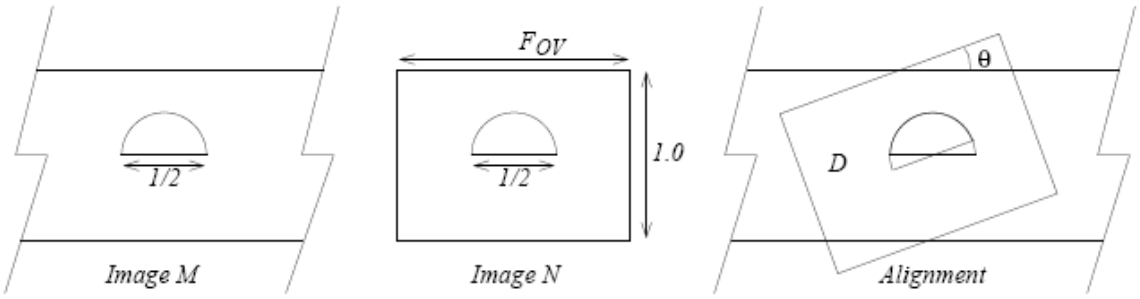

Figure C.2[B] Image M and N to be registered. A simple registration model where the only mis-alignment comes from θ will be used.

The result of applying the negated joint entropy metric to this registration model is shown in Figure C.3. Joint entropy is plotted as a function of θ and F_{OV}. As expected the peak occurs at $\theta = 0$. A downside of joint entropy is that the metric value is related to the F_{OV}, and the peak smoothes out as the F_{OV} increases. This makes joint entropy a difficult metric to use for multi-modal registration where the peak will be further flattened and may be lost due to differences between the modalities.

[B] Image courtesy of Colin Studhome, Ph.D., Associate Professor, Department of Radiology, University of California, San Francisco. Used with permission.

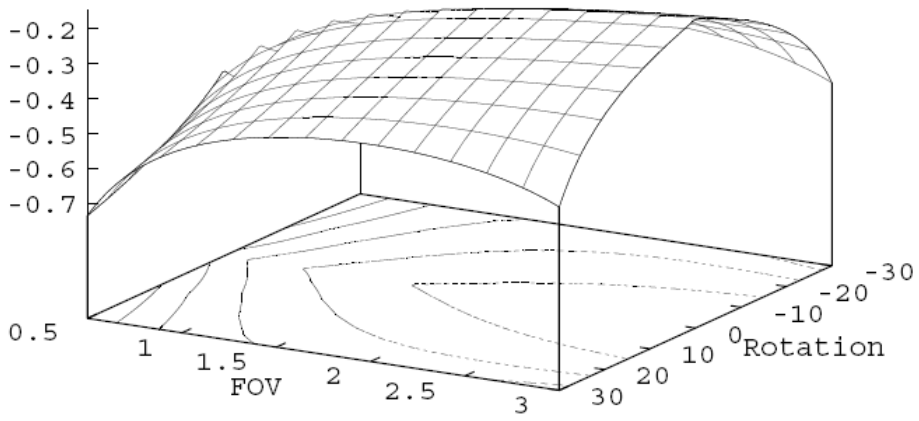

Figure C.3[C] The value of the joint entropy metric for variations in F_{OV} and θ for the registration model shown in Figure C.2.

A similar plot for the mutual information metric is shown as Figure C.4. Again the metric value varies with the F_{OV}. A significant issue occurs as the F_{OV} increases. Eventually the metric response for the correct registration changes from a minimum to a maximum. This is a result of the marginal entropies having a larger effect on the metric than the joint entropy at larger F_{OV}. This issue can render mutual information useless as a measure of registration.

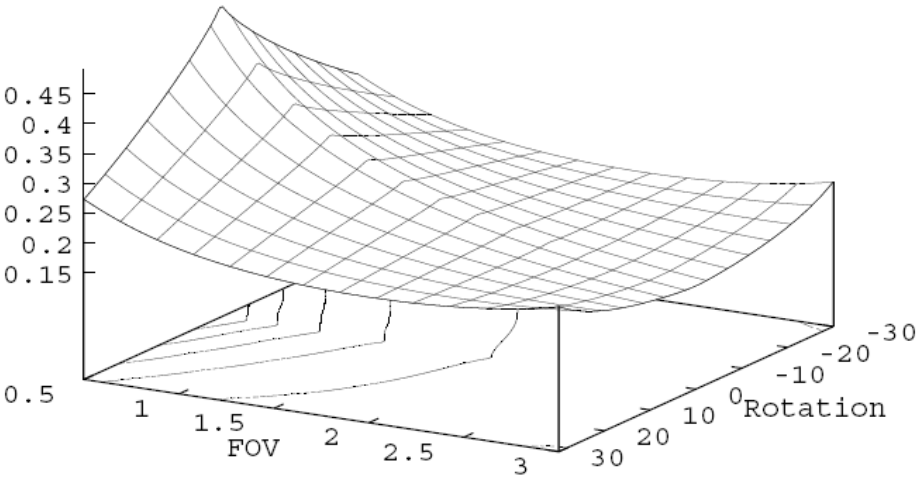

Figure C.4[D] The value of the mutual information metric for variations in F_{OV} and θ for the registration model shown in Figure C.2.

[C] Image courtesy of Colin Studhome, Ph.D., Associate Professor, Department of Radiology, University of California, San Francisco. Used with permission.

A matching plot for normalized mutual information is shown as Figure C.5. The plot demonstrates that normalized information is nearly independent of F_{OV}, and maintains a sharper peak with respect to θ. Normalized mutual information correctly adjusts for the F_{OV} due to the placement of the marginal entropies in Equation 2.40.

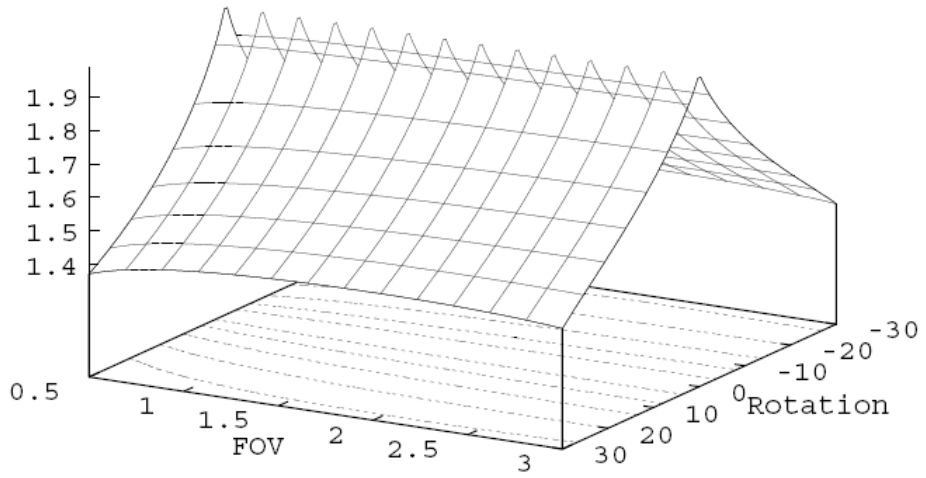

Figure C.5[E] The value of the normalized mutual information metric for variations in F_{OV} and θ for the registration model shown in Figure C.2.

[1] Studholme C, Hill DLG, Hawkes DJ: "An Overlap Invariant Entropy Measure of 3D Medical Image Alignment." *Pattern Recognition*, 32:71-86, 1999.

[2] Studholme C: *Measures of 3D Medical Image Alignment*. Ph.D. Dissertation, London, UK: University of London, 1997.

[3] Viola PA, Wells WM III: "Alignment by Maximization of Mutual Information." *Proceedings of the Fifth International IEEE Conference on Computer Vision*, 15-23, 1995.

[D] Image courtesy of Colin Studhome, Ph.D., Associate Professor, Department of Radiology, University of California, San Francisco. Used with permission.

[E] Image courtesy of Colin Studhome, Ph.D., Associate Professor, Department of Radiology, University of California, San Francisco. Used with permission.

Appendix D Sample ANSYS Script

This appendix contains an example ANSYS script for generating the patient specific breast geometry and propagating the displacements throughout the model in a single direction. The model in this example contains six coronal cross-sections, each defined by six key points.

```
C*** Displacement component is analogous to temperature.  Slices start
at breastbone (Y=0), with the Y-axis normal to the breastbone.
Dimensions are in isotropic voxels based on resolution of MRI.
The program is run three times, once for each direction (X, Y, Z).
Only the data for step 2 needs to be changed between runs.
C*** ------------------------------------------------------
C*** Using Script:
C*** 1. Six key points per cross-section are obtained from breast
geometry visible in the MRI scan.  The cross-sections are parallel to
breast bone.  There must be key points located at fiducial marker
locations.  The K command specifies the key point as "K, key point
number, X coordinate, Y coordinate, Z coordinate."
C*** 2. The differences between the fiducial marker locations in MRI
and PET are entered using the DK command as "DK, key point displacement
occurs at, TEMP, displacement".  The displacement is only provided for
one direction at a time.
C*** 3. Run the script.  Enter the "/POST1" command.  The resulting
displacement field can be found from the ANSYS menu using "List
Results"->"Nodal Solution"->"DOF Solution"
C*** ------------------------------------------------------
/PREP7
C*** ------------------------------------------------------
C*** Define elements
ET,1,SOLID87
ET,2,SHELL57
C*** Thickness of shell elements
R,1,0.0001
C*** Thermal conductivities
MP,KXX,1,1E3
MP,KXX,2,1E-3
C*** ------------------------------------------------------
C*** Define cross-sections
C*** -------------------------
C*** Cross-Section 1
C*** -------------------------
K,1,423,315,98
K,2,413,315,42
K,3,341,315,7
K,4,366,315,87
K,5,371,315,115
K,6,420,315,144
C*** The key points are connected by splines
SPLINE,1,2,3,4
SPLINE,4,5,6,1
```

```
C*** -------------------------
C*** Cross-Section 2
C*** -------------------------
K,7,424,333,87
K,8,410,333,47
K,9,341,333,29
K,10,338,333,87
K,11,354,333,144
K,12,419,333,142
SPLINE,7,8,9,10
SPLINE,10,11,12,7
C*** -------------------------
C*** Create volumes between cross-section 1 & 2
C*** Volume 1 & 2  Cross-sections 1 & 2
V,1,2,3,4,7,8,9,10
V,4,5,6,1,10,11,12,7
C*** -------------------------
C*** Cross-Section 3
C*** -------------------------
K,13,427,367,118
K,14,380,367,45
K,15,298,367,48
K,16,239,367,118
K,17,311,367,165
K,18,376,367,184
SPLINE,13,14,15,16
SPLINE,16,17,18,13
C*** -------------------------
C*** Volume 3 & 4  Cross-sections 2 & 3
V,7,8,9,10,13,14,15,16
V,10,11,12,7,16,17,18,13
C*** -------------------------
C*** Cross-Section 4
C*** -------------------------
K,19,412,400,118
K,20,376,400,53
K,21,300,400,52
K,22,259,400,109
K,23,306,400,173
K,24,372,400,177
SPLINE,19,20,21,22
SPLINE,22,23,24,19
C*** -------------------------
C*** Volume 5 & 6  Cross-sections 3 & 4
V,13,14,15,16,19,20,21,22
V,16,17,18,13,22,23,24,19
C*** -------------------------
C*** Cross-Section 5
C*** -------------------------
K,25,408,404,118
K,26,373,404,57
K,27,299,404,50
K,28,262,404,118
K,29,309,404,168
K,30,345,404,175
SPLINE,25,26,27,28
SPLINE,28,29,30,25
```

```
C*** -------------------------
C*** Volume 7 & 8  Cross-sections 4 & 5
V,19,20,21,22,25,26,27,28
V,22,23,24,19,28,29,30,25
C*** -------------------------
C*** Cross-Section 6
C*** -------------------------
K,31,383,425,118
K,32,347,425,74
K,33,306,425,62
K,34,272,425,118
K,35,315,425,158
K,36,360,425,156
SPLINE,31,32,33,34
SPLINE,34,35,36,31
C*** -------------------------
C*** Volume 9 & 10  Cross-sections 5 & 6
V,25,26,27,28,31,32,33,34
V,28,29,30,25,34,35,36,31
C*** -------------------------
C*** Mesh volumes
SHPP,WARN
TYPE,1
MAT,2
ESIZE,8
VMESH,1,10
C*** Mesh areas (surfaces)
TYPE,2
MAT,1
REAL,1
SHPP,WARN
C*** Volumes 1 & 2 (bottom)
AMESH,6
AMESH,11
C*** VOLUMES 9 & 10 (top)
AMESH,43
AMESH,47
C*** VOLUMES 1 & 2 (side)
AMESH,2
AMESH,3
AMESH,4
AMESH,8
AMESH,9
AMESH,10
C*** VOLUMES 3 & 4 (side)
AMESH,12
AMESH,13
AMESH,14
AMESH,17
AMESH,18
AMESH,19
C*** VOLUMES 5 & 6 (side)
AMESH,21
AMESH,22
AMESH,23
AMESH,26
AMESH,27
```

```
AMESH,28
C*** VOLUMES 7 & 8 (side)
AMESH,30
AMESH,31
AMESH,32
AMESH,35
AMESH,36
AMESH,37
C*** VOLUMES 9 & 10 (side)
AMESH,39
AMESH,40
AMESH,41
AMESH,44
AMESH,45
AMESH,46
C*** -------------------------
C*** Couple together nodes at seams
CPINTF,TEMP,0.001
C*** -------------------------
C*** Fiducial marker loads (displacements)
C*** -------------------------
DK,1,TEMP,-2
DK,9,TEMP,3
DK,22,TEMP,-5
DK,30,TEMP,-6
DK,32,TEMP,-3
C*** -------------------------
/SOLU
SOLVE
FINISH
```

For models containing a larger number of key points (ex. 24) per cross-section, definitions of volumes can be simplified by adding key points along the y-axis of the breast. Area meshing can also be simplified by using “ASEL,S,EXT” command to select all the areas on the exterior of the volume and “AMEAH,ALL” to mesh those areas.

Appendix E Genetic Algorithm Code

The following MATLAB,[156] Version 6.5.0, code files implement the genetic algorithm discussed in Section 3.4.

E.1 script.m

script.m is the main script that accomplishes the task of generating the color tables.

```
% variables
    % number of genes in each generation
    numberOfGenes=100;
    % number of genes to take from the current generation into
          the next generation
    numberToReproduce=30;
    % number of points on one side of the generated LUT, generated
          LUT will be NxN
    N=50;
    % number of generations to run algorithm for
    numberOfIterations = 150000;

% initialize algorithm
    % create genes, each row is a gene
    gene=rand(numberOfGenes,12)*2-1;
    % generation loop counter
    iterationNumber=0;
    % stores the magnitude of the change in the gene coefficients
          of the 'best' gene
    change=0;
    % best gene from last generation
    lastBestGene=[0,0,0,0,0,0,0,0,0,0,0,0];

% run algorithm
    while (iterationNumber<numberOfIterations)
        % evaluate genes
            fitness=geneFitness(gene,N);
            [a,I]=sort(fitness);
            lut = showLUT(gene(I(numberOfGenes),:),N);
            figure(1);
            image(lut);
            bestGene=gene(I(numberOfGenes),:);
            drawnow;
        % track statistics
            iterationNumber=iterationNumber+1
            change(iterationNumber) =
                sum(abs(gene(I(numberOfGenes),:)-lastBestGene),2)
            lastBestGene=gene(I(numberOfGenes),:);
        % reproduce
            gene = nextGeneration(gene, fitness, numberToReproduce);
    end % end while
```

E.2 geneFitness.m

geneFitness.m contains the functions responsible for finding the fitness factors for a set of genes. The geneFitness fuction calculates the fitness factors of a set of genes. The evaluate2 function and its helper, evaluate, calculate the fitness values (the measurements that are combined to form the fitness factors) for a single gene. The colorDifference function calculates the perceived closeness of two colors.[151,152]

```
function fitness=geneFitness(genes,N)
    % genes = set of genes, each row is a single gene
    % N = number of points on one side of the generated LUT, each
          gene will be evaluated as if it represented an NxN LUT

    % get fitness values used to calculate the fitness score for
          each gene
    for i=1:size(genes,1)
        % avg = average difference between neighboring points in the
              color table (vertical and horizontal only)
        % var = the variance of the previously described differences
        % diffaxis = the difference between the mean values on the
              two source axis through the resulting color table
        % diffaxis1 = difference between the first and last value on
              the source 1 axis
        % diffaxis2 = difference between the first and last value on
              the source 2 axis
        % calculate fitness values for each gene
        [avg(i), var(i), diffaxis(i), diffaxis1(i), diffaxis2(i),
            diffcorn(i)] = evaluate2(genes(i,:),N);
    end % end for

    % normalize fitness values
        avg=avg(:)/mean(avg(:));
        var=var(:)/mean(var(:));
        diffaxis=diffaxis(:)/mean(diffaxis(:));
        diffaxis1=diffaxis1(:)/mean(diffaxis1(:));
        diffaxis2=diffaxis2(:)/mean(diffaxis2(:));
        diffcorn=diffcorn(:)/mean(diffcorn(:));

    % cap features to keep from dominating result
        if find(avg>2)
            temp=avg>=2;
            avg=avg.*(avg<2)+2*temp;
        end
        if find(var>2)
            temp=var>=2;
            var=var.*(var<2)+2*temp;
        end
        if find(diffaxis>2)
```

```
            temp=diffaxis>=2;
            diffaxis=diffaxis.*(diffaxis<2)+2*temp;
        end
        if find(diffaxis1>2)
            temp=diffaxis1>=2;
            diffaxis1=diffaxis1.*(diffaxis1<2)+2*temp;
        end
        if find(diffaxis2>2)
            temp=diffaxis2>=2;
            diffaxis2=diffaxis2.*(diffaxis2<2)+2*temp;
        end
        if find(diffcorn>2)
            temp=diffcorn>=2;
            diffcorn=diffcorn.*(diffcorn<2)+2*temp;
        end

    % create fitness factors from fitness values
        fitness = .25*avg - var + diffaxis + .25*diffaxis1
            + .25*diffaxis2 + .25*diffcorn;

    % shift the fitness factors so they are always positive
        if (min(fitness(:)) < 0)
            fitness=fitness+abs(min(fitness(:)));
        end

%----------------------------------------%
function [avg, var, diffaxis, diffaxis1, diffaxis2,
diffcorn]=evaluate2(gene,N)
    % gene = a single gene
    % N = number of points on one side of the generated LUT, each
          gene will be evaluated as if it represented an NxN LUT
    [avg, var, diffaxis, diffaxis1, diffaxis2, diffcorn] =
        evaluate(gene(1), gene(2), gene(3), gene(4), gene(5),
        gene(6), gene(7), gene(8), gene(9), gene(10), gene(11),
        gene(12), N);

%----------------------------------------%
function [avg, var, diffaxis, diffaxis1, diffaxis2, diffcorn] =
evaluate(r1, g1, b1, r2, g2, b2, R1, G1, B1, R2, G2, B2, N)
    % N = number of points on one side of the generated LUT, each
          gene will be evaluated as if it represented an NxN LUT
    % all other parameters represent the values defining the gene

    % create color table corresponding to gene
        [s1,s2] = meshgrid(linspace(0,1,N), linspace(0,1,N));
        [R,G,B] = colorMix(r1, g1, b1, r2, g2, b2, R1, G1, B1, R2,
            G2, B2, s1, s2);

    % prepare neighboring pairs of colors
        RDown=R(2:N,1:N);
        RUp=R(1:N-1,1:N);
        GDown=G(2:N,1:N);
        GUp=G(1:N-1,1:N);
        BDown=B(2:N,1:N);
        BUp=B(1:N-1,1:N);
        RLeft=R(1:N,2:N);
        RRight=R(1:N,1:N-1);
```

```
        GLeft=G(1:N,2:N);
        GRight=G(1:N,1:N-1);
        BLeft=B(1:N,2:N);
        BRight=B(1:N,1:N-1);

    % get color differences
        vert=colorDifference(RDown, GDown, BDown, RUp, GUp, BUp);
        horz=colorDifference(RLeft, GLeft, BLeft, RRight, GRight,
            BRight);

    % calculate fitness values
        avg=mean([vert(:);horz(:)]);
        var=cov([vert(:);horz(:)]);
        % Note, averaging the colors (done below next 6 lines) to
              calculate a single color corresponding to one side,
              does not follow our color difference model.  We really
              want the average calculated using our distance model.
              This has only a minor effect on diffaxis.
        source1R=mean(R(1,1:N));
        source1G=mean(G(1,1:N));
        source1B=mean(B(1,1:N));
        source2R=mean(transpose(R(1:N,1)));
        source2G=mean(transpose(G(1:N,1)));
        source2B=mean(transpose(B(1:N,1)));
        diffaxis = colorDifference(source1R, source1G, source1B,
            source1R, source2G, source2B);
        diffaxis1 = colorDifference(R(1,1), G(1,1), B(1,1), R(1,N),
            G(1,N), B(1,N));
        diffaxis2 = colorDifference(R(1,1), G(1,1), B(1,1), R(N,1),
            G(N,1), B(N,1));
        diffcorn = colorDifference(R(1,1), G(1,1), B(1,1), R(N,N),
            G(N,N), B(N,N));

%----------------------------------------%
function distance=colorDifference(r1,g1,b1,r2,g2,b2)
    % uses metric designed by Thiadmer Riemersma
    % r1, g1, b1, r2, g2, b2 range from 0 to 1 and represent the
          red, green, and blue of the two colors

    % scale appropriately for use in below equations
        r1=r1*255;
        g1=g1*255;
        b1=b1*255;
        r2=r2*255;
        g2=g2*255;
        b2=b2*255;

    % calculate color difference
        rmean = (r1+r2)./2;
        rdel = r1-r2;
        gdel = g1-g2;
        bdel = b1-b2;
        distance = sqrt( (2+rmean./256).*rdel.*rdel
            + 4.*gdel.*gdel+(2+(255-rmean)./256).*bdel.*bdel );
```

E.3 nextGeneration.m

nextGeneration.m contains the code for taking the current generation of genes and using their fitness factors to create the next generation.

```
function newGenes = nextGeneration(genes, fitness,
numberToReproduce);
    % genes = current genes
    % fitness = fitness factors of current genes
    % numberToReproduce = the number of genes in this generation
          that will move onto the next generation

    % number of genes to have in the next generation (same as this
          one)
    numberToMake=size(genes,1);
    % the size of each gene
    geneLength=size(genes,2);

    % select genes to use for reproduction
        usedJ=0;

        % always use 'best'
            [a,I]=sort(fitness);
            newGenes(1,:)=genes(I(numberToMake),:);
            usedJ(1)=I(numberToMake);

        % select other genes
        % lessen the domination of the 'best'
        fitness=log10(fitness+1);
        % change fitness to a distribution
            fitness=fitness/sum(fitness);
            fitness=cumsum(fitness);

        % create genes by replication
            i=2;
            while i<=numberToReproduce
                next=rand(1);
                j=1;
                while fitness(j)<=next
                    j=j+1;
                end % end while
                if find(usedJ==j)
                else
                    usedJ(i)=j;
                    newGenes(i,:)=genes(j,:);
                    i=i+1;
                end % end if else
            end % end while

        % generate remainder of new genes
            while i<=numberToMake
                if rand(1)<0.3
                    % we have decided to create by splicing
                    % decide where to split
                    where = round(rand(1) * (geneLength-1));
```

```
                % select sources
                    which=0;
                    j=1;
                    while size(which,2)<2
                        next = round(rand(1)
                            * numberToReproduce);
                        if find(which==next)
                        elseif next==0
                        else
                            which(j)=next;
                            j=j+1;
                        end % end if
                    end % end while
                % splice
                    newGenes(i,:) = linspace(0, 0, geneLength);
                    newGenes(i,1:where) = newGenes(which(1),
                        1:where);
                    newGenes(i, where+1:geneLength) =
                        newGenes(which(2), where+1:geneLength);
            else
                % we have decided to create by mutation
                % select source
                    next=0;
                    while (next==0)
                        next=round(rand(1) * numberToReproduce);
                    end % end while
                % mutate it
                    range=[linspace(-1, -1, geneLength);
                        linspace(1, 1, geneLength)];
                % mutreal is part of GEATbx: Genetic and
                      Evolutionary Algorithm Toolbox for use
                      with MATLAB version 3.70 by Hartmut
                      Pohlheim available at
                      http://www.geatbx.com/ver_3_7/index.html,
                      accessed 11/10/2007
                    newGenes(i,:) = mutreal(newGenes(next,:),
                        range, [2/12, 1, 16]);%[2/12,.2,16]
            end % end if else
            i=i+1;
        end % end while
```

E.4 colorMix.m

colorMix.m uses the parameters of the extended color mixing model and two sources images, and creates a fused image.

```
function [R,G,B]=colorMix(r1,g1,b1,r2,g2,b2,R1,G1,B1,R2,G2,B2,s1,s2)
    % s1 and s2 are the sources and the rest of the parameters
          define the color mixing procedure
    R=r1+R1*s1+r2+R2*s2;
    G=g1+G1*s1+g2+G2*s2;
    B=b1+B1*s1+b2+B2*s2;
    if find(R<0) % set negative R values to 0
        R=R.*(R>0);
    end
```

```
if find(R>1) % cap R vales at 1
    temp=R>=1;
    R=R.*(R<1)+temp;
end
if find(G<0) % set negative G values to 0
    G=G.*(G>0);
end
if find(G>1) % cap G values at 1
    temp=G>=1;
    G=G.*(G<1)+temp;
end
if find(B<0) % set negative B values to 0
    B=B.*(B>0);
end
if find(B>1) % cap B values at 1
    temp=B>=1;
    B=B.*(B<1)+temp;
end
```

E.5 showLut.m

showLUT.m is used to display the color table corresponding to a gene.

```
function image=showLUT(gene,N)
    % gene = gene to use when creating color table
    % N = size of color table
    [s1,s2]=meshgrid(linspace(0,1,N),linspace(0,1,N));
    [R,G,B] = colorMix(gene(1), gene(2), gene(3), gene(4), gene(5),
        gene(6), gene(7), gene(8), gene(9), gene(10),
        gene(11),gene(12), s1, s2);
    image = cat(3,R,G,B);
```

Appendix F Visualization Study Instructions

The following instructions were provided to those administering and participating in the visualization study. Section F.1 contains instructions provided to those administering the examination. They discuss setting up the software and dealing with the generated data (study results). Section F.2 contains instructions for study participants, providing an introduction to fusion and explanation of the testing procedures. Section F.3 contains a supplement to the instructions that was to be provided when the participant was going to be tested with the interlace technique.

F.1 Administration Instructions

Using the Fuze software

- Follow the set up instructions below (in the next section of this document) to create configuration files for each test subject.
- Before a subject's first test, have them thoroughly read a copy of the "Test Procedure.pdf" document included in the "Fuze > Documentation" directory. It is preferable that you print a color copy of the document, but displaying it on the screen for them is an acceptable alternative. Make sure all participants in the study view the document in the same way (on paper or on screen).
- Ensure that the same computer and lighting conditions are used for each test.

- Following the testing instructions (located later in this document), have each subject complete each of the eight techniques with the “Fuze.exe” program. Run the tests in the order that they appear in the “Available Techniques” box seen when creating a new test.
- After all eight tests have been completed, follow the procedure for running an Un-Fuze test as outlined below (later in this document). This test must only be completed once for each subject.
- Each test (technique) should be completed no earlier than two days after the previous test has been taken.
- **For technique 4, have the subject thoroughly read a copy of the “Technique 4 Supplement.pdf” document included in the “Fuze > Documentation” directory. You may print out color copies or display the document on the screen for this step.**

Set up

- Copy the entire “Fuze” directory onto the desktop.
- To create a configuration file for each test subject
    - Run the “XMLRandomizer.exe” program from the “Fuze > Applications” directory.
    - Enter the subject’s full first and last name. Use this same name when prompted to input a name in other Fuze applications.

- For the XML input file, browse to the “TestConfig.xml” file in the “Fuze > Test Files” directory.
- For the XML output directory, browse to the “Fuze > Test Files > Config Files” directory.
- Click “Create” to create the file.
- To create files for additional subjects, change the name values and click “Create”. It is not necessary to restart the program.
- Once finished with all subjects, exit the program.

Testing

- Run the “Fuze.exe” program from the “Fuze > Applications” directory.
- From the “File” menu, click “New Test”.
- Enter the subject’s full first and last name. Use the same name that you used to create the XML file.
- For the XML input file, browse to the file that appears like “UserLastName_UserFirstName_TestConfig.xml” and that corresponds to the subject’s name from the “Fuze > Test Files > Config Files” directory.
- For the XML output directory, browse to the “Fuze > Test Files > Output Files” directory.
- Select the subject’s next test from the “Available Techniques” box at the bottom of the window. Do not select the numerically next test from the box. Select the one below the last test taken by the subject. The order of

techniques will be random, this is intentional. If no tests have been taken by the subject, select the first test that appears in the box.

- Record the technique number being taken by the subject. You will need to know this later. The next time the same subject takes a test you will need to select the next one in the "Available Techniques" box.
- Click "Start Test" to begin the test.
- When the subject has completed the entire test, you may select "New Test" from the "File" menu to begin a test for another subject or you may quit the program.

To run an Un-Fuze test

- Run the "Un-Fuze.exe" program from the "Fuze > Applications" directory.
- From the "File" menu, click "New Test".
- Enter the subject's full first and last name. Use the same name that you used to create an XML file and that you used to start other tests.
- For the XML output directory, browse to the "Fuze > Test Files > Output Files" directory.
- Click "Start Test" to begin the test.
- When the subject has completed the entire test, you may select "New Test" from the "File" menu to begin a test for another subject or you may quit the program.

F.2 Participant Instructions

Color Maps

Color maps, also known as color tables, are a simple yet powerful tool for displaying two images as one. The grayscale intensities of the two source images serve as indices in the color map. Looking up the color defined by these indices will give the color that is to be displayed in the joint display.

To demonstrate this concept we will use the color table below.

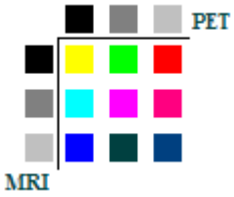

If a point in the registered MRI image has a grey intensity , and the same point in the PET image has a grey intensity , then the joint display of the two images will have color at the same position. Similarly, if the joint display image has a color , we know that the MRI has a grey intensity , and that the PET has a grey intensity .

As a final example consider the MRI and PET images below.

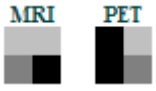

Using the same color table above, we would get the following joint display.

The color tables used in the study have 65536 colors instead of the 9 shown in the example above. Because of this the white spaces in the color table will be eliminated. Often the colors will appear to have a continuous gradient across the color table instead of the distinct colors shown in this example. Also, the grey intensities for the MRI and PET image will not be shown. For each of the color tables it will be assumed that the PET intensity varies gradually from black to white as you move from left to right across the color table. Similarly, the MRI intensity varies gradually from black to white as you move from the top to the bottom of the color table. The above color table displayed as it would be if used in the study is shown below.

Testing

Step 1:

After inspecting the images and reading the description click next to begin the test. This is where you will receive an overview of how the image was constructed.

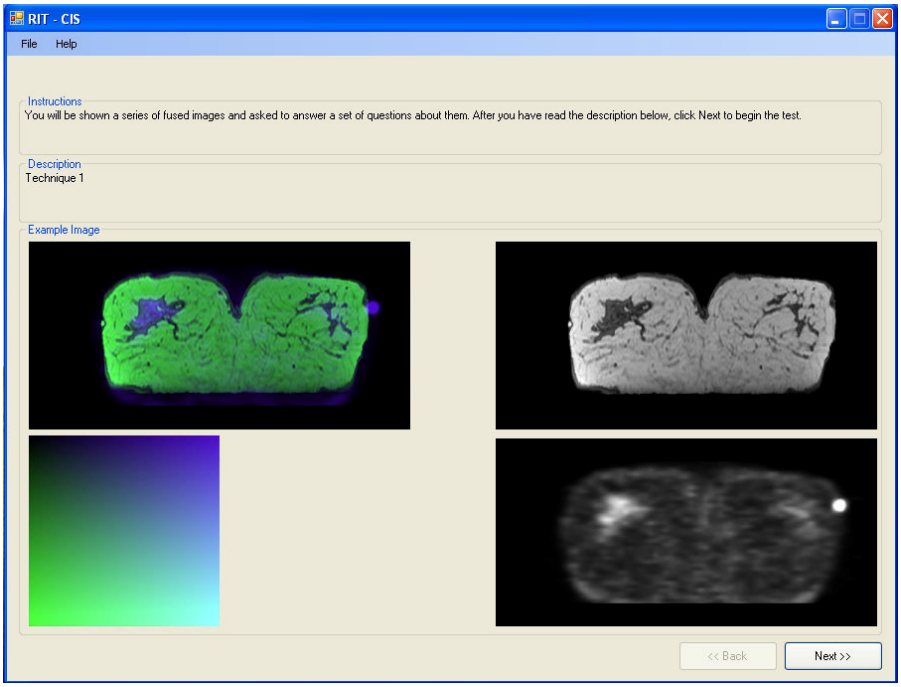

Step 2:

On this screen you will be instructed to click on the most metabolically active region. When performing this task ignore the heart and the fiducial markers.

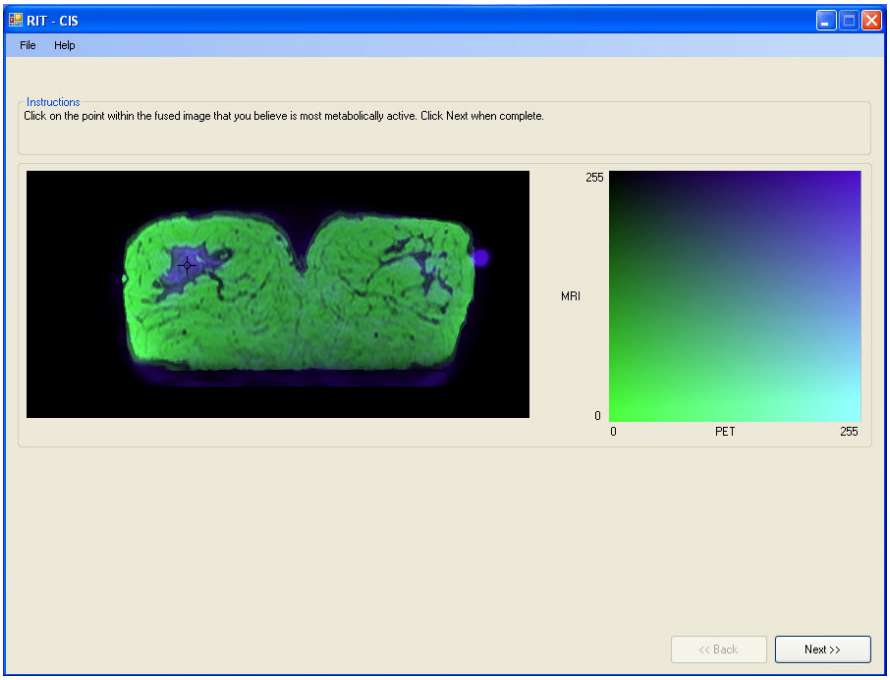

Step 3:

In this step you will be told to select a color, from the color table on the right, which corresponds to the color at the point that you selected in the last step.

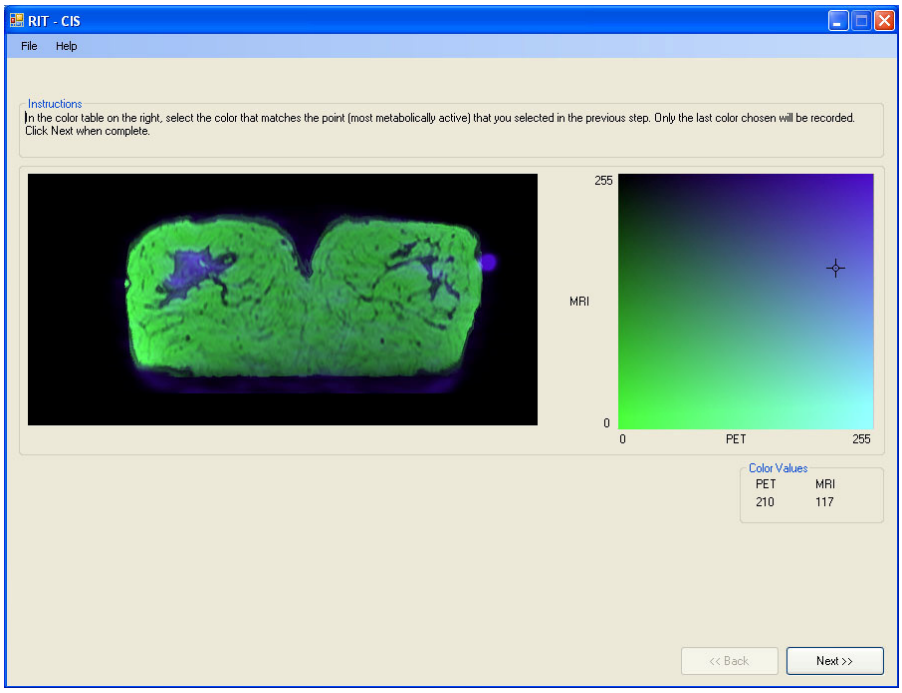

Step 4:

In this step you will be asked to trace around the outline of the metabolically active region. Click and drag the mouse while closely tracing the outline of the active region. Remember to consider both the PET and MRI information when identifying the active region.

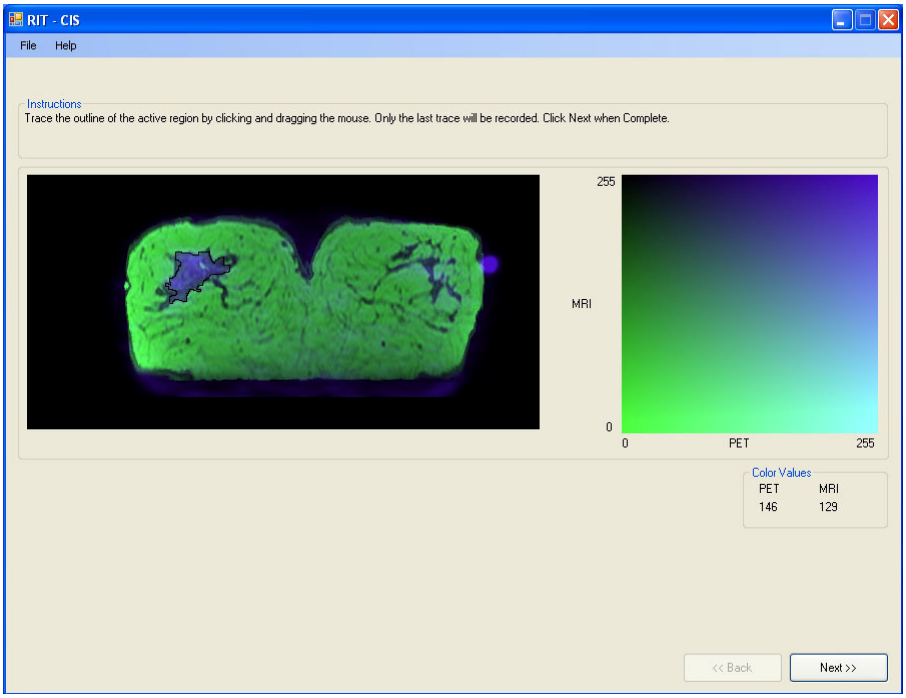

Step 5:

Rate your ability to perform the previous tasks on this image. To give you a starting point, use a rating of 3 the first time you see this screen.

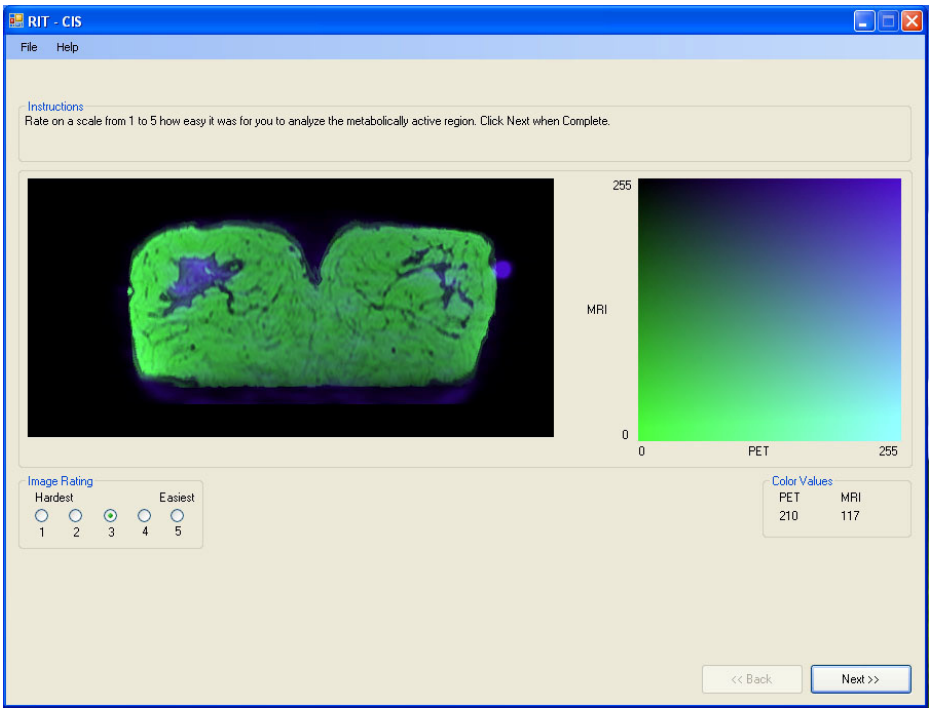

Step 6:

You will repeat this process for nine images total. All nine images will be based on the same joint display technique.

Step 7:

After you complete the rating for the last image, you will be asked to give any additional comments you have about the technique as a whole, and give the technique two ratings. You may write as much or as little as you would like, but the more in-depth the comments we receive are, the more effective our study will be.

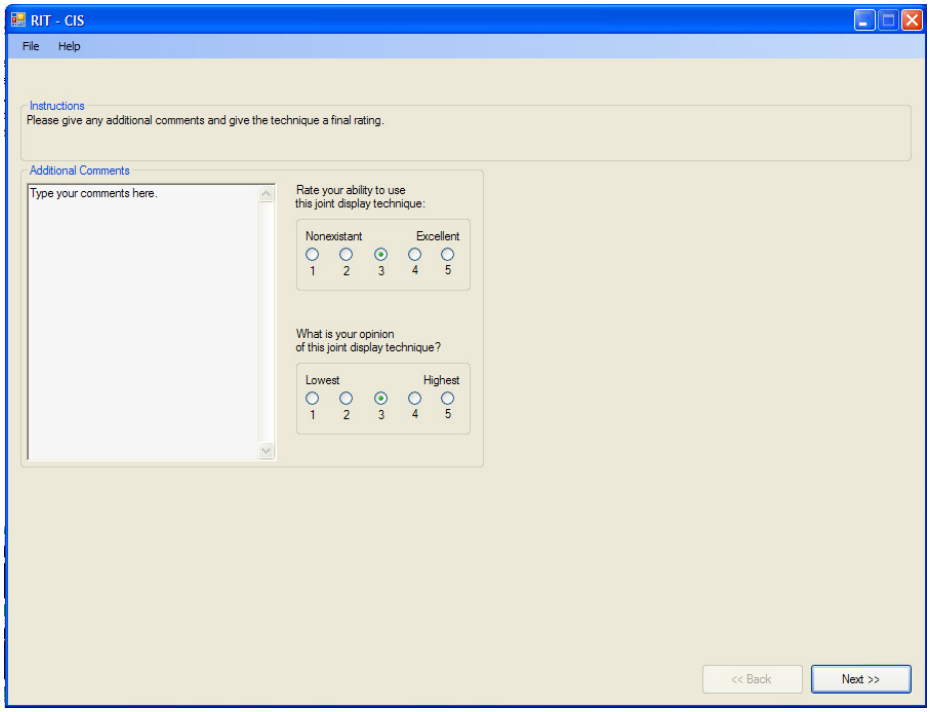

Step 8:

At this point you may quit the test.

F.3 Technique 4 Supplement

With technique 4 a two dimensional color table is not used to create the joint display. Instead the joint display is created by alternating pieces of the MRI and the PET image. First the PET image is colored red. Then the joint image is created by alternating the columns of the red PET image with the MRI image. The image below shows this. Around the edges of the image the brighter grey vertical lines are from the MRI while the alternating dark red lines are from the PET. In the region with the strong red color the red comes from the PET while the alternating dark grey comes from the MRI.

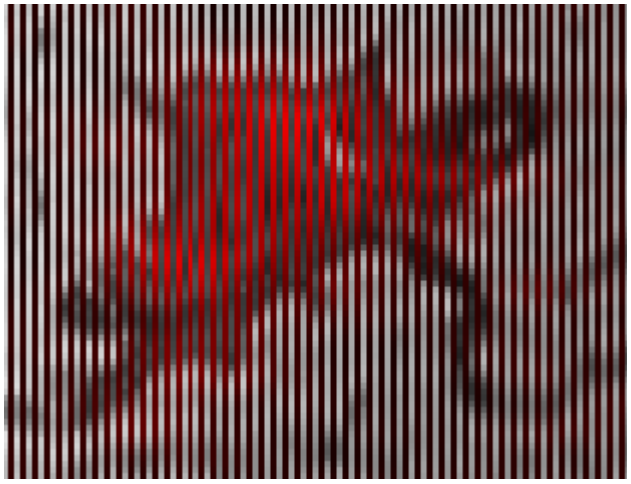

The image above has been enlarged so that the alternating effect is easily visible. In technique 4 this is done at a high resolution that is not always visible to the human eye.

The color table presented for the technique and used in the study was created in a similar manner. When using this color table you are not looking for an exact match of color, but a similar red/grey alternating pattern to that shown in the joint display.

Selected Related Publications

Papers listed approximately in reverse chronological order.

Baum KG, Helguera M, Krol A: "Fusion Viewer: A New Tool for Fusion and Visualization of Multimodal Medical Data Sets." *Journal of Digital Imaging*, in press.

Baum KG, McNamara K, Helguera M: "Design of a Multiple Component Geometric Breast Phantom." *Proceedings of SPIE Medical Imaging*, 6913:69134H, 2008.

Baum KG, Schmidt E, Rafferty K, Helguera M, Feiglin DH: "Investigation of PET/MRI Image Fusion Schemes for Enhanced Breast Cancer Diagnosis." *IEEE Nuclear Science Symposium Conference Record*, 5: 3774-3780, 2007.

Baum KG, Helguera M: "Distributed Wrapper for SimSET Monte Carlo PET/SPECT Simulator." *Journal of Digital Imaging*, 20(Supplement 1):72-82, 2007.

Krol A, Lisi M, Joy S, Kort K, Feiglin DH, Magri A, Tiwari NS, Fawcett J, Baum KG, Helguera M: "Fusion of SPECT and MRI Images for Improved Localization of Parathyroid Adenomas in Patients with Persistent or Recurrent Hyperparathyroidism." *Journal of Nuclear Medicine*, 48(Supplement 2):155, 2007 (abstract only).

Rafferty K, Baum KG, Schmidt E, Krol A, Helguera M: "Multimodal Display Techniques with Application to Breast Imaging." *RIT Digital Media Library*, http://hdl.handle.net/1850/4648, 2007.

Baum KG, Helguera M, Krol A: "A New Application for Displaying and Fusing Multimodal Data Sets." *Proceedings of SPIE Multimodal Biomedical Imaging II*, 6431:64310Y, 2007.

Krol A, Unlu MZ, Baum KG, Mandel JA, Lee W, Coman IL, Lipson ED, Feiglin DH: "MRI/PET Nonrigid Breast-Image Registration Using Skin Fiducial Markers." *Physica Medica European Journal of Medical Physics*, 21(Supplement 1):39-43, 2006.

Baum KG, Helguera M, Krol A: "Genetic Algorithm Automated Generation of Multivariate Color Tables for Visualization of Multimodal Medical Data Sets." *Proceedings of IS&T/SID's Fourteenth Color Imaging Conference*, 138-143, 2006.

Baum KG, Helguera M, Hornak JP, Kerekes JP, Montag ED, Unlu MZ, Feiglin DH, Krol A: "Techniques for Fusion of Multimodal Images: Application to Breast Imaging." *Proceedings of IEEE International Conference on Image Processing*, 2521-2524, 2006.

Krol A, Unlu MZ, Magri A, Lipson E, Coman IL, Mandel JA, Baum KG, Feiglin DH: "Iterative Finite Element Deformable Model For Nonrigid Coregistration of

Multimodal Breast Images." *IEEE International Symposium on Biomedical Imaging*, 852-855, 2006.

Unlu MZ, Krol A, Coman IL, Mandel JA, Baum KG, Lee W, Lipson ED, Feiglin DH: "Deformable Model for 3D Intramodal Nonrigid Breast Image Registration with Fiducial Skin Markers." *Proceedings of SPIE Medical Imaging*, 5747:1528-1534, 2005.

Coman IL, Krol A, Feiglin DH, Lee W, Lipson ED, Mandel JA, Baum KG, Unlu MZ: "Intermodality Nonrigid Breast-Image Registration." *Proceedings of IEEE International Symposium on Biomedical Imaging*, 2:1516-1519, 2004.

Coman IL, Krol A, Mandel JA, Baum KG, Luo M, Lipson ED, Feiglin DH: "Finite-Element Method for Intermodality Nonrigid Breast Registration Using External Skin Markers." *Proceedings of SPIE Medical Imaging*, 5370:1152-1155, 2004.

Krol A, Coman IL, Mandel JA, Baum KG, Luo M, Feiglin DH, Lipson ED, Beaumont J: "Inter-Modality Non-Rigid Breast Image Registration Using Finite-Element Method." *IEEE Nuclear Science Symposium Conference Record*, 3:1958-1961, 2003.